

**UNIVERSITÉ DE LILLE**

École Doctorale Sciences Pour l'Ingénieur

Institut d'électronique de microélectronique et de nanotechnologie

Thèse présentée par **Nathali Alexandra FRANCHINA VERGEL**

Soutenue le 28 février 2020

En vue de l'obtention du grade de docteur de l'Université de Lille

Discipline **Électronique, microélectronique, nanoélectronique et micro-ondes**

# **Dirac antidot superlattices for electrons in III-V semiconductors**

---

## **Super-réseau d'antipoints de Dirac pour les électrons dans les semiconducteurs III-V**

**Thèse dirigée par** BRUNO GRANDIDIER directeur  
CHRISTOPHE DELERUE co-directeur

### **Composition du jury**

<i>Rapporteurs</i>	Guillaume SCHULL Massimiliano MARANGOLO	directeur de recherche à l'IPCMS professeur au Sorbonne Université	
<i>Examineurs</i>	Gilles DAMBRINE Maria TCHERNYCHEVA	professeur à l'Université de Lille directeur de recherche au C2N	président du jury
<i>Directeurs de thèse</i>	BRUNO GRANDIDIER CHRISTOPHE DELERUE	directeur de recherche à l'IEMN directeur de recherche à l'IEMN	





**DIRAC ANTIDOT SUPERLATTICES FOR ELECTRONS IN III-V SEMICONDUCTORS****Abstract**

Graphene is one of the most fascinating materials ever discovered. The achievement of this single-layer carbon atoms in 2004, generated a lot of enthusiasm in the physics community. It represents the first realization of a naturally occurring two-dimensional material. In addition, the unique organization of the carbon atoms confers graphene exotic electronic properties, that are difficult to observe in any other conventional systems. Nevertheless, being a natural material, the carbon sheet comes in only one atomic arrangement: the atoms are organized in a hexagonal lattice and their positions are fixed. Nowadays, the electronic properties of graphene can be obtained by creating artificial materials having a triangular symmetry. These materials, known as "Dirac materials", represent a perfect platform for testing new quantum mechanical phenomena that cannot be observed in graphene.

Based on previous works and predictive atomistic tight-binding calculations, this thesis aims at creating a periodic potential with a honeycomb geometry in a two-dimensional electron gas. The electron gas will be hosted by an InGaAs quantum well grown on an InP layer by molecular beam epitaxy. Low temperature scanning tunneling microscopy and spectroscopy will be employed to characterize the InGaAs quantum well and evaluate the robustness of its two-dimensional nature as a function of the growth parameters. By pushing to their limit high resolution electron-beam or block copolymer lithographies, potential barriers with a honeycomb geometry will be nanopatterned in the InGaAs layer to directly confine the motion of the electrons. Thus, the realization of such hexagonal arrays of pores having between 45 and 20 nm periodicity will allow the formation of Dirac cones and non-trivial flat bands covering energy ranges up to tens of meV. The final Dirac material and its exciting physics will be investigated using low temperature scanning tunneling microscopy and spectroscopy. Based on the versatility of the nanopatterning process, the demonstration of the existence of Dirac cones and flat bands in the InGaAs/InP heterostructure could open new avenues in the engineering of more complex band structures in condensed matter physics.

**Keywords:** Antidot superlattices, III-V heterostructures, band structure engineering, Dirac cones, scanning tunneling microscopy, nano-fabrication

---

**Résumé**

Le graphène est l'un des matériaux les plus fascinants jamais découverts. L'observation de cette monocouche d'atomes de carbone en 2004, a suscité beaucoup d'enthousiasme dans la communauté de la physique. Il représente en fait la première réalisation d'un matériau bidimensionnel naturel. De plus, l'organisation unique des atomes de carbone en réseau hexagonal lui confère des propriétés électroniques exotiques qui n'existent pas dans d'autres systèmes conventionnels. Néanmoins, étant un matériau naturel, les positions des atomes dans un feuillet de graphène sont figées et l'application d'une contrainte pour modifier le réseau ne permet pas d'altérer significativement la structure de bande du graphène. Ces dernières années, les propriétés électroniques du graphène ont été obtenues dans d'autres systèmes artificiels qui possédaient la particularité d'avoir une symétrie triangulaire. Ces matériaux, connus sous le nom de « matériaux de Dirac », représentent une plate-forme parfaite pour tester de nouveaux phénomènes quantiques non observables dans le graphène.

A partir des travaux antérieurs et de prédictions théoriques basées sur la méthode des liaisons fortes, ce travail de thèse vise à appliquer un potentiel périodique avec une géométrie en nid d'abeille à un gaz d'électrons bidimensionnel. Le gaz d'électrons sera créé dans un puits quantique d'InGaAs épitaxié par jet moléculaire sur une couche d'InP. Le puits d'InGaAs et en particulier, sa nature bidimensionnelle, seront d'abord caractérisées par microscopie et spectroscopie à effet tunnel à basse température pour déterminer les paramètres de croissance qui donnent la densité d'états électroniques la plus homogène possible. En poussant à leur limite les lithographies de faisceau d'électrons à haute résolution ou de copolymères à blocs, des barrières de potentiel en nid d'abeilles seront ensuite nanostructurées dans la couche d'InGaAs pour confiner directement le mouvement des électrons. Ainsi, la réalisation de réseaux hexagonaux ayant une périodicité comprise entre 45 et 20 nm permettra la formation de cônes de Dirac et de bandes plates non triviales couvrant des gammes d'énergie allant de quelques meV jusqu'à des dizaines de meV. Le matériau de Dirac obtenu et notamment sa densité d'états seront étudiés en utilisant la microscopie et la spectroscopie à effet tunnel à basse température. En raison de la souplesse des procédés de nanofabrication utilisés, la démonstration de l'existence de cônes de Dirac et de bandes plates dans la bande de conduction de l'hétérostructure InGaAs/InP donne des perspectives intéressantes pour élargir le champ des matériaux artificiels possédant des structures de bandes toujours plus complexes.

**Mots clés :** Super-réseau d'antipoints, hétérostructures à base III-V, ingénierie de structure de bande, cônes de Dirac, microscopie à effet tunnel, nano-fabrication

---

**Institut d'électronique de microélectronique et de nanotechnologie**

Avenue Henry Poincaré – CS60069 – 59652 – Villeneuve d'Ascq – FRANCE



# Acknowledgements

This PhD would not have been possible without the support and guidance received from many people. I would like to present them all my gratitude.

Firstly, I would like to express my sincere gratitude to my supervisors Bruno Grandidier and Christophe Delerue, for giving me this incredible opportunity and endless support during these three years. Thanks for their expertise, motivation, enthusiasm and immense knowledge.

I am also very grateful to Didier Stievenard, for his important contribution to this work. Thanks for all the discussions and advice. Together with Bruno and Christophe, they inspired me by their hardworking and passionate attitude.

Many thanks also go to the members of the Physic research group of the IEMN laboratory. Thanks for sharing their ideas, for giving me support and encouragement during these three years.

I gratefully acknowledge the members of the Epiphy research group, the engineers of Centrale de Micro Nano Fabrication and Plate-forme Centrale Microscopie Champ Proche of the IEMN laboratory. Thanks for their availability in every moment of the day, for their expertise and motivation.

My thanks also go to our collaborators. Thanks for welcoming me as a member of the group and share with me their time and knowledge.

I thank again all of you because every day you remembered me that scientific research is a fascinating world made of exchange, sharing and cohesion.

Thanks to our administrative assistants Florence Senez and Emmanuelle Gillmann for their availability and support.

A huge thanks goes to my family and Mariano for their encouragement, patience and unconditional love. Thanks for their support on whatever choice I make. It represents the strength that keeps me going through all the difficulties. This goal belongs to the whole family.



# Contents

<b>Abstract</b>	<b>iii</b>
<b>Acknowledgements</b>	<b>v</b>
<b>Contents</b>	<b>vii</b>
<b>Introduction</b>	<b>1</b>
<b>1 Context of the thesis</b>	<b>3</b>
1.1 Two-dimensional electron gases . . . . .	4
1.1.1 Quantum confinement in one dimension . . . . .	4
1.1.2 Signature of a 2D-DOS in tunneling spectroscopy . . . . .	6
1.2 Dirac materials . . . . .	10
1.2.1 Graphene . . . . .	10
1.2.2 From graphene to Dirac materials . . . . .	14
1.2.3 Artificial honeycomb lattices from top-down approaches . . . . .	18
1.2.4 Our artificial Dirac material . . . . .	18
<b>2 Experimental Techniques</b>	<b>23</b>
2.1 Molecular Beam Epitaxy . . . . .	24
2.2 Plasma-enhanced chemical vapor deposition . . . . .	26
2.3 Electron beam lithography . . . . .	28
2.3.1 EBL exposure . . . . .	30
2.4 Dry etching . . . . .	31
2.4.1 Reactive ion etching . . . . .	32
2.4.2 Inductively coupled plasma - RIE . . . . .	34
2.5 Scanning Tunneling Microscopy and Spectroscopy . . . . .	35
2.5.1 Basis of the STM . . . . .	36
2.5.2 STS basic principles . . . . .	40
2.5.3 STS energy resolution . . . . .	40
2.5.4 STM based setups . . . . .	42
2.6 Scanning Electron Microscopy . . . . .	45
2.7 Atomic Force Microscopy . . . . .	46
2.7.1 AFM resolution . . . . .	48

<b>3 Resolving the two-dimensional density of states of an <math>\text{In}_{0.53}\text{Ga}_{0.47}\text{As}/\text{InP}</math> quantum well</b>	<b>51</b>
3.1 Defining the critical parameters for the $\text{In}_{0.53}\text{Ga}_{0.47}\text{As}/\text{InP}$ heterostructure . . .	52
3.2 Sample structures . . . . .	53
3.3 Influence of the surface preparation on the surface morphology . . . . .	55
3.4 Measurement of a 2D-DOS . . . . .	58
3.4.1 Tunneling spectroscopy of the $\text{In}_{0.53}\text{Ga}_{0.47}\text{As}/\text{InP}$ heterostructure . . . . .	58
3.4.2 Importance of the hole concentration in the QW . . . . .	63
3.4.3 Transport mechanisms through the quanta states . . . . .	66
3.5 Conclusion . . . . .	69
<b>4 Pushing to the spatial limit the nanoporation of the <math>\text{In}_{0.53}\text{Ga}_{0.47}\text{As}/\text{InP}</math> quantum well</b>	<b>73</b>
4.1 Preliminary tests . . . . .	74
4.1.1 EBL dose test on a thin $\text{SiO}_2$ layer . . . . .	74
4.1.2 Minimizing the lattice disorder: EBL writing tests . . . . .	77
4.2 Creating honeycomb structures on the $\text{In}_{0.53}\text{Ga}_{0.47}\text{As}$ QW using EBL . . . . .	81
4.2.1 Alignment marks fabrication . . . . .	82
4.2.2 The honeycomb structure fabrication . . . . .	84
4.2.3 The final 40 nm periodicity honeycomb lattice . . . . .	88
4.3 Creating honeycomb structures on the $\text{In}_{0.53}\text{Ga}_{0.47}\text{As}$ QW using BCPL . . . . .	89
4.3.1 Honeycomb mask from BCP self-assembly . . . . .	90
4.3.2 Transfer of the BCP mask on the $\text{In}_{0.53}\text{Ga}_{0.47}\text{As}$ QW . . . . .	92
4.3.3 The final 35 nm periodicity honeycomb lattice . . . . .	92
4.4 Hydrogen cleaning and arsenic capping . . . . .	92
4.5 Conclusion . . . . .	93
<b>5 Characterization of the <math>\text{In}_{0.53}\text{Ga}_{0.47}\text{As}/\text{InP}</math> quantum well nanostructured</b>	<b>95</b>
5.1 Morphology of the honeycomb array . . . . .	96
5.2 Interplay between surface states and FL position . . . . .	98
5.3 Electronic features in the DOS . . . . .	101
5.4 Conclusion . . . . .	105
<b>Conclusion</b>	<b>107</b>
<b>Bibliography</b>	<b>109</b>
<b>List of publications</b>	<b>117</b>

# Introduction

The discovery of graphene and its remarkable properties has had an important impact on condensed matter physics and its technological applications. Graphene is a single layer of carbon atoms organized in a honeycomb configuration. Its band structure is unusual: the valence band and the conduction band meet at the K and K' points of the Brillouin zone causing a linear dispersion relation between energy and wavevector. These points, known as Dirac cones, confer graphene massless fermions (Dirac fermions). This property is linked to the geometry of the atomic network and can be achieved in other systems, as long as the triangular symmetry is preserved. On this basis, a new field of research has emerged: the physics of Dirac materials.

Recently, artificial honeycomb structures have attracted wide attention for fundamental research due to the tunable interplay between topology and quasiparticle interactions. They offer a fascinating platform for studying Dirac physics especially thanks to the possibility to vary the physical parameters in regimes which are not accessible in graphene or in other two-dimensional atomic crystals.

One way to create an artificial honeycomb structure consists in modifying the confinement potential of a two-dimensional electron gas. By turning the quantum well obtained from conventional III-V semiconductor heterostructures into a triangular antidot lattice, we will nanofabricate and characterize the electronic properties of this artificial material. The basic idea is to grow an InGaAs quantum well on an InP layer by molecular beam epitaxy and to create a periodic array of cylindrical holes with honeycomb arrangement directly in the quantum well. By doing this, we will form a periodic array of potential barriers for the electrons. The structuration will be obtained by combining high-resolution electron-beam or block copolymer lithographies with highly plasma based dry etching. The main objective is to push the patterning to the limit in order to reach dimensions that are suitable with the detection of the Dirac cones with scanning tunneling spectroscopy at low temperature. These experiments should not only reveal the Dirac nature of the fermions but show the existence of non-trivial band structures predicted in artificial 2D materials.

The dissertation is divided in five chapters. The first one starts with the description of the project framework. We will look through the different ways to create a two-dimensional electron gas and focus on those created in III-V semiconductor heterostructures. The attention will be then turned to the field of Dirac materials and, in particular, to graphene and its unique electronic properties. After that, we will show how it is possible today to observe similar features in artificial honeycomb structures. The chapter ends by presenting the idea behind the realization of a Dirac material from III-V semiconductor heterostructures.

The second chapter describes the experimental techniques required to nanofabricate and characterize the artificial honeycomb structure. It begins by presenting the setups used for the patterning transfer such as plasma-enhanced chemical vapor deposition, electron-beam lithography and dry etching tools, namely the reactive ion etching and the inductively coupled plasma techniques. At this point we will address the characterization techniques that will be

useful to ascertain the quality of the nanofabrication processes and attest the formation of Dirac cones: electron microscopies and scanning probe microscopies. We will stress on the ability of scanning tunneling microscopy to perform spatially resolved spectroscopic measurements.

In the third chapter, we will examine the electronic properties of the as-grown quantum well. We will explore five  $\text{In}_{0.53}\text{Ga}_{0.47}\text{As}/\text{InP}$  heterostructures grown with different conditions and doping levels to find out the sample that yields the most homogeneous two-dimensional electron gas. Scanning tunneling microscopy and spectroscopy will be used to study the morphology and the electronic properties of the semiconductor quantum wells. The experimental results will reveal that the signature of a two-dimensional gas strongly depends on both the hole concentration in the quantum well and the current injected into the quantized states. Supported by scanning tunneling microscopy-induced light emission experiments and four-probe scanning tunneling microscopy transport measurements we will explain the charge-transport mechanisms that account for the presence of a two-dimensional density of states in the tunneling spectra. The chapter ends with a discussion on the possible source of disorders that could lead to deleterious potential fluctuations for the creation of a Dirac material.

The fourth chapter explains all the technological processes that lead to the realization of honeycomb arrays of pores in the  $\text{In}_{0.53}\text{Ga}_{0.47}\text{As}/\text{InP}$  semiconductor heterostructure. Two routes have been followed to determine the resolution limits of the combined lithography/etching processes. The first one, using electron-beam lithography, allows the patterning of triangular array of holes down to 40 nm periodicity on  $60 \times 20 \mu\text{m}^2$  areas. The second one, the block copolymer lithography, allows to reach a periodicity of 35 nm, with the advantage that the honeycomb pattern extends over the whole sample. Fluctuations in the periodicity of the arrays and in the pore size will be assessed and will prompt us to improve the writing method with an electron beam.

The last chapter reports the study of the artificial honeycomb structure obtained from the block copolymer approach by employing scanning tunneling microscopy and spectroscopy at low temperature. Exciting and promising results will be presented. Albeit the number of technological steps, the quality of the sample surface is extremely high. Furthermore, the spectroscopy reveals unique electronic properties that could inspire the physics community for the investigation of new quantum mechanical phenomena.



# Context of the thesis

## Outline of the current chapter

<b>1.1 Two-dimensional electron gases</b>	<b>4</b>
1.1.1 Quantum confinement in one dimension . . . . .	4
1.1.2 Signature of a 2D-DOS in tunneling spectroscopy . . . . .	6
<b>1.2 Dirac materials</b>	<b>10</b>
1.2.1 Graphene . . . . .	10
1.2.2 From graphene to Dirac materials . . . . .	14
1.2.3 Artificial honeycomb lattices from top-down approaches . . . . .	18
1.2.4 Our artificial Dirac material . . . . .	18

Graphene is a single layer of carbon atoms bonded together in a honeycomb lattice that show excellent electronic properties. Its band structure is in fact unique: the valence band and the conduction band intersect at the K and K' points of the Brillouin zone, creating the Dirac cones. A remarkable aspect that emerges from this band structure is the zero effective mass of the charge carriers (Dirac fermions), meaning that the electrons can move in the graphene sheet as if they were massless. This property is directly related to the geometry of the atomic network and can be realized with other materials. Therefore, inspired by the great qualities of graphene, researchers started to look for alternative two dimensional materials offering more "tunable" electronic states, that could give access to the observation of new physical phenomena, and this, represents the heart of our work.

This chapter is divided in two parts. In the first part, we will introduce the concept of two-dimensional electron gas and we will briefly look towards the different ways to obtain such structures. We will assess the effects of the confinement on semiconductor materials and explore their consequences especially in the two-dimensional case: the quantum well. The second part of the chapter will address the rising new field of Dirac materials. We will start with a discussion about graphene and its exciting properties. After that, we will explain how it should be possible today to investigate Dirac physics not only in carbon based systems but also by employing other materials. We will show that one of the possible routes to create a Dirac material is to use two-dimensional electron gases, in particular those findable in III-V semiconductor heterostructures. The idea is to confine the motion of a two-dimensional electron

gas with potential barriers having triangular symmetry. Being the Dirac material for excellence, graphene will be the bridge between the two dimensional electron gases and the artificial Dirac structures.

## 1.1 Two-dimensional electron gases

One of the most significant developments in the domain of semiconductors, both from the point of view of fundamental physics and for the purpose of technological applications, has been the achievement of structures in which the electronic behavior is essentially Two-Dimensional (2D). This means that the carriers are confined in a potential such that their motion is restricted in one dimension, leaving only a free movement in a plane normal to the confining potential. In the case of electrons this system is called Two-Dimensional Electron Gas (2DEG) while the analogous for holes, is known as Two-Dimensional Hole Gas (2DHG).

2DEG exist in different systems<sup>[1]</sup>. They can be observed in transistor-like structures, as Metal-Oxide-Semiconductor Field-Effect transistors (MOSFETs) and High Electron Mobility Transistors (HEMTs). In the case of MOSFETs, the application of a voltage across the structure creates an accumulation region leaving the electrons underneath the gate oxide confined to the semiconductor-oxide interface and forming a 2DEG. On the other hand, HEMTs use a semiconductor heterojunction to confine the electrons in a potential well or between potential barriers. This last type of confinement will be discussed in the next sections.

High-mobility electron gases can also rise at the interface between two insulating perovskite oxides  $\text{LaAlO}_3$  and  $\text{SrTiO}_3$ <sup>[2, 3, 4]</sup> or can be induced by surface doping of low band gap III-V semiconductors<sup>[5]</sup>. By studying the interface of III-V semiconductors with adsorbates it was observed that the interface Fermi Level (FL) is in the Conduction Band (CB) of the semiconductor. In particular, the absorption of Fe atoms on the passivated InAs (110) surface leads to a shift of the FL of 0.1–0.6 eV above the CB minimum. With adequate doping of the semiconductor, the corresponding surface band bending causes the formation of a 2DEG at the surface.

These are some examples about how it is possible to realize 2DEGs. Among all these approaches, one of the most common is the use of semiconductor heterostructures. This topic will be fundamental in the following of the work. But before entering inside this subject, we should remind the reader of the effects of the size confinement in semiconductor materials.

### 1.1.1 Quantum confinement in one dimension

Quantum Confinement Effects (QCE) occur when the dimensions of the material are of the same magnitude as the electron's de Broglie wavelength  $\lambda_e$

$$\lambda_e = \frac{h}{\sqrt{2m_e^*k_B T}}, \quad (1.1)$$

where  $h$  is the Planck constant,  $m_e^*$  is the effective mass of the electron,  $k_B$  is the Boltzmann constant and  $T$  is the temperature. To have an idea, the electron's de Broglie wavelength  $\lambda_e$  for GaAs is 28 nm and for InSb is 62 nm. In general, the length scale corresponding to the QCE regime is typically in the nanoscale for typical semiconductors in which the spatial extension of the electronic wavefunction is comparable with the confined size. As a result of these geometrical constrains, the electrons feel the presence of the material boundaries and respond to these changes in size by adjusting their energy. The confinement produces discreteness of allowed electron energies giving rise to quantum size effects that can be directly observed in the

Density Of States (DOS) (see Figure 1.1). Drastic changes are directly seen from the evolution of the DOS shape with the dimensionality of the confinement.

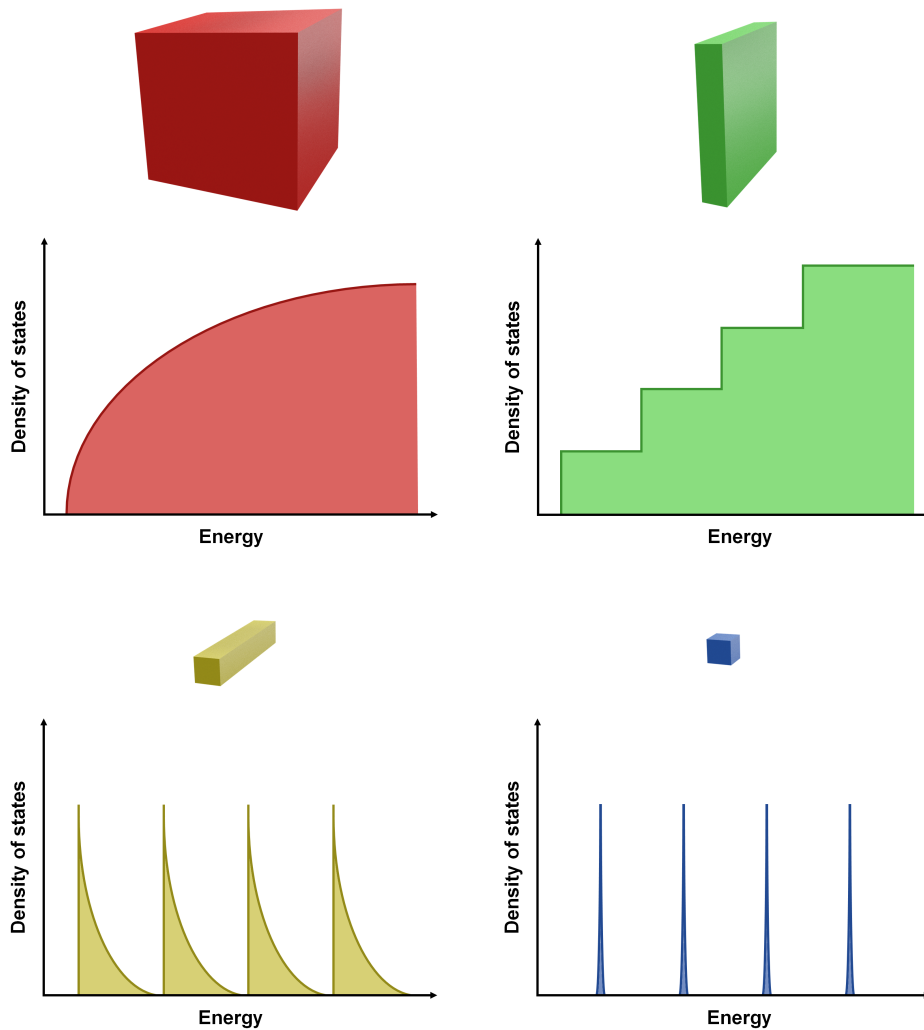


Figure 1.1 – Schematics of DOS as a function of energy in bulk semiconductors (red), quantum wells (green), quantum wires (yellow) and quantum dots (blue).

### The quantum wells

The most successful method to create a 2DEG is to employ semiconductor heterostructures grown Molecular Beam Epitaxy (MBE)<sup>[6, 7]</sup>. Using this technique, tiny towers with different layers of distinct materials superimposed on each other with atomically abrupt interfaces can be created. Employing semiconductors, in particular III-V compound materials, the band structure along the growth direction can be adapted in a nearly arbitrary way<sup>[8]</sup>. In fact, because of the different band gaps in two semiconductors, potential wells and barriers are formed. In this way, in such heterostructures, it is possible to realize 2DEG by confining the motion of the electrons (and/or

holes) in a plane perpendicular to the growth direction. Two different semiconductors with different band gaps can be joined to form a heterojunction [see Figure 1.2 (a)]. As illustrated in Figure 1.2 (b), the discontinuity in either the conduction or the valence band can be used to form potential barriers for the charge carriers. If a thin layer of a narrower-band gap material A, is sandwiched between two layers of a wider-band gap material B, then they form a double heterojunction. If layer A is sufficiently thin for quantum confinement effects to be exhibited, then such a structure is called Quantum Well (QW).

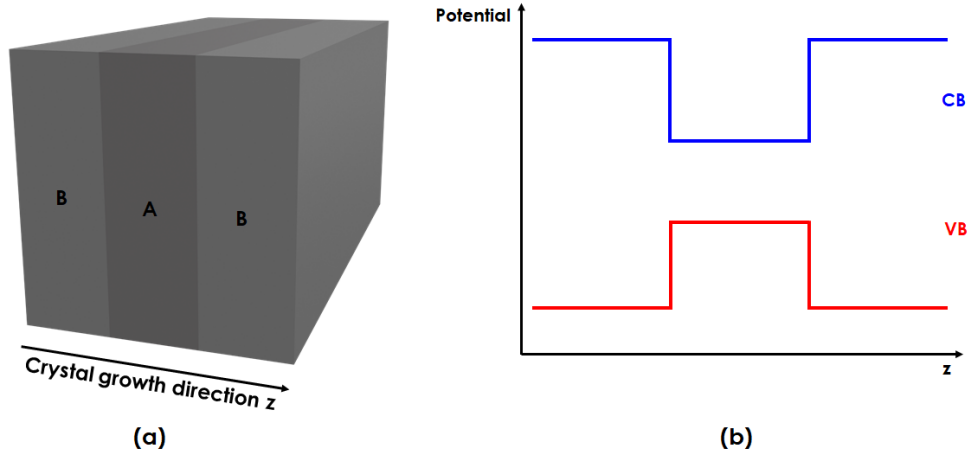


Figure 1.2 – (a) Schematic of the realization of a QW: two different semiconductors A and B with different band gaps  $E_{gA}$  and  $E_{gB}$ , with  $E_{gB} > E_{gA}$  and (b) the resulting band diagram along the growth direction. CB electrons in the QW are bounded on each side by the potential barriers.

### 1.1.2 Signature of a 2D-DOS in tunneling spectroscopy

The electronics properties of a material are of key importance for its transport properties. The electronic structure has been studied by Scanning Tunneling Microscopy (STM) and Spectroscopy (STS), one of the most relevant experimental techniques to provide a direct measurement of the Local Density Of States (LDOS) in quantum semiconductor structures<sup>[9, 10, 11]</sup>. In particular, as showed in Figure 1.1, when the electrons are confined in a QW, the DOS exhibits a sequence of steps related to the quantized energy levels. This signature was directly observed in conductance spectra of cleaved III-V semiconductor QWs, each step corresponding to an electron sub-band in the CB<sup>[12, 13]</sup>.

2DEGs can also be found at the surface of some semiconductors, as for example InAs or InSb. They form from a downward band bending at the surface that leads to a potential well in which the electrons are confined<sup>[14, 15]</sup>. This band bending at the surface is caused by the balancing of the FL between the charged surface states and the space-charge region in the semiconductor crystal. In the case of the p-doped InAs [reported in Figure 1.3 (a)], the filling of surface states leads to a depletion of holes near the surface and thus to the downward band bending. As a consequence, an inversion layer with accumulated electrons is formed at the surface. For example, the research group of R. Wiesendanger, at the University of Hamburg, analyzed a Co island-induced 2DEG on a p-doped InAs (110) by employing low temperature (LT) STS<sup>[16]</sup>. The InAs (110) surface was cleaved *in situ* under ultra high vacuum (UHV) and the Co was deposited by an electron-beam (e-beam) evaporator<sup>[17]</sup>. As illustrated in Figure 1.3 (b), their

curve reveals the presence of three steps that correspond to the three lowest quanta states in the CB demonstrating the 2D behavior. In addition, the authors solved the one-dimensional Poisson and Schrödinger equations to determine the position of the steps and obtained good agreement with the experimental results.

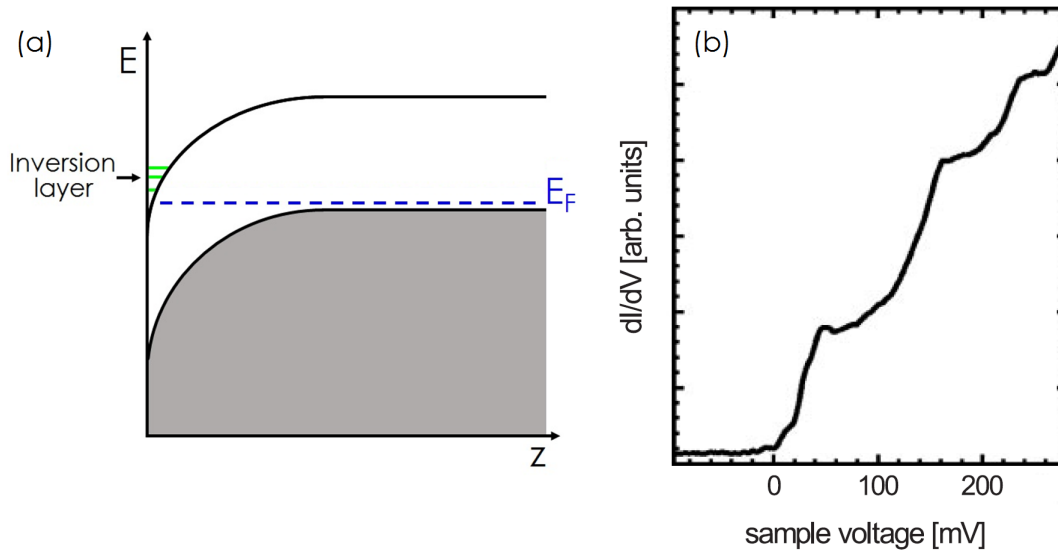


Figure 1.3 – (a) Schematic of a downward band bending that leads to the formation of a 2DEG. (b) Spatially averaged  $dI/dV$  curve of an island-induced 2DEG in 15% Co/p-InAs (110). Figure taken and adapted from [16].

Similar results were obtained using InSb, a smaller band gap material. M. Morgenstern and collaborators studied a p-doped InSb (110) cleaved surface, in which they use a Cs-doping to induce the 2DEG directly at the surface of the low-gap III-V semiconductor [18]. The obtained  $dI/dV$  spectrum reported in Figure 1.4, reveals the presence of two quanta states in the CB, in which only the first sub-band is occupied by electrons since the second is positioned above the FL given by a sample voltage  $V_s = 0$ .

Crucial to the successful observation of a 2DEG is the absence of surface states in the energy range corresponding to the electron sub-bands, a phenomenon which occurs when III-V zinc-blende semiconductor are cleaved to expose a (110) surface [19, 20]. The buckling effect of the adatoms repels the surface states far away from the band edges, allowing a direct tunneling into bulk states such as those corresponding to the low-lying states of the electron gas. However, even in the absence of surface states, the observation of the Two-Dimensional Density of States (2D-DOS) may not be straightforward. First, the probability amplitude distribution varies from one sub-band to the other one. If the maximum of the distribution of a sub-band is too deep below the passivated surface, the contribution of this sub-band to the tunneling current becomes negligible due to the exponential decay of the current with the distance between the STM tip and the surface of the sample [21]. Fluctuations in the distribution of subsurface dopants or point defects also affect the surface potential and as a result might prevent the observation of the 2D-DOS. Next, the electric field induced by the STM tip can penetrate into the semiconductor, causing a local modification of the band. This *Tip Induced Quantum Dot* (TIQD) effect results from the work function difference between sample and tip leading to an electric field, which is screened by the charge carriers of the sample. Depending on the tip work function and shape,

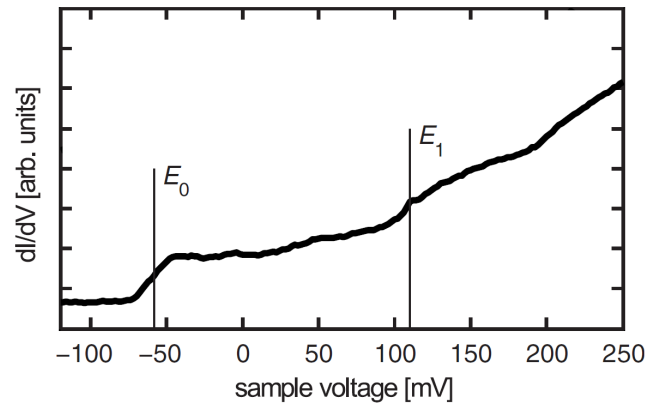


Figure 1.4 – Spatially averaged  $dI/dV$  curve of Cs-induced 2DEG in p-InSb (110). Figure extracted and adapted from [18].

the TIQD may lead to the formation of additional peaks superimposed to the 2D-DOS, that differs from the expected step-like function<sup>[22]</sup>. This effect was reported for example by M. Morgenstern et al. when studying adsorbate-induced 2DES on p-InAs (110). An example of the spatially averaged  $dI/dV$  curve of the Fe-induced 2DES without TIQD is shown in Figure 1.5 (a). It exhibits a clear step-like dependence through two quanta states in the CB. The curves in Figure 1.5 (b), were acquired with a different tip with respect to the one used in the previous case of Figure 1.5 (a). The same tip was employed before and after the Fe deposition. Without

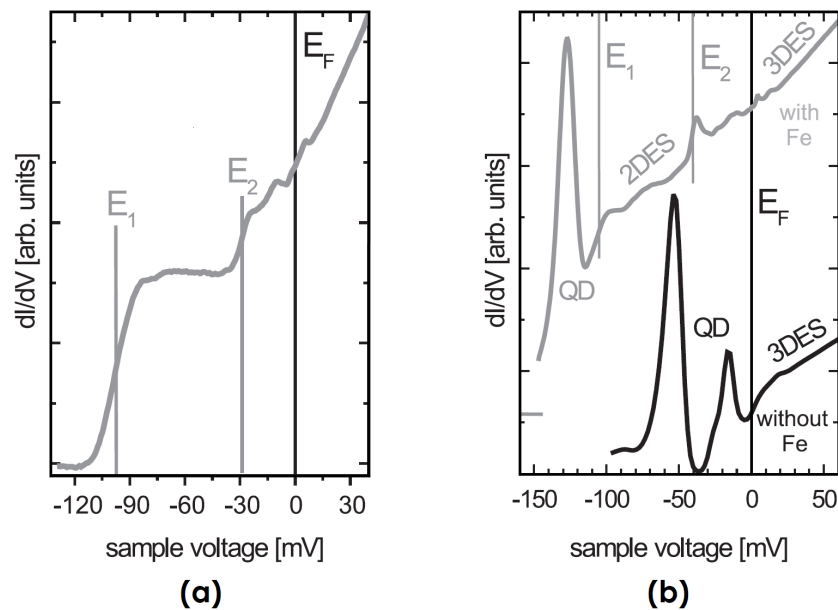


Figure 1.5 – (a) Spatially averaged  $dI/dV$  curve of an adsorbate-induced 2DEG in 2.7% Fe/n-InAs (110); (b) spatially averaged  $dI/dV$  curve of n-InAs (110) (lower curve) and 4.5% Fe/n-InAs (110) (upper curve). Figure taken and adapted from [22].

Fe, two peaks caused by the TIQD appear. On the other hand, with Fe, the first peak shifts to lower energy while the second one found at the edge of the CB disappears. The shift of the lower peak is caused by the adsorbate-induced band bending. In summary, depending on the tip, a clear hallmark of the presence of the 2DES or the TIQD related peaks below the FL can be observed. Finally, the observation of a 2D-DOS does not only depend on the injection of the current into the related states of the electron gas, but also on how the electrons escape.

As discussed in Subsection 1.1.1, confining the electrons in a QW usually implies the existence of potential barriers. Tunneling spectroscopy of a QW requires the transmission probability through the potential barriers to be high enough. A 2D-DOS is then probed<sup>[23]</sup>. Perraud et al. have studied an  $\text{In}_{0.53}\text{Ga}_{0.47}\text{As}/\text{In}_{0.52}\text{Al}_{0.48}\text{As}$  QW structure grown by MBE on lattice-matched InP (111)A. The schematic of their sample is illustrated in Figure 1.6 (a). Electronic states in

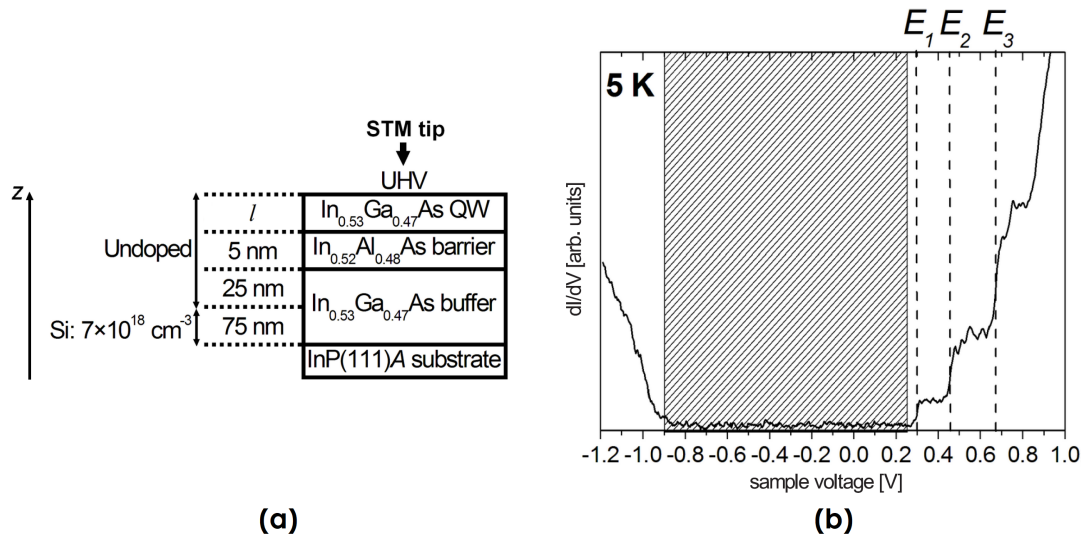


Figure 1.6 – (a)  $\text{In}_{0.53}\text{Ga}_{0.47}\text{As}/\text{In}_{0.52}\text{Al}_{0.48}\text{As}$  QW structure grown by MBE on lattice-matched InP (111)A substrate and (b) typical  $dI/dV$  spectrum acquired at a given point of the QW surface. Figure extracted and adapted from <sup>[23]</sup>.

the  $\text{In}_{0.53}\text{Ga}_{0.47}\text{As}$  surface QW are confined on one side by vacuum and on the other side by the  $\text{In}_{0.52}\text{Al}_{0.48}\text{As}$  barrier. Figure 1.6 (b) shows a typical  $dI/dV$  spectrum acquired at a given point of the  $\text{In}_{0.53}\text{Ga}_{0.47}\text{As}$  QW surface. The signal in the CB has a clear step-like voltage dependence, which again is the typical signature of 2DES. In particular they show three quanta states formed in the CB. The FL is within the band gap, i.e., the sub-bands are empty and this comes from the fact that both the QW and the barrier are un-doped. Finally, they measured a band gap value of 0.8 eV. The authors performed theoretical calculations and found out some discrepancies with the experimental results. The calculation indicates that three sub-bands are formed in the QW, with the sub-band spacings given by:  $E_1 - E_{CBM} = 0.045$  eV (where  $E_{CBM}$  is the CB minimum),  $E_2 - E_1 = 0.117$  eV, and  $E_3 - E_2 = 0.150$  eV. The values found from the  $dI/dV$  spectrum of Figure 1.6 (b) ( $E_2 - E_1 = 0.16$  eV,  $E_3 - E_2 = 0.21$  eV and a band gap of 1.15 eV) were larger than the expected ones. These differences were attributed to a voltage drop in the barrier during STS measurements. The authors performed STS on a reference Si-doped QW ( $1 \times 10^{16}$   $\text{Si} \cdot \text{cm}^{-3}$ ) [the schematic of the sample is illustrated in Figure 1.7 (a)] in direct electrical contact with the STM stage<sup>[24]</sup>. Thus, the sample voltage  $V$  was directly applied between the QW layer and the STM tip, meaning that there was no voltage drop in the  $\text{In}_{0.52}\text{Al}_{0.48}\text{As}$  barrier. In this case they obtained a

good agreement between theoretical and experimental results:  $E_2 - E_1 = 0.13$  e,  $E_3 - E_2 = 0.17$  eV and a band gap of 0.8 eV. Moreover, as we can see from Figure 1.7 (b), the position of the FL is within the first step  $E_1$ , value expected considering the doping of the QW.

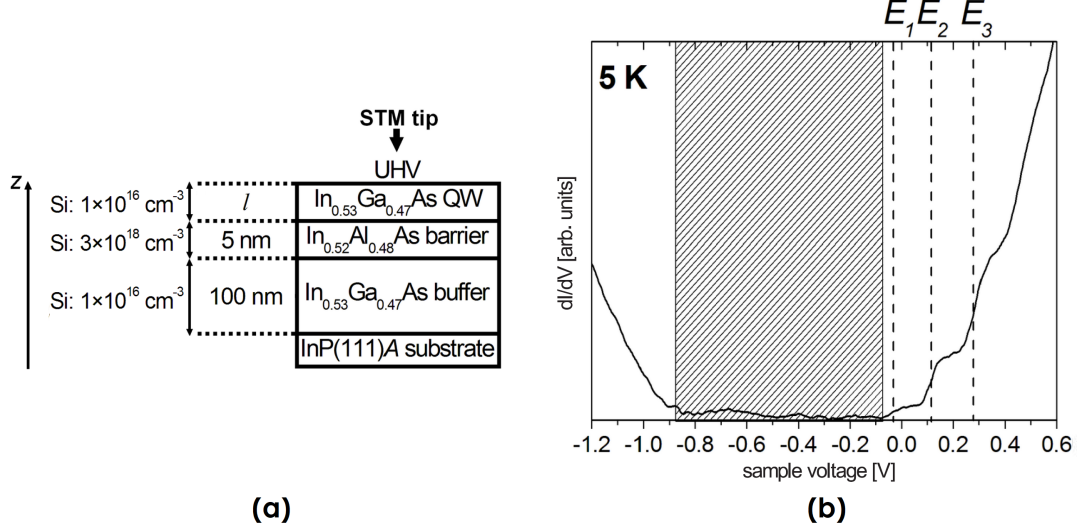


Figure 1.7 – (a)  $\text{In}_{0.53}\text{Ga}_{0.47}\text{As}/\text{In}_{0.52}\text{Al}_{0.48}\text{As}$  QW structure grown by MBE on lattice-matched InP (111)A substrate and (b) typical  $dI/dV$  spectrum acquired at a given point of the QW surface. Figure taken and adapted from [24].

## 1.2 Dirac materials

Let us now turn to the most recognized 2D material, the well-known C-monolayer: Graphene. As discussed in the following of this section, this material present stunning electronic properties. Among them, carriers in graphene are described by the Dirac equation rather than the Schrödinger equation. Together with graphene, there are other structures that obey to the relativistic equation, as for example topological insulators. This emergent behavior in condensed matter systems defines the unifying framework for a class of materials called *Dirac materials*.

### 1.2.1 Graphene

The isolation of graphene in the early 2000s had an important impact on science and technology<sup>[25]</sup>. Fascination with this material stems from the discovery of its remarkable peculiarities that was soon after recognized by the award of the 2010 Nobel Prize in Physics to Andre Geim and Konstantin Novoselov. It is the thinnest material that occurs naturally, just one atom thick layer of carbon atoms arranged in a honeycomb structure [see Figure 1.8 (a)]. The lattice of graphene can be seen as a triangular Bravais lattice with a two-atom basis, A and B. As showed in Figure 1.8 (b), these two sites are not equivalent and each one can form a sub-triangular lattice. The lattice vectors can be written as

$$a_1 = \frac{a}{2}(3, \sqrt{3}), \quad a_2 = \frac{a}{2}(3, -\sqrt{3}), \quad (1.2)$$



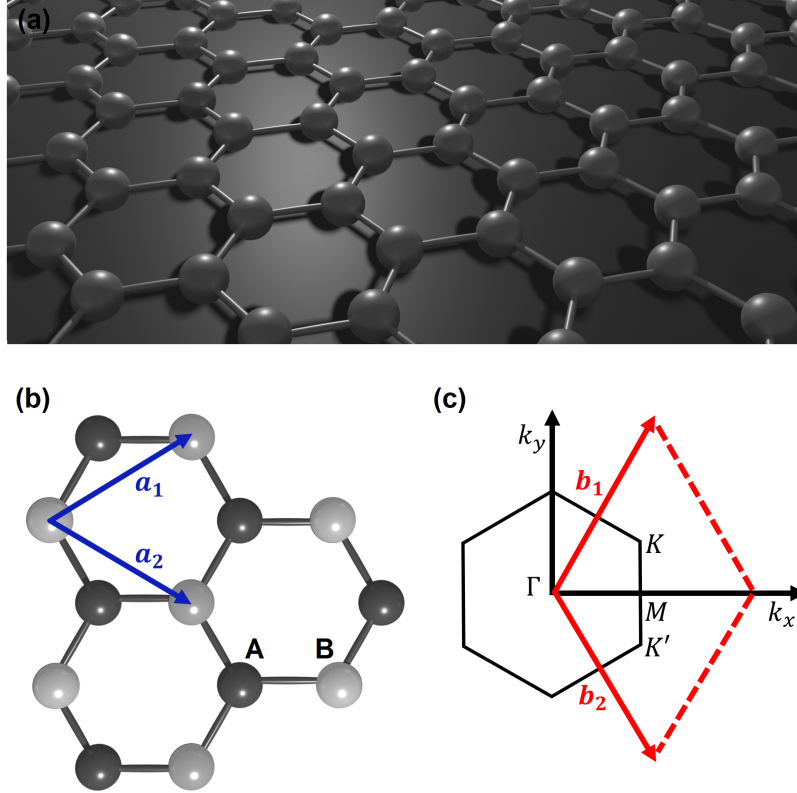


Figure 1.8 – (a) Atomic structure of graphene: a honeycomb monolayer of carbon atoms. (b) Zoom on the lattice showing the vectors  $a_1$  and  $a_2$  that are basis vectors of the triangular Bravais lattice. (c) First Brillouin zone defined by the reciprocal lattice vectors  $b_1$  and  $b_2$  containing the high symmetry point  $\Gamma, M, K$  and  $K'$ .

where  $a$ , is the distance between nearest neighbors carbon atoms and is equal to 0.142 nm. Its reciprocal lattice, which is defined with respect to the triangular Bravais lattice, is depicted in Figure 1.8 (c). As we can see, it has also hexagonal symmetry and the reciprocal lattice vectors are

$$b_1 = \frac{2\pi}{3a}(1, \sqrt{3}), \quad b_2 = \frac{2\pi}{3a}(1, -\sqrt{3}), \quad (1.3)$$

For an atom of the sub-lattice A, the nearest neighbors are in the sub-lattice B at the positions

$$\delta_1 = \frac{a}{2}(1, \sqrt{3}), \quad \delta_2 = \frac{a}{2}(1, -\sqrt{3}), \quad \delta_3 = a(-1, 0). \quad (1.4)$$

From nearest-neighbor tight-binding calculation, the energy dispersion, i.e., energy as a function of lattice momentum, can be obtained<sup>[26]</sup>

$$E(\mathbf{k}) = \pm t\sqrt{3 + f(\mathbf{k})}, \quad (1.5)$$

where  $t$  is the nearest neighbor hopping term and  $f(\mathbf{k}) = 2\cos(\sqrt{3}ak_y) + 4\cos(\sqrt{3}ak_y/2)\cos(3ak_x/2)$ . The relation dispersion is showed in Figure 1.9 through the full band structure of graphene<sup>[27]</sup>.

Two bands are visible, formed from the weakly coupled  $2p_z$  orbital. The lower  $\pi$  bonding band forms the Valence Band (VB) and the upper  $\pi^*$  antibonding band forms the CB. The VB and the CB touch at six points in the Brillouin zone, forming the so-called *Dirac cones*. This point is clearly visible in the zoom in of the band structure of Figure 1.9, close to one of the Dirac points at the K or K' point. In the proximity of these points the energy dispersion relation, is linear, this entails that charge carriers in graphene behave like zero-mass quasi-relativistic particles (Dirac fermions). This dispersion obeys the quantum electrodynamics physics for massless fermions characterized by a Fermi velocity  $v_F$  which is roughly two orders of magnitude smaller than the speed of light  $c$ .

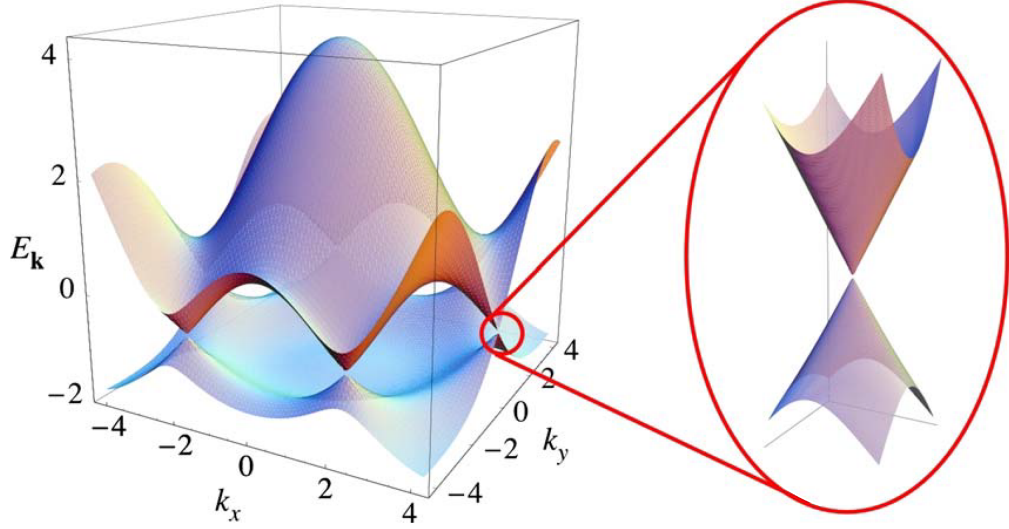


Figure 1.9 – Electronic dispersion of graphene. Right: zoom in of the energy band close to a Dirac cone. Figure taken from [27].

Dirac fermions are also known to lead to interesting properties under magnetic field. In particular, the presence of a perpendicular magnetic field  $B$  allows the appearance of a unique Landau Level (LL) sequence with square-root dependence on field[28],

$$E_N = \text{sgn}(N)\sqrt{2e\hbar v_F^2 |N| B} \quad N = 0, \pm 1, \pm 2, \dots, \quad (1.6)$$

where  $e$  is the electron charge,  $\hbar$  is the reduced Planck constant and  $v_F$  is the Fermi velocity. It is in contrast with the non-relativistic case where the LL energy  $E_n$  is linear in  $B$ . This uncommon response of massless fermions to a magnetic field is highlighted further in its unconventional Quantum Hall Effect (QHE). In fact, as experimentally observed by Novoselov and collaborators[29] and showed in Figure 1.10, the Hall conductivity  $\sigma_{xy}$  of graphene as a function of charge-carrier concentrations, presents pronounced QHE plateaux that correspond to half-integer of the quantum conductance

$$\sigma_{xy} = \left(N + \frac{1}{2}\right) \frac{4e^2}{h} = \nu \frac{4e^2}{h} \quad (1.7)$$

where  $\nu$  is known as the *filling factor*.

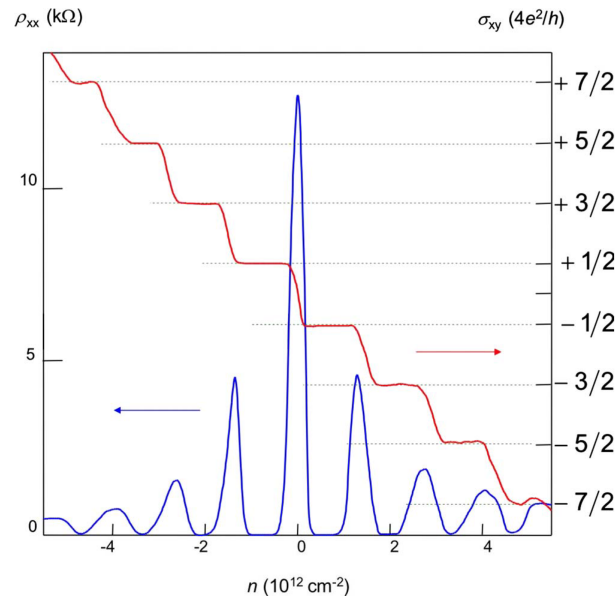


Figure 1.10 – QHE in graphene: Hall conductivity  $\sigma_{xy}$  and longitudinal resistivity  $\rho_{xx}$  as a function of charge-carrier concentration acquired at  $B = 14$  T and  $T = 4$  K. Figure extracted and adapted from [29].

In the previous section, we have observed that the LDOS can be probed by employing STS. Moreover, these measurements can be performed in a magnetic field, giving access to exotic properties as the ones just discussed for graphene. E. Y. Andrei together with her collaborators studied graphene electronically decoupled from a graphite substrate and their results are reported in Figure 1.11 [30]. As expected and reported in the tunneling spectrum (black line) of

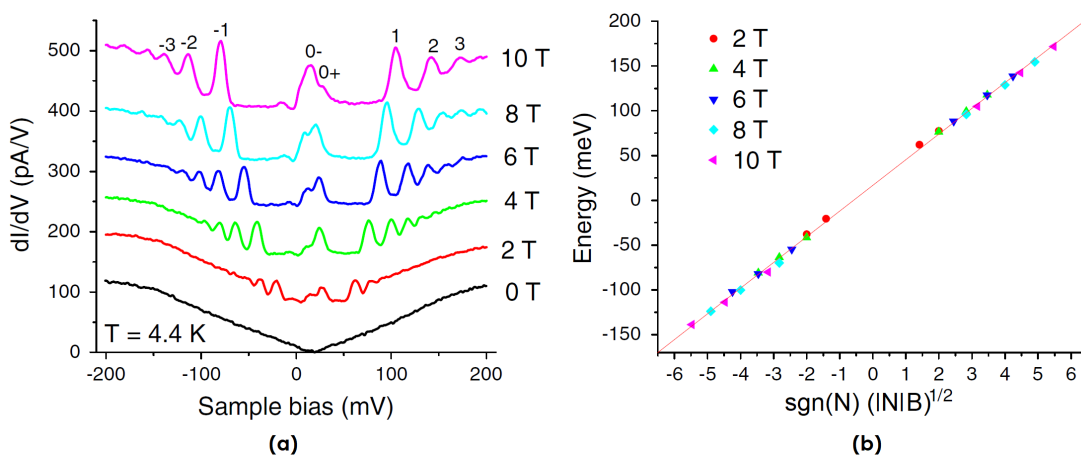


Figure 1.11 – (a) Magnetic field dependence of tunneling spectra on graphene showing a single sequence of LL. LL energy showing square-root dependence on level index and field. Figure taken from [30].

Figure 1.11 (a), the LDOS as a function of energy is linear and vanishes at the Dirac point. In the presence of a magnetic field  $B$  normal to the surface, the spectra develop into a sequence of well-defined LL peaks with the increasing of magnetic field. In Figure 1.11 (b), by plotting the peak energies as a function of  $|N|B^{1/2}$ , the authors show the massless Dirac fermion character.

Another powerful method that allows the access to the DOS are capacitance measurements. Capacitance spectroscopy in fact gives access to the chemical potential change with carrier density variations. In a perfect metal (infinite density of states) no change occurs and no feature is observed. On the other hand, as measured at the University of Manchester<sup>[31]</sup> and illustrated in Figure 1.12, when approaching peculiar points in the band structures (for instance a Dirac cone with a vanishing DOS), strong deviations appear. The quantum capacitance is modeled by a capacitance in series with the geometric one and thus lowers the resulting total capacitance. Nevertheless, albeit capacitance spectroscopy allows a straightforward access to the DOS, it might prove to be experimentally more challenging to perform. In fact, it requires an optimization of sample geometry to reduce parasitic capacitance effects associated with wiring.

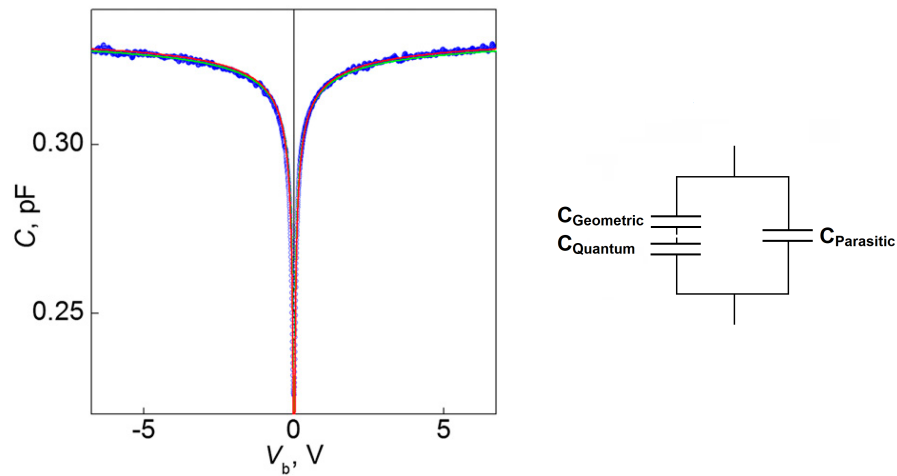


Figure 1.12 – (Left) Quantum capacitance of graphene as a function of gate voltage. Figure extracted from <sup>[31]</sup>. (Right) Element model of the system.

## 1.2.2 From graphene to Dirac materials

In addition to graphene, Dirac fermions and relative properties can emerge in various other 2D systems. As anticipated in the beginning of the section, materials characterized by a band structure with Dirac cones are referred to Dirac materials. In this context important efforts have been undertaken by scientists giving rise to intensive research for alternative 2D Dirac materials<sup>[32, 33]</sup>. One of the main motivations to study particles in artificial lattices is the possibility to vary the physical parameters in regimes which are not accessible in natural graphene. Furthermore, these systems are specifically designed to generate complex band structures, including Dirac cones and non-trivial flat bands. On the theoretical side, different types of artificial lattices have been predicted<sup>[34]</sup>. Among them, silicene and germanene, the equivalent of graphene for Silicon and Germanium, have attracted strong attention since several years because of their importance in microtechnology<sup>[35]</sup>. The graphene-like Si structure was first observed by the group of G. Le Lay in self-aligned nanoribbons by depositing Si on Ag (110)<sup>[38]</sup>. In 2012, the same research team published about the evidence of the existence of silicene<sup>[36]</sup>.

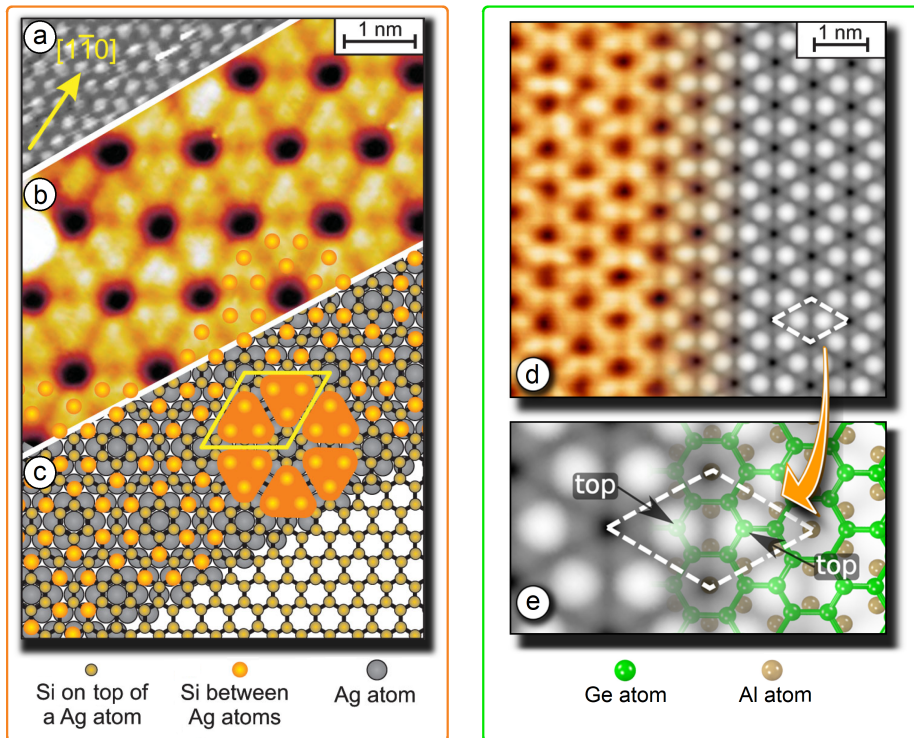


Figure 1.13 – (Orange frame) Silicene: STM images of a) the clean Ag(111) surface and b) the silicene sheet; c) model of silicene on Ag(111). Extracted and adapted from [36]. (Green frame) Germanene: Experimental and calculated STM images of the germanene layer; sketch of the germanene layer on Al(111). Figures taken and adapted from [37].

In this study, they deposited Si on top of an Ag(111) substrate instead of Ag(110). As a result and reported in Figure 1.13 (orange frame), a monolayer of silicene was formed. Similarly to silicene, a germanene 2D layer was realized by depositing Ge on an Al(111) substrate<sup>[37]</sup>. As showed in Figure 1.13 (green frame) the authors obtained a good agreement between the topography and the model. Despite the successful synthesis of Si and Ge honeycomb lattices, the experimental evidence of the Dirac cone remains in these materials quite challenging in both cases.

Symmetry arguments show that Dirac cones appear naturally in lattices with triangular symmetry at the edges of the Brillouin zone. Within this framework, significant studies were done on particles such as electrons, photons, phonons, or atoms moving in artificial honeycomb lattices<sup>[39]</sup>. Theoretical calculations show that the band structure of these artificial superstructures can be extremely rich due to their multi-orbital ( $s, p_x, p_y, p_z, \dots$ ) character<sup>[40]</sup>. This leads to the formation of several Dirac cones and non-trivial flat bands in the  $p$  sector. These non-dispersive bands, in which the particles have an infinite effective mass, are made of localized states induced by the frustration of the ( $p_x, p_y$ ) orbitals in a triangular geometry.

Honeycomb lattices were formed in the group of H. C. Manoharan by manipulating CO molecules on a Cu (111) surface using the metallic tip of a STM<sup>[41]</sup>. In Figure 1.14 (a) a schematic of the STM tip manipulation and the arrangement of the CO molecules is illustrated. A STM



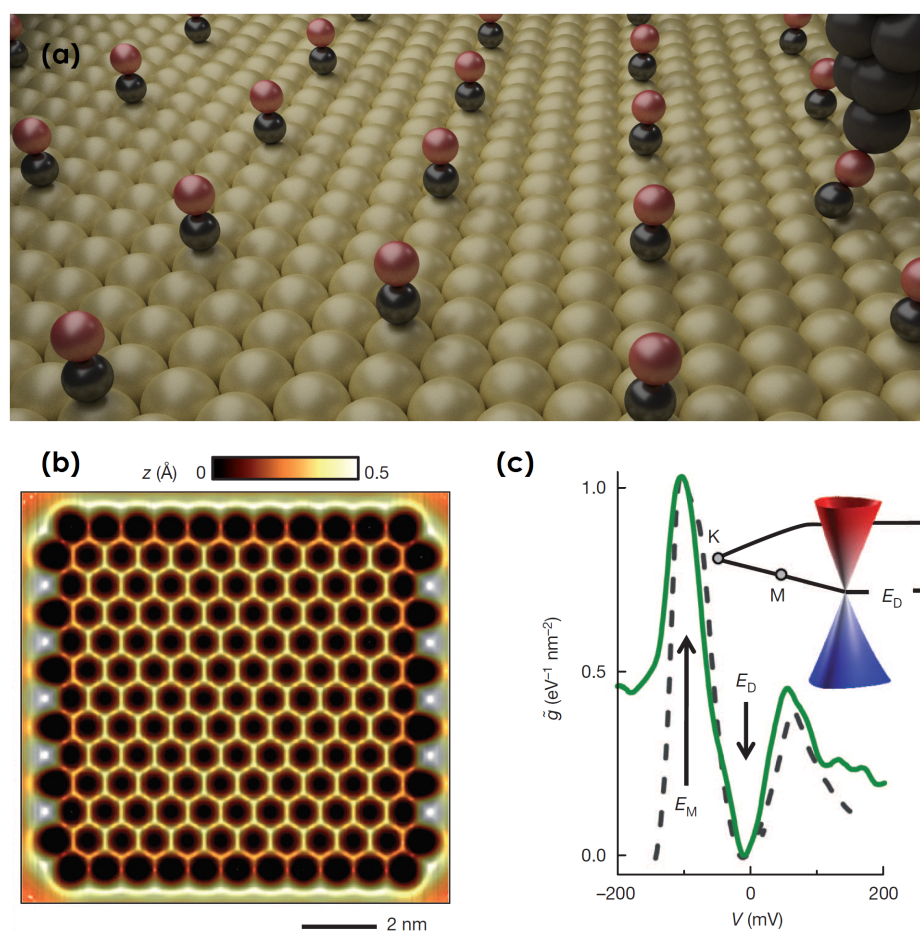


Figure 1.14 – a) Artificial honeycomb lattice obtained from the atomic manipulation of CO molecules on a Cu (111) surface by employing a STM tip; b) STM topography of the artificial lattice composed of 149 CO molecules (lattice constant,  $d = 0.88$  nm; c) spatially averaged and normalized  $dI/dV$  curve. Figures taken and adapted from [41].

image of the built lattice is reported in Figure 1.14 (b). It shows the result of the manipulation of 149 CO molecules. The STS study of this lattice showed the existence of linearly dispersing, massless quasi-particles accompanied by a DOS characteristic of graphene [see Figure 1.14 (c)]. This work represents the first observation of Dirac cones in these kind of artificial graphene-like structures. Dirac cones were also observed in ultracold atoms trapped in the periodic potential of interfering laser beams<sup>[42]</sup> and in microwave photonic crystals<sup>[43]</sup>. Honeycomb superstructures were also built using the process based on the 2D self-assembly of colloidal semiconductor Nanocrystals (NCs) reported in Figure 1.15<sup>[44]</sup>. A suspension of PbSe NCs is cast onto a surface of an immiscible liquid, ethylene glycol, and the solvent is then evaporated at room temperature (RT). During the evaporation, extended sheets of square lattices are formed with a thickness of one NC monolayer. To obtain a honeycomb arrangement of the NCs instead of the square one, the reaction rate was lowered. The final lattice, made by PbSe or CdSe NCs when Pb atoms are further replaced by Cd atoms through a cationic exchange process, was characterized by a

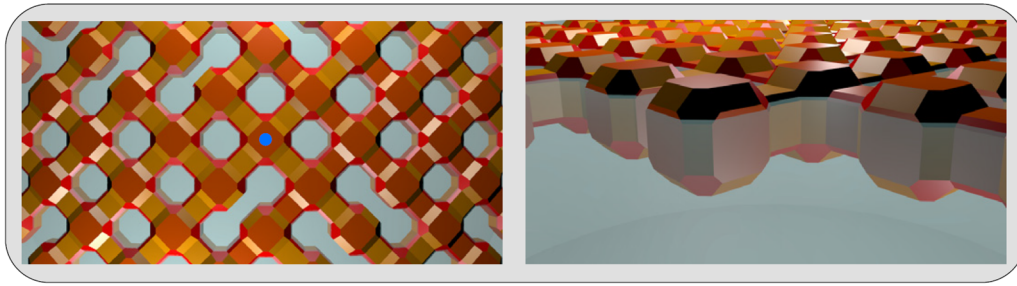


Figure 1.15 – Square lattice based on the 2D self-assembly of colloidal semiconductor NCs. Figure taken and adapted from [44].

lattice constant of around 5 nm<sup>[45]</sup>. Atomistic calculations for CdSe NCs superlattice show the formation of Dirac cones at several energies, non-trivial flat bands, and topologically protected edge states. Nevertheless, the disorder of the lattices does not allow to probe these predictions.

Dirac physics can also emerge in lattices with different geometries such as the Lieb<sup>[46]</sup> and Kagome<sup>[47]</sup> lattices. The Lieb lattice, characterized by three atoms in a square unit cell [see Figure 1.16 (a)], was soon realized as photonic Lieb lattice formed by an array of optical waveguides<sup>[48]</sup>. This work reported about the first experimental observation of a flat band in these kind of structures. Interesting results were also obtained by creating a Lieb lattice by atomic manipulation<sup>[49]</sup>. The structure was in fact created by the surface state electrons of Cu (111) confined in an array of carbon monoxide molecules positioned by using an STM tip. An

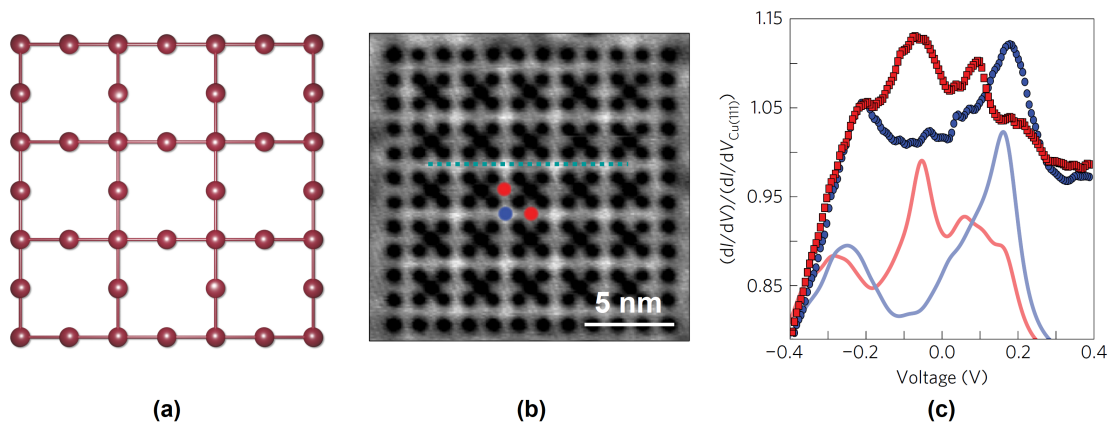


Figure 1.16 – a) Schematic of the Lieb lattice; b) STM image of the artificial lattice formed by manipulating CO molecules on Cu (111); c) Normalized  $dI/dV$  spectra acquired above edge (red squares) and corner (blue circles) sites and LDOS at these sites calculated using the tight-binding method (solid lines).

STM image of this study is reported in Figure 1.16 (b). STS measurements were performed in different parts of the lattice (underlined by the blue and red circles in the STM image). As one can see from Figure 1.16 (c), in the spectrum acquired above the corner, the LDOS shows a minimum that should correspond to a Dirac cone. On the other hand, the curve presents a maximum that can be assigned to the flat band. The authors performed also theoretical calculations [indicated

by the blue and red lines in Figure 1.16 (c)] and the results are in good agreement with the STS curves. This work opened the path to the realization of other 2D geometries for which important properties have been already predicted. An example is the Kagome superlattice. Such a lattice was experimentally realized as electronic Kagome lattice on the surface of a twisted multilayer silicene<sup>[50]</sup>. The twisting was done by interlayer manipulation using a STM tip. The derivative of the conductance spectrum acquired on the lattice shows a typical flat band peak.

### 1.2.3 Artificial honeycomb lattices from top-down approaches

A more natural way to fabricate artificial graphene materials is by modulating the potential seen by a 2DEG found in conventional III-V semiconductor heterostructures. Following previous works on laterally modulated superlattices<sup>[51]</sup>, it was proposed to form a triangular lattice of antidots in the active layer in order to confine the electrons in an interconnected honeycomb network. The nodes of the network play the role of the carbon atoms in graphene. Pioneering works in this field used a modulation-doped AlGaAs/GaAs heterostructure subjected to a lateral potential with triangular geometry<sup>[52, 53]</sup>. An array of pillars with honeycomb symmetry is created at the surface of the semiconductor by employing Electron Beam Lithography (EBL) and dry etching. The dimension of the system remains quite large in terms of Dirac fermions detection: the lattice parameter was 130 nm, inducing a too small Dirac band to be identified. Important improvements in the reduction of the lattice parameter size were achieved few years

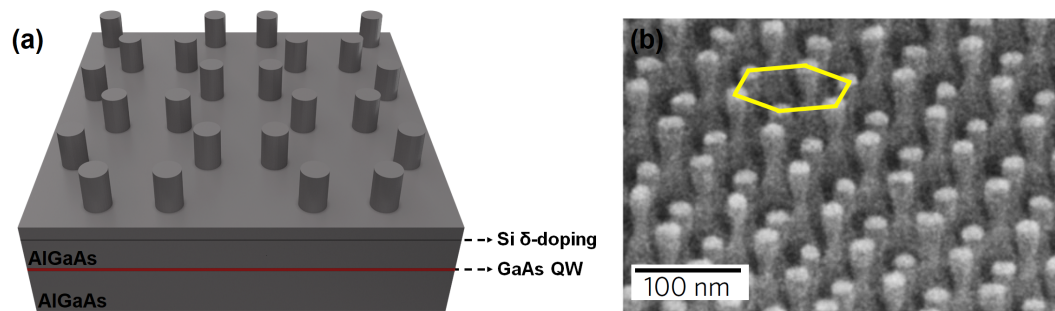


Figure 1.17 – a) Illustration of the artificial graphene structure and b) SEM image of the lattice. Figure taken and adapted from<sup>[54]</sup>.

later at Columbia University by S. Wang et al<sup>[55]</sup>. In this work the authors employed high resolution EBL and Reactive Ion Etching (RIE) to create the artificial honeycomb lattices of pillars with period as small as 50 nm on GaAs/AlGaAs QWs. The same research group have reported about the existence of Dirac physics in these artificial graphene material, by using resonant inelastic light-scattering<sup>[56, 54]</sup>. Nevertheless, direct evidence of massless fermions has not been reported yet.

### 1.2.4 Our artificial Dirac material

The idea of our project is similar to the one of S. Wang and coworkers just discussed in the last section. In our case, the 2DEG will be created in a QW inserted at the surface, between a barrier and the vacuum. Instead of modulating the electron gas by realizing a periodic electrostatic potential with honeycomb topology on the surface, we will act directly inside the 2DEG. By creating a periodic array of cylindrical holes straight in the active layer these holes



will act as potential barriers for the electrons inside the 2DEG. In this work, we will use an  $\text{In}_{0.53}\text{Ga}_{0.47}\text{As}/\text{InP}$  QW heterostructure. The choice of the materials is justified by several points:

- The low effective mass of InGaAs ( $0.041 m_0$  for  $\text{In}_{0.53}\text{Ga}_{0.47}\text{As}$  lattice-matched to InP) enhances QCE and leads in superlattices with wider mini-bands and larger energy splitting between them.
- The heterostructures are based on standard materials, they can be grown by MBE on InP substrates using well-established routes, leading to electron gases characterized by high carrier mobilities ( $> 130\,000 \text{ cm}^2/\text{V.s}$  at 77 K)<sup>[57]</sup>.
- The technological processes are also well mastered. In particular, the different materials composing the heterostructures can be selectively etched, which is of great advantage for the realization of complex patterns.

Furthermore, these materials are extensively used as a primary building block for electronic devices, thus playing a crucial role in modern semiconductor industry. The  $\text{In}_{0.53}\text{Ga}_{0.47}\text{As}$  ternary compound semiconductor lattice matched to InP is widely used as channel for high frequency III-V MOSFETs, due to its high electron mobility<sup>[58]</sup>. With its light emission in the wavelength range from 1.3 to 1.6  $\mu\text{m}$ , close to the minimum attenuation and dispersion in optical fibers, it is also a key material for fiber-optic communication systems<sup>[59]</sup>. The optical properties of these QW structures were first studied, with photoluminescence (PL) or photoconductivity techniques<sup>[60, 61, 62]</sup>, leading to the determination of the optical gap as well as the ratio of the CB to VB discontinuities. Radiative and non-radiative lifetimes were also determined, versus the QW width and the doping level, both experimentally and theoretically<sup>[63, 64, 65, 66]</sup>. They range typically from ns to a few 10 ns.

Band structures, predicted by Athmane Tadjine and Christophe Delerue using a tight-binding approach, are reported in Figure 1.18. The calculations were done for arrays with periodicities  $a = 45 \text{ nm}$  and  $a = 30 \text{ nm}$ , with hole radius  $r = 13.5 \text{ nm}$  and  $r = 9 \text{ nm}$  respectively. To obtain those results, they considered a 10 nm thick  $\text{In}_{0.53}\text{Ga}_{0.47}\text{As}$  layer including a triangular array of cylindrical holes filled with InP, a higher band gap material. The two lowest bands look very similar with the  $\pi - \pi^*$  bands found in graphene. These bands result from the nearest neighbor coupling between  $s$ -like states localized at the vertices of the honeycomb lattice. The linearity between energy and wavevector is clearly present at  $K$  for both lattices. As we can see from Figure 1.18, the width of the linear dispersion increases with the reduction of the periodicity, reaching 5 meV for  $a = 30 \text{ nm}$ . Higher in energy, there is a non-trivial flat band coming from the frustration of the  $p$ -like states in a triangular geometry. As observed in Section 1.2.2, these bands are particularly interesting for exploration of correlated electron systems.

The realization of such structures should allow us to reveal the multi-orbital character of the system, a physical phenomenon that has not been demonstrated in electronic systems and is absent in graphene. Our laboratory has a good expertise in nanolithography of Si and III-V materials. Honeycomb structures tests were created in 10 nm thick Silicon dioxide  $\text{SiO}_2$  layer deposited on InP samples by employing EBL and RIE etching. 45 nm of Poly(methyl methacrylate) (PMMA) 950 K resist were used to etch 10 nm of  $\text{SiO}_2$ . The results showed good patterns with periodicities  $a = 100 \text{ nm}$  and  $a = 50 \text{ nm}$ , with hole radius  $r = 60 \text{ nm}$  and  $r = 28 \text{ nm}$  respectively. A square lattice of 14 nm holes separated by  $a = 44 \text{ nm}$  has already been obtained on Si substrate<sup>[67]</sup>. Of course, due to higher proximity effect on III-V materials than on Si, we expect bigger holes sizes. Therefore, the use of EBL could be limiting in the achievement of arrays with periodicities smaller than 40 nm. For this reason, we will also test an artificial

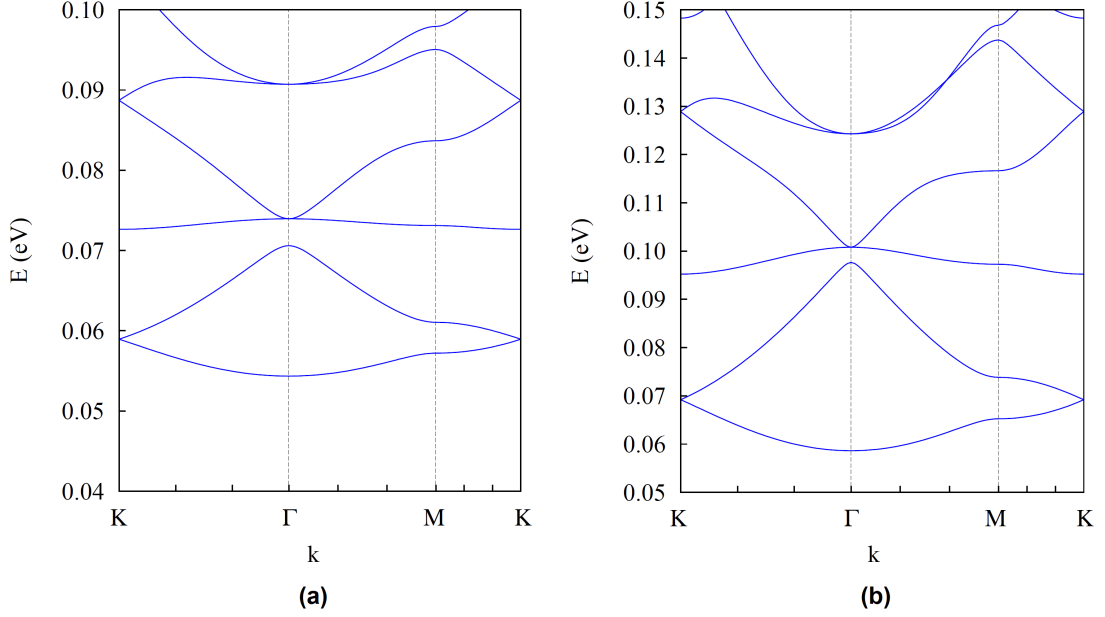


Figure 1.18 – CB structures predicted for a nanoperforated  $\text{In}_{0.53}\text{Ga}_{0.47}\text{As}$  QW with a honeycomb structure when the barrier material is InP: (a) Periodicity  $a = 45$  nm and hole radius  $r = 13.5$  nm (b)  $a = 30$  nm and  $r = 9$  nm. The  $\text{In}_{0.53}\text{Ga}_{0.47}\text{As}$  QW thickness is  $t = 10$  nm.

graphene-like InGaAs/InP heterostructures with a second approach known as Block Copolymer Lithography (BCPL). This technique, based on the self-assembly copolymer behavior, which leads to the formation of spatially periodic patterns, could push the periodicity of the arrays down to 20 nm<sup>[68]</sup>. In Figure 1.19 we report tight binding calculations performed for arrays having  $a = 30$  nm and  $a = 22$  nm, with  $r = 8.4$  nm and  $r = 6.2$  nm respectively. In this case we considered an infinite barrier instead of the InP one. Extremely rich band structures are again visible for both lattice periodicities, characterized by a Dirac cone and a non-trivial flat band. In particular Figure 1.19 (b) reveals a dispersion relation between energy and wavevector linear over  $\sim 14$  meV.

To reveal the electronic properties of the antidot superlattices, LT-STs measurements will be carried out. For this purpose, we must ensure that the disorder in the superlattice is weak enough so that the band structure is preserved. Different sources of disorder have to be taken into account in order to build the appropriate structures. Firstly, disorder could arise from monolayer roughness along the interface between the QW and the barrier underneath, that can lead to an energy shift of the ground state. In our case, such a shift should be in the meV range so that, it is small enough to preserve the band structure of the superlattice, at least in the network with a 30 nm periodicity. As second source of disorder can come from the phase separation in the ternary alloys that could cause spatial fluctuations of the band offset. As observed from S. Perraud and coworkers<sup>[23]</sup>, the spatial variations of the CB offset in an InGaAs/InAlAs heterostructure cause a shift of the ground state smaller than 1 meV and thus can be considered as weak. Other sources of disorder, could arise during the STs measurements as a consequence of the proximity between the metallic tip and the semiconducting surface, as for example a shift of the bands in the semiconductor and in some cases can even induce the formation of a quantum dot under the tip (see Section 1.1.2 the discussion about the TIQD). To avoid these effects, the  $\text{In}_{0.53}\text{Ga}_{0.47}\text{As}$

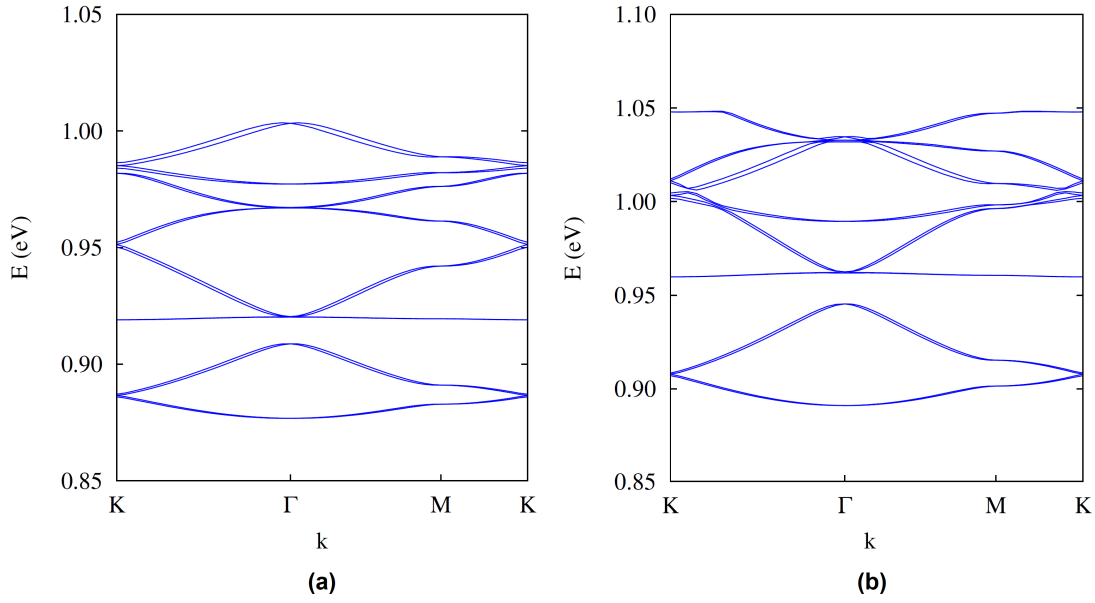


Figure 1.19 – CB structures predicted for a nanoporated  $\text{In}_{0.53}\text{Ga}_{0.47}\text{As}$  QW with a honeycomb structure when the barrier is infinite:  $a = 30$  nm and  $r = 8.4$  nm (a),  $a = 22$  nm and  $r = 6.2$  nm (b). The  $\text{In}_{0.53}\text{Ga}_{0.47}\text{As}$  QW thickness is  $t = 10$  nm.

QW should be highly doped so that the voltage applied between the tip and the sample drops in the vacuum barrier and/or the  $\text{In}_{0.53}\text{Ga}_{0.47}\text{As}$  surface should contain a high density of surface states in the band gap to screen the electric field in the STM junction. As we have discussed at the end of Section 1.1.2, the presence of surface states induces a FL pinning at the semiconductor surface that depends on the nature and level of the doping and can lead to the formation of a triangular potential well (or accumulation layer) along the growth axis of the sample. In the case of a n-type  $\text{In}_{0.53}\text{Ga}_{0.47}\text{As}$  (001)-(2x4) surface, a midgap FL pinning causing an upward band bending was observed<sup>[69]</sup>. On the other hand, the FL is expected to be close to the VB for a p-type  $\text{In}_{0.53}\text{Ga}_{0.47}\text{As}$  (001)-(2x4) surface due to the absence of kinks in the dimer-vacancy rows of the (001) surface, as observed by Pashley et al. for the GaAs (001)-(2x4) surface<sup>[70]</sup>. Therefore, the  $\text{In}_{0.53}\text{Ga}_{0.47}\text{As}$  QW will be doped with a hole density in the range  $10^{18}$ - $10^{19}$   $\text{cm}^{-3}$  to satisfy the flat band conditions and make the antidot lattice barely sensitive to the voltage applied between the STM tip and the sample.

Our III-V semiconductor heterostructures will be grown by MBE. A sketch of a typical as-grown sample is reported in Figure 1.20 (a). They will be first characterized with STS to assess the experimental DOS structure and verify its 2D nature. Based on these results, the growth will be optimized to minimize the disorder effects described above. Once the best growth conditions and sample preparation scheme have been established, we will be ready to start the nanofabrication processes. As anticipated, we will follow two different routes to pattern the triangular array of holes in the  $\text{In}_{0.53}\text{Ga}_{0.47}\text{As}$  QW: EBL and BCPL. After that, the pattern transfer will be done employing two different dry etching techniques, namely RIE and Inductively Coupled Plasma (ICP). The nanofabrication will be followed step by step using Scanning Electron Microscopy (SEM) and Atomic Force Microscopy (AFM). Once ready [as showed in Figure 1.20 (b)], the final samples with the triangular array of holes in the  $\text{In}_{0.53}\text{Ga}_{0.47}\text{As}$  QW, will be probed with STM

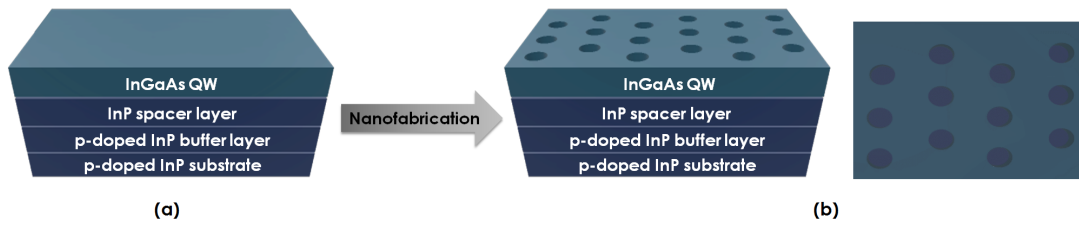


Figure 1.20 – (a) Cross-sectional of the as-grown heterostructure and (b) cross-sectional top and side views of structures made of an  $\text{In}_{0.53}\text{Ga}_{0.47}\text{As}$  layer including a triangular array of cylindrical holes. Structures not in scale.

and STS. This last step will require to develop UHV compatible cleaning processes and maybe regrowth processes to recover clean and well-ordered  $\text{In}_{0.53}\text{Ga}_{0.47}\text{As}$  surfaces.

# Experimental Techniques

## Outline of the current chapter

---

<b>2.1 Molecular Beam Epitaxy</b>	<b>24</b>
<b>2.2 Plasma-enhanced chemical vapor deposition</b>	<b>26</b>
<b>2.3 Electron beam lithography</b>	<b>28</b>
2.3.1 EBL exposure . . . . .	30
<b>2.4 Dry etching</b>	<b>31</b>
2.4.1 Reactive ion etching . . . . .	32
2.4.2 Inductively coupled plasma - RIE . . . . .	34
<b>2.5 Scanning Tunneling Microscopy and Spectroscopy</b>	<b>35</b>
2.5.1 Basis of the STM . . . . .	36
2.5.2 STS basic principles . . . . .	40
2.5.3 STS energy resolution . . . . .	40
2.5.4 STM based setups . . . . .	42
<b>2.6 Scanning Electron Microscopy</b>	<b>45</b>
<b>2.7 Atomic Force Microscopy</b>	<b>46</b>
2.7.1 AFM resolution . . . . .	48

---

The realization of the artificial Dirac material of interest requires the use of different experimental setups. This part of the manuscript presents the techniques employed during this thesis work. We will start by introducing the molecular beam epitaxy, technique used for the growth of our semiconductor heterostructures. After that, we will describe all the tools employed for the realization of the artificial honeycomb lattice in the  $\text{In}_{0.53}\text{Ga}_{0.47}\text{As}$  QW, in the same order as the technological steps. We will discuss about the plasma-enhanced chemical vapor deposition (PECVD), the EBL and the dry etching tools, namely the RIE and the ICP techniques. At this point we will focus the attention on the characterization techniques. We will begin with STM and STS, powerful techniques used to characterize the as-grown samples and the final artificial honeycomb lattices, both from the morphological and electronic point of view. The chapter will end with a brief presentation of the SEM and the AFM, systems used to check the state of the nanofabrication step by step.

## 2.1 Molecular Beam Epitaxy

The MBE was developed by Alfred Cho and John Arthur at Bell Telephone Labs in the late 1960s<sup>[71]</sup>. It represents a versatile technique for growing thin epitaxial structures under UHV conditions ( $10^{-9}$ - $10^{-10}$  Torr). It is widely used in the manufacture of semiconductor devices and it is one of the fundamental tools for the development of nanotechnologies<sup>[72]</sup>. What makes the MBE a unique machine is the UHV environment that allows the growth to be governed mainly by the kinetics of the surface processes occurring when the beams react with the outermost atomic layers of the substrate.

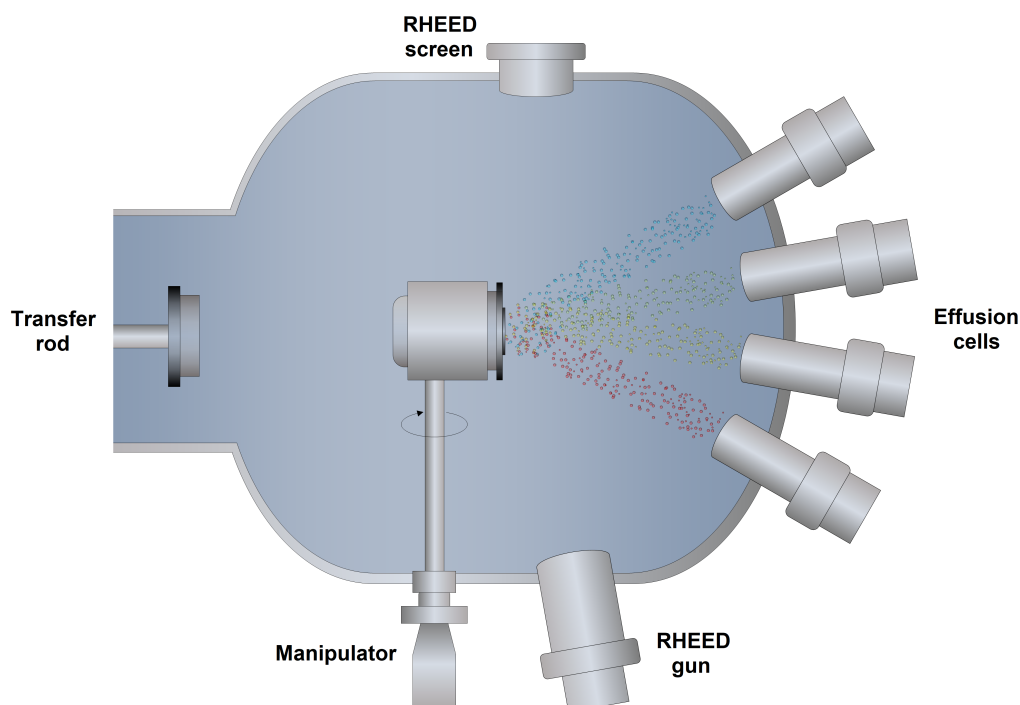


Figure 2.1 – Sketch of the MBE growth chamber. This is only one part of the MBE machine, which includes multi chambers (introduction and extraction chambers, two more growth chambers, an analysis chamber, and a preparation chamber), all kept under UHV.

A simplified sketch of a MBE chamber is showed in Figure 2.1. During a MBE growth, the thin films of different compounds are formed via reactions between separated thermal-energy molecular or atomic beams of the constituent elements (effusion cells) and the heated crystalline substrate, monolayer by monolayer. The result is an ordered growth of crystalline films. The UHV conditions together with the high purity source materials allow to achieve a low unintentional impurity concentration in the grown thin films. Since the growth rate is slow (about one monolayer per second) and beam controllers consist of fast action shutters (operational time shorter than one second), the thickness of grown layers can be controlled with an accuracy of less than a monolayer. Therefore, layers with different chemical compositions can be grown on each other, with atomically abrupt interfaces. In order to follow the crystallographic structure in the course of a growth, the MBE machine is equipped with a Reflection High-Energy Electron Diffraction (RHEED) setup. From the arrangement, intensity and profile of the

diffraction RHEED pattern, this technique yields structural information during the process.

In our laboratory there are two reactors, one dedicated to III-V semiconductor heterostructure growth and the second is devoted to graphene and BN epitaxy. Here we will discuss about the first one. A picture of this MBE system is reported in Figure 2.2. Four main areas are underlined by boxes: the growth chamber (green line), part of the effusion cells, valve cracker sources and shutters (red line), the RHEED screen with the camera (yellow line) and the pumping system (blue line). The substrates are introduced from the load lock (not visible in the picture) and

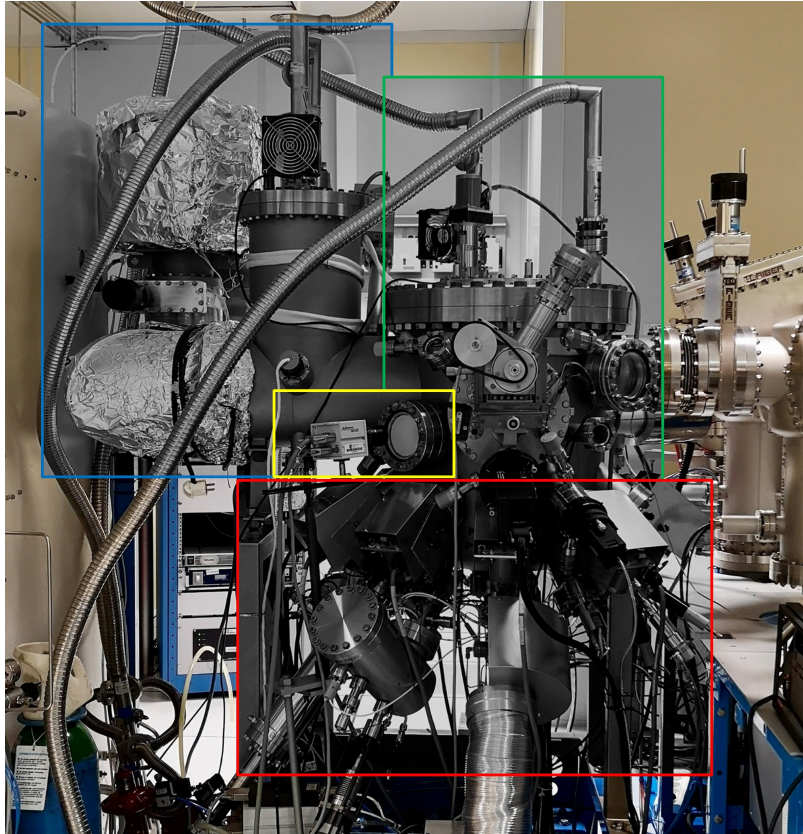


Figure 2.2 – Part of the IEMN MBE system: III-V growth chamber (green line), part of the effusion cells, valve cracker sources and shutters (red line), the RHEED screen with the camera (yellow line) and the pumps (blue line).

guided through the UHV transfer modules with a long transfer rod until being in front of the growth chamber (right part in the picture). In this position, another transfer rod, perpendicular to the first, keeps the sample and introduces it inside the main chamber; here is of course where the grown process happens. The MBE is equipped with standard effusion cells for Gallium, Aluminum and Indium group-III elements, Silicon for n-type doping, Beryllium and Carbon (via a  $\text{CBr}_4$  injector) for p-type doping. Group-V elements Arsenic and Phosphorus are produced as molecules  $\text{As}_2$  and  $\text{P}_2$ , from Arsine  $\text{AsH}_3$  and Phosphine  $\text{PH}_3$  cracked in a high temperature injector. As can also be produced, from a solid source thanks to an As valved cracker. Same mechanisms for the Antimony production. The system is also furnished with an atomic Hydrogen source. The whole chamber is pumped down by a combination of ionic and cryo pumps and



cooled down by a LN<sub>2</sub> Vacuum Barrier system.

This setup allows us the growth of 10 nm thick In<sub>0.53</sub>Ga<sub>0.47</sub>As QW on a series of InP layers (buffer and spacer), all grown on a p-doped InP substrate. The MBE growth temperature for an In<sub>0.53</sub>Ga<sub>0.47</sub>As thin layer lattice matched to InP is normally between 450 and 525 °C<sup>[57]</sup>. We use As and P coming from gas sources to form our In<sub>0.53</sub>Ga<sub>0.47</sub>As and InP layers. To confer p-doping to the samples we employ the Be solid source. Once the III-V semiconductor heterostructure is grown, the thin QW has to be protected and preserved during the various coming technological steps. For this reason, we will deposit either a thin As amorphous layer in the growth chamber or a thin layer of SiO<sub>2</sub> by employing PECVD.

## 2.2 Plasma-enhanced chemical vapor deposition

The PECVD is a technique that allows the deposition of thin films from a gas-phase source with activation in a glow discharge environment. The key advantage of the PECVD process is that it occurs at LT (typically ranging from near RT with no intentional heating, to about 400 °C, when additional heating is applied) compared to the other chemical vapor deposition (CVD) techniques in which the energy for reaction is supplied thermally.

Let us have a look on the basis of the technique. First of all, what does plasma mean? Plasma is one of the four fundamental states of matter containing many interacting free electrons and ionized atoms or molecules<sup>[73]</sup>. It can be produced by raising the temperature of a substance until a reasonably high fractional ionization is obtained. In the specific case of the PECVD,

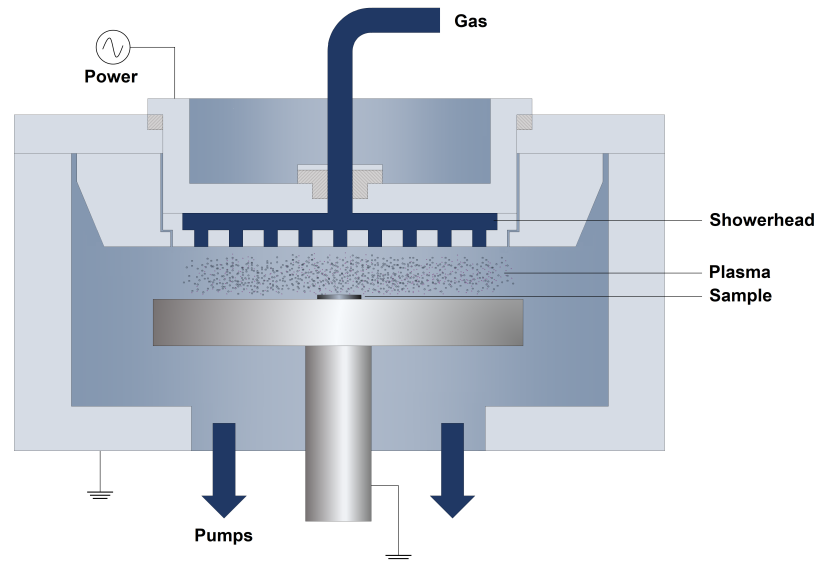


Figure 2.3 – Schematic of the PECVD.

the plasma is generated from a gas ionized by applying a strong Radio Frequency (RF) electromagnetic field. As showed in Figure 2.3, the gas is injected into the process chamber via a “showerhead” inlet in the top electrode (cathode) and the plasma is generated by the RF potential applied to the showerhead. The field is typically set to a frequency of 13.56 MHz, applied with a power of a few hundred watts. Energetic electrons in the plasma ionize or dissociate reactant



gases to generate more chemically reactive radicals. These radicals react to form the thin film of deposition materials on top of the sample, directly seated on the lower electrode (anode).



Figure 2.4 – Oxford Instruments Plasmalab 80 Plus PECVD. Main chamber (green box), pumps and electronics (yellow box) and controller (red box).

The PECVD used in this work is the Plasmalab 80 Plus PECVD, by Oxford Instruments, illustrated in the picture of Figure 2.4. The instrument is maintained under vacuum ( $10^{-6}$ - $10^{-7}$  Torr) thanks to a turbomolecular pump and piloted from a computer. It allows the deposition of  $\text{SiO}_2$ , Silicon nitride  $\text{Si}_3\text{N}_4$  and Silicon oxynitride  $\text{Si}_2\text{N}_2\text{O}$ , using temperatures ranging from 20 °C up to 350 °C. The thickness of the films can vary from 5 nm to 3  $\mu\text{m}$ . Once the gas is

Temperature (°C)	Pressure (Torr)	RF Power (W)	Deposition rate (nm/min)
300	1	20	66.2

Table 2.1 –  $\text{SiO}_2$  recommended parameters.

chosen, i.e. its precursors, the main parameters varied during a typical PECVD deposition are the temperature, the pressure, the RF power and the etching time. In our case, we are interested in depositing 15 nm of  $\text{SiO}_2$ . Therefore, we will use 5%  $\text{SiH}_4/\text{N}_2$  and  $\text{N}_2\text{O}$  as precursors and consider the following recommended recipe for a good quality  $\text{SiO}_2$  (see Table 2.1).

After the deposition of this protective layer, the sample is ready to face up with all the following processes run for the creation of the honeycomb lattice in the  $\text{In}_{0.53}\text{Ga}_{0.47}\text{As}$  QW. First of all, we need "to sketch" the pattern on the  $\text{SiO}_2$  surface to be able to create a mask on it thanks to EBL.

## 2.3 Electron beam lithography

Appeared in the 60s, the EBL is one of the fundamental techniques in nanofabrication allowing the direct writing of structures down to the nanometer scale. In brief, the EBL technique consists of scanning a beam of electrons across a surface covered with a resist film sensitive to those electrons. The thin layer of resist, deposited on the substrate is chemically changed under exposure to the e-beam. At the end of the EBL, the exposed (non-exposed) areas are dissolved in a specific solvent. This process is known as *development*.

The system we used, the Raith EBPG5000Plus, is illustrated in Figure 2.5. It is composed of a load lock to load the samples (yellow box) and the EBL column (green box) that consists of the electron gun, the optical control system and the writing chamber where the sample is located during the lithography. Part of the system can be controlled directly from the screen on the left part of the picture (red box) and is kept under vacuum thanks to turbomolecular and ionic pumps ( $10^{-9}$  mbar in the electron gun and  $10^{-6}$  mbar in the chamber). The EBL column

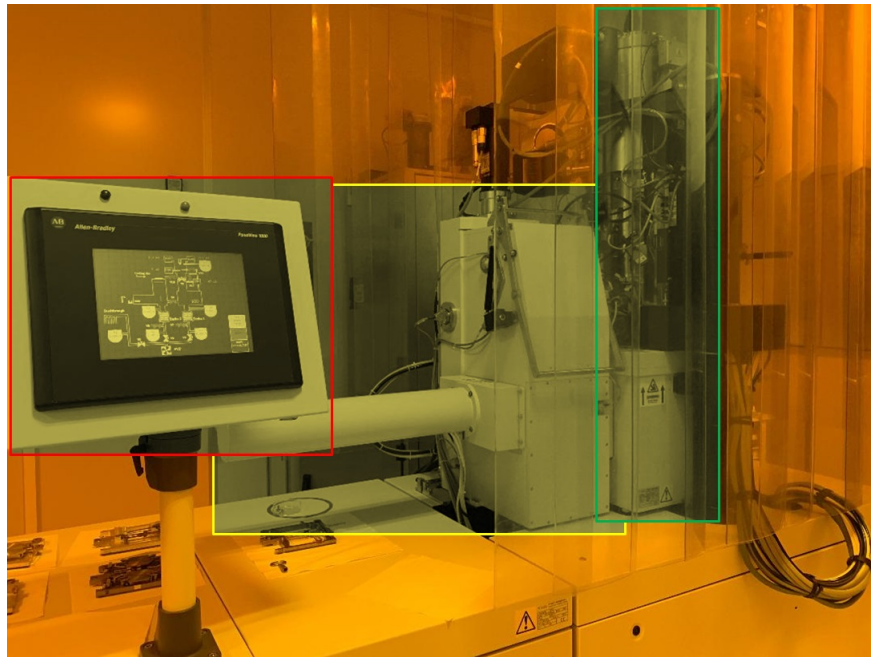


Figure 2.5 – Raith EBPG5200 Plus EBL System. EBL column (green box), load lock (yellow box) and controller (red box).

is summarized in Figure 2.6. The source of the e-beam is a thermal field emission electron gun, which is positioned at the top of the column. It is based on the application of a strong electric field between a sharply pointed tungsten tip (cathode) and a nearby electrode (extractor). As a consequence, the electrons are extracted by tunneling effect, allowing the formation of

a tightly-focused e-beam (diameter  $\sim 20$  nm). The cathode is heated to facilitate the electron extraction and it is surrounded by a suppressor that cancels the emissions from the sides of the tip. After that, the beam is accelerated through the anode (the applied voltage can be 20 kV, 50 kV or 100 kV) and sent to the area of the instrument in which it will be focused and aligned. This part of the system comprises electrostatic and magnetic lens for the focus and coils for

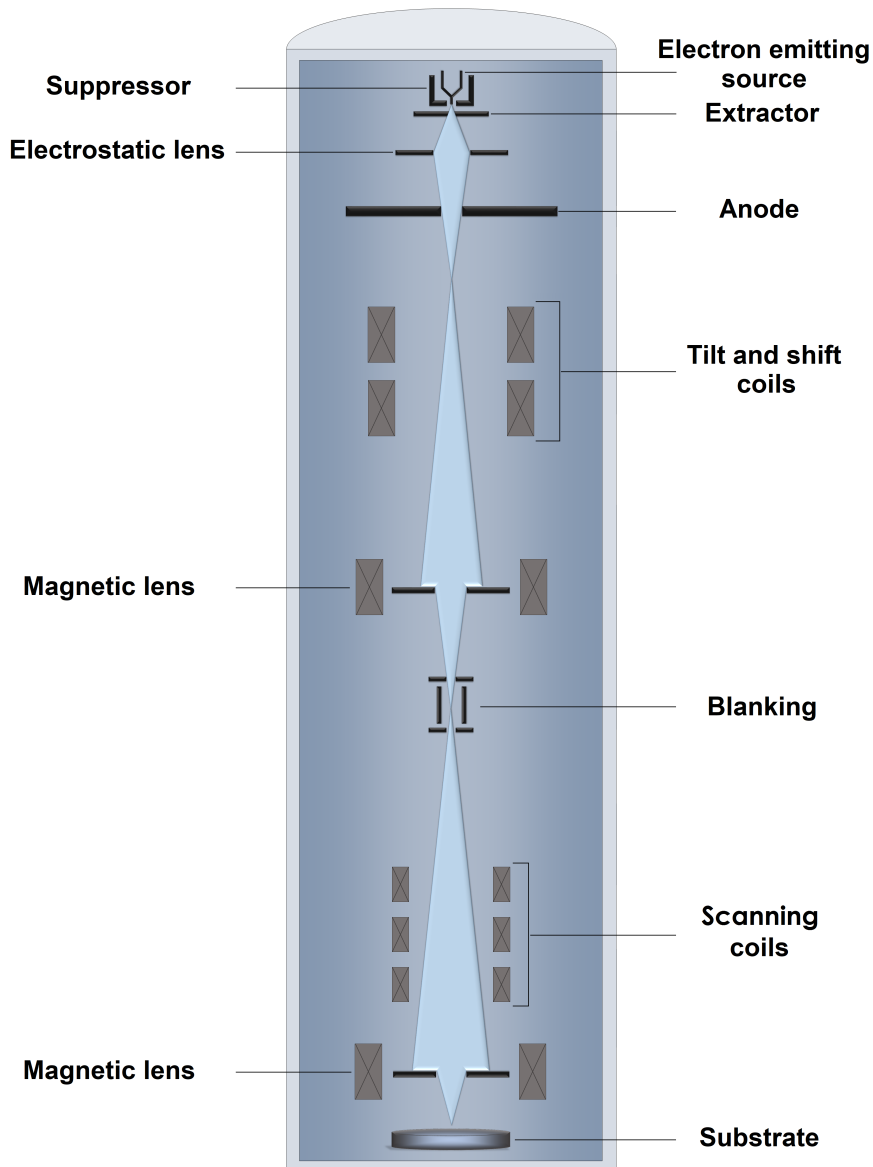


Figure 2.6 – Schematic of the EBL column.

the alignment of the beam. During the writing, the beam needs to be "turned off" between the different parts of the patterns. This is done by a beam blanker which deflects the e-beam far away from the optical axis so that the beam will not reach the sample. The blanking is obtained by applying an electric field perpendicular to the optical axis. After the blanking, scanning coils

are used to deflect the e-beam and be able to scan the surface of the sample. At the end of all the paths, after the last focus lens, a spot size of  $\sim 5$  nm is achieved on the sample surface.

### 2.3.1 EBL exposure

As anticipated in the beginning of the section, the EBL exposure is a direct writing technique that modifies the resist composition of the exposed areas and thus the pattern features materialize with the development. In order to push the EBL to the limits, we must take care of several factors, in particular related to the resist properties. Four mainly characteristics have to be taken into account:

- *Tone* determines the areas that will be removed in the development. In the case of positive resist, patterned areas are removed during the development, while for the negative one, the exposed parts do not dissolve in the developer.
- *Sensitivity* quantifies the minimum amount of electrons per unit area (*dose*) that is necessary to achieve the selective development.
- *Contrast* describes how abrupt is the dependence of thickness on dose. It is determined from the linear slope of the sensitivity curves.
- *Resolution* defines the minimum feature size or the smallest distance between two patterns that can be resolved.
- *Etch resistance* determines the resist integrity under the etching processes.

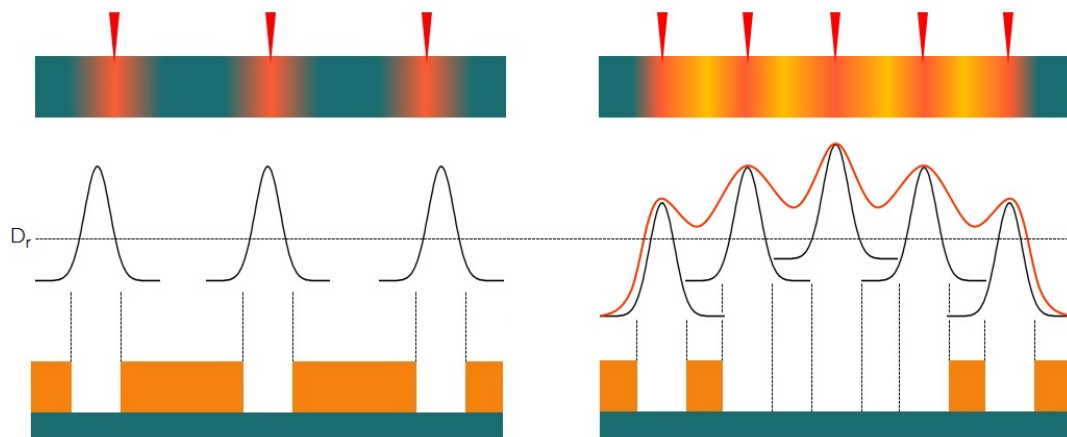


Figure 2.7 – Schematics of the proximity effects: in the case of closer and high density patterns (right) the dose received from the resist is higher than the effectively required dose to obtain a good development  $D_r$  and, as a result, the holes in the center will not be separated.

We want to transfer a triangular array directly in the  $\text{In}_{0.53}\text{Ga}_{0.47}\text{As}$  QW. For this purpose, the most appropriate choice is a positive resist. We will employ PMMA, one of the most commonly used positive resist. PMMA has extremely high resolution, and its ultimate resolution has been demonstrated to be less than 10 nm<sup>[74]</sup>. Another important point that has to be taken into account are the *proximity effects*. These effects are due to the interactions of the primary electrons with the resist and substrate that cause secondary scatterings. As a result, the dose received from

the resist will be higher than the expected, leading to a broadening of the patterns. As reported in Figure 2.7 the proximity effects become more important when the patterns are close to each other and their density is high. To limit these effects, correction files generated by Monte-Carlo simulations will be considered during the EBL writing. Hence, we will be able to apply different doses as a function of the pattern geometry. Furthermore, the use of a high energy e-beam will reduce the proximity effects<sup>[75]</sup>.

As we will discuss more in detail in Chapter 4, once the e-beam exposure is finished and the development done, the pattern of the mask is transferred on the sample surface by using dry etching. In particular, we firstly need to transfer the triangular array on the  $\text{SiO}_2$  layer, before a second transfer on the  $\text{In}_{0.53}\text{Ga}_{0.47}\text{As}$  QW. In fact, this two layers being composed by different materials, they react with different species. So, two different dry etching techniques has to be employed in order to perforate the  $\text{SiO}_2$  first and then the  $\text{In}_{0.53}\text{Ga}_{0.47}\text{As}$  QW. In the following the RIE and the ICP techniques are presented.

## 2.4 Dry etching

When a material is etched by a plasma or a liquid, it is removed isotropically (uniformly in all directions) or anisotropically (uniformity in vertical direction). Dry etching is one of the most widely used processes in semiconductor manufacturing since it produces highly anisotropic etching, is easier to control and is capable of defining feature sizes smaller than 50 nm. It may remove the materials by purely physical methods, by chemical reactions, or with a combination of both physical bombardment and chemical reaction. The physical dry etching is based on physical bombardment with ions or atoms. A sketch of the process is reported in Figure 2.8. The particles are energized by a plasma so that they have a high kinetic energy when they strike

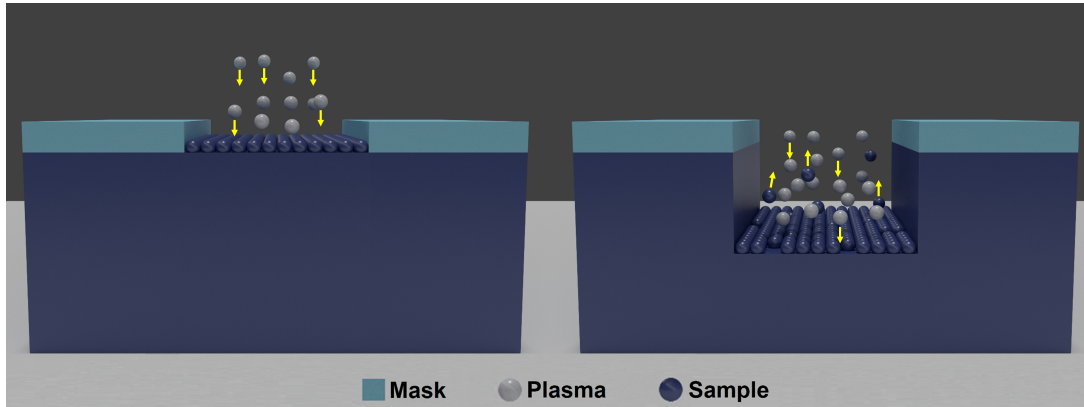


Figure 2.8 – Physical etching: (left) the energized particles strike the atoms of the surface; (right) the atoms are removed from the surface.

the sample. During the collision, momentum is transferred from the projectiles to the material atoms that are dislodged if the projectile energy exceeds bonding energy. This type of dry etching is not selective but it allows to obtain anisotropic etched profiles. In contrast, the chemical dry etching involves a chemical reaction between etchant gases and the sample surface, as showed in Figure 2.9. In particular, the reactive species from the plasma diffuse towards the surface of the sample. After that, they are adsorbed and the chemical reactions start. The interaction



gives soluble species that diffuse and are transported away. The chemical dry etching process is usually isotropic and exhibits high selectivity.

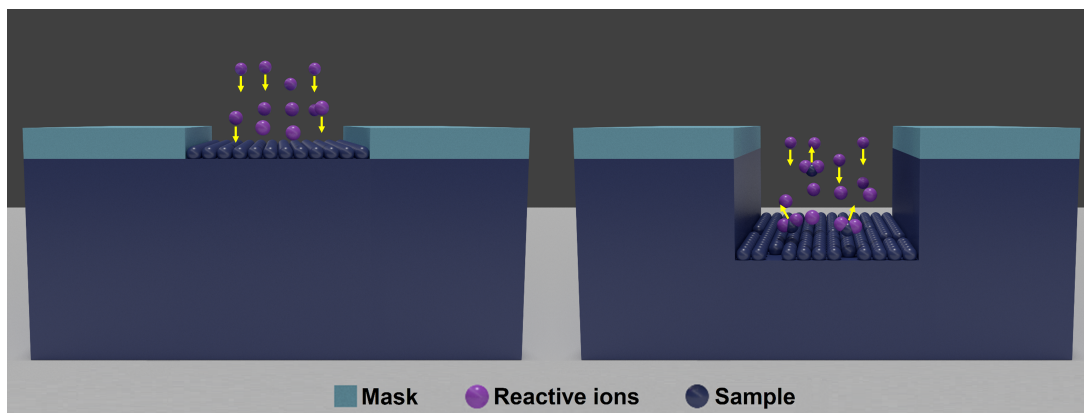


Figure 2.9 – Chemical etching: (left) the interaction between the reactive ions and the sample atoms; (right) chemical reactions between reactive ions and sample atoms remove the material from the surface.

### 2.4.1 Reactive ion etching

The RIE is a plasma dry etching technology that uses both physical and chemical mechanisms to achieve high levels of resolution. Similar to what we have seen for the PECVD, a schematic of the RIE is reported in Figure 2.10. Again the gas is introduced inside the chamber through the showerhead. The plasma now is initiated in the system by applying a strong RF electromagnetic field (13.56 MHz) to the wafer platter. The electrons are electrically accelerated up and down in the chamber, sometimes striking both the walls of the chamber and the wafer platter, the least building up charge due to its DC isolation. These charges cause a large negative voltage on the platter, that, together with the slightly positive charge of the plasma, generate a large voltage difference. In this way, the positive ions tend to drift toward the wafer platter, where they collide with the sample to be etched. The ions react chemically with the atoms of the surface of the sample, but they are also able to remove material by transferring their kinetic energy, as we have observed for the physical etching.

In particular, the physical and the chemical etchings can be dosed by adjusting the main parameters: the gas flow rate (sccm), the pressure, the RF power, the etching time and the substrate temperature. For example, high pressure values promote a chemical etching. In fact, an increase of the pressure produces an increase of the number of species and as a result, particle collisions becomes more frequent. In addition, the particles could lose kinetic energy during those impacts and deviate from the vertical direction, furthering the chemical process. On the other hand, the physical etching is favored by high values of power and low values of pressure. The effect of the substrate temperature acts mostly on the etching rate<sup>[76]</sup>.

The RIE machine used during this work is the Oxford Plasmalab 80 Plus RIE by Oxford Instruments. A picture illustrates this tool in Figure 2.11. It consists of a main chamber where the process happens, maintained under vacuum ( $10^{-6}$ - $10^{-7}$  Torr) by a turbomolecular pump, an interferometer that allows the endpoint detection and two computers to pilot both the entire system and the interferometer. The available gases in this RIE machine are: Ar, N<sub>2</sub>, CF<sub>4</sub>, O<sub>2</sub>, SF<sub>6</sub>, CHF<sub>3</sub>. These gases are usually employed for the etching of dielectric (SiO<sub>2</sub>, SiN<sub>x</sub>, etc.) or

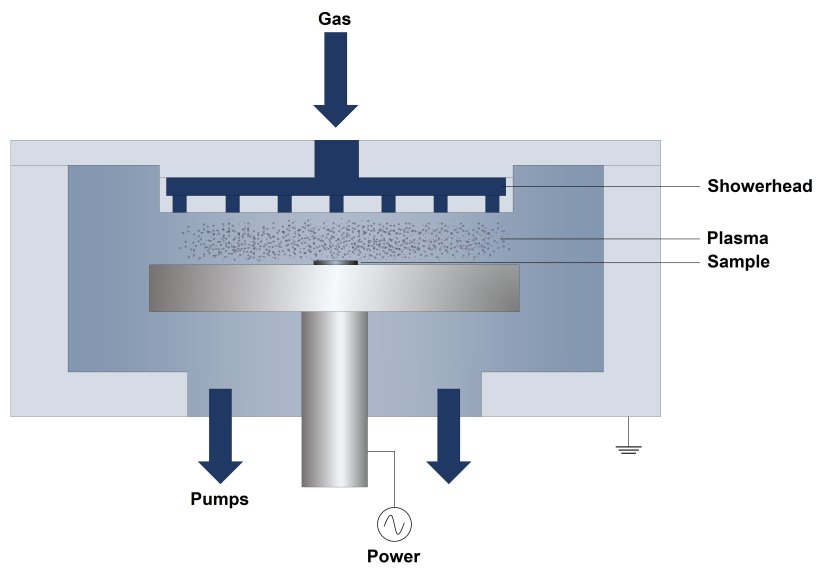


Figure 2.10 – Schematic of the RIE.



Figure 2.11 – Oxford Instruments Plasmalab 80 Plus RIE. Main chamber (green box), pumps and electronics (yellow box), interferometer (blue box) and controller (red box).

silicon-based materials. For this reason, we will use this setup to etch the 15 nm of  $\text{SiO}_2$  and, in particular we will use a mixture of  $\text{CHF}_3$  and  $\text{CF}_4$ . In addition, oxygen plasma  $\text{O}_2$  will be employed to clean residual resist.

## 2.4.2 Inductively coupled plasma - RIE

The ICP-RIE is a technology that combines both chemical reactions and ion-induced etching<sup>[77]</sup>. In fact, in a ICP-RIE process, the excitation is again generated from a RF source, but is delivered inductively via a coil wrapped around the RIE plasma discharge region, resulting in a changing magnetic field. This effect induces an electric field that tends to circulate the plasma in a plane parallel to the chamber plates. As a result, the collisions of the fast electrons with the slowly moving ions cause further ionizations. Increasing the ICP power rises the vertical magnetic field through the plasma. This will increase the number of collisions in the plasma and create more ions. Since the ion density in the plasma is increased, there will be more reactive ions being sent to the substrate increasing the chemical aspect of the etch. This highlights the most

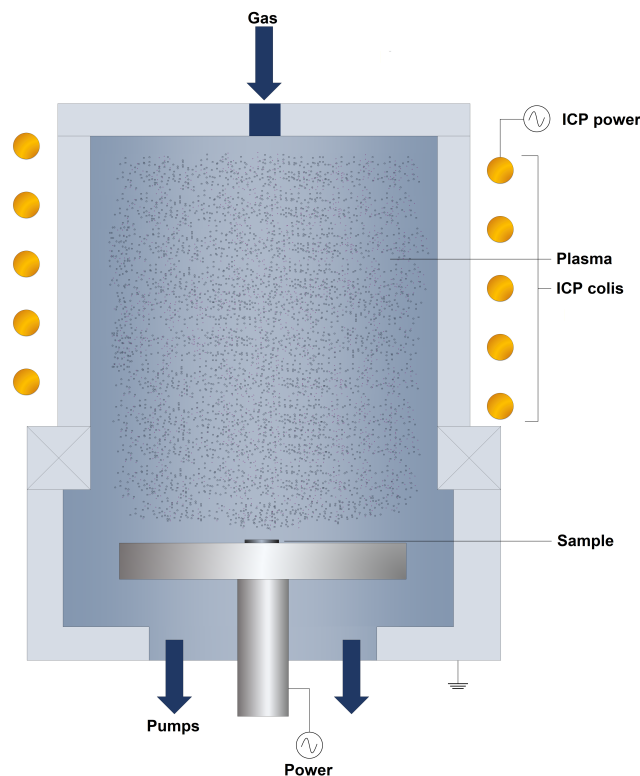


Figure 2.12 – Schematic of the ICP-RIE process.

significant advantage of etching with an ICP-RIE: variations in ion density and ion velocity become decoupled unlike other RIE systems. As showed in Figure 2.12 the gas is introduced into the system from the top part of the chamber. Once inside, it is ionized in reactive plasma with the help of a RF generator that excites a coil placed around the chamber. In particular, it creates an alternating RF magnetic field and induces RF electric fields, which energize the electrons



that participate in the ionization of gas molecules and atoms at low pressure. The independent control of ion flux enables high process flexibility.

In our laboratory, we have a Plasmalab 100 Plus ICP-RIE fabricated by Oxford Instruments. The ICP-RIE setup consists of two chambers, each one using specific gases, a load lock to introduce the samples inside the tool and a system of turbomolecular pumps that keep the setup under vacuum ( $10^{-6}$ - $10^{-7}$  Torr). In the blue box of the picture showed in Figure 2.13, we can see the first chamber where the available gases are: Ar, CH<sub>4</sub>, Cl<sub>2</sub>, O<sub>2</sub>, SF<sub>6</sub>, H<sub>2</sub>. It is used for InP, InGaAsP and InGaAs etching. On the other hand, the green box underline the second chamber which available gases are Ar, BCl<sub>3</sub>, Cl<sub>2</sub>, O<sub>2</sub>, SF<sub>6</sub>. It is mainly used for GaAs, AlGaAs and GaN etching. Between the two chambers it is possible to see the load lock (yellow box) that is connected with both chambers. Finally, the whole system is controlled from a computer.

Albeit the first chamber is also used to etch the InGaAs ternary alloy, here the BCl<sub>3</sub> gas is not available. ICP-RIE etching of III-V semiconductors in BCl<sub>3</sub>-based chemistries have shown good pattern transfer<sup>[78]</sup>. Therefore, we will perform the etching of the In<sub>0.53</sub>Ga<sub>0.47</sub>As QW by employing the BCl<sub>3</sub> gas in the second chamber.



Figure 2.13 – Oxford Instruments Plasmalab 100 Plus ICP-RIE. Chamber one (blue box), chamber two (green box), load lock (yellow box) and controller (red box).

Once the nanoperforation of the In<sub>0.53</sub>Ga<sub>0.47</sub>As QW has been achieved, the next steps consist in removing the top SiO<sub>2</sub> layer and in loading the sample back to the MBE chamber. Here, the surface of the nanoperforated In<sub>0.53</sub>Ga<sub>0.47</sub>As QW is treated with a H plasma source to make it clean and deoxidized. The last step deals with the protection of the surface with a thin As capping layer. This layer protects the artificial honeycomb structure against its oxidation and contamination during air exposure, prior to its characterization with STM and STS.

## 2.5 Scanning Tunneling Microscopy and Spectroscopy

Developed in 1981 at IBM Zurich Research Laboratories in Switzerland by Gerd Binnig and Heinrich Rohrer, the STM is one of the keystones technique for nanoscience today<sup>[79, 80]</sup>. Based on the *tunnel effect*, this technique allows to investigate the surface and electronic structure of

electrically conductive materials with sub-nanometer spatial resolution by employing a metallic probe tip. As shown in Figure 2.14, the measurement is performed by scanning a sharp tip over

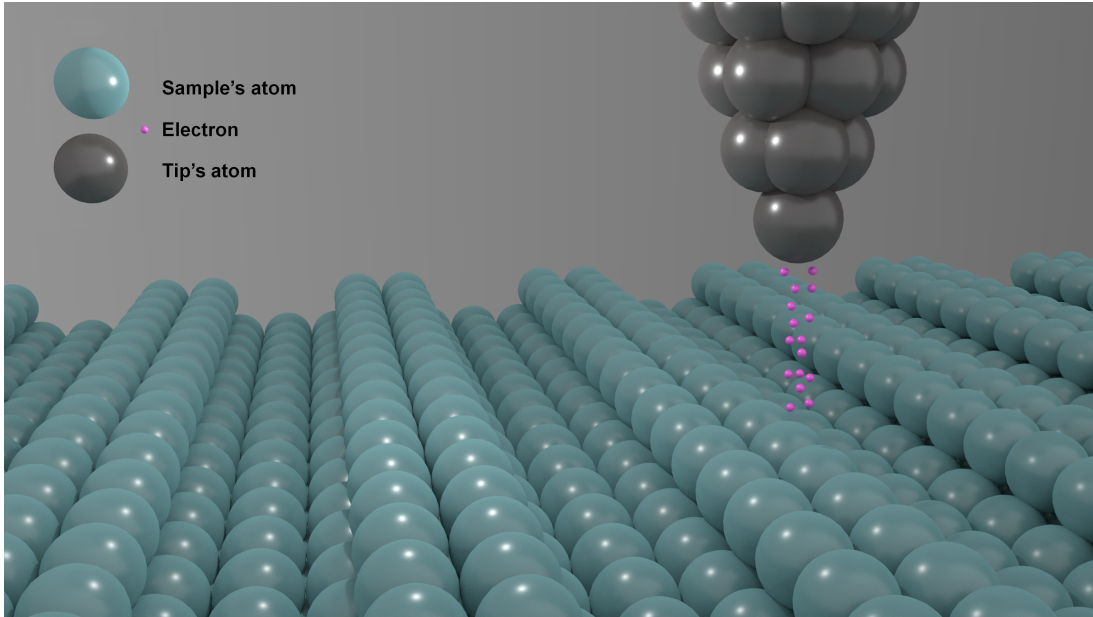


Figure 2.14 – Illustration of a STM at the atomic scale: A metallic tip is approached close to a (semi)conducting surface. When the tip and the sample surface are faced at a distance of a few angstroms, electrons can tunnel from one to the other.

a (semi)conducting sample at a distance of a few angstroms. When a bias voltage is applied between both electrodes, there is a non-zero probability for the electrons to tunnel through the barrier. This quantum mechanical effect, called tunnel effect, gives a resulting tunneling current that is a function of tip position, applied voltage, and LDOS of the sample. The surface can be scanned with the tip keeping either the height of the tip or the tunneling current constant. These two modes are called constant height mode and constant current mode, respectively. In constant current mode, feedback electronics adjust the height by a voltage to the piezoelectric height control mechanism. The feedback signal provides the information of the structural details of the surface.

### 2.5.1 Basis of the STM

#### The tunnel effect

Let us have a look closer to the tunnel effect. In classical physics an electron cannot penetrate through a potential barrier if its energy is smaller than the potential within the barrier. A quantum mechanic treatment predicts an exponential decaying solution for the electron wave function in the barrier. Let's consider the time-independent Schrödinger equation in one dimension

$$\left[ -\frac{\hbar^2}{2m} \frac{\partial^2}{\partial z^2} + U(z) \right] \cdot \Psi(z) = E \cdot \Psi(z), \quad (2.1)$$

where  $\hbar$  is the reduced Planck constant,  $m$  is the mass of an electron,  $U(z)$  is the potential barrier, and  $E$  is the energy of the state. The solutions of this equation inside a rectangular barrier have the form

$$\Psi(z) = \Psi(0)e^{\pm kz}, \quad (2.2)$$

with

$$k = \sqrt{\frac{2m(U(z) - E)}{\hbar^2}}. \quad (2.3)$$

### Tip-sample junction

Imagine now a situation as the one reported in Figure 2.15: a tip and a sample are placed at a distance  $d$  one from each other and a voltage  $V$  is applied between them. The barrier can be

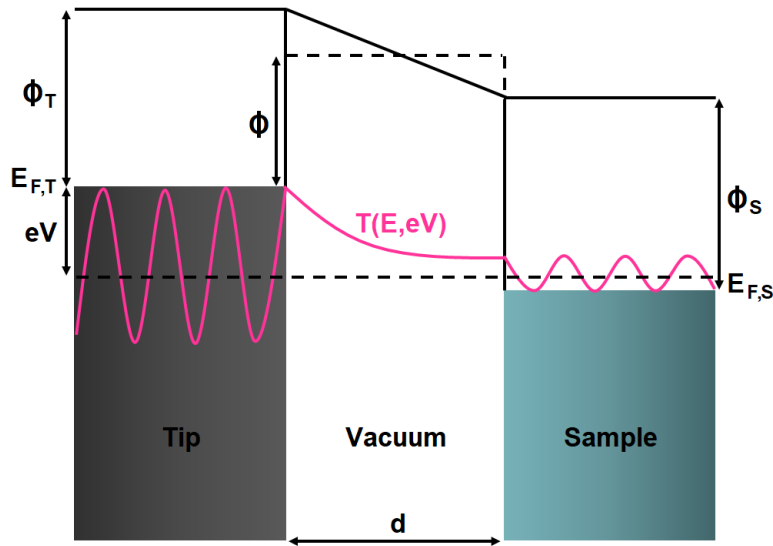


Figure 2.15 – Schematic diagram of the tunnel junction in a STM.

approximated by a square barrier (vacuum) which magnitude is

$$\phi = \frac{\phi_T + \phi_S}{2} - \frac{eV}{2}, \quad (2.4)$$

where  $\phi_T$  and  $\phi_S$  are the workfunctions of the tip and the sample respectively. In this configuration, the probability  $P$  of finding an electron behind the barrier is proportional to the wave function squared

$$P \propto |\Psi(d)|^2 = |\Psi(0)|^2 e^{-2kd}. \quad (2.5)$$

If  $V$  is small, only electron states within  $eV$  are excited and therefore tunneling mainly involves electrons near the FL  $E_F$ . However, tunneling does require that there is an empty level of the same energy for the electron to tunnel on the other side of the barrier. For this reason the tunneling current depends on the LDOS and on the number of electron states between  $E_F$  and  $eV$  in the sample

$$I \propto \sum_{E_F - eV}^{E_F} |\Psi(0)|^2 e^{-2kd} \quad (2.6)$$

Remembering the definition of the LDOS, for some energy  $E$  in an interval  $\varepsilon$

$$\rho(z, E) = \frac{1}{\varepsilon} \sum_{E-\varepsilon}^E |\Psi(z)|^2, \quad (2.7)$$

the tunneling current can be expressed as

$$I \propto V \rho_S(0, E_F) e^{-2kd}, \quad (2.8)$$

where  $\rho_S(0, E_F)$  is the LDOS near the sample FL at the surface.

### Tunneling Hamiltonian Approach

Using the Bardeen method, in the first order of the perturbation theory, the tunneling current is found to be

$$I = \frac{2\pi e}{\hbar} \sum_{\mu, \nu} f(E_\mu) [1 - f(E_\nu + eV)] |M_{\mu\nu}|^2 \delta(E_\mu - E_\nu), \quad (2.9)$$

where  $f(E)$  is the Fermi-Dirac distribution,  $V$  is the applied voltage,  $M_{\mu\nu}$  is the tunneling matrix element between states  $\Psi_\mu$  and  $\Psi_\nu$  of the tip and the sample surface respectively and  $E_\mu$  and  $E_\nu$  are the energy of the states  $\Psi_\mu$  and  $\Psi_\nu$ . The tunneling matrix element  $M_{\mu\nu}$  is

$$M_{\mu\nu} = \frac{\hbar^2}{2m} \int (\Psi_\mu^* \nabla \Psi_\nu - \Psi_\nu^* \nabla \Psi_\mu) dS, \quad (2.10)$$

a surface integral of the wave functions (and its normal derivatives) of the sample and tip, evaluated at the separation surface.

Equation 2.9 can be simplified in the limit of small bias  $V$ , assuming the tip as a mathematical point source of current whose position is denoted with  $\mathbf{r}_t$ . Thus, in this case, for LT and a constant  $M_{\mu\nu}$ , the tunneling current reduces to

$$I \propto \sum_\nu |\Psi(\mathbf{r}_t)|^2 \delta(E_\nu - E_F) \equiv \rho(\mathbf{r}_t, E_F), \quad (2.11)$$

proportional to the LDOS at  $E_F$ .

This result has been generalized for larger voltages of a few volts for which the tunneling current arises from a range of states lying within an electronvolt from the FL. The tunneling current can be approximated as

$$I \approx \int_0^{eV} \rho_S(E) \rho_T(E - eV) T(E, eV) dE. \quad (2.12)$$

where  $\rho_S$  and  $\rho_T$  are the LDOS of the sample and the tip respectively, at the energy  $E$ , measured with respect to their individual FL.  $T(E, eV)$  is the barrier transmission coefficient given by

$$T(E, eV) \approx \exp\left(-\frac{2d\sqrt{2m}}{\hbar} \sqrt{\phi + \frac{eV}{2} - E}\right). \quad (2.13)$$

Thus, the tunneling current depends on the tip-sample distance  $d$ . Considering for example tungsten probes, with a workfunction  $\phi$  of 4.5 eV, we can estimate the value of the exponent present in Equation 2.13, obtaining  $\approx 1 \text{ \AA}^{-1}$ . This means that an increase of 1  $\text{\AA}$  in the tip-sample distance  $d$  leads to a current variation of a factor  $e^2 \approx 0.1$ . This change is enough for the detection of vertical variations at atomic-scale.

### STM lateral resolution

As for the lateral resolution of the STM, we can assume that only the last atom of the tip take part to the tunneling process. Following the Tersoff-Hamann approach<sup>[81]</sup>, let us consider the tip apex as a perfect spherical ball characterized by an  $s$ -type wavefunction

$$|\Psi|^2 = \frac{e^{-2kr}}{r^2}, \quad (2.14)$$

with  $r = \sqrt{x^2 + z^2}$  (see Figure 2.16). If  $z \gg x$ ,  $r$  can be approximated with

$$r \approx z + \frac{x^2}{2z}. \quad (2.15)$$

Considering this value, Equation 2.14 becomes

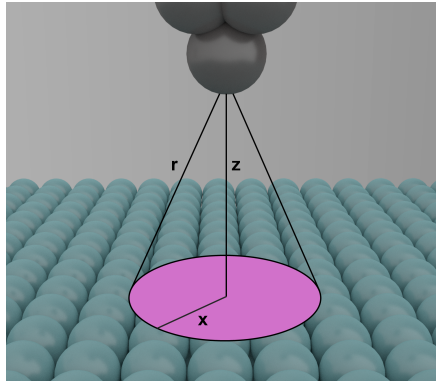


Figure 2.16 – STM lateral resolution.

$$|\Psi|^2 = \frac{e^{-2kz}}{z^2} e^{-k\frac{x^2}{z}}, \quad (2.16)$$

that represents a Gaussian function in  $x$  with Full Width at Half Maximum (FWHM)

$$\Delta x \approx \frac{2z}{k}. \quad (2.17)$$

The height of tip can be written as  $z = R + d$ , where  $R$  is the tip apex radius and  $d$  the tip-sample distance. As we already observed in the case of tungsten tips,  $k \approx 1 \text{ \AA}^{-1}$ , so that, the lateral resolution evolves into

$$\Delta x \approx 1.4\sqrt{R}. \quad (2.18)$$

For a sharp tip with radius  $R=100 \text{ \AA}$ , we obtain a  $\Delta x$  of  $14 \text{ \AA}$ . In real experiments, the atomic resolution is frequently a consequence of atomic-sized protrusions at the tip apex. As a result, lateral resolutions  $\Delta x$  around  $5 \text{ \AA}$  can be achieved.

## 2.5.2 STS basic principles

As observed in the beginning of the STM description, it is also possible to obtain information about the electronic properties of a sample. This technique is called STS. To perform spectroscopy, the tip is kept at a predefined position (constant  $x$  and  $y$ ) and the bias voltage is ramped to obtain the  $I - V$  characteristics. At positive bias voltages, the empty states of the sample are probed while at negative bias, we look for those that are filled. Thanks to a lock-in amplifier, it is possible to modulate the voltage and measure  $dI/dV$  directly. The advantage of measuring the derivative of the conductance lies in the fact that it is proportional to LDOS. From Equation 2.12 we get:

$$\frac{dI}{dV} \propto e\rho_T\rho_S(eV)T(eV, eV) + e\rho_T \int_0^{eV} \frac{d}{d(eV)} [T(E, eV)]\rho_S(E) dE. \quad (2.19)$$

This expression depends on  $\rho_S(E)$ . But the exponential increase of the signal as a function of the bias due to  $T(E, eV)$  induces a large contribution of the states lying at higher energy with respect to the states closer to the FL. Feenstra and collaborators have shown that it is possible to cancel the dependence rising from  $T(E, eV)$  by normalizing the differential conductance by the ratio  $I/V$ [82]

$$\frac{\frac{dI}{dV}}{\frac{I}{V}} \propto \frac{\rho_S(eV) + \int_0^{eV} \frac{\partial}{\partial(eV)} T(E, eV) \frac{\rho_S(E)}{T(E, eV)} dE}{\frac{1}{eV} \int_0^{eV} \frac{T(E, eV)}{T(eV, eV)} \rho_S(E) dE}. \quad (2.20)$$

The second term of the numerator divided by the denominator of the equation is a slowly varying background term and therefore, the mainly dependence comes from  $\rho_S(eV)$ . Thus

$$\frac{\frac{dI}{dV}}{\frac{I}{V}} \propto \rho_S(eV). \quad (2.21)$$

Again meaning that it is possible to get a measure of the LDOS of the sample from  $dI/dV$  curves. Experimentally, the LDOS is usually obtained by averaging hundred of  $dI/dV$  curves on a given position on the sample surface. This type of acquisition is what we call single point mode. It is also possible to acquire  $dI/dV$  spectra for every point of a selected area. In this case the technique is known as CITS (Continuous Imaging Tunneling Spectroscopy). The advantage of this mode is that topographic and spectroscopic information are registered nearly simultaneously.

## 2.5.3 STS energy resolution

### Temperature broadening

At finite temperatures, the thermal broadening of the electron energy distribution due to the Fermi-Dirac distribution limits the spectroscopic resolution. Equation 2.9, can be written as

$$I \propto \int_{-\infty}^{+\infty} [f_S(E) - f_T(E - eV)] T(E, eV) \rho_T(E - eV) \rho_S(E) dE. \quad (2.22)$$

Here  $f_n(E)$  is the Fermi-Dirac distribution, defined as

$$f_n(E) = \frac{1}{1 + \exp\left(\frac{E - E_{F_n}}{k_B T}\right)}, \quad (2.23)$$

where  $k_B$  and  $T$  are the Boltzmann constant and the temperature, respectively.  $T(E, eV)$  adds a background to the spectra and can be neglected for small energies compared to the barrier height. Let's also assume that the LDOS of the tip  $\rho_T$  is constant. Thus, the first derivative of the current with respect to the bias is

$$\frac{\partial I}{\partial V} \propto \rho_T \int_{-\infty}^{+\infty} \frac{\partial}{\partial V} f_T(E - eV) \rho_S(E) dE, \quad (2.24)$$

a convolution between the derivative of the tip Fermi-Dirac distribution (temperature dependent)

$$\frac{\partial}{\partial V} f_T(E - eV) = -\frac{1}{k_B T} \frac{\exp\left(\frac{E - eV - E_F}{k_B T}\right)}{\left[1 + \exp\left(\frac{E - eV - E_F}{k_B T}\right)\right]^2} \quad (2.25)$$

and the sample LDOS  $\rho_S$ . In Figure 2.17 an example of the temperature broadening<sup>[83]</sup> is

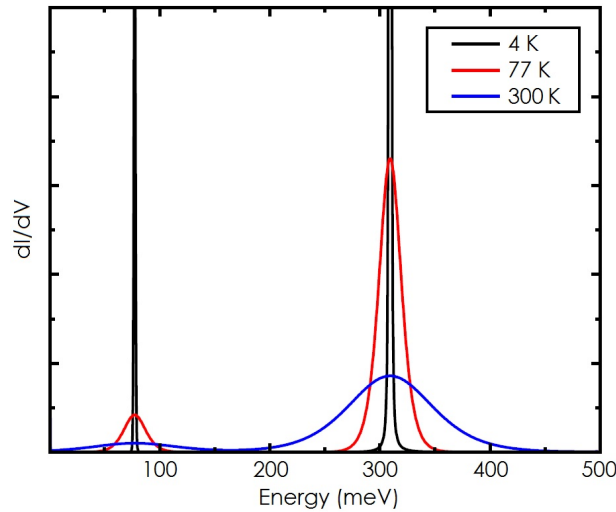


Figure 2.17 – Temperature broadening. Figure extracted from <sup>[83]</sup>.

reported. As one can see, the sharp peaks that are obtained at  $T = 4$  K are progressively smoothed by the  $\frac{\partial}{\partial V} f_T(E - eV)$  term with the temperature increasing. Therefore, in the context of this project, where high spectral resolution is needed to resolve the Dirac cone and the flat band, fundamental will be the investigation of the electronic properties at LT.

### Lock-in amplifier

As anticipated in the STS subsection 2.5.2, the experimental detection of the  $dI/dV$  signal is done by employing a lock-in amplifier. A small high-frequency sinusoidal signal,  $V_{mod} \sin(\omega t)$ ,

is superimposed to the tunneling voltage. This modulation lead to a sinusoidal response in the tunneling current. The amplitude of the modulated current is sensitive to the slope of the I-V curve. For small modulations, the tunneling current can be expanded in a Taylor series:

$$I(V_{bias} + V_{mod} \sin(\omega t)) \sim I(V_{bias}) + \frac{d}{dV} I(V_{bias}) \cdot V_{mod} \sin(\omega t) + \frac{d^2}{dV^2} I(V_{bias}) \cdot V_{mod}^2 \sin(\omega t) + \dots \quad (2.26)$$

meaning that, in a first approximation the amplitude of the current modulation at the tunneling voltage is proportional to the first derivative of the  $I(V)$  curve and therefore proportional to the LDOS in the sample.

Nevertheless, the use of a lock-in amplifier leads to capacitive effects coming from the electrical contacts between the tip-sample system and the lock-in preamplifier. They induce a parasitical sinusoidal current in the modulation. This current can be huge compared to the tunneling current and hinders the dynamical resolution of the lock-in. Due to the capacitance, this current is phase shifted by  $90^\circ$  with respect to the modulation and can be removed easily by adding the opposite signal, derived from the reference. Furthermore, the modulation amplitude has to be carefully chosen. It has been shown that the detected  $dI/dV$  signal is broadened because of being a convolution of the sample LDOS and the instrumental resolution function<sup>[84]</sup>. As long as  $V_{mod}$  is smaller than the desired energy resolution, the spectrum will not be significantly affected. Based on the theoretical predictions reported at the end of Chapter 1, the value of the modulation has to be carefully chosen. In order to measure a linear dispersion relation between the energy and the wavevector lower then 10 meV, a modulation less than or equal to 2 mV RMS has to be selected.

#### 2.5.4 STM based setups

Different STM setups were used during this thesis work. The topography and the electronic properties of the samples were studied with two LT-STM: the Omicron microscope of the Physics group of IEMN at the Insitut Supérieur d'Électronique et du Numérique (ISEN) in Lille, and the Unisoku USM 1300 at the Centre de Nanosciences et de Nanotechnologies (C2N) in Marcoussis. Here we will detail the first one, since it was predominantly used in this work. In-line four-probe (4-probe) STM measurements were carried out with an Omicron Nanoprobe, to measure the DC conductivity of the  $\text{In}_{0.53}\text{Ga}_{0.47}\text{As}$  QW. This microscope is at IEMN, Villeneuve d'Ascq. Finally, STM induced light-emission (STM-LE) was performed with a home-built LT-STM coupled with a system of lenses mounted inside the vacuum chamber. This microscope is in the Institut für Experimentelle und Angewandte Physik (IEAP) at the Kiel University.

##### The Omicron LT-STM

A picture of the UHV LT-STM from Omicron is illustrated in Figure 2.18. It is essentially divided in three parts: the analysis chamber (green box), the preparation chamber (red box) and the load lock (yellow box). The load lock allows the introduction of the samples and the tips into the vacuum system. It is connected with the preparation chamber where the tip and the samples can be prepared and stored. The transfer between both chambers is possible thanks to a first transfer rod. A second one allows to move the materials on the manipulator for the preparation of samples and tips or to introduce them directly into the STM chamber. Here, there is a carousel where samples and tips can be stored and a wobblestick for the transfers into the LT-STM. The preparation chamber and the STM chamber are maintained in UHV ( $10^{-11}$ - $10^{-10}$  Torr) by an ion pump and a Titanium Sublimation Pump (TSP). The LT-STM is equipped with two cryostats to cool down the system. The first one (outer) is like a shield for the second one (inner) and is



filled with nitrogen; while the inner cryostat can be filled both with nitrogen and with helium, depending on the desired temperature (77 K or 5 K).

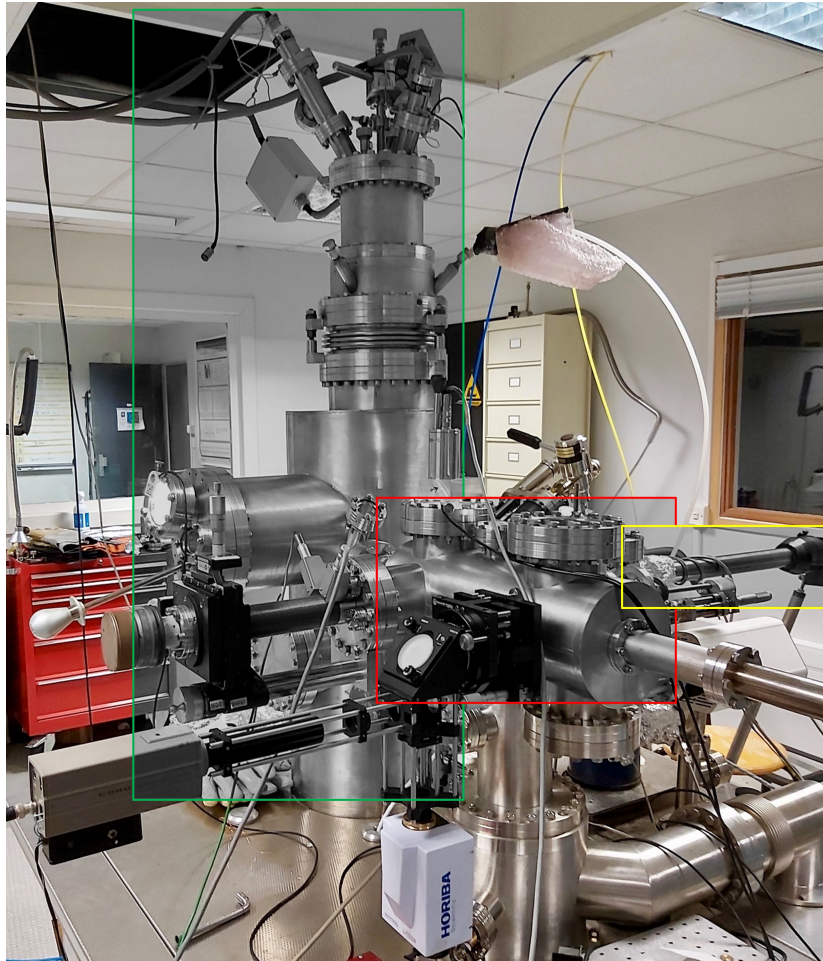


Figure 2.18 – The Omicron LT-STM. STM chamber (green box), preparation chamber (red box) and load lock (yellow box).

### The Omicron four-probe STM

Another STM system used in this work is a 4-probe STM. It is a sophisticated instrument specifically designed for local and non-destructive 4-point probe measurements, operable also at LT<sup>[85]</sup>. Basically, in the in-line 4-probe geometry, a voltage  $V$  between the two inner contacts is measured while a current  $I$  is injected through the two outer contacts. The ratio  $V/I$  is a measure of the sample resistance  $R$ . The power of this instrument is the possibility of performing electrical measurements at the nanoscale, as let us say, a "nano-multimeter". Therefore, we will employ it to study the transport in the 10 nm thick  $\text{In}_{0.53}\text{Ga}_{0.47}\text{As}$  QW.

A picture of the Omicron Nanoprobe is reported in Figure 2.19. It consist of an analysis chamber (green box), a SEM [this technique will be discussed in Section 2.6] (blue box), a preparation chamber (red box) and a load lock (yellow box). The samples and the tips are

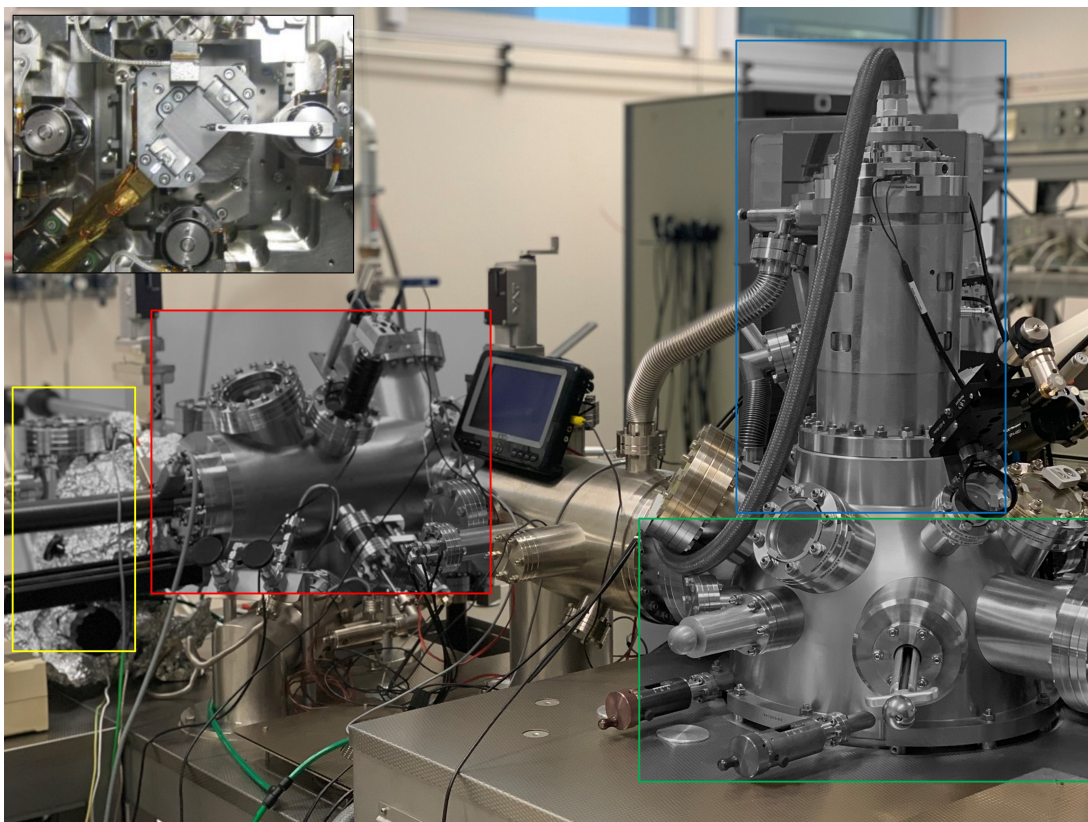


Figure 2.19 – The Omicron 4-probe STM chamber (green box), SEM (blue box), preparation chamber (red box) and load lock (yellow box). Top left inset: four independent scanners, three of them consist of a tube, the fourth one of a stack of piezoceramics to improve the stability of the tip. One tip is seen on top of a low resolution scanner.

loaded from the load lock where there are six storage available. Connected to this part, there is the preparation chamber. Here it is possible to prepare the samples and the tips before their transfer into the analysis chamber through a long transfer rod. On the right part of the picture it is possible to see the SEM column on the analysis chamber. The presence of such a microscope is essential for the probe positioning on the sample, especially when the spacing between the probes are in the nm-scale. The analysis chamber is where the experiment occurs. As showed in the inset of Figure 2.19, inside the chamber there are 4 probes that can be operated independently, under the supervision of the SEM. The preparation chamber and the STM chamber are maintained in UHV ( $10^{-11}$ - $10^{-10}$  Torr) by an ion pump and a TSP.

### STM induced light emission

STM-LE is a technique that allows the study of the light emission induced by the tunneling current flowing in a tip-sample STM junction. STM-LE measurements were performed thanks to a home-built LT-STM coupled with a system of lenses mounted inside the vacuum chamber<sup>[86]</sup>. As showed in Figure 2.20, similar to the LT-STM (see Figure 2.18), the system consists of a preparation chamber (red box), a load lock (not visible in the picture, behind the preparation



chamber) and a STM chamber (green box). In addition, it is equipped with an optical system that allows the emitted light from the tip-sample to be collected. The collected tip-sample junction emission is guided via an optical fiber to a spectrometer (Horiba iHR 320) and a liquid-nitrogen-cooled CCD detector (Horiba Symphony II CCD).

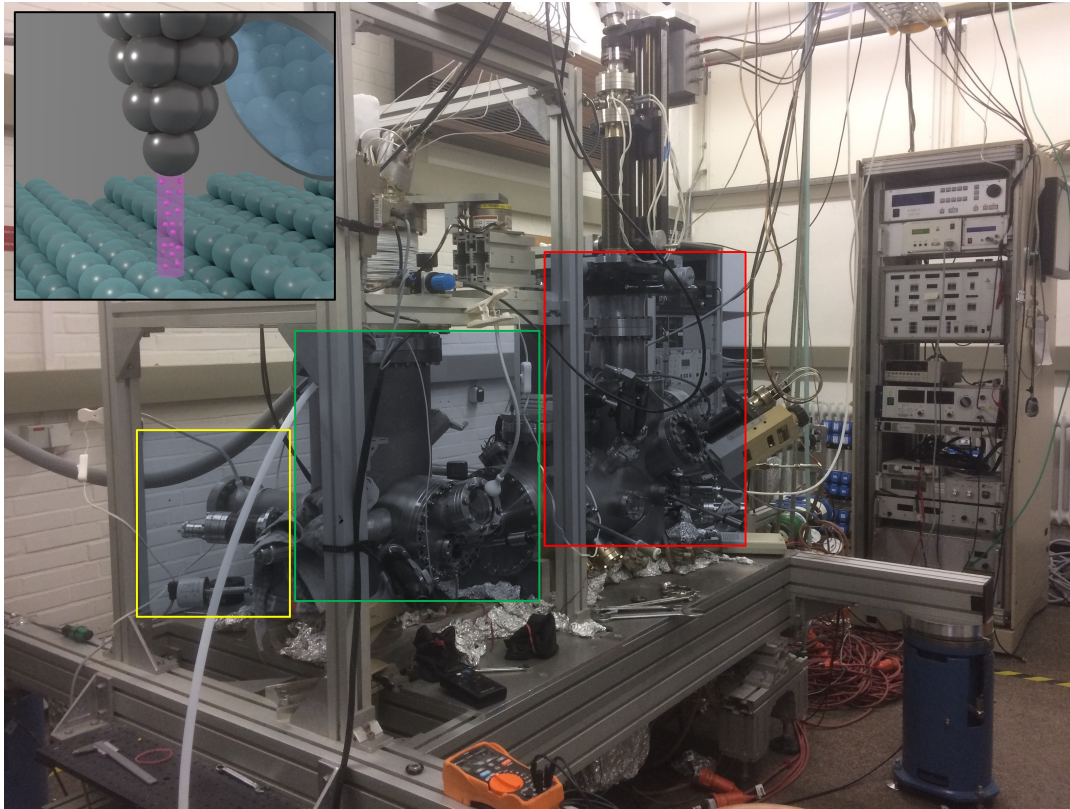


Figure 2.20 – The STM-LE setup: STM chamber (green box), preparation chamber (red box), and system of lens (yellow box). Top left inset: Illustration of a STM at the atomic scale with the system of lens collecting the signal from the tip-sample junction.

Two additional microscopes were used during this thesis work. The technological processes had to be followed step by step in order to know if the patterning transfer on the heterostructure was being successful. For this purpose, the SEM and the AFM, were employed.

## 2.6 Scanning Electron Microscopy

The SEM, is a versatile technique that allows the investigation of the surface morphology and the chemical composition of materials. The basic principle of the SEM is to produce images of a sample by scanning the surface with a focused beam of electrons. Similar to the description seen in Section 2.3 for the EBL, the column of the SEM consists of an electron gun that generates the e-beam. After that, the electrons are accelerated by an electric field and sent to the electron-optical control system, where they are focused and aligned by the lens and the coils. At this point, the beam strikes the sample and different phenomena occur. In particular, as illustrated in Figure 2.21, the interaction between the e-beam and the sample produces different emissions from the

sample: backscattered electrons, secondary electrons, x-ray electrons and Auger electrons<sup>[87]</sup>. This region of the sample is also known as *primary excitation region*, and its shape depends on the energy of the e-beam and the atomic number of the sample atoms. The emitted particles are then collected by different detectors that transfer the information to the computer. The most

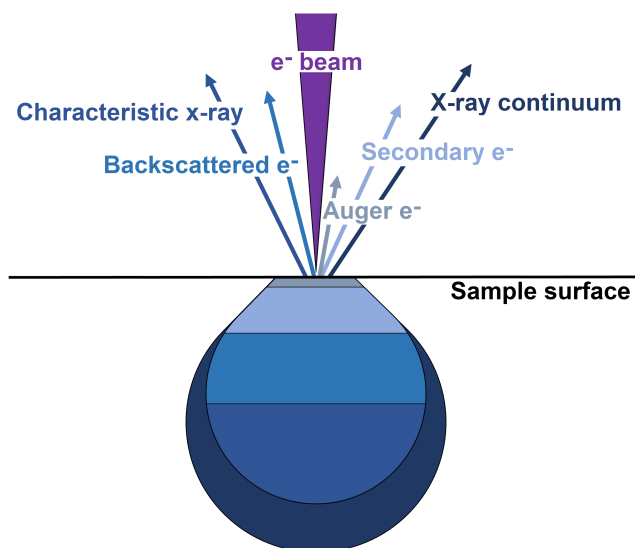


Figure 2.21 – Schematic of the various interactions between the electron beam and the sample.

widely used signal produced by the interaction of the e-beam with the sample is the secondary electron emission. When the primary beam strikes the sample surface causing the ionization of sample atoms, loosely bound electrons may be emitted and these are referred to as secondary electrons. These electrons have low energy (<10 eV) and are emitted from very close to the sample surface. Consequently, they can produce high-resolution images of a sample surface (3 to 5 nm). The backscattered electrons are the result of an elastic collision between the beam and the sample atoms. They have high energy (>50 eV) and can emerge from deeper location within the sample, meaning that the resolution of the images in this case is lower. Nevertheless, being strongly related to the atomic number of the sample atoms, they can form images giving information about the chemical composition of the sample. Finally, the x-ray electrons and the Auger electrons, can give also access to the chemistry of the sample.

The SEM used during this work is the Gemini SEM by Zeiss. A picture of this microscope is reported in Figure 2.22. It is equipped by an Energy Dispersive X-ray spectroscopy (EDX) setup (yellow box) that allows the elemental analysis of the sample and piloted by a dual joystick and a control panel. We used both SEM and EDX techniques to look at the surface topography and its chemical composition during the various steps of the nanofabrication. We take advantage from the speed of the SEM image acquisition (less than a minute) and its high resolution.

## 2.7 Atomic Force Microscopy

In 1986, five years after the development of the STM, Gerd Binnig and coworkers invented the AFM, another powerful scanning probe microscopy technique that allows the investigation of



Figure 2.22 – Gemini SEM by Zeiss. Microscope (green box), EDX (yellow box), controllers (red box).

the insulating materials at the nanoscale<sup>[88]</sup>. While the STM depends on the conductive samples, the AFM allows also the use of non-conductive samples. But how such a microscope works? A typical AFM consists of a cantilever with a small tip (probe) at the free end, a laser, a four-quadrant photodiode and a scanner. As summarized in Figure 2.23, when the tip, attached to the cantilever, comes very close to the surface, attractive and repulsive forces due to the interactions between the tip and the sample surface cause the deflection of the cantilever. This bending is detected by the help of a laser beam and a detector. The latter measures the displacement of the cantilever with respect to the equilibrium position, and converts it into an electrical signal. The scanner made from piezoelectric materials allows the movement of the sample in the three directions. The cantilever can be thought as a spring, so that, the force between the tip and the sample surface depends on its spring constant and the distance between the tip and the sample. As the tip travels across the sample, it moves up and down according to the surface properties. The displacement of the tip is measured and a topographical image is obtained.

The AFM can operate in different modes: the static mode (also known as contact mode), the dynamic mode (also called tapping mode) and the non-contact mode<sup>[89]</sup>. In contact mode, the tip is kept in contact with the surface during the scanning and the contours of the surface are measured either using the deflection of the cantilever directly or using the feedback signal required to keep the cantilever at a constant position. As suggested from the name, in the non-contact mode, the tip does not contact the sample surface. The cantilever is oscillating close to its resonant frequency, with a given amplitude. The interaction detection is based on the variations of the frequency oscillations of the cantilever. Finally, the tapping mode is in between the just discussed AFM modes. As for the non-contact mode, the cantilever is driven to oscillate up and down at or near its resonance frequency. The frequency and amplitude of the driving

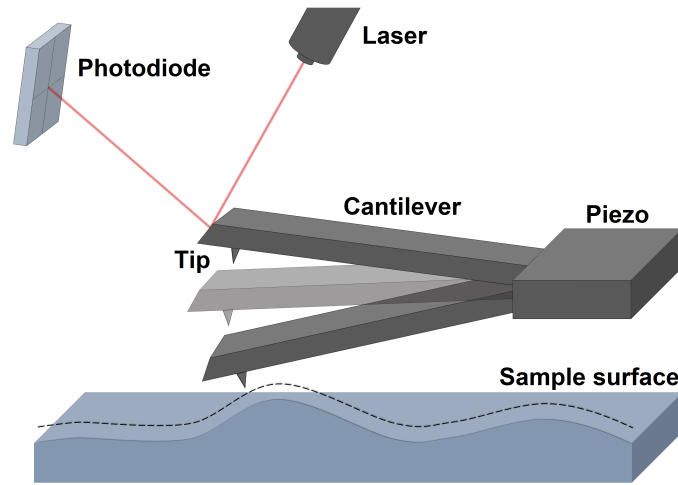


Figure 2.23 – Schematic of the AFM.

signal are kept constant, leading to a constant amplitude of the cantilever oscillation while the interaction with the surface changes. In this case the system reacts to maintain the amplitude constant by adjusting the vertical position.

### 2.7.1 AFM resolution

The AFM vertical resolution, is mainly limited by the thermal noise of the deflection detection system<sup>[90]</sup>. In most of the commercial available systems, the thermal noise of a free cantilever can be estimated by

$$\Delta z = \sqrt{\frac{4k_B T}{k}} = \frac{0.074 \text{ nm}}{\sqrt{k}}, \quad (2.27)$$

where  $k_B$  is the Boltzmann constant,  $k$  the spring constant of the cantilever and  $T$  the temperature. At RT for example,  $\Delta z$  for a free cantilever of  $k = 1 \text{ N/m}$  is 0.074 nm. Most of the commercial AFM microscopes can reach a vertical resolution as low as 0.01 nm for more rigid cantilevers.

As concerns the lateral resolution of an AFM, it is defined as the minimum detectable distance  $d$  between two sharp peaks of different heights. It is given by

$$d = \sqrt{2R}(\sqrt{\Delta z} + \sqrt{\Delta z + \Delta h}). \quad (2.28)$$

where  $R$  represents the curvature radius of the tip,  $\Delta z$  the vertical resolution and  $\Delta h$  the relative height of the two peaks. Ideally, an AFM should be capable of atomic and sub-nanometer resolution, if a sharp enough tip is used (typical aspect ratio at 200 nm from the tip apex in the order of 4:1). Therefore, we will use it to check the depth of the holes of the triangular array and have an idea about the  $\text{In}_{0.53}\text{Ga}_{0.47}\text{As}$  surface roughness.

The AFM used in this thesis is the Dimension 3100 produced by Veeco. A picture of the AFM head is showed in Figure 2.24. The tip mounted on a tip holder is inserted in the bottom part of the AFM head (purple box). Once mounted, the laser has to be positioned on the cantilever by using the laser alignment screws (red box). In a similar way, by turning the screws for the detector alignment, the beam reflected from the cantilever has to be aligned with the center of



the four-quadrant photodiode (blue box). Furthermore, the system is equipped with a camera that allows to see both the cantilever and the sample surface.

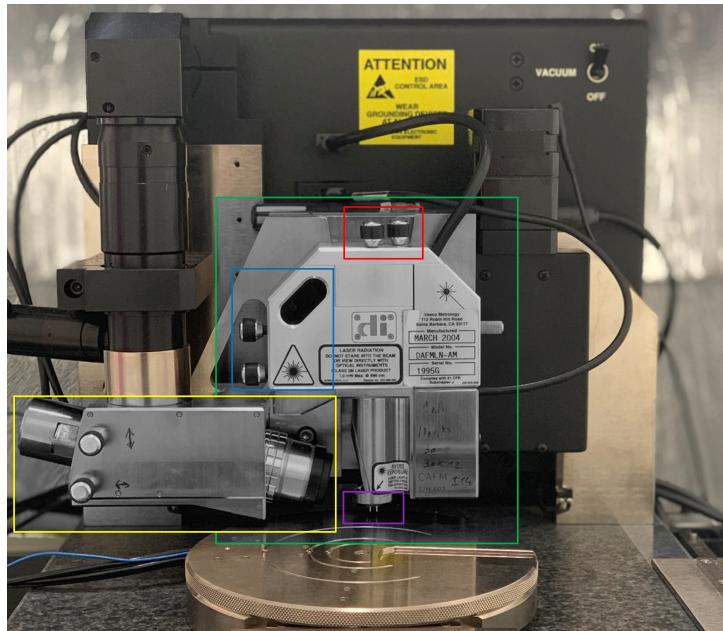


Figure 2.24 – Veeco Dimension 3100 AFM. AFM head (green box), optical camera and adjustments (yellow box), detector alignment screws (blue box), laser alignment screws (red box) and tip holder position (purple box).





# Resolving the two-dimensional density of states of an $\text{In}_{0.53}\text{Ga}_{0.47}\text{As}/\text{InP}$ quantum well

## Outline of the current chapter

---

<b>3.1 Defining the critical parameters for the <math>\text{In}_{0.53}\text{Ga}_{0.47}\text{As}/\text{InP}</math> heterostructure</b>	<b>52</b>
<b>3.2 Sample structures</b>	<b>53</b>
<b>3.3 Influence of the surface preparation on the surface morphology</b>	<b>55</b>
<b>3.4 Measurement of a 2D-DOS</b>	<b>58</b>
3.4.1 Tunneling spectroscopy of the $\text{In}_{0.53}\text{Ga}_{0.47}\text{As}/\text{InP}$ heterostructure	58
3.4.2 Importance of the hole concentration in the QW . . . . .	63
3.4.3 Transport mechanisms through the quanta states . . . . .	66
<b>3.5 Conclusion</b>	<b>69</b>

---

As anticipated in the first chapter, extremely important for the following of the work is the characterization of the as-grown semiconductor heterostructures. In particular, we must ensure the presence of a 2D-DOS prior to the nanoperforation of the heterostructure. As discussed in the second chapter, measurement of the DOS should be performed at low temperature to ensure the highest spectral resolution. Therefore, fundamental will be the doping level of the  $\text{In}_{0.53}\text{Ga}_{0.47}\text{As}$  QW and the nature of the doping so that electrons can be transferred through the CB states of the  $\text{In}_{0.53}\text{Ga}_{0.47}\text{As}$  QW. After that, we must verify that the disorder in the system is weak enough so that the band structure is preserved. Different sources of disorder have to be kept in mind in order to build the appropriate structures, as for example the roughness of the surface or the spatial fluctuations of the band offset due to clustering in InGaAs alloys. To have access to this information, the semiconductor heterostructures will be characterized with STM and STS. In this way we will probe the morphology of the samples, assess the experimental DOS structure and verify its 2D nature.

In this chapter we report studies that we performed on the as-grown III-V heterostructures. We investigated five  $\text{In}_{0.53}\text{Ga}_{0.47}\text{As}/\text{InP}$  QWs, to be able to find out both the best growth and sample preparation conditions. First of all, we will describe our semiconductor heterostructures and introduce the fundamental step of As capping deposition and evaporation to be able to analyze clean and well-ordered surfaces. After that, we will focus our attention on the study of the surface roughness of the samples. In the second part, we will look to their electronic properties in order to probe a 2D-DOS in the  $\text{In}_{0.53}\text{Ga}_{0.47}\text{As}$  QW. We will show that the appearance of a step-like function in the CB strongly depends on both the hole concentration in the QW and the current injected into the quantized states. Based on STM-LE experiments and 4-probe STM transport measurements, we will be able to rationalize the observed behaviors and explain the charge-transport mechanisms that account for the presence of a 2D-DOS in the tunneling spectra. The chapter will end with a discussion of the fluctuations of the measured spectral features.

### 3.1 Defining the critical parameters for the $\text{In}_{0.53}\text{Ga}_{0.47}\text{As}/\text{InP}$ heterostructure

To reveal the electronic properties of the semiconductor heterostructures, LT-STs measurements will be carried out. Therefore, the structure and the doping nature of our samples have to be chosen accordingly with the possible tunneling processes during the STM measurements. As anticipated at the end of the first chapter, our 2DEG will be created on a p-doped  $\text{In}_{0.53}\text{Ga}_{0.47}\text{As}/\text{InP}$  QW heterostructure. In Figure 3.1 a comparison between the expected n-doped and p-doped band diagrams for an  $\text{In}_{0.53}\text{Ga}_{0.47}\text{As}/\text{InP}$  QW heterostructure are reported. For the n-type structure, the electrons tunneling from the tip to the sample will charge the CB of the QW preventing the 2DEG detection. As one can see from Figure 3.1 (a), there is no available hole to recombine with the electrons in the QW VB and a CB offset between InP and  $\text{In}_{0.53}\text{Ga}_{0.47}\text{As}$  QW of around 200 meV, prevents the transfer of electrons from the QW into the InP CB. As a result, the electrons can not escape, leading to a charging of the QW CB. On the contrary, a p-doped heterostructure seems to satisfy the conditions for the 2DEG electronic properties to be properly

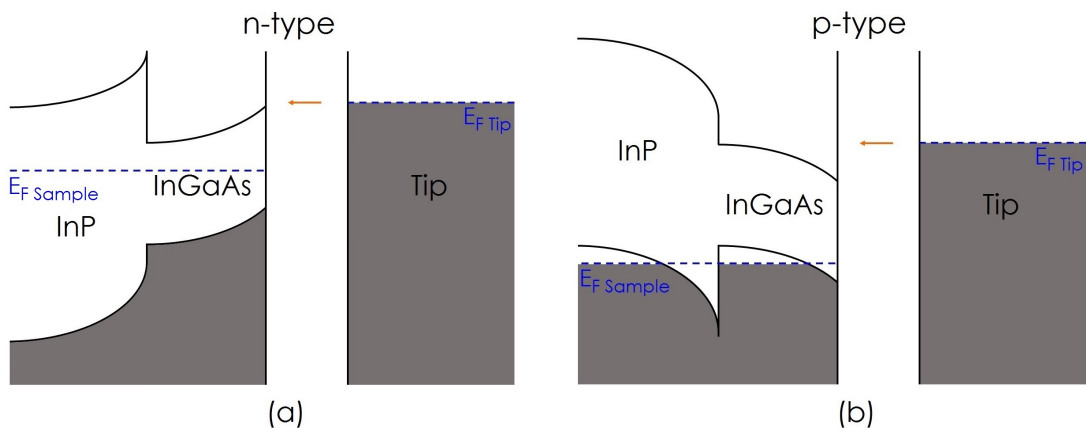


Figure 3.1 – Band diagrams along the growth direction  $z$  for (a) n-doped and (b) p-doped heterostructures.

probed. As illustrated in Figure 3.1 (b), the p-doping nature of the structure causes a downward band bending. As a consequence, the QW VB is filled with the majority charge carriers only close to the interface with the InP buffer layer. Therefore, the electrons tunneling from the tip to the QW CB recombine with the holes in the QW VB and the derivative of the tunneling current should be proportional to the 2D-DOS.

Another important point concerns the FL position. The FL can be accurately tuned in the bulk of a semiconductor by introducing small amounts of dopants. However, in the case of semiconductor surfaces it depends not only on bulk doping, but also on the presence of surface states. In particular, for high density of surface states, the FL appears in most cases pinned near midgap<sup>[91, 92]</sup> or in the CB<sup>[93]</sup>. An example of FL pinning was observed for the GaAs (001)-(2x4) surface<sup>[94, 70]</sup>. On n-type GaAs (001), it is pinned midgap for all doping levels due to the formation of surface acceptor states by a self compensation mechanism. On the other hand, on the p-type GaAs (001), the FL position is controlled by intrinsic defects. It has been observed that the position of the FL strongly depends on the substrate orientation. In fact, a notable exception of the pinning was demonstrated for the (110) and (111) clean surfaces<sup>[69, 95, 96]</sup>, with a possible unpinning for the (100) surface using hydrogen<sup>[97]</sup> or trimethylaluminum<sup>[98]</sup> passivation. As illustrated in Figure 3.1 (a), in the case of the n-type  $\text{In}_{0.53}\text{Ga}_{0.47}\text{As}$  (001)-(2x4) surface, the FL remains pinned near midgap by a high density of acceptor surface states. While at the (111)A-(2x2) surface, the density of acceptor surface states is much lower and not enough to keep the FL pinned, so that it results unpinned. A FL pinning at the top of the VB is expected for a p-type  $\text{In}_{0.53}\text{Ga}_{0.47}\text{As}$  (001)-(2x4) surface due to the absence of kinks in the dimer-vacancy rows of the (001) surface, as demonstrated for the GaAs (001)-(2x4) surface [see Figure 3.1 (b)]. Therefore, the last heterostructure configuration could be the most appropriate choice for our objectives. We will set an hole density in the range  $10^{18}$ - $10^{19}$   $\text{cm}^{-3}$  to satisfy the flat band conditions and make the  $\text{In}_{0.53}\text{Ga}_{0.47}\text{As}$  QW barely sensitive to the voltage applied between the STM tip and the sample. In this way, the CB states will be probed at positive sample voltages higher than 0.8 V, once the FL of the STM tip is aligned with those unoccupied states. Albeit surface states on the (001) surface exist, their density is low enough that it is not going to hide the LDOS of the  $\text{In}_{0.53}\text{Ga}_{0.47}\text{As}$  QW in tunneling spectroscopy<sup>[95]</sup>.

### 3.2 Sample structures

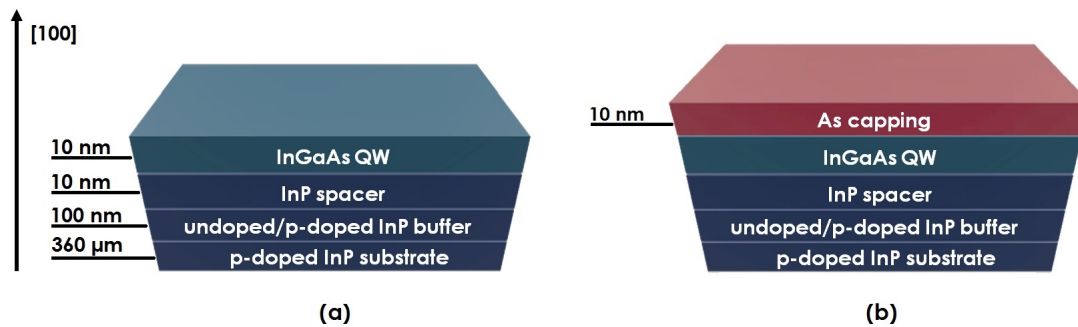


Figure 3.2 – Detailed layer structure of the  $\text{In}_{0.53}\text{Ga}_{0.47}\text{As}$  QW grown on InP (001) by MBE without (a) and with (b) the As capping.

The  $\text{In}_{0.53}\text{Ga}_{0.47}\text{As}/\text{InP}$  QW heterostructures were grown by MBE on a Zn p-type doped InP (001) substrate with a concentration of  $4 \times 10^{18} \text{cm}^{-3}$ . As illustrated in Figure 3.2 (a), the

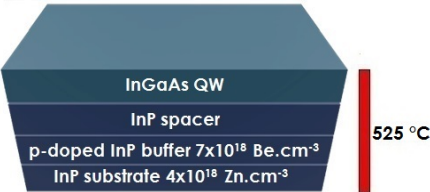
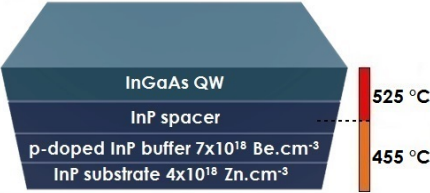
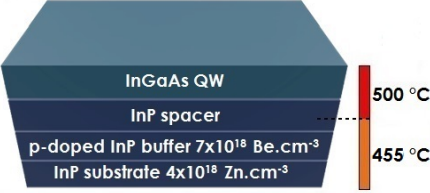
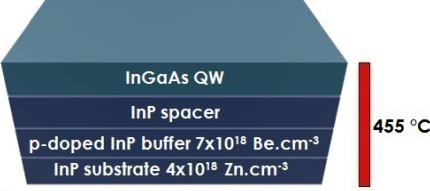
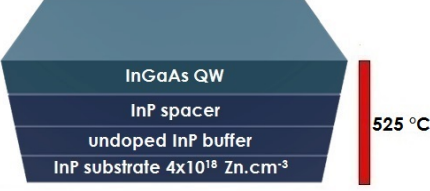
Sample	Description
	<b>G170401 and G180301.</b> MBE growth at $T = 525$ °C. The buffer layer is p-doped. As capped at the end of the growth.
	<b>G170301 and G180102.</b> MBE growth: InP buffer layer + 5 nm of InP spacer layer at $T = 460$ °C, 5 nm of InP spacer layer + $\text{In}_{0.53}\text{Ga}_{0.47}\text{As}$ QW at $T = 525$ °C. The buffer layer is p-doped. As capped at the end of the growth.
	<b>G170108.</b> MBE growth: InP buffer layer + 5 nm of InP spacer layer at $T = 460$ °C, 5 nm of InP spacer layer + $\text{In}_{0.53}\text{Ga}_{0.47}\text{As}$ QW at $T = 500$ °C. The buffer layer is p-doped. As capped at the end of the growth.
	<b>G170101.</b> MBE growth at $T = 460$ °C. The buffer layer is p-doped. As capped at the end of the growth.
	<b>G170402.</b> MBE growth at $T = 525$ °C. The buffer layer is undoped. As capped at the end of the growth.

Table 3.1 – Sample names and descriptions.

samples consist of a top 10 nm thick  $\text{In}_{0.53}\text{Ga}_{0.47}\text{As}$  QW, a 10 nm thick InP spacer layer and a 100 nm thick undoped/p-doped InP buffer layer. At the end of the growth, a 10 nm thick amorphous As layer was deposited on top of the samples to protect their surface from air exposure [see Figure 3.2 (b)]. This layer was then removed in UHV by thermal treatment.

Five  $\text{In}_{0.53}\text{Ga}_{0.47}\text{As}/\text{InP}$  heterostructures with different Be dopant concentrations were prepared. In Table 3.1 we summarize the name of the samples and give some details about their growth temperature and layer composition. For the sample labeled as G170401, the whole structure was grown at 525 °C. This high temperature favors the diffusion of Be in the QW<sup>[99]</sup>. In order to reduce the amount of dopants in the QW, which could lead to potential fluctuations induced by the inhomogeneous subsurface distribution of Be acceptors, a second structure, the G170301, was prepared at a lower temperature of 455 °C up to the half part of the InP spacer layer. The growth was then interrupted and the temperature was raised to 525 °C before growing the  $\text{In}_{0.53}\text{Ga}_{0.47}\text{As}/\text{InP}$  heterointerface. The third sample, labeled G170308, was almost grown as G170301, only the QW growth temperature was set at 500 °C instead of 525 °C in order to see the influence of the growth temperature on their surface morphology. For the sample called G170101, the temperature was set at 455 °C during the whole process. In these four samples the InP buffer layer was doped. The last structure, denoted as G170402, was also entirely grown at 525 °C, but in this case no dopant was intentionally incorporated during the growth.

### 3.3 Influence of the surface preparation on the surface morphology

The amorphous As layer preserves the surface from contamination during the transfer in air from the MBE to the STM. This layer is usually removed by annealing the sample in the UHV preparation chamber of the STM system. Since the temperature used to desorb the As capping layer of an InGaAs (001) surface is known to affect the surface reconstruction<sup>[100]</sup> and the surface structure leads to different pinning of the FL, we examined the surface by employing RHEED. The monitoring was directly done after the deposition of the protective layer in the MBE growth system. In this way, we were able to follow the temperature dependence of the surface reconstruction. To perform this analysis, the temperature was increased from 25 °C to 455 °C, 10 °C/min. A summary of what we observed is reported in Table 3.2. The first clear diffraction pattern was observed at 320 °C. It showed a typical 4×3 surface reconstruction. After 8 minutes at 340 °C, the surface exhibited a 2×3 reconstruction. After 11 minutes at 340 °C, the surface reconstruction changed from the 2×3 to the 2×4. This As-rich surface reconstruction survived up to 445 °C before being replaced by the group-III rich 4×2 reconstruction. Albeit a stable 2×4 surface reconstruction was observed from 340°C up to 445°C, we decided to desorb the As protective layer at the LT of 350 °C for two hours to limit the diffusion of impurities.

Surface reconstruction	Temperature (°C)
(4×3)	320
(2×3)	after 8' at 340
(2×4)	after 11' at 340
(4×2)	455

Table 3.2 – Temperature dependence of the surface reconstruction.

Any modification of the surface properties due to this annealing step was further analyzed with ultraviolet photoelectron spectroscopy (UPS). This study was performed with a discharge lamp operating at 21.2 eV (He-I) in the same UHV system as the growth chamber. These measurements were performed on the G170301 sample and the results are shown in Figure 3.3. Both UPS spectra measured prior to the As capping or after the sublimation of the As capping layer exhibit a FL pinning  $0.50 \pm 0.05$  eV above the top of the VB edge. A stable position of the FL is consistent with the preservation of the  $(2 \times 4)$  As reconstruction. It also indicates that the dopant concentration in the QW is not significantly affected by the annealing, since a strong diffusion of p-type dopants close to the surface is known to shift the FL towards the VB edge, despite a high concentration of surface states in the bulk band gap<sup>[70]</sup>.

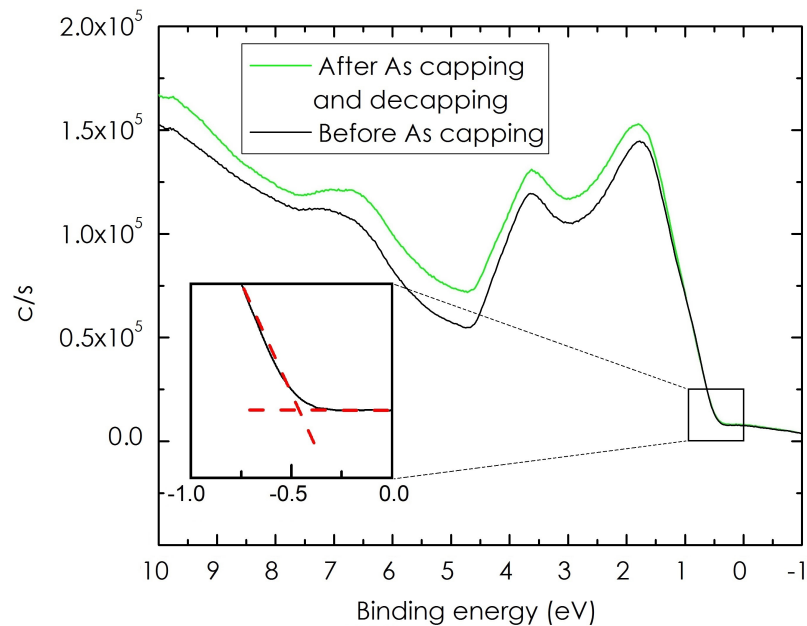


Figure 3.3 – UPS spectra acquired on G170301 sample, before the As capping (black line) and after the As decapping (green line). Inset: high magnification of the VB edge. The top of the VB is given by the intersection of the dashed straight lines.

Additional structural information was obtained from STM measurements. In Figure 3.4 we report the STM images of the surface of the samples presented in Table 3.1. The images were acquired on a  $100 \times 100 \text{ nm}^2$  area of the surfaces and at RT, except for G170401 sample, performed at 77 K. Figure 3.4 (a) shows a STM image of G170401 sample. A typical step growth mode with jagged terraces characterized by an average width of 40-50 nm is observed. Similar results obtained on G170301 sample are illustrated in Figure 3.4 (b). The surface reveals a step growth mode of jagged terraces but in this case, their width is in the range of 30-40 nm. As for G170108 sample, the STM topography of Figure 3.4 (c) reports an island growth mode. The measured width of the terraces is 40-50 nm. As visible in Figure 3.4 (d), the island growth mode is also observed for sample G170101. Nevertheless, the terraces appear smaller (20-30 nm). Concerning G170402 sample, the acquisition of a stable STM topography was not possible at low temperature. We suggest that it could be related to the absence of dopants in the heterostructure. The step height of the terraces was measured on the four STM topographies. A value of around

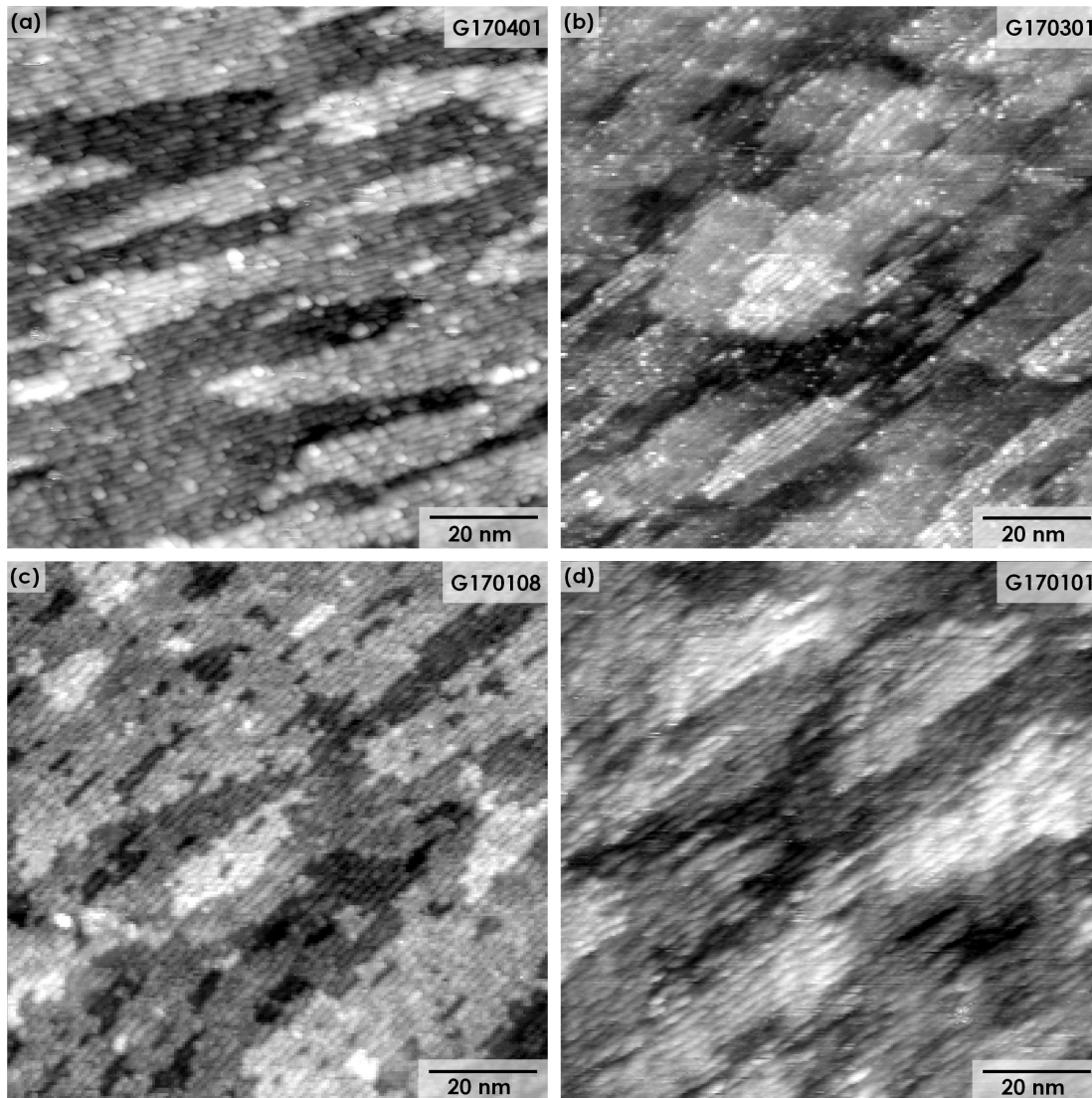


Figure 3.4 – STM images acquired on a  $100 \times 100 \text{ nm}^2$  area of (a) G170401, (b) G170301, (c) G170108 and (d) G170101 sample surface. Topographies acquired using  $V_S = +1.80 \text{ V}$ ,  $I_{\text{setpoint}} = 10 \text{ pA}$  and at room temperature except (a), acquired at 77 K.

0.29 nm, corresponding to an atomic bilayer thickness ( $\text{In}_{0.53}\text{Ga}_{0.47}\text{As}$  lattice constant  $a = 0.587 \text{ nm}$ ) was obtained.

High resolution STM images were acquired on the surface of sample G170401 at 77 K. In Figure 3.5 (a), a topography of a  $10 \times 10 \text{ nm}^2$  area shows that rows of bright protrusions were clearly resolved. The separation of the rows is about 1.6 nm, corresponding to the expected value of  $2\sqrt{2}a$ . As illustrated in the structural model of Figure 3.5 (b), the largest protrusions correspond to two adjacent As dimers. The trenches between the rows are caused by missing dimers and it is about 1.6 nm. The zigzag structure indicates that the smallest protrusions are



single As dimers, located either on the left or the right of a row. This reconstruction is typical of the As-rich ( $2 \times 4$ ) structure observed for the  $\text{In}_{0.53}\text{Ga}_{0.47}\text{As}$  (001) surface<sup>[100]</sup>.

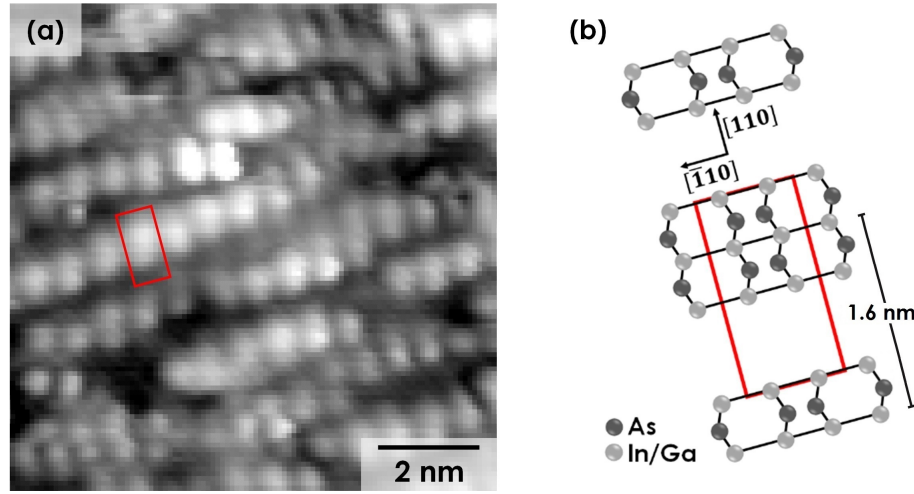


Figure 3.5 – (a) High-resolution STM image of a  $10 \times 10 \text{ nm}^2$  area of sample G170401 surface. Feedback parameters:  $V_S = +1.8 \text{ V}$  and  $I_{\text{setpoint}} = 10 \text{ pA}$ ,  $T = 77 \text{ K}$ . (b) Structural model of the  $\text{In}_{0.53}\text{Ga}_{0.47}\text{As}$  (001)-( $2 \times 4$ ) surface reconstruction with the rectangular unit cell.

Further analysis of the surfaces are presented in Figure 3.6. Here we report the depth histogram and the Abbott-Firestone curve, computed from the depth graph. The values obtained for the surface roughness (RMS, nm) are summarized in Table 3.3.

Sample	G170401	G170301	G170108	G170101
Surface roughness (RMS, nm)	0.30	0.08	0.13	0.23

Table 3.3 – Surface roughness.

The samples grown in two temperature steps (G170108 and G170301), show lowest values of roughness (0.13 and 0.08 nm respectively) with respect to those in which the whole structure was grown at the same temperature (G170101 and G170401). This effect could be a consequence of the lower amount of dopants diffused at their surface. Albeit sample G170401 is characterized by a higher surface roughness (0.30 nm) comparing to sample G170101 (0.23 nm), its surface reveals bigger terraces (flatter surface).

## 3.4 Measurement of a 2D-DOS

### 3.4.1 Tunneling spectroscopy of the $\text{In}_{0.53}\text{Ga}_{0.47}\text{As}/\text{InP}$ heterostructure

STS was performed on three of the five semiconductor heterostructures presented in Table 3.1, G170401, G170301 and G170402. The main difference between these samples is the doping level of the  $\text{In}_{0.53}\text{Ga}_{0.47}\text{As}$  QW: G170401 sample is the highly doped one, G170402 is the undoped and G170301 is the semi-doped sample. In Figure 3.7 (a) we report the results obtained on the



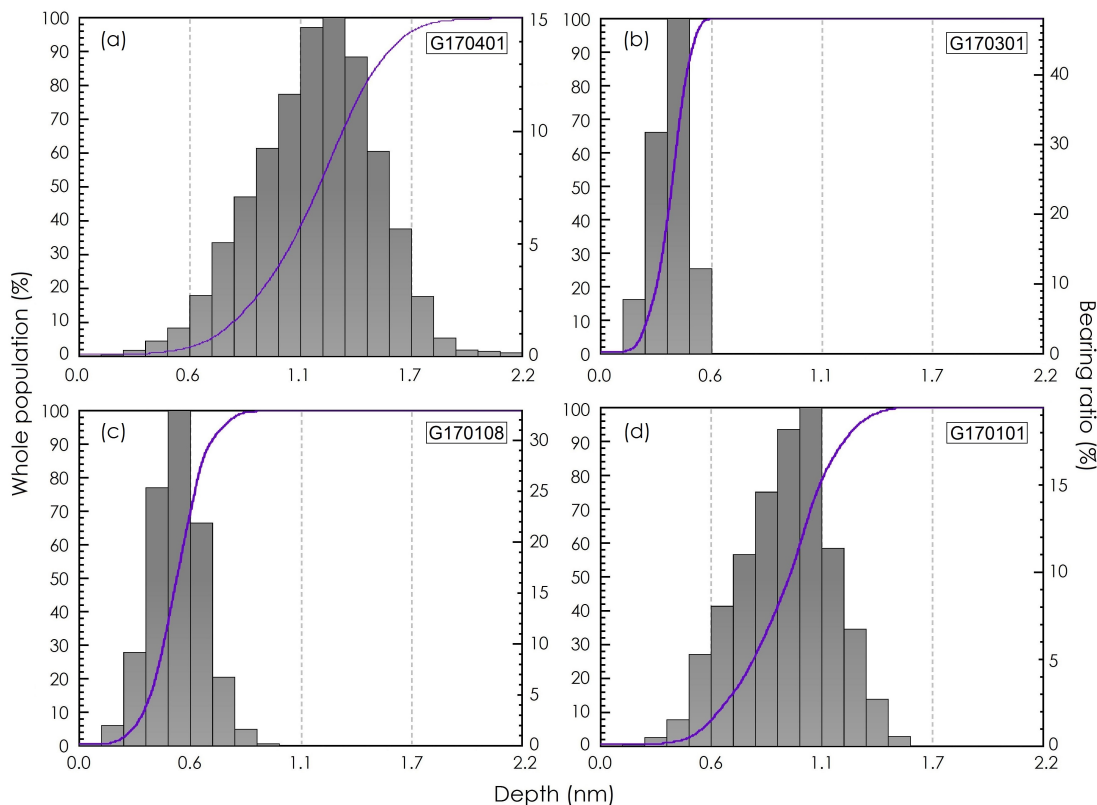


Figure 3.6 – (Left) Depth histogram and (right) Abbott-Firestone curve of (a) sample G170401 surface, (b) sample G170301 surface, (c) sample G170108 surface and (d) sample G170101 surface. The analysis was performed on a  $80 \times 80 \text{ nm}^2$  area of the sample surfaces.

doped G170401 sample. In the spectra, the VB states are probed at negative bias. The position of the FL (energy  $E_F$ ) is determined at 0 V, and based on the onset of the VB (energy  $E_V$ ), it is found to be positioned  $0.17 \pm 0.03 \text{ eV}$  above the top of the VB. Three steps are clearly visible at positive voltages, labeled  $E_1$ ,  $E_2$  and  $E_3$ . From the position of the first step edge and the onset of the VB, we determined an apparent band gap of  $0.90 \pm 0.03 \text{ eV}$ , which is consistent with the energy of the PL peak obtained for a 10 nm thick  $\text{In}_{0.53}\text{Ga}_{0.47}\text{As}$  QW inserted between two InP potential barriers<sup>[101, 65]</sup>. As discussed in the first Chapter, Subsection 1.1.2, Perraud et al. attributed the three steps to the electron sub-bands produced in the QW due to the quantum confinement<sup>[23]</sup>. Despite an identical thickness of the  $\text{In}_{0.53}\text{Ga}_{0.47}\text{As}$  QW grown on InP (111)A was identical, the potential barrier consisted of an  $\text{In}_{0.58}\text{Al}_{0.42}\text{As}$  layer, resulting in a stronger confinement in the CB. Moreover, the doping of the InP buffer was n-type instead of p-type in our work. Therefore, to understand the origin of the three steps, we decided to evaluate the confinement potential profile in the semiconductor heterostructure that is likely to change with the type of doping.

For that purpose, we estimated the band bending at the surface of the QW, taking into account the proximity of the STM tip. This tip-induced band bending (TIBB) was calculated with the SEMITIP code<sup>[102]</sup>. To simplify the problem, we considered a bulk  $\text{In}_{0.53}\text{Ga}_{0.47}\text{As}$  sample and solved the Poisson equation, taking into account the boundary condition at the vacuum/semiconductor interface. We assumed a Gaussian band of surface states centered 0.4 eV

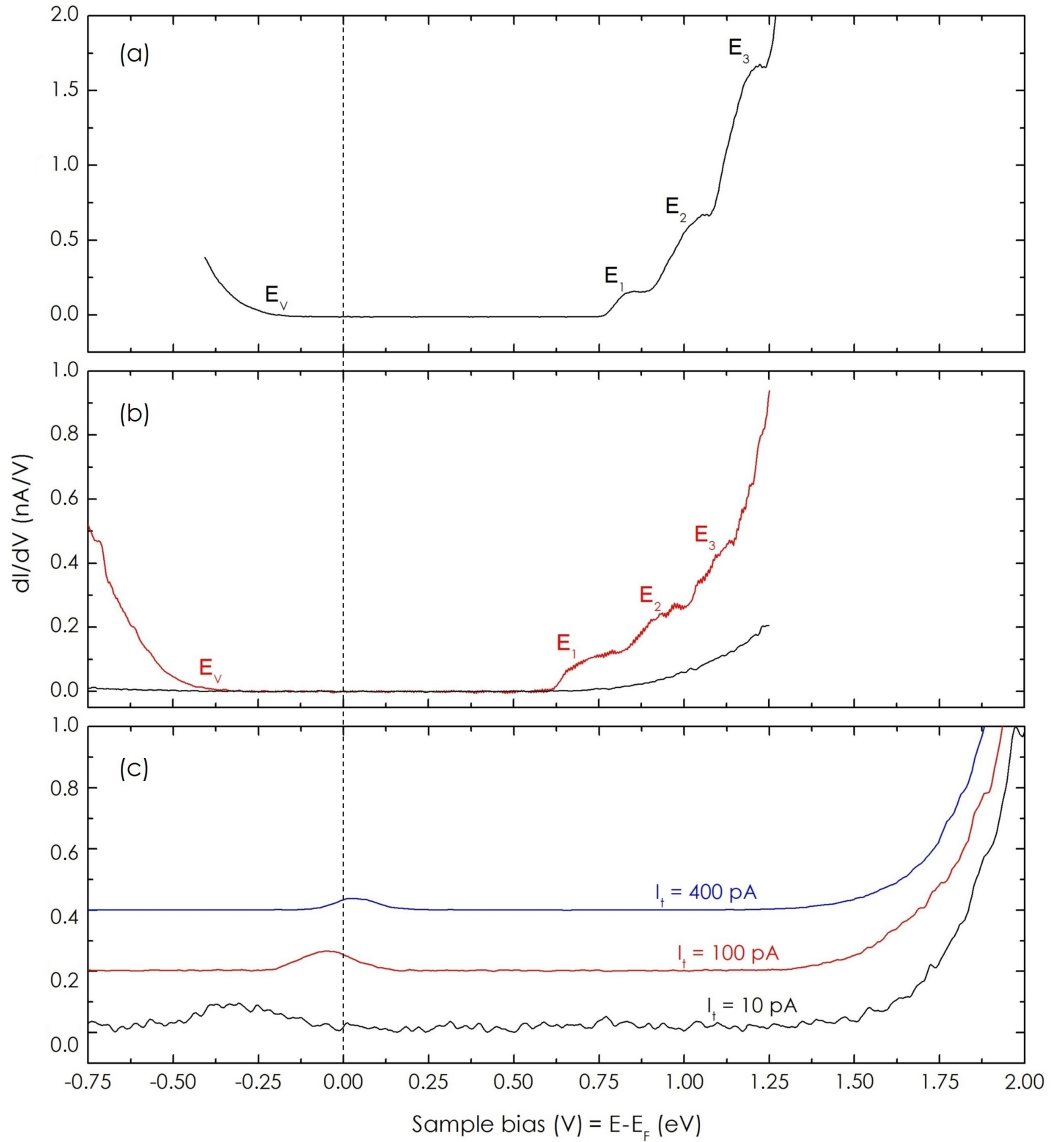


Figure 3.7 –  $dI/dV$  spectra acquired on the (a) G170401, (b) G170301, and (c) G170402  $\text{In}_{0.53}\text{Ga}_{0.47}\text{As}/\text{InP}$  heterostructures measured at 77 K. For the G170301 sample, two different types of spectra were measured as a function of the area probed by the STM tip. For the G170402 sample, the same area was probed with different setpoint currents indicated in the graph. The three electron sub-bands and the top of the VB are labeled  $E_1$ ,  $E_2$  and  $E_3$  and  $E_V$  in (a) and (b). Feedback parameters: (a)  $V_S = +1.30 \text{ V}/I_{\text{setpoint}} = 400 \text{ pA}$ , (b)  $V_S = +1.25 \text{ V}/I_{\text{setpoint}} = 400 \text{ pA}$ , and (c)  $V_S = +2.0 \text{ V}$ . The differential conductance  $dI/dV$  was acquired with a lock-in amplifier using a bias modulation of 10 mV RMS at a frequency of 490 Hz. The apparent band gap was measured by plotting the differential conductance in a log scale to precisely determine the noise level.

above the top of the VB with a density of  $3 \times 10^{12} \text{cm}^{-2}$ , value that was found for a p-type GaAs (001) surface having the same reconstruction<sup>[70]</sup>. This density pins the FL close to midgap for small doping levels, consistent with the UPS measurements of the sample G170301 previously presented in Figure 3.3. It is, however, insufficient to keep the FL midgap at higher doping levels, so that it complies with a shift of the FL closer to the VB, as the doping level in the QW increases. As reported in Figure 3.8, taking a p-type doping concentration of  $1 \times 10^{18} \text{cm}^{-3}$

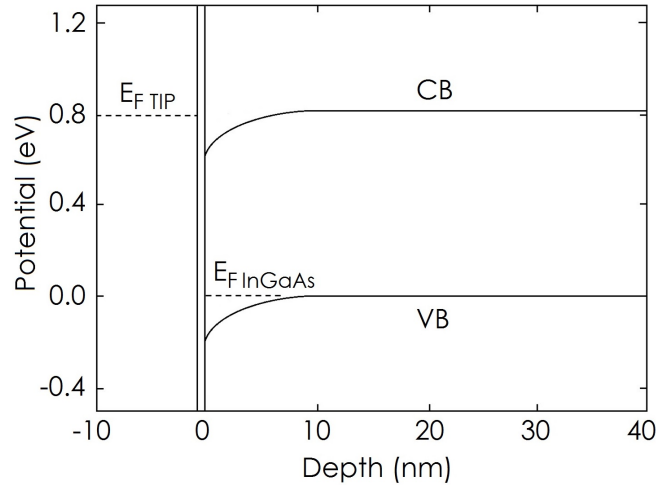


Figure 3.8 – Band diagram of the metal-vacuum- $\text{In}_{0.53}\text{Ga}_{0.47}\text{As}$  at 77 K for a sample bias of 0.8 V. The TIBB was calculated with the SEMITIP code, assuming a doping level of  $1 \times 10^{18} \text{cm}^{-3}$ , a tip radius of 5 nm, a tip-sample distance of 5 Å, and a band of surface states positioned at an energy of 0.4 eV above the top of the VB with a density of  $3 \times 10^{12} \text{cm}^{-2}$ . The dashed lines indicate the positions of the FL in the tip (left) and in  $\text{In}_{0.53}\text{Ga}_{0.47}\text{As}$  (right).

results in a downward band bending extending over 10 nm in the semiconductor material, even at a positive bias of 0.8 V. This bias corresponds to the alignment of the tip FL with the first electron sub-band of the QW. A similar band profile is also found at a bias of +1.0 V, although the band bending is reduced by 50 meV. These results indicate that the potential distribution in the well can be considered as triangular over the whole range of positive bias used to probe the LDOS of the QW.

Tight-binding calculations were performed by Athmane Tadjine to further understand our STS results. The  $\text{In}_{0.53}\text{Ga}_{0.47}\text{As}$  alloy was considered as a virtual crystal in which a virtual atom (Va) replaces each In or Ga atom. Each atom in the heterostructure (Va, As, In, P) was described by 20 atomic orbitals,  $sp^3d^5s^*$  for each spin orientation. We used the tight-binding parameters of Ref. [103] which give an energy gap of 816 meV for the  $\text{In}_{0.53}\text{Ga}_{0.47}\text{As}$  bulk, consistent with Ref. [104]. Based on the literature<sup>[105]</sup>, we assumed a CB offset between  $\text{In}_{0.53}\text{Ga}_{0.47}\text{As}$  and InP of 204 meV and an infinite potential barrier at the vacuum/ $\text{In}_{0.53}\text{Ga}_{0.47}\text{As}$  interface. Free surfaces were saturated by pseudohydrogen atoms described by a single  $s$  orbital. The calculations were not only obtained for a flat potential distribution across the heterostructure but also for a triangular well. This potential shape results from the pinning of the FL by the surface states existing at the vacuum/ $\text{In}_{0.53}\text{Ga}_{0.47}\text{As}$  interface. The results related to a flat potential distribution revealed the formation of two quantized states in the CB. On the other hand, the calculations performed considering a triangular well showed three steps at positive energies. As we can see from Figure 3.9 the obtained LDOS is in agreement with the STS measurements obtained on the G170401

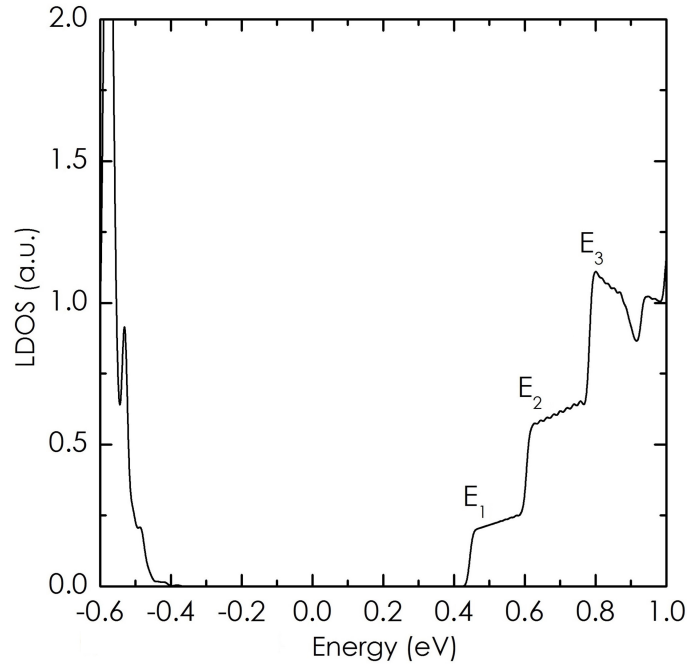


Figure 3.9 – Theoretical LDOS obtained from tight-binding calculations. The three electron sub-bands are labeled  $E_1$ ,  $E_2$  and  $E_3$ .

sample. We note that small oscillations in the curve are induced by the finite  $k$  sampling in the Brillouin zone. Furthermore, the theoretical separation between the quantized states  $E_2 - E_1$  of 0.16 eV and  $E_3 - E_2$  of 0.18 eV fits well with the experimental values of 0.17 eV and 0.19 eV. So that, the potential in the tip/vacuum/sample junction almost fully drops in the vacuum due to a high concentration of holes in the QW.

In contrast to G170401 sample, where the step-like voltage dependence was observed on the whole surface, G170301 sample shows two types of spectra [Figure 3.7 (b)]. The first one is similar to the one of G170401 sample: the  $dI/dV$  yields three steps at positive bias. As we can observe, the step width and the apparent band gap ( $1.00 \pm 0.03$  eV) are slightly larger. Moreover,  $E_F$  is shifted to a higher energy at the surface of the  $\text{In}_{0.53}\text{Ga}_{0.47}\text{As}$  QW. It is now  $0.38 \pm 0.03$  eV above the onset of the VB, closer to the energy measured with UPS in Figure 3.3. Concerning the second type of spectra, the differential conductance does not show the step-like function expected for a QW at positive bias. The weaker signal measured at both positive and negative biases corresponds to an exponential increase of the current with the bias, yielding an apparent band gap of  $1.20 \pm 0.03$  eV. Finally, for G170402 sample, spatially resolved tunneling spectra do not show any features in the energy range corresponding to the three steps [Figure 3.7 (c)]. The onset at positive bias is shifted to 1.25 V at a setpoint current of 400 pA. This value corresponds to the transition between the third step and the exponential increase obtained for the G170301 sample. At negative bias, no signal is measured and a peak is clearly seen in the vicinity of the FL. This peak is found to shift towards the FL with increasing setpoint currents and its origin will be discussed later.

From the different STS results observed among the three samples, it appears clear that the doping level of the structure has a direct consequence on the occurrence of the 2D-DOS. Despite the similarity of the doping level incorporated during the growth of G170401 and G170301 samples, the different spectra showed in Figure 3.7 indicate a significant modification of the doping profile in the heterostructure.

### 3.4.2 Importance of the hole concentration in the QW

Secondary ion mass spectrometry (SIMS) measurements, were done on two samples similar to G170401 and G170301 respectively. Instead of capping the semiconductor heterostructure with a thin As layer, a 10 nm thick undoped InP layer was deposited on top of the  $\text{In}_{0.53}\text{Ga}_{0.47}\text{As}$  QW

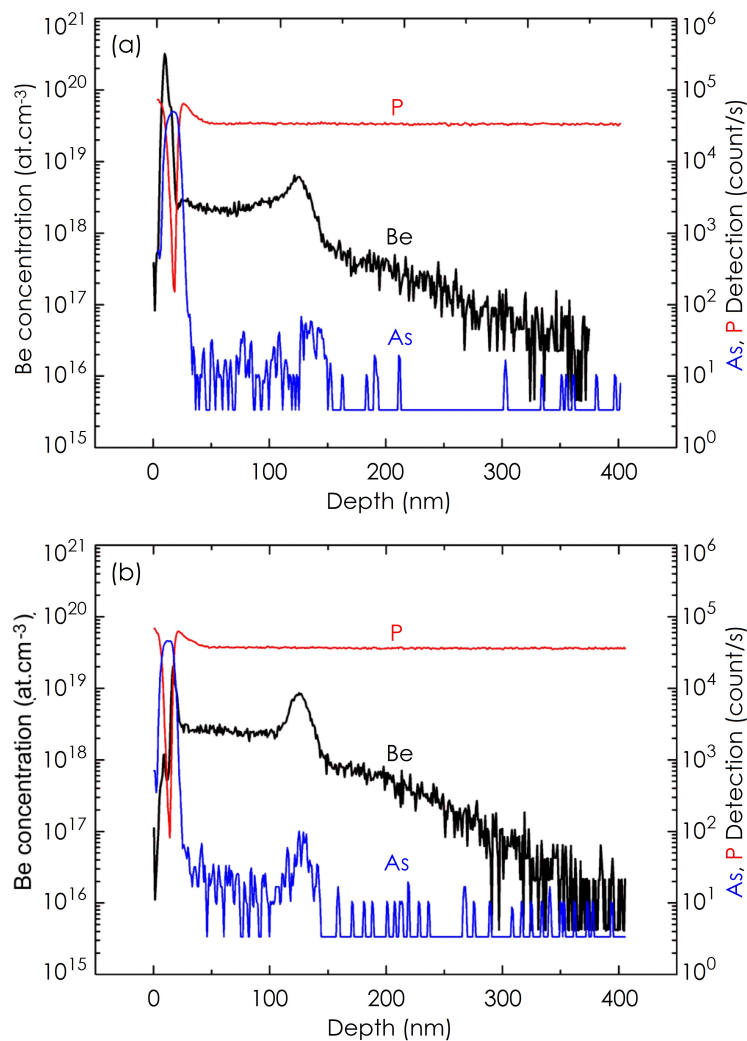


Figure 3.10 – Depth profiles of the Be, P, and As atomic elements in the (a) G170401 sample and (b) G170301 sample both capped with a 10 nm thick InP layer instead of the As amorphous layer.

in order to minimize SIMS artefacts during the initial stage of the sputtering process<sup>[106]</sup>. The results obtained from this analysis are reported in Figure 3.10. The curves reveal a strong Be dopant redistribution with respect to the intended dopant profile, since the incorporation of Be during the growth occurred in the 100 nm thick InP buffer located 30 nm below the surface only. In both profiles, a smaller Be concentration than  $7 \times 10^{18} \text{cm}^{-3}$  was measured in this region, whereas several peaks are visible at the interfaces and surface of the sample. This redistribution is in good agreement with previous analyses of InGaAs and InGaAs/InP heterostructures upon annealing<sup>[99, 107, 108]</sup>. It increases with higher growth temperatures and results in a much higher doping level of the QW for the G170401 sample with respect to G170301 sample, consistent with the STS findings.

To study the electrical activation of the Be dopants in the QW region, 4-probe STM measurements of the resistivity were carried out. As reported in the schematics of Figure 3.11 (a) and the SEM image acquired on the  $\text{In}_{0.53}\text{Ga}_{0.47}\text{As}$  surface [Figure 3.11 (b)], the tips were arranged in a collinear array with equidistant probe spacing  $d$ . Once the current was injected through the two outer tips, the V-I curve between the two inner ones was acquired. In this way we could exclude the contact resistances at the positions of the probes. The V-I curve was acquired for different probe

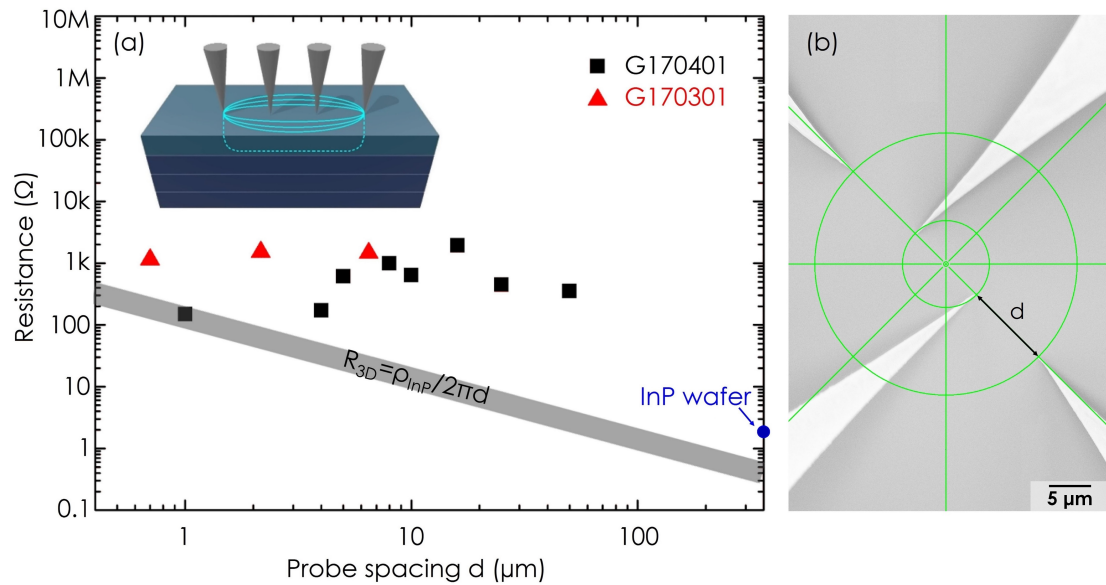


Figure 3.11 – (a) RT 4-probe resistance of the  $\text{In}_{0.53}\text{Ga}_{0.47}\text{As}/\text{InP}$  heterostructure for G170401 and G170301 samples as a function of the probe spacing  $d$ . The probes are arranged in a collinear array with equidistant contact spacing, as shown by the inset and (b) the SEM image acquired on the  $\text{In}_{0.53}\text{Ga}_{0.47}\text{As}$  QW surface. The penetration depth of the current distribution is limited to the QW. The light-gray band highlights the variation of the resistance for three-dimensional semi-infinite bulk InP, which is inversely proportional to the probe spacing  $d$  with a bulk resistivity of  $0.08 \Omega\text{cm}$ . The blue circle shows the measured 4-probe resistance of the InP substrate only.

distances and allows us to know the value of the resistance as a function of  $d$ . For G170402 sample, the absence of doping in the whole structure led to poor electrical contact between the tips and the surface, preventing the measurement of the 4-probe resistance  $R_{4P}$ , in agreement with the difficulties encountered during the STM measurements on the same sample. On the

contrary, on the G170401 and G170301 samples, we were able to measure  $R_{4P}$  as a function of the tip separation  $d$ . The results are showed in Figure 3.11 (a). Although the data scatter more for the doped sample due to a repositioning of the tips in different areas of the sample and along different crystallographic orientations, the resistance can be considered independent of the distance between the probes<sup>[109]</sup>. This behavior is in contrast to the typical increase of the resistance for a homogeneous and isotropic thick-enough three-dimensional resistive doped InP semiconductor indicated by the grey tilted band in Figure 3.11 (a)<sup>[110]</sup>. It is the signature of a 2D transport<sup>[85]</sup>. While the band offset is large enough to prevent the penetration of the current into the InP layers, transport involves two current paths that we consider to be spatially separated: one in the QW and one at its surface through the band of surface states. Thus we assume a parallel-circuit model, where the 4-probe resistance  $R_{4P}$  is given by

$$\frac{1}{R_{4P}} = \frac{1}{R_{QW}} + \frac{1}{R_{SS}}, \quad (3.1)$$

where  $R_{QW}$  is the resistance of the QW and  $R_{SS}$  is the resistance related to the transport through the surface states. The conductivity of the QW varies with the hole concentration, which itself imposes the position of the FL at the surface of the QW. Due to the pinning of the FL midgap at the surface of the G170301 sample and a hole concentration that is smaller than  $1 \times 10^{19} \text{cm}^{-3}$  over a large fraction of the QW thickness, the QW of the G170301 sample is largely depleted in holes. Taking a conductance channel with a width  $t$  smaller than the full width of the QW, the resistance of the QW is

$$R_{QW} = \frac{\ln(2)}{\pi t e \mu_p p}, \quad (3.2)$$

where  $\mu_p$  and  $p$  are the hole mobility and the hole concentration, respectively. A hole concentration of  $1 \times 10^{19} \text{cm}^{-3}$  results in a mobility of about  $70 \text{cm}^2 \text{V}^{-1} \text{s}^{-1}$ <sup>[111]</sup>. Assuming a QW width of 5 nm at most yields a  $R_{4P}$  higher than 4 k $\Omega$ , which cannot explain the measured resistance of 1373  $\Omega$ . Therefore, the second channel through the band of surface states is less resistive. Neglecting the transport through the QW gives a sheet resistance

$$R_{Sheet} = \frac{\pi R_{4P}}{\ln(2)} \quad (3.3)$$

which corresponds to a surface conductivity of  $1.6 \times 10^{-4} \text{S}/\square$ . This value is in the range of the typical surface conductivities measured for the Ge (001) and Si (001) surfaces consisting of rows of dimers<sup>[112]</sup> and accounts for the transport properties at the surface of sample G170301. For the doped sample, the resistance  $R_{4P}$  is smaller. Due to the high doping level of the QW, as found by SIMS, the contribution of the QW cannot be neglected anymore. Also, the surface-state density should not be affected by the change of the p-type doping level<sup>[70]</sup>. Therefore, assuming a similar surface conductivity as the one found for G170301 sample, a mean resistance  $R_{4P}$  of 661  $\Omega$  yields a conductivity in the QW of  $173 \text{S cm}^{-1}$ . This high conductivity matches an average hole concentration of a few  $10^{19} \text{cm}^{-3}$ , for which the mobility is about  $50 \text{cm}^2 \text{V}^{-1} \text{s}^{-1}$ <sup>[111]</sup>. Such a concentration, which is smaller than the measured concentration of Be atoms in the QW, suggests that the Be atoms that have segregated to the surface of the sample might not be electrically active.



### 3.4.3 Transport mechanisms through the quanta states

It is clear that a high concentration of holes in the QW is a key point for the detection of a 2D-DOS. What is still not obvious, is its impact for the formation of a steady-state current measured through the QW states. So that, we will now look to the transport mechanisms through the structure. At LT, a CB offset around 200 meV prevents the transfer of electrons from  $E_1$  into the InP CB. As a consequence, we think that the electrons must recombine with the holes in the VB [see band diagram in Figure 3.12 (b)]. This effect is clearly demonstrated by the tunneling

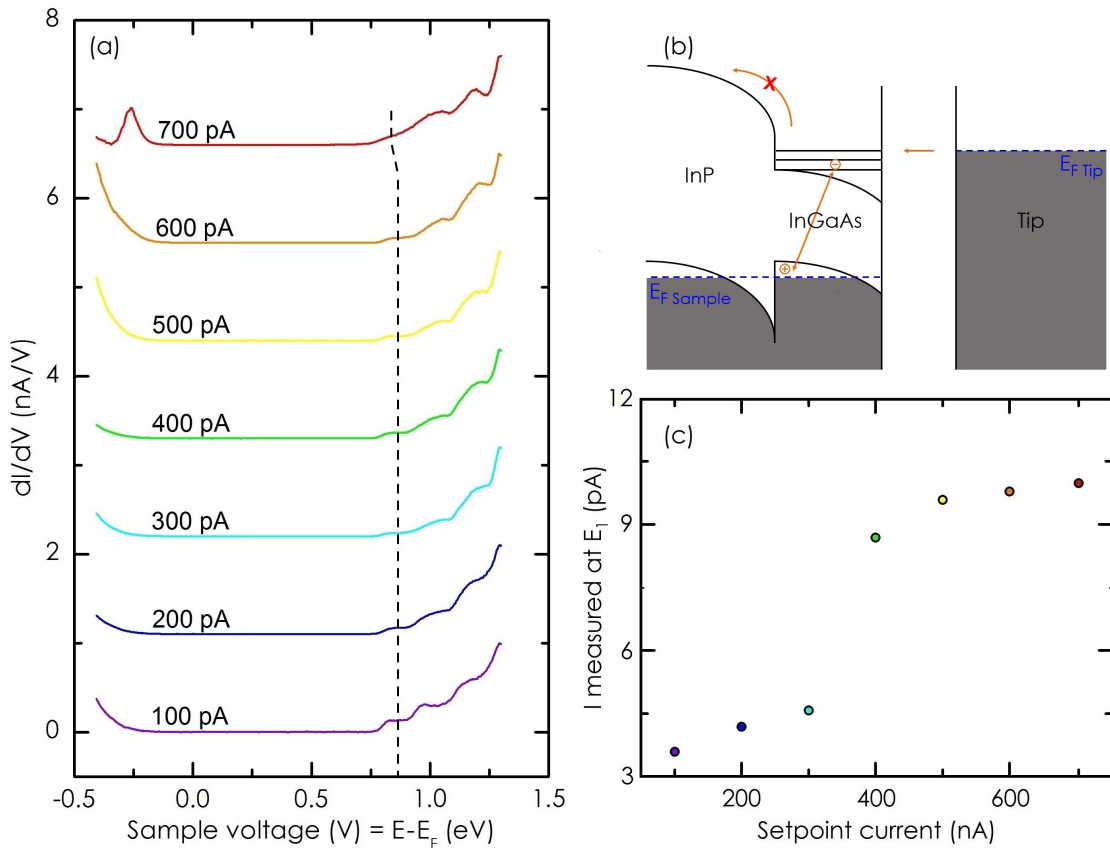


Figure 3.12 – (a) Normalized  $dI/dV$  spectra acquired on the doped  $\text{In}_{0.53}\text{Ga}_{0.47}\text{As}/\text{InP}$  heterostructure (G170401 sample) with different setpoint currents at 77 K. Feedback parameters:  $V_S = +1.30$  V, the setpoint currents are indicated in the graph. (b) Band diagram of the tunneling junction. At LT the CB offset between the InP and the  $\text{In}_{0.53}\text{Ga}_{0.47}\text{As}$  QW is around 200 meV, so that, the electrons can not escape by transferring from  $E_1$  into the InP CB. Consequently, they must recombine with the holes in the VB. (c) Current measured as a function of the setpoint current at a bias of +0.86 V between 100 and 600 pA and +0.83 V for 700 pA. These biases, highlighted by the dashed line in the Figure (a), correspond to the plateau of the first electron sub-band  $E_1$  in the  $dI/dV$  characteristics.

spectra of G170402 sample showed in Figure 3.7 (c), where the step-like voltage dependence is not visible. When holes are absent, the tunneling electrons that are transferred from the tip to the first electron sub-band cannot recombine with holes in the QW, causing the charging of



the QW. A higher voltage is thus required to transfer electrons from the tip states to the InP CB via the delocalized states of the QW. The onset of the exponential increase of the current occurs at a bias of +1.25 V instead of +0.50 V, which corresponds to the resonance of the tip FL with the bottom of the InP CB via the delocalized states of an uncharged QW. In the G170401 and G170301 samples, the presence of holes in the QW allows a current to run through the electron sub-bands. With increasing setpoint currents, we expect the TIBB to be stronger, causing a local modification of the potential that is known to extend over tens of nanometers laterally<sup>[113]</sup>. This effect induces a weak confinement of  $E_1$ . Assuming a small degree of localization for  $E_1$  allows the current injected from the STM tip via  $E_1$  to be written as

$$I = -e(1 - f)W_t, \quad (3.4)$$

with  $e$  the electron charge,  $W_t$  the transmission probability per unit of time across the tunneling barrier, and  $f$  the occupation probability of the QW. In the steady-state regime, this current is equal to the current emitted from  $E_1$  to the VB of the QW:

$$I = -efW_r, \quad (3.5)$$

where  $W_r$  is the recombination rate of the electron on  $E_1$ . Eliminating  $f$  from both equations results in the following expression for the current

$$I = -e \frac{1}{\left(\frac{1}{W_t} + \frac{1}{W_r}\right)}, \quad (3.6)$$

Therefore, the current should be limited by the slowest process. As shown in Figure 3.12 (a), the differential conductance  $dI/dV$  was acquired at different setpoint currents on G170401 sample. The three electron sub-bands are visible up to 600 pA without any energy shift in their position. Focusing on the variation of the current measured at the plateau corresponding to the ground states  $E_1$  [Figure 3.12 (c)], the current increases smoothly below 300 pA, more abruptly between 300 and 400 pA, and then saturates at around 10 pA, consistent with transport through a single quantum level involving two processes. As long as the probability  $W_t$ , which increases exponentially with setpoint current, is smaller than  $W_r$ , the current increases. Once it exceeds  $W_r$ , the current transferred through  $E_1$  saturates, yielding a recombination rate  $W_r$  of one electron every 16 ns. We note that a further increase of the setpoint current to 700 pA causes a change of the differential conductance characteristic. At positive bias, the onset is shifted to a smaller bias, whereas at negative bias, a strong peak appears, indicating a change of the potential distribution across the heterostructure that could be caused by the proximity of the STM tip. From these observations, we infer a stronger downward band bending, which causes the depletion of the wells with holes. As a result, once the tunneling electrons have left the highest occupied valence quantized states, the states become charged, which accounts for the asymmetric peak measured at negative bias.

In order to determine the nature of the recombination processes, G170401 sample was analyzed with STM-LE. High currents had to be used to detect the emission of photons with energies smaller than the InP bulk band gap. The data of Figure 3.13 were recorded at a sample voltage of +3.0 V, i.e., for electron injection, and a current of 20  $\mu$ A. The spectrum exhibits several emission bands with photon energies smaller than the bulk band gap of InP (1.42 eV at 5 K). The most intense band at high energy (HEB), with a maximum centered at 1.37 eV, is similar to the peak found in typical PL spectra of p-type InP substrates<sup>[114]</sup>. Its shape is known to change with the acceptor chemical nature, the acceptor concentration, and the excitation

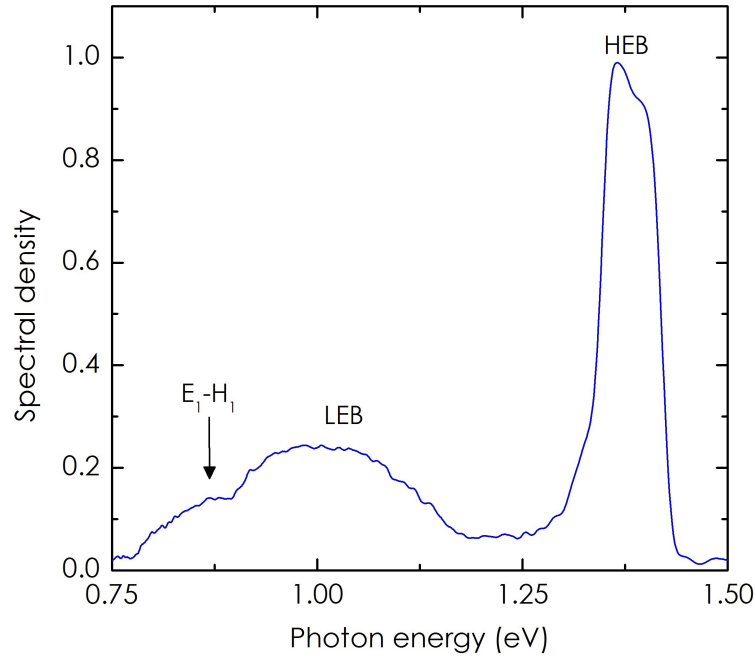


Figure 3.13 – Normalized tunneling-induced luminescence spectrum recorded at a sample voltage  $V_S = +3.0$  V and tunneling current  $I = 20 \mu\text{A}$  over an integration time of 400 s. The spectrum is corrected for detector response. The direct transition in the  $\text{In}_{0.53}\text{Ga}_{0.47}\text{As}$  QW is labeled  $E_1-H_1$ , while the low and high energy bands arising from the InP layers and substrates are labeled LEB (low-energy band) and HEB (high energy band), respectively.

power<sup>[115, 116]</sup>. The origin of the PL has been attributed to the free-to-bound exciton transition at higher energy and transitions between donor and acceptor bands at lower energy, accounting for two contributions in this band. At lower energies, the spectrum exhibits a broad band extending from 0.9 to 1.2 eV. Comparison with PL experiments of InP substrates with a high concentration of Zn acceptor impurities suggests that this band is the so called low-energy band (LEB)<sup>[117]</sup>. It was found to be stable over a wide range of excitation powers in PL<sup>[117]</sup> and has been attributed to deep levels of the p-type InP substrate. Conversely, the band below 0.9 eV has never been reported from p-type InP. It is centered at an energy of 0.85 eV, which matches the energy of the exciton measured in an  $\text{In}_{0.53}\text{Ga}_{0.47}\text{As}/\text{InP}$  heterostructure with the same QW thickness<sup>[101, 65]</sup>. As a result, we assign it to the radiative emission of the  $\text{In}_{0.53}\text{Ga}_{0.47}\text{As}$  QW. Comparison of the recombination rate  $W_r$  with the exciton lifetime of similar heterostructures reveals a slightly longer lifetime with respect to a few to tens of nanoseconds range usually measured<sup>[64, 63]</sup>. This difference could be caused by a reduced overlap between the electron and hole wave functions in the triangular well of the STM junction, with the electron localized at the surface and the hole at the  $\text{In}_{0.53}\text{Ga}_{0.47}\text{As}/\text{InP}$  interface. However, the proximity of the STM tip in the light-emission experiments may modify the potential across the well. Moreover, the high current used is likely to saturate all non-radiative recombination centers at the surface, allowing a large fraction of the tunneling electrons to recombine radiatively<sup>[118]</sup>. We therefore believe that the relaxation of the tunneling electrons transferred to the conduction quantum levels also involves a non-radiative recombination process through the surface states<sup>[119, 120]</sup>. While it is not clear why the surface

states are not detected in the tunneling spectra measured in both G170401 and G170301 samples, consistent with previous studies<sup>[23, 70, 91]</sup>, the existence of surface states clearly appears when tunneling spectroscopy is performed on the undoped G170402 sample. As observed in the  $dI/dV$  spectra of Figure 3.7 (c), a peak appears at small negative bias. This peak shifts towards higher energies as the tip gets closer to the surface, to become finally centered at the FL position. Furthermore, by plotting the current  $I$  as a function of the sample voltage  $V$  (see Figure 3.14), we can see that  $I$  converges towards zero as  $V$  becomes more negative. We attribute this effect to the charging of the surface states near the FL. Due to the lack of enough free charge carriers in the

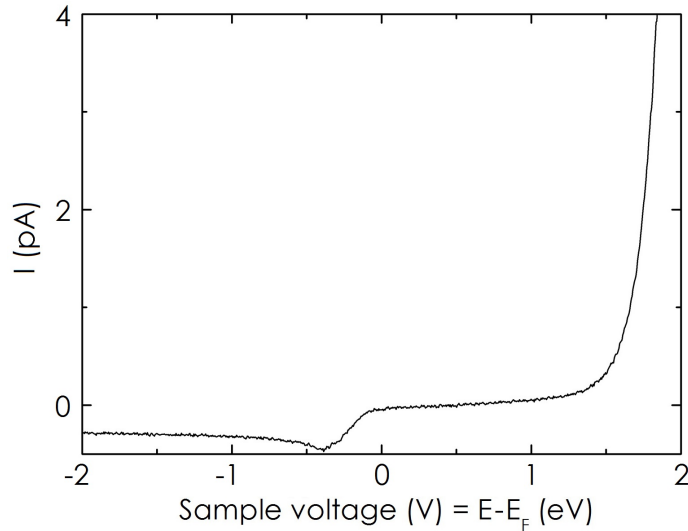


Figure 3.14 –  $I(V)$  characteristic measured at a setpoint current of 10 pA.

QW, the electrons transferred at negative bias from the surface states to the unoccupied tip states cannot be replaced at a rate high enough, leading to positively charged surface states. Hence, the downward band bending increases, preventing the unoccupied tip states from becoming resonant with the VB states of the QW for voltages higher than -2.0 V. In this voltage range, the number of states contributing to the current does not significantly increase, but the transmission across the tunneling barrier gets smaller as the bias decreases. This effect accounts for the  $I(V)$  characteristic obtained at negative bias and demonstrates the key role of the surface states in the tunneling spectra of the sample G170402. We note that the significant surface conductivity of the  $\text{In}_{0.53}\text{Ga}_{0.47}\text{As}$  (001) surface could help in discharging the surface states. However, similar to the localization of the electron sub-bands induced by the proximity of the polarized STM tip, we expect a localization of the surface states under the STM tip that strongly decouples the states from the band of surface states.

### 3.5 Conclusion

The study of the surface morphology had already anticipated G170401 as a good candidate for the following of the work. Its surface was in fact characterized by large terraces (40-50 nm) with a roughness of 0.30 nm RMS. A good surface reconstruction was also observed toward the different areas analyzed. The appropriate choice of the heterostructure was then confirmed by the STS results. The  $dI/dV$  spectra have shown the 2D-DOS signature over the whole surface.

Furthermore, we have observed that the appearance of this step-like function in the tunneling spectra, is directly related to the hole concentration in the  $\text{In}_{0.53}\text{Ga}_{0.47}\text{As}$  QW. At this point the first objective was accomplished.

We now examine the spatial distribution of the LDOS in the  $\text{In}_{0.53}\text{Ga}_{0.47}\text{As}$  QW. For this purpose CITS measurements were carried out on sample G170401 (see discussion about CITS in Subsection 2.5.2). The  $dI/dV$  signal shows small spatial fluctuations. Figure 3.15 shows a STM image of a  $100 \times 100 \text{ nm}^2$  area of the G170401 sample surface. A  $dI/dV$  spectrum was acquired on each pixel of a  $128 \times 128$  grid of this area, for sample voltages ranging from  $-0.5 \text{ V}$  to  $+1.3 \text{ V}$ . The spatial maps are taken at several values of the sample voltages covering the transitions from the band gap to the first sub-band  $E_1$ , from  $E_1$  to the second sub-band  $E_2$ , and from  $E_2$  to the third sub-band  $E_3$ . The contrast in all these differential conductance images is rather homogeneous. These results suggest that the spatial variations in energy are small.

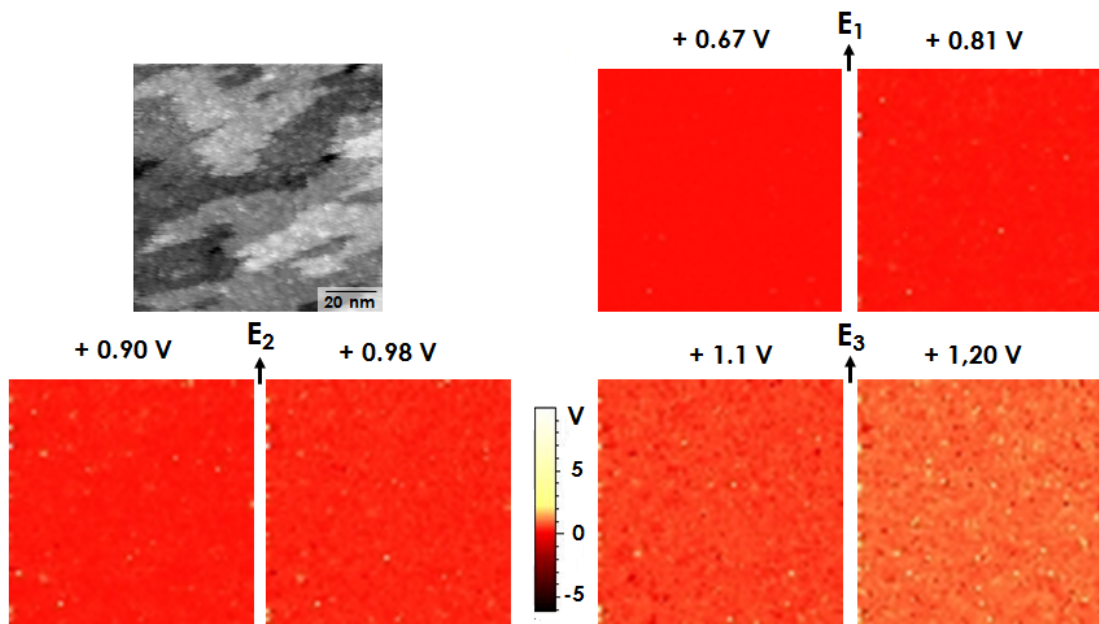


Figure 3.15 – STM topography of a  $100 \times 100 \text{ nm}^2$  area of the G170401 sample surface;  $dI/dV$  spatial maps of the STM image, at values of sample voltages (V) in the transition from the band gap to the first sub-band  $E_1$ , from  $E_1$  to the second sub-band  $E_2$ , and from  $E_2$  to the third sub-band  $E_3$ .

Figure 3.16 (a) shows the same area of the G170401 sample surface showed in Figure 3.15. Here, in addition, we underline three different terraces, namely *bottom terrace*, *middle terrace* and *top terrace*. The  $dI/dV$  spectra acquired on each terrace were averaged and are summarized in Figure 3.16 (b). As one can see, the curves have the same behavior and the step edges on the surface do not show significant potential fluctuations. Nevertheless, by zooming into the recorded spectra for a terrace, it is possible to measure a fluctuation from the mean value of around  $\pm 20 \text{ mV}$ . The main contribution to this value comes from the lock-in modulation. For the acquisition of the  $dI/dV$  curves we use the lock-in amplifier with  $V_{mod} = 9 \text{ mV RMS}$ . Therefore, more than the 60 % of the fluctuations are due to the modulation of the lock-in. 10-15 % can be

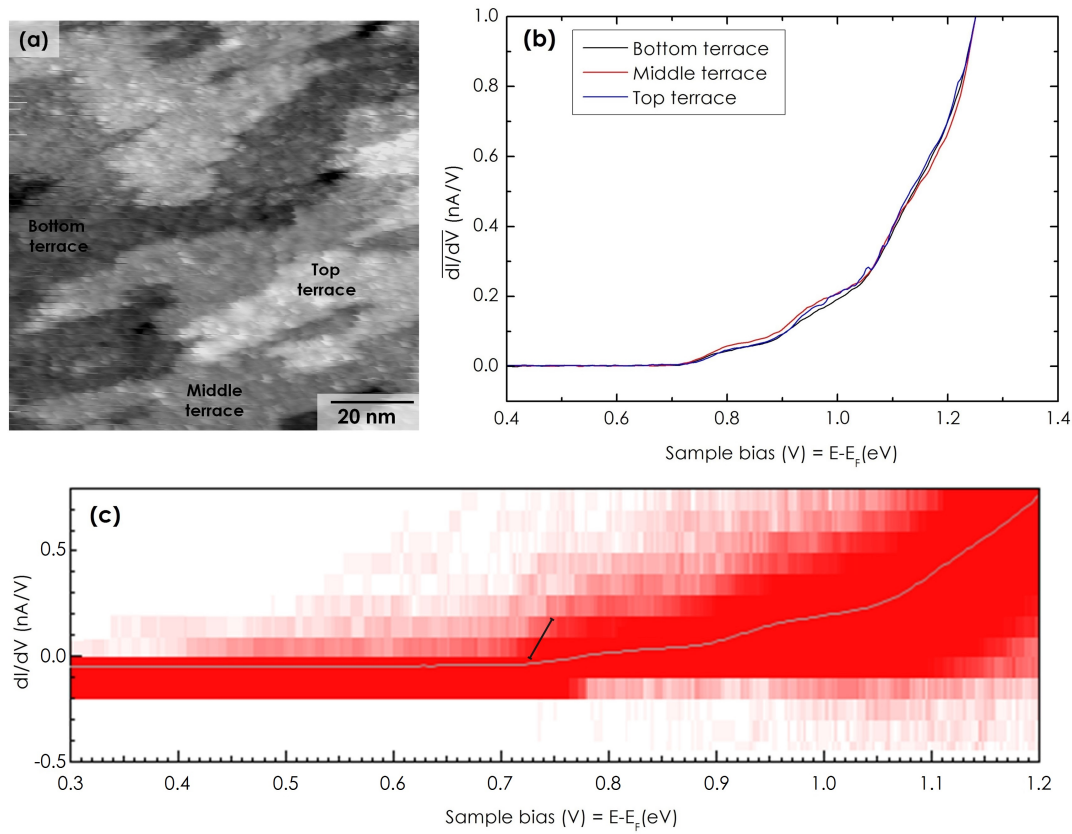


Figure 3.16 – (a) STM topography of the same area as in Figure 3.15, (b) normalized  $dI/dV$  spectra averaged over the three different terraces of the G170401 sample surface and (c) fluctuations of  $dI/dV$  curves with respect to the average spectrum. CITS measurement acquired at 77 K. Feedback parameters:  $V_S = +1.30$  V and  $V/I_{setpoint} = 100$  pA. Lock-in parameters:  $f_{mod} = 490$  Hz,  $V_{mod} = 9$  mV RMS.

attributed to the potential fluctuations induced by interface roughness and QW composition. Finally, we can consider to have fluctuations of the order of 10 meV. As observed from the calculations of Figure 1.19 (b), Subsection 1.2.4, the dispersion relation between energy and wavevector for a honeycomb array with 30 nm periodicity, is linear over  $\sim 14$  meV. Therefore, for the study of the honeycomb structures, we will push to the limit the spectral resolution by decreasing as much as possible the modulation of the lock-in  $V_{mod}$ .

Figure 3.17 (b) shows a  $dI/dV$  spatial map of the area showed in Figure 3.15 at  $V = +0.87$  V. In Figure 3.17 (c) the normalized  $dI/dV$  spectra acquired on three points of the  $\text{In}_{0.53}\text{Ga}_{0.47}\text{As}$  QW surface are reported. These points are underlined by colored circles on both the STM image and the spatial map of Figures 3.17 (a) and 3.17 (b). The black curve represents the typical 2D-DOS behavior of the  $\text{In}_{0.53}\text{Ga}_{0.47}\text{As}$  QW spectrum recorded along the whole G170401 sample surface, similar to the one showed in Figure 3.7 (a). In contrast, the other spectra of Figure 3.17 (b) (blue, cyan and green) do not show a step-like voltage dependence. These spectra are randomly distributed and very localized. We attribute them to point defects. Due to their very small concentration, they do not disturb the 2D-DOS of the QW. If the nanoperforation process

does not increase their concentration, they will not hinder the measurement of the Dirac cones in tunneling spectroscopy. We would like to emphasize that the signature of the QW showing the 2D-DOS was observed in most of the  $dI/dV$ .

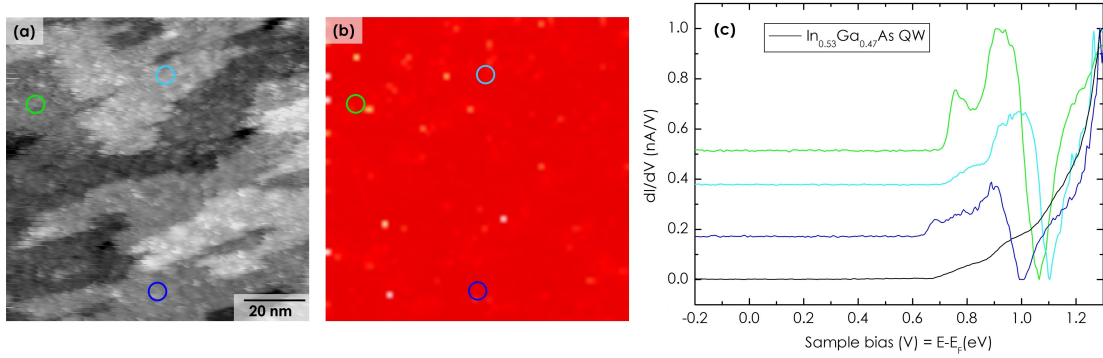


Figure 3.17 – (a) STM topography of the same area as in Figure 3.15, (b)  $dI/dV$  spatial map at  $V = +0.87$  V and (c)  $dI/dV$  spectra acquired on three points of the surface (highlighted in the STM topography), showing a different behavior from the  $\text{In}_{0.53}\text{Ga}_{0.47}\text{As}$  QW curve. CITS measurement performed at 77 K. Feedback parameters:  $V_S = +1.30$  V and  $V/I_{\text{setpoint}} = 100$  pA.

# Pushing to the spatial limit the nanoperforation of the $\text{In}_{0.53}\text{Ga}_{0.47}\text{As}/\text{InP}$ quantum well

## Outline of the current chapter

<b>4.1 Preliminary tests</b>	<b>74</b>
4.1.1 EBL dose test on a thin $\text{SiO}_2$ layer . . . . .	74
4.1.2 Minimizing the lattice disorder: EBL writing tests . . . . .	77
<b>4.2 Creating honeycomb structures on the <math>\text{In}_{0.53}\text{Ga}_{0.47}\text{As}</math> QW using EBL</b>	<b>81</b>
4.2.1 Alignment marks fabrication . . . . .	82
4.2.2 The honeycomb structure fabrication . . . . .	84
4.2.3 The final 40 nm periodicity honeycomb lattice . . . . .	88
<b>4.3 Creating honeycomb structures on the <math>\text{In}_{0.53}\text{Ga}_{0.47}\text{As}</math> QW using BCPL</b>	<b>89</b>
4.3.1 Honeycomb mask from BCP self-assembly . . . . .	90
4.3.2 Transfer of the BCP mask on the $\text{In}_{0.53}\text{Ga}_{0.47}\text{As}$ QW . . . . .	92
4.3.3 The final 35 nm periodicity honeycomb lattice . . . . .	92
<b>4.4 Hydrogen cleaning and arsenic capping</b>	<b>92</b>
<b>4.5 Conclusion</b>	<b>93</b>

This chapter will address all the technological steps performed to create a honeycomb lattice on the semiconductor heterostructure that showed the best characteristics to probe a 2D-DOS. It is essentially divided in three parts. The first one concerns the tests performed on a commercial GaAs substrate in order to adjust the critical parameters in the EBL. In these tests the periodicities of the triangular array and the electron doses will be varied to find out the good conditions to expose each pattern. Also, great cares were taken to select an appropriate writing mode. The second part focuses on the transfer of the pattern on the  $\text{In}_{0.53}\text{Ga}_{0.47}\text{As}$  QW. The last one presents the fabrication of the triangular array by using the BCP approach. The chapter will end with a discussion about the final step of cleaning and protecting the surface to make it compatible with the STM analysis in UHV.



## 4.1 Preliminary tests

The realization of the triangular array on the  $\text{In}_{0.53}\text{Ga}_{0.47}\text{As}$  QW consists of several technological steps. As the  $\text{InGaAs}$  (001) surface is highly reactive to oxidization and contamination, it has to be protected during all the nanofabrication processes. For this reason, a thin film of  $\text{SiO}_2$  will be deposited on the surface by PECVD after the MBE growth. This layer will be used as a mask for the nanoscale etching. Therefore, its thickness has to be of the order of the  $\text{In}_{0.53}\text{Ga}_{0.47}\text{As}$  QW one, to bear the different technological steps. It can be removed at the end of the honeycomb fabrication by Hydrofluoric acid HF wet etching.

In order to minimize the number of  $\text{In}_{0.53}\text{Ga}_{0.47}\text{As}$  samples, which had to be grown by MBE, preliminary EBL tests were performed on a commercial GaAs substrate. As a result, the GaAs (001) surface was also protected with a thin  $\text{SiO}_2$  layer.

### 4.1.1 EBL dose test on a thin $\text{SiO}_2$ layer

Figure 4.1 shows a summary of the triangular array transfer on the  $\text{SiO}_2$  layer. 16 nm of  $\text{SiO}_2$  are deposited by PECVD on the GaAs substrate to perform the EBL dose tests. After that, to create a mask of a triangular array of holes, the resist is deposited by spin coating and locally modified by EBL and development. Once the mask is prepared, we dry-etch the  $\text{SiO}_2$  layer using RIE etching and remove the resist mask with a specific solvent. At this point, the array of holes is transferred on the  $\text{SiO}_2$  surface.

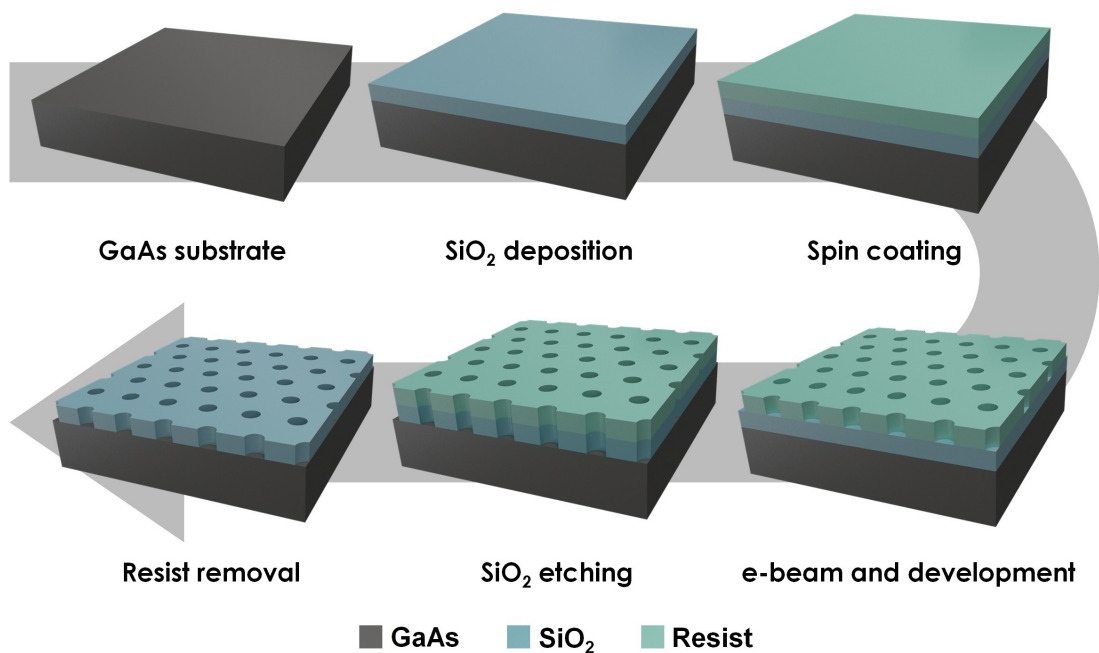


Figure 4.1 – Schematic of the technological processes used to pattern a honeycomb structure on  $\text{SiO}_2/\text{GaAs}$ .

### SiO<sub>2</sub> deposition

More in detail, the technological process starts with the deposition of a 16 nm thick SiO<sub>2</sub> layer (thickness measured per ellipsometry with a measurement uncertainty of 5%) on top of the GaAs substrate. This step is done by PECVD deposition using the parameters reported in Table 4.1. 150 sccm of 5% SiH<sub>4</sub>/N<sub>2</sub> and 700 sccm of N<sub>2</sub>O are used as precursors to form the SiO<sub>2</sub>.

Temperature (°C)	Pressure (Torr)	RF Power (W)	Deposition time (s)
300	1	20	13

Table 4.1 – Parameters used for the PECVD deposition of 16 nm thick SiO<sub>2</sub> layer.

### Realization of the mask

The realization of a mask using the EBL technique requires three main steps:

- Resist deposition
- EBL exposure
- Development

The resist essentially consists of a solution and a solvent, and its deposition is done with a spin coating system [see Figure 4.2 (blue box)]. As illustrated in the bottom part of Figure 4.2, spin coating is performed in three steps: deposition, spin on, spin off and evaporation. First a small puddle of resist is deposited onto the center of the substrate (on 60 % of the surface). Then the substrate is rotated at high speed and the majority of the resist is flung off the side. Spin up and spin off occur in sequence while the solvent evaporation stage occurs throughout the process. The higher the angular speed of spinning, the thinner the film. The thickness of the film also depends on the viscosity and concentration of the solution, and the solvent. In our spin coater, it is possible to let the lid open during the rotation of the substrate. A closed lid favors the control of the experimental conditions. Nowadays, there are well established recipes (resist, angular speed, time and lid open/close option) to obtain the desired deposition. One can chose to work with the lid open, close or with a combination of both. The airflow dries the majority of the solvent, leaving the final film. Lastly, most of the resist depositions end with an annealing of the substrate to evaporate residual solvent and allow a better homogeneity in the resist thickness. For this purpose, usually there is a hot plate close to the spin coater [see Figure 4.2 (green box)].

After the resist deposition, the sample is ready to be exposed to the e-beam. The interaction with the beam changes the solubility of the resist, enabling selective removal of either the exposed or non-exposed regions of the resist by immersing it in a solvent. This last step is the development.

The SiO<sub>2</sub>/GaAs structure was dehydrated by heating at 180 °C for 10 minutes. A diluted PMMA 950 K 4% (5:3) resist was spin-coated in two steps on top of the sample by using the parameters reported in Table 4.2. The sample was then placed on a hot plate and annealed by the rear contact at 80 °C for 1 minute. Finally it was baked out at 180 °C for 10 minutes. This recipe allows the deposition of a 50 nm thick PMMA resist. The EBL exposure was performed to generate honeycomb patterns with different periodicities (100, 70, 50 and 40 nm). Each pattern size was 20x5 μm<sup>2</sup> and was exposed by varying the dose from 5000 to 17000 μC/cm<sup>2</sup>, in steps of

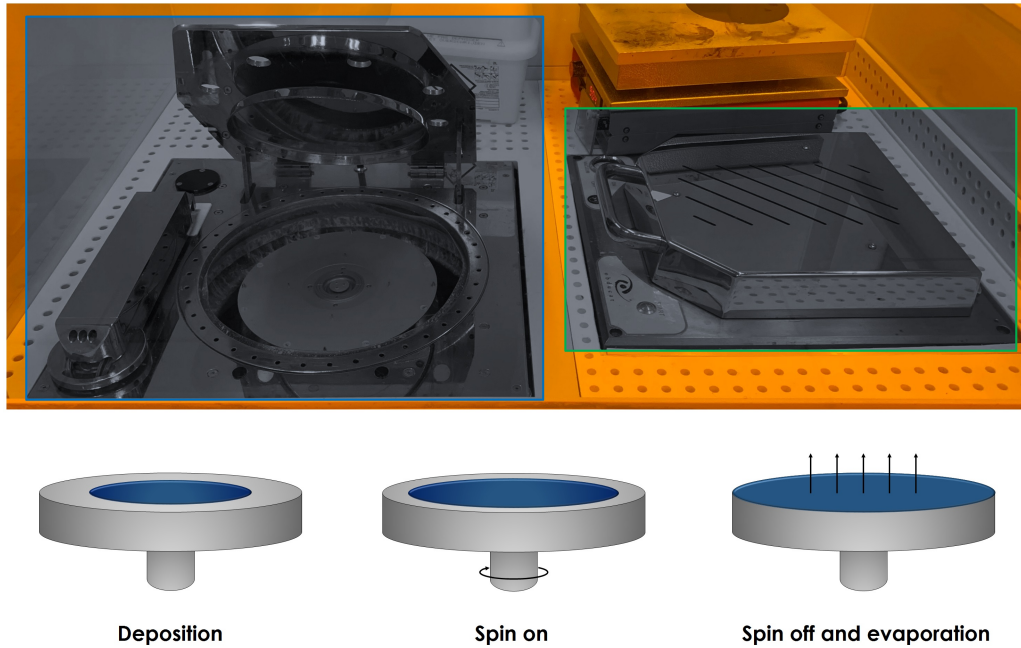


Figure 4.2 – Top: Spin coater (blue box) and hot plate (green box); bottom: schematic representation of the spin-coating steps.

Step	Acceleration (rpm/s)	Speed (rpm)	Time (s)	Lid mode
1	4000	1000	12	Close
2	800	1000	8	Open

Table 4.2 – Parameters used for the PMMA 950 K 4% (5:3) deposition.

$500 \mu\text{C}/\text{cm}^2$ . Therefore, we had 25 patterns for each periodicity. In addition to the honeycomb lattice, a  $200 \times 200 \mu\text{m}^2$  square was exposed as a way to place the spot of the interferometer and precisely detect the end point of the etching. The other main EBL exposure parameters are reported in Table 4.3.

Acceleration voltage (kV)	e-beam current (pA)	Resolution (nm)	Dose ( $\mu\text{C}/\text{cm}^2$ )
100	200	5	5000 - 17000

Table 4.3 – EBL exposure parameters used for the patterning of different triangular arrays, varying the dose from 5000 to 17000 in steps of  $500 \mu\text{C}/\text{cm}^2$ .

The EBL exposure was followed by the development. First, we plunged the sample inside the developer for 60 s. For the development of the PMMA resist, it is a mixture of methyl isobutyl ketone (MIBK) and isopropyl alcohol (IPA) (1:2). After that, the sample was rinsed in IPA for 40 s in order to stop the reaction. Finally, the sample was dried under nitrogen flow.

### Transfer of the mask on the SiO<sub>2</sub>

The definitive transfer of the mask on the SiO<sub>2</sub> layer was done in two steps, by using the RIE technique. The first one consists on the etching of the SiO<sub>2</sub> layer and the second one is the resist removal. Consequently, the triangular patterns are transferred onto the SiO<sub>2</sub> layer.

CHF <sub>3</sub> /CF <sub>4</sub> (sccm)	Pressure (Torr)	RF power (W)	Etching time (s)
40/40	0.050	180	40

Table 4.4 – RIE parameters used for the SiO<sub>2</sub> etching.

For the etching of the 16 nm thick SiO<sub>2</sub> layer, we used a mixture of CHF<sub>3</sub>/CF<sub>4</sub> gases. The parameters used to perform the etching are summarized in Table 4.4. The PMMA removal was done by using an O<sub>2</sub> plasma. As for the SiO<sub>2</sub> etching, the interferometer was employed for the end point detection. The parameters used to perform the etching are summarized in Table 4.5.

O <sub>2</sub> (sccm)	Pressure (Torr)	RF power (W)	Etching time (s)
25	0.050	50	60

Table 4.5 – RIE parameters used for the PMMA resist etching.

### The honeycomb structures on the SiO<sub>2</sub> layer

To check the different periodicities and relative doses, the honeycomb structures in the SiO<sub>2</sub> layer were characterized by SEM. Figure 4.3 shows SEM images acquired on the patterns with different periodicities, from 100 nm down to 40 nm. On the left side, one can see the triangular arrays for which the applied EBL dose was not enough to open the holes. For all the periodicities, a dose value of 10000  $\mu\text{C}/\text{cm}^2$  appears to be not enough to obtain an homogeneous triangular array of holes. Here we do not report all the images acquired for each dose but as expected, for values smaller than 10000  $\mu\text{C}/\text{cm}^2$ , the number of missing holes increases with decreasing the e-beam dose. On the other hand, the right side of Figure 4.3 reports about the good values of doses needed to create the array on the SiO<sub>2</sub> surface. The pattern with a periodicity of 100, 70 and 50 nm are obtained with the same dose value of 16500  $\mu\text{C}/\text{cm}^2$  while the one with 40 nm periodicity needs a smaller dose of 10500  $\mu\text{C}/\text{cm}^2$ . The honeycomb structures are well ordered and they reveal a good radial and periodicity distributions. Nevertheless, the arrays with 50 and 40 nm periodicity [see Figures 4.3 (f) and (h)] show a pairing effect of adjacent rows of holes, causing a smaller spacing in between.

#### 4.1.2 Minimizing the lattice disorder: EBL writing tests

Additionally EBL writing tests were performed directly on the commercial GaAs substrate to optimize the triangular array order. What we mean by EBL writing is the way the e-beam is scanned along the surface, how the beam goes on the areas to be exposed. The honeycomb structures created up to now were exposed by scanning the e-beam from the left to the right side of the area of interest [see Figure 4.4 (a)]. The beam irradiates one hole site and then goes to the next one, by being blanked in between. At the end of the first line the e-beam is blanked until it comes back to the left side again, it skips the second line and repeats the process from the left side to the right one by exposing the third line. Once the e-beam exposed all the odd

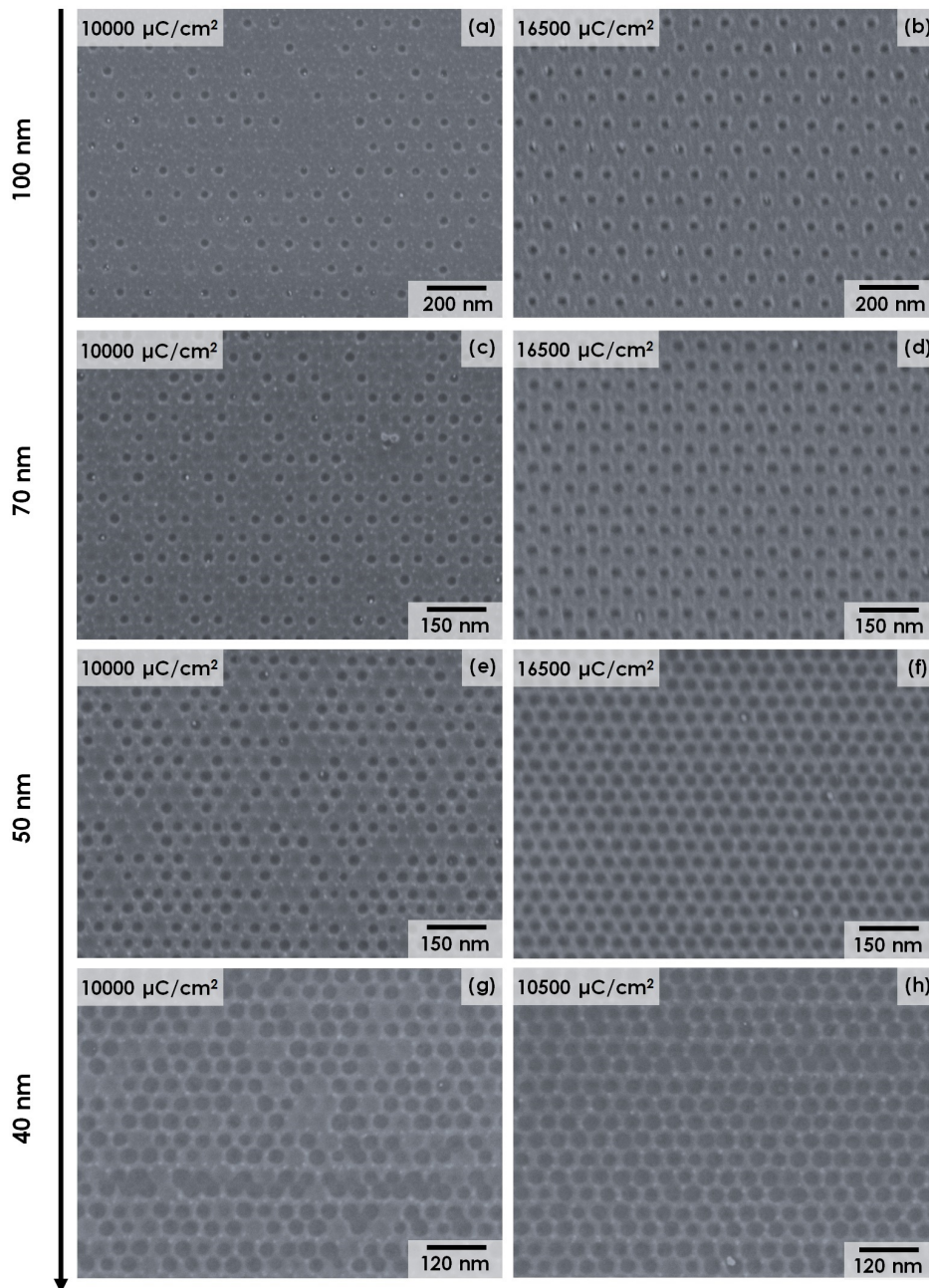


Figure 4.3 – SEM images of the triangular arrays of holes patterned on the  $\text{SiO}_2$  layer: (a) and (b), dose value of  $10000 \mu\text{C}/\text{cm}^2$  and  $16500 \mu\text{C}/\text{cm}^2$  respectively for an array periodicity of  $100 \text{ nm}$ ; (c) and (d), dose value of  $10000 \mu\text{C}/\text{cm}^2$  and  $16500 \mu\text{C}/\text{cm}^2$  respectively for an array periodicity of  $70 \text{ nm}$ ; (e) and (f), dose value of  $10000 \mu\text{C}/\text{cm}^2$  and  $16500 \mu\text{C}/\text{cm}^2$  respectively for an array periodicity of  $50 \text{ nm}$ ; (g) and (h), dose value of  $10000 \mu\text{C}/\text{cm}^2$  and  $10500 \mu\text{C}/\text{cm}^2$  respectively for an array periodicity of  $40 \text{ nm}$ .

lines of holes it comes back to the bottom part of the entire pattern by exposing the even lines of holes from the right to the left side, by being blanked in between two holes and two lines. For simplicity we will call this writing mode LR (Left-Right). Another way to perform the exposure is by scanning the e-beam from the left to the right side and then from the right to the left side the next line. This writing mode that will be called LRRL (Left-Right-Right-Left) is illustrated in Figure 4.4 (b). Finally, one can address the e-beam in the desired  $(x, y)$  point to be exposed. This last writing mode is what we call Sequence (SEQ). In this case the e-beam is never blanked during the exposure and the exposure is faster than the first two writing modes.

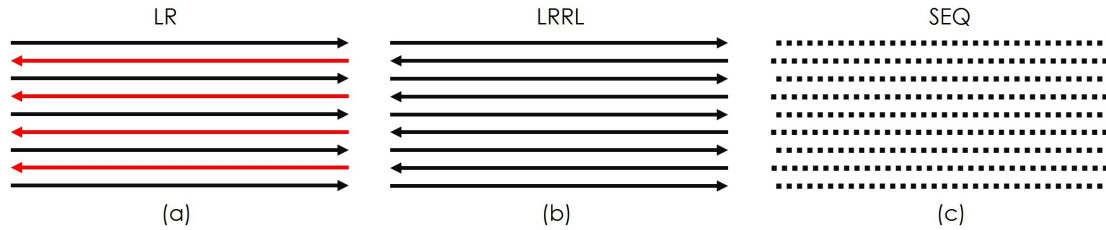


Figure 4.4 – Schematic descriptions of the employed EBL writing strategies: (a) Left-Right (LR), the e-beam exposes the odd lines of holes from the left to the right side and comes back by exposing the even lines from the right to the left side; (b) Left-Right-Right-Left (LRRL), the e-beam exposes one line of holes from the left to the right side and then exposes the next one by coming back from the right to the left side; (c) SEQ, the e-beam is addressed exactly on the coordinates of the pattern to be exposed.

For the EBL writing tests, the GaAs substrate was spin coated with diluted PMMA 950 K 4% (5:3) resist as described in Subsection 4.1.1. The used EBL parameters are summarized in Table 4.6. The exposure was performed on honeycomb patterns with 40 nm periodicity by varying

Acceleration voltage (kV)	e-beam current (pA)	Resolution (nm)	Dose ( $\mu\text{C}/\text{cm}^2$ )
100	200	5	10500

Table 4.6 – EBL exposure parameters used for the patterning of honeycomb structures with 40 nm periodicity on a GaAs substrate.

the writing mode: LR, LRRL and SEQ, respectively. Each pattern was  $5 \times 5 \mu\text{m}^2$ . After the EBL exposure the following development was done by plunging the sample inside a mixture of MIBK and IPA (1:2) for 60 s. Next, the sample was rinsed in IPA for 40 s and dried under nitrogen flow. After that, the honeycomb patterns were transferred on the GaAs surface by employing the ICP dry etching.

For the etching of the III-V material we used the  $\text{BCl}_3$  gas and set the well established ICP parameters reported in Table 4.7. Finally, the residual PMMA resist was removed by an  $\text{O}_2$  plasma in the RIE setup. The parameters used to perform the RIE etching were previously summarized in Table 4.5.

$\text{BCl}_3$ (sccm)	Pressure (Torr)	ICP/RIE power (W)	Etching time (s)
30	0.002	50/200	40

Table 4.7 – ICP parameters used for the GaAs etching.



SEM measurements were done on the three honeycomb arrays to check the different EBL writing modes. The results are reported in Figure 4.5. The LR writing mode reveals the presence of multiple lines closer than the others, causing a huge distortion of the triangular array [see Figure 4.5 (a)]. As shown in Figure 4.5 (b), this distortion appears less evident by exposing the patterns in the LRRL mode. On the contrary, the honeycomb lattice obtained with a SEQ mode gives a well ordered structure. We will now use all these results to create the honeycomb structures on the  $\text{In}_{0.53}\text{Ga}_{0.47}\text{As}$  QW.

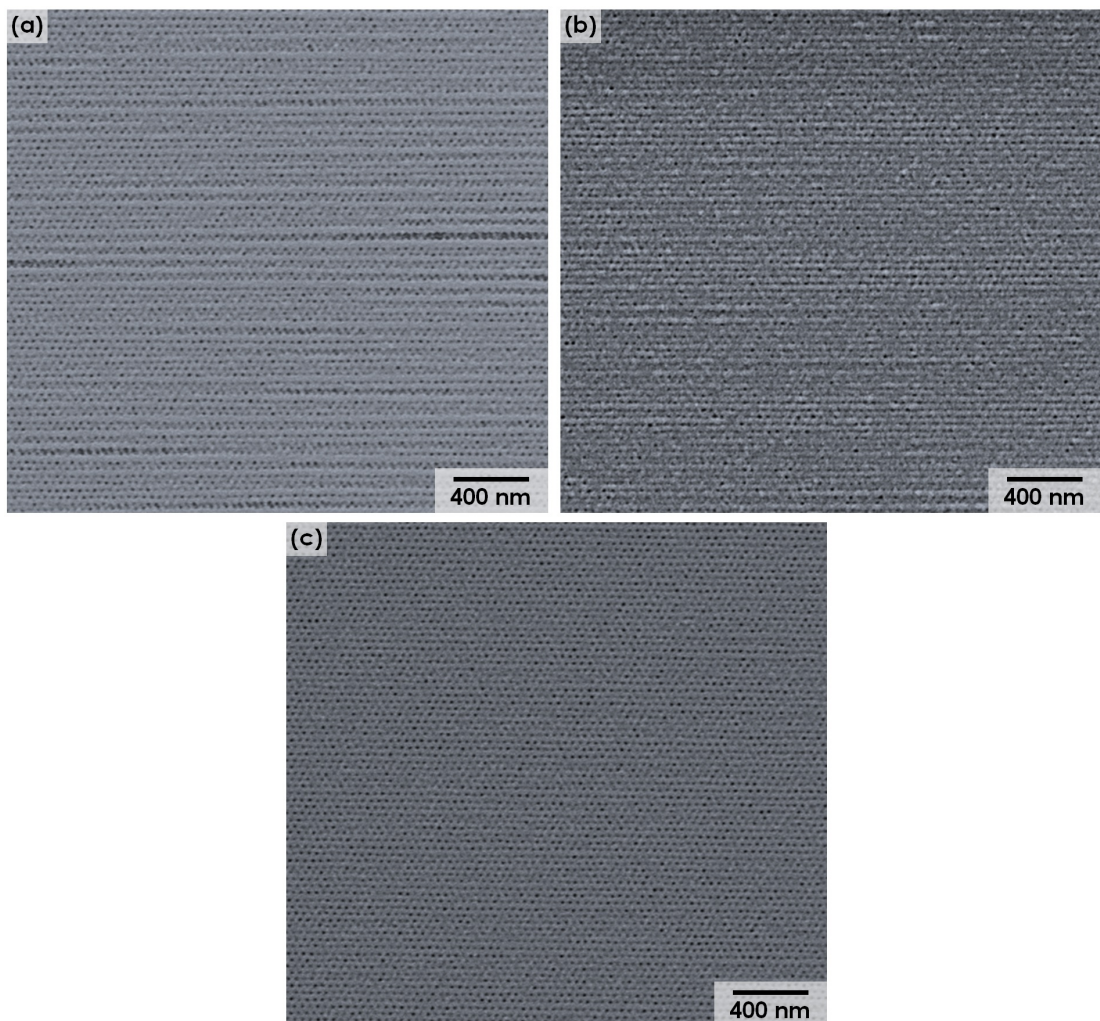


Figure 4.5 – SEM images acquired on the three honeycomb structures obtained by changing the EBL writing mode: (a) LR, (b) LRRL and (c) SEQ.



## 4.2 Creating honeycomb structures on the $\text{In}_{0.53}\text{Ga}_{0.47}\text{As}$ QW using EBL

Based on the successful pattern transfer process used on the  $\text{SiO}_2/\text{GaAs}$  structure, the same method has been applied to the  $\text{In}_{0.53}\text{Ga}_{0.47}\text{As}$  QW. In Figure 4.6 a summary of the full process that allows the realization of the antidot lattice is reported. 16 nm of  $\text{SiO}_2$  are deposited by PECVD on the  $\text{In}_{0.53}\text{Ga}_{0.47}\text{As}/\text{InP}$  heterostructure after the MBE growth. Then, a mask of a triangular array of holes is created in the  $\text{SiO}_2$  layer. To do this, we deposit the resist, and perform EBL and development. Once the mask is prepared, we dry-etch the  $\text{SiO}_2$  layer using RIE etching and finally we remove the resist with a specific solvent. At this point, the array of holes is transferred on the  $\text{SiO}_2$  film. This nanopatterned  $\text{SiO}_2$  layer is then used as a mask to transfer the honeycomb lattice on the 10 nm thick  $\text{In}_{0.53}\text{Ga}_{0.47}\text{As}$  QW, by employing the ICP etching technique. HF wet etching allows the removal of the 16 nm of  $\text{SiO}_2$ . The fabrication process ends with the reintroduction of the sample in the MBE chamber in order to clean it by H plasma and protect it with a 10 nm thick amorphous As layer.

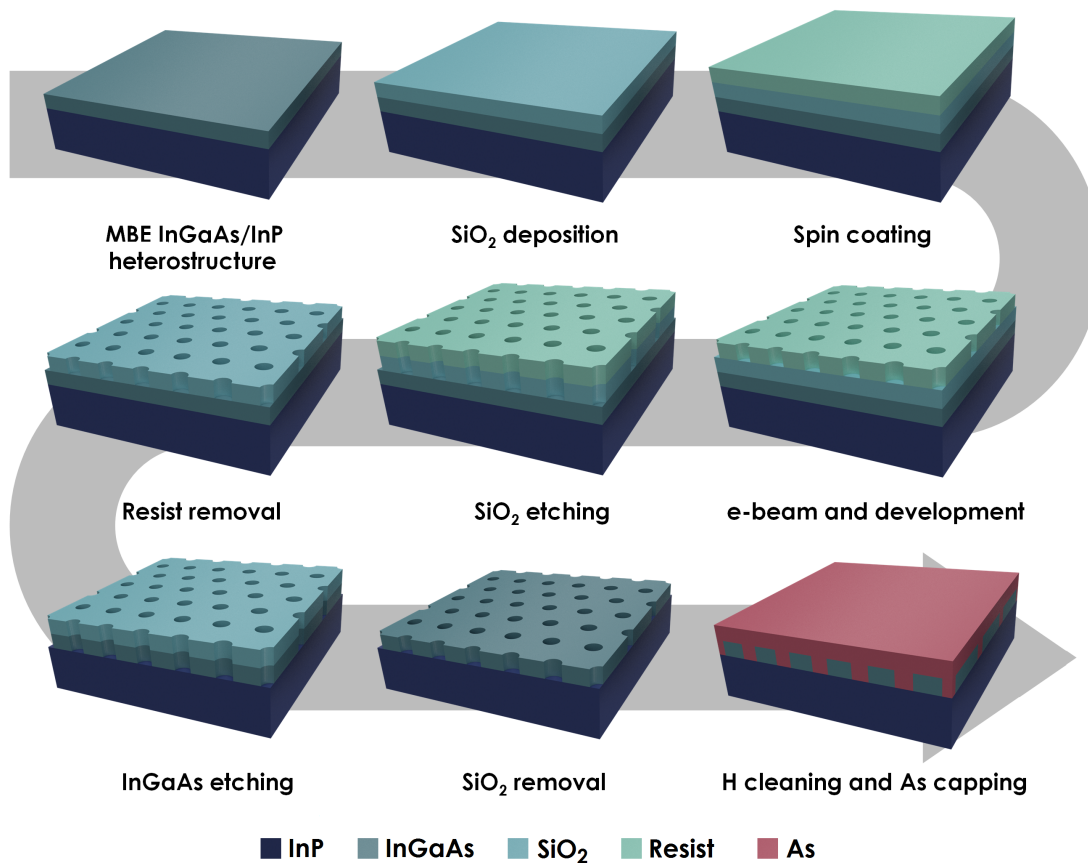


Figure 4.6 – Schematic of the technological processes used to pattern a honeycomb structure on the  $\text{In}_{0.53}\text{Ga}_{0.47}\text{As}$  by EBL.

This sample will be characterized by STM in UHV. In STM, the image scans are made thanks to a piezoelectric tube on which the tip is mounted. The lateral displacement of the tip is thus

limited: at RT, it can move over an area of  $10 \times 10 \mu\text{m}^2$  while, at 4 K, it is able to scan  $1.8 \times 1.8 \mu\text{m}^2$  only. In order to make the search of the array easier for the tip, the fabrication process requires an additional step, in which we create microscopic marks on the surface of the sample that can be located with an optical camera.

### 4.2.1 Alignment marks fabrication

The EBL requires the use of files in which most of the patterning details are included. These files are usually composed of several layers. What we call alignment marks are the markers used in EBL to align the different layers. On the other hand, the STM marks, are done to simplify the research of the arrays with the optical camera inside the STM chamber. Our LT-STM is in fact equipped with a camera that allows the positioning of the tip with an accuracy of around  $100 \mu\text{m}$ . Therefore, a mark size of  $250 \times 250 \mu\text{m}^2$  is enough to be visible at the camera. We start by transferring the alignment and the STM mark patterns on the sample and, in a second step, we create the honeycomb structure. Therefore, during the realization of the honeycomb arrays,

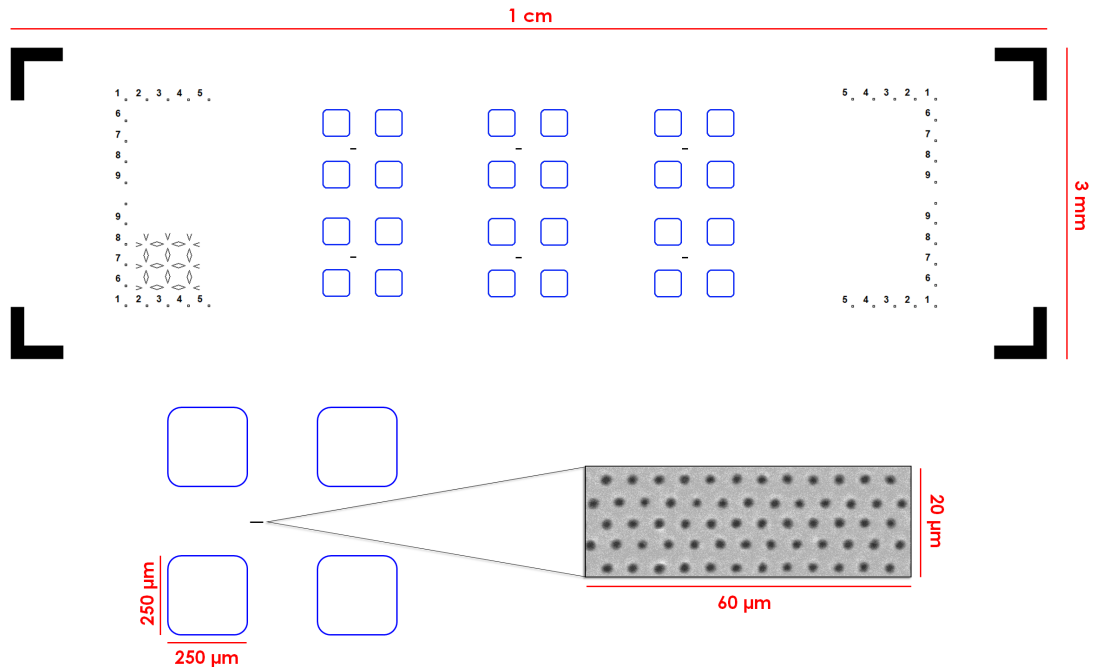


Figure 4.7 – Schematics of a typical sample with a size of  $1 \text{ cm} \times 3 \text{ mm}$ . The alignment marks of the EBL and the STM marks are highlighted in black and blue, respectively. The small line close to the blue squares represents the future position of the arrays.

the related EBL layer has to be aligned with the one of the markers. In Figure 4.7 a sketch of a sample optimized for STM measurements is illustrated. The size of the samples ( $1 \text{ cm} \times 3 \text{ mm}$ ) is adapted to the STM sample holders. In black we present the alignment marks and in blue the STM ones. These two sets of pattern are part of the first EBL layer. The small lines almost in the middle of four blue squares are the positions of the future honeycomb patterns.

The realization of the alignment and the STM mark patterns on the  $\text{SiO}_2$  surface is again a combination of EBL and RIE techniques. These patterns are few microns in size and have to be

deep etched in the heterostructure in order to be easily located both with the optical microscope for the EBL alignment and the optical camera for the STM setup. This means that the 10 nm thick  $\text{In}_{0.53}\text{Ga}_{0.47}\text{As}$  QW and the InP layers underneath have to be deep etched, by 200 nm at least. The etching of both III-V materials are done with ICP by using the  $\text{BCl}_3$  gas.

#### Fabrication of the mask for the markers

As already discussed, the alignment and the STM mark patterns have a lateral size of a few hundreds of microns and have to be deep etched. Therefore, a different resist is required. The  $\text{In}_{0.53}\text{Ga}_{0.47}\text{As}$  QW was dehydrated by heating the substrate at 180 °C for 10 minutes. PMMA copolymer 33 % AR-P 617.14 resist was spin-coated on top of the sample by using the parameters reported in Table 4.8. The sample was finally annealed at 80 °C for 1 minute on a hot plate and baked out at 180 °C for 10 minutes. This recipe allows the deposition of a 2000 nm thick PMMA resist.

Acceleration (rpm/s)	Speed (rpm)	Time (s)	Lid mode
2000	1000	12	Close

Table 4.8 – Parameters used for the PMMA copolymer 33 % AR-P 617.14 deposition.

As to the e-beam exposure, a lower accuracy is required for these patterns with respect to the honeycomb structures one. Therefore, both the e-beam current and resolution values were increased. The used parameters are summarized in Table 4.9. The following development was done by plunging the sample inside a mixture of MIBK and IPA (1:2) for 120 s. Finally, the sample was rinsed in IPA for 60 s and dried under nitrogen flow. The depth of the markers was measured with a profilometer. We obtained an average value of 2.1  $\mu\text{m}$  that fits well with the expected resist thickness (2  $\mu\text{m}$ ).

Acceleration voltage (kV)	e-beam current (nA)	Resolution (nm)	Dose ( $\mu\text{C}/\text{cm}^2$ )
100	20	25	200

Table 4.9 – EBL exposure parameters used for the patterning of the alignment and the STM marks.

#### Transfer of the marker mask on the structure

The  $\text{SiO}_2$  etching was performed using RIE, by employing the parameters previously reported in Table 4.4. After the etching of this layer, the next step was the transfer of the markers on the III-V materials by keeping the resist on the surface. For this purpose, we used the ICP setup and in particular, the  $\text{BCl}_3$  gas. The etching parameters used during this step are reported in Table 4.10. After the ICP etching we measured the etched profile and obtained an average value of 1.5  $\mu\text{m}$ . To remove the resist, the sample was plunged in SVC 14 at 70 °C, in ultra sound, for 1 hour. At this point, both the alignment and the STM marks were well transferred on the heterostructure. We measured the depth profile and obtained an average value of 250 nm, meaning that the  $\text{In}_{0.53}\text{Ga}_{0.47}\text{As}/\text{InP}$  etching rate was around 0.4 nm/s. Furthermore, the 1.2  $\mu\text{m}$  thick resist survive to both RIE and ICP processes. Therefore, the sample surface was well protected during all the previous processes. This depth should be enough for the markers to

be easily visible with the optical microscope for the alignment of the next layer or the optical camera inside the STM chamber.

$\text{BCl}_3$ (sccm)	Pressure (Torr)	ICP/RIE power (W)	Etching time (s)
30	0.002	50/200	600

Table 4.10 – ICP parameters used for the  $\text{In}_{0.53}\text{Ga}_{0.47}\text{As}/\text{InP}$  etching.

## 4.2.2 The honeycomb structure fabrication

### Realization of the $\text{SiO}_2$ honeycomb mask

50 nm of diluted PMMA 950 K 4% (5:3) resist were deposited on the  $\text{SiO}_2/\text{In}_{0.53}\text{Ga}_{0.47}\text{As}/\text{InP}$  structure using the parameters presented in Table 4.2. The EBL exposure was performed on honeycomb patterns with different periodicities (60, 50, 40 and 30 nm), each pattern being  $20 \times 5 \mu\text{m}^2$  in size. The parameters of Table 4.3 were chosen for two doses: following the SEM results previously reported in Figure 4.3,  $16500 \mu\text{C}/\text{cm}^2$  and  $10500 \mu\text{C}/\text{cm}^2$  were chosen as doses for the honeycomb patterns with 60/50 nm and 40/30 nm periodicity, respectively. In addition to the honeycomb lattice, a  $200 \times 200 \mu\text{m}^2$  square was exposed as a way to place the spot of the interferometer and detect the end point of the etching. Check a region allows to precisely measure the etched depth and make sure that the pores in the lattice have the correct depth. The following development was done similar to the  $\text{SiO}_2/\text{GaAs}$  test structure, by plunging the sample inside a mixture of MIBK and IPA (1:2) for 60 s. Finally, the sample was rinsed in IPA for 40 s and dried under nitrogen flow.

The 16 nm thick  $\text{SiO}_2$  etching was performed by RIE, employing the parameters previously reported in Table 4.4. After the etching of this layer, the residual PMMA we removed by using an  $\text{O}_2$  plasma, employing the parameters reported in Table 4.5. Therefore, the  $\text{SiO}_2$  layer became the mask to be transferred on the 10 nm thick  $\text{In}_{0.53}\text{Ga}_{0.47}\text{As}$  QW.

AFM measurements were performed on the  $200 \times 200 \mu\text{m}^2$  square to measure the etched depth on the  $\text{SiO}_2/\text{In}_{0.53}\text{Ga}_{0.47}\text{As}$  structure after the RIE etching. In Figure 4.8 (a) the topography shows the left side of the square area. The measured profile along the red line in the AFM image reveals that the 16 nm thick  $\text{SiO}_2$  was completely etched [see Figure 4.8 (b)]. The chemical composition on the  $\text{SiO}_2$  side of the AFM topography was analyzed by EDX. The detection of a Si peak as reported in Figure 4.8 (c) confirms that the thin  $\text{SiO}_2$  mask was well protecting the  $\text{In}_{0.53}\text{Ga}_{0.47}\text{As}$  QW during the RIE.

### Transfer of the honeycomb lattice mask on the $\text{In}_{0.53}\text{Ga}_{0.47}\text{As}$ QW

The honeycomb patterns were transferred in the III-V material by employing ICP etching. The parameters employed are the ones showed in Table 4.10, except for the etching time. Based on the etching rate found during the etching of the markers (0.4 nm/s), 30 s is enough to etch the 10 nm thick  $\text{In}_{0.53}\text{Ga}_{0.47}\text{As}$  QW. Nevertheless, based on the small radius of the pores, it could be more difficult for the etchants to go straight inside the holes. Therefore, we decided to perform the process for 40 s. The last step to obtain the honeycomb structure on the  $\text{In}_{0.53}\text{Ga}_{0.47}\text{As}$  QW surface was the removal of the  $\text{SiO}_2$  layer. For this purpose, the sample was plunged in a solution of HF diluted at 1% for 30 s.

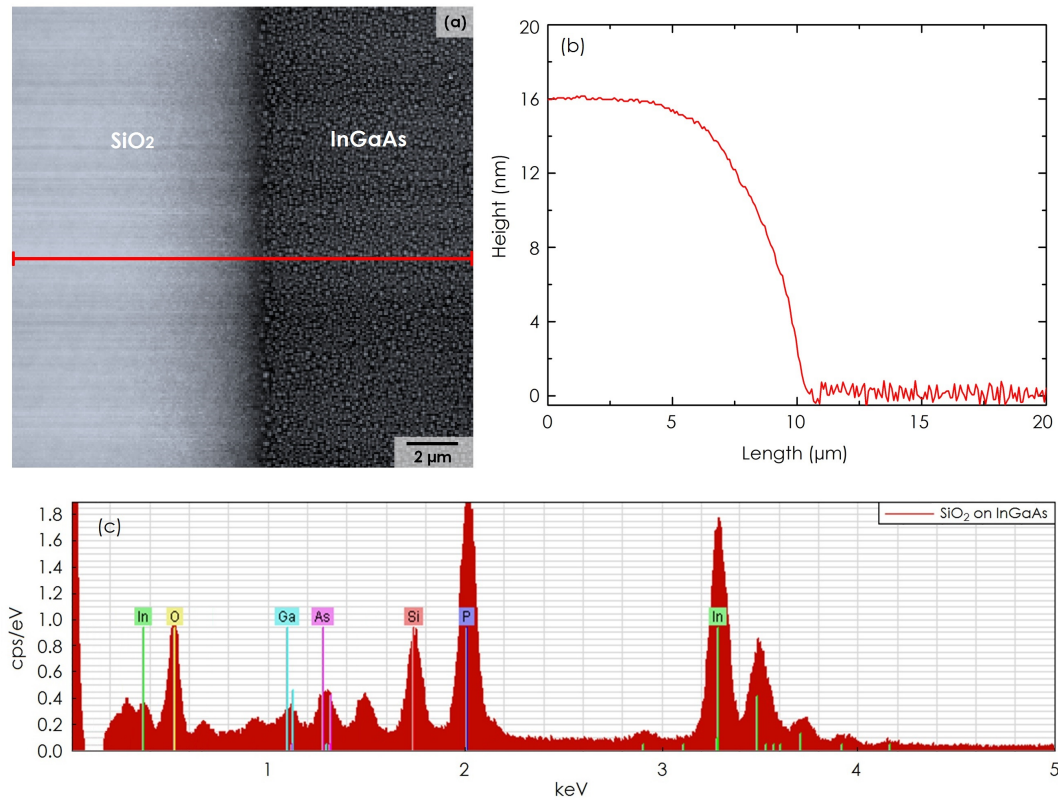


Figure 4.8 – Structural and chemical characterization of the nanoperforated  $\text{SiO}_2/\text{In}_{0.53}\text{Ga}_{0.47}\text{As}$  structure. (a) AFM image acquired on the left side part of the  $200 \times 200\ \mu\text{m}^2$  square area, (b) height profile acquired along the red line in the AFM image and (c) chemical EDX analysis of the  $\text{SiO}_2$  area after the RIE etching.

AFM measurements were performed on the  $200 \times 200\ \mu\text{m}^2$  square to check the etched profile on the  $\text{In}_{0.53}\text{Ga}_{0.47}/\text{InP}$  structure after the HF wet etching of the thin  $\text{SiO}_2$  layer. In Figure 4.9 (a) the topography showing the left side of the square is reported. The measured profile along the red line in the AFM image, reveals a step of about 17 nm, indicating that the  $\text{In}_{0.53}\text{Ga}_{0.47}\text{As}$  QW with initial thickness of 10 nm is completely removed [see Figure 4.9 (b)]. Anyway, the  $200 \times 200\ \mu\text{m}^2$  square is huge with respect to the holes radius. Therefore, we should expect a less efficient etching inside the holes and consequently, a lower depth value for the array. The chemical composition on the  $\text{In}_{0.53}\text{Ga}_{0.47}\text{As}$  side of the AFM topography was analyzed by EDX. The results reported in Figure 4.9 (c) confirm that the thin  $\text{SiO}_2$  mask was totally removed, leaving the  $\text{In}_{0.53}\text{Ga}_{0.47}\text{As}$  QW exposed at the sample surface.

SEM images were acquired in the nanoperforated part of both the  $\text{SiO}_2$  and the  $\text{In}_{0.53}\text{Ga}_{0.47}\text{As}$  QW surfaces at two different steps of the honeycomb array fabrication. The results are presented in Figure 4.10. On the left side of the picture, we show the  $\text{SiO}_2$  surface after the RIE etching and on the right side, the  $\text{In}_{0.53}\text{Ga}_{0.47}\text{As}$  QW surface after the HF etching of the  $\text{SiO}_2$  film. From the top to the bottom, the periodicities of the triangular arrays are 60 nm [Figure 4.10 (a) and (b)], 50 nm [Figure 4.10 (c) and (d)], 40 nm [Figure 4.10 (e) and (f)] and 30 nm [Figure 4.10 (g) and (h)], respectively. The differences in intensities at the edges of the holes on the  $\text{SiO}_2$  surface

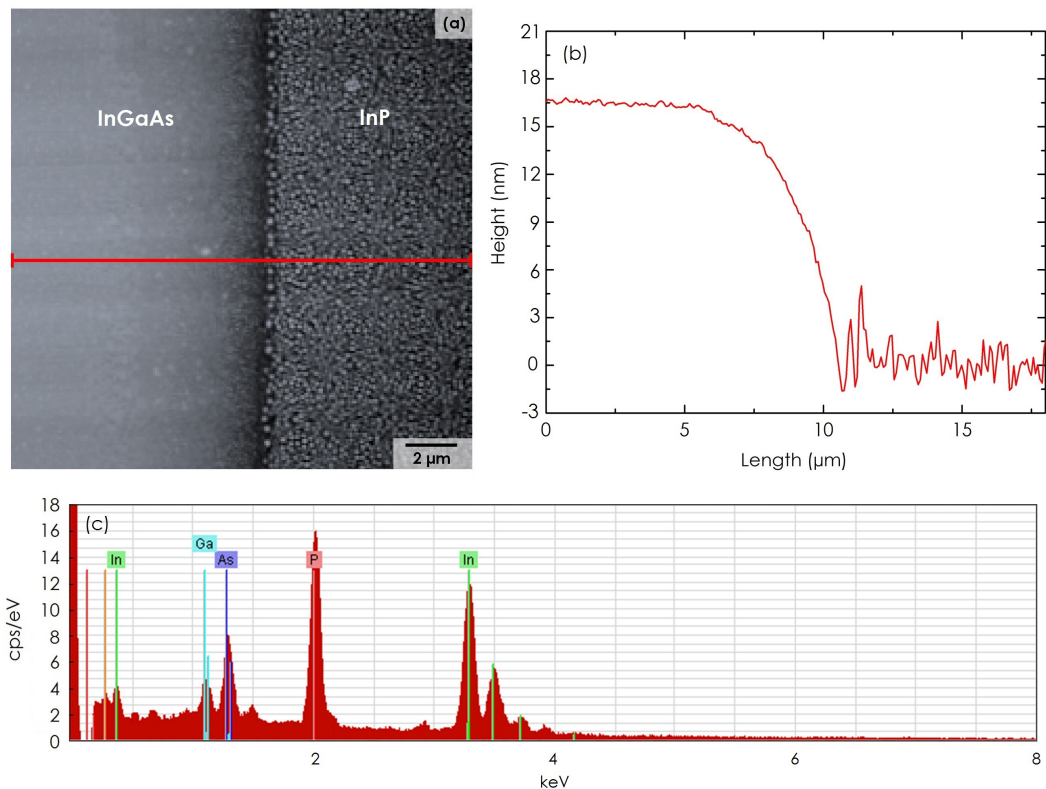


Figure 4.9 – Structural and chemical characterization of the nanoporated  $\text{In}_{0.53}\text{Ga}_{0.47}\text{As}/\text{InP}$  structure. (a) AFM image acquired on the left side part of the  $200 \times 200 \mu\text{m}^2$  square area, (b) height profile acquired along the red line in the AFM image and (c) chemical EDX analysis of the sample after the HF etching.

are attributed to accumulation of electrons around the holes. As visible from Figures 4.10 (b) and (d), the honeycomb structures having a periodicity of 60 and 50 nm appear well ordered and show a good homogeneity of the pore size. On the contrary, the 40 nm periodicity array exhibits a few missing sites. This effect is a consequence of a short development time, meaning that the resist was not well removed from the holes. As one can see from Figure 4.10 (e), the  $\text{SiO}_2$  prevents the  $\text{In}_{0.53}\text{Ga}_{0.47}\text{As}$  from being etched with the  $\text{BCl}_3$  and, as a result, missing holes appear. As already observed in Figure 4.3 for the  $\text{SiO}_2/\text{GaAs}$  sample test, the arrays with 50 and 40 nm periodicity [see Figures 4.10 (d) and (f)] reveal some pairing effect of adjacent rows of holes, causing a smaller spacing in between. We attribute this effect to the writing mode of the EBL, namely the way the e-beam exposes the patterns along the surface. Finally, as shown in Figure 4.10 (h), the 30 nm periodicity honeycomb structure sets a limit for the array fabrication using the EBL technique.

Fabricating a high quality triangular array of holes with 40 nm periodicity is essential for our work. The smaller the periodicity of the lattice, the bigger the confinement effects. As the EBL technique is limited to a periodicity of 40 nm, it is fundamental to reduce the disorder effects, coming from missing pores or closer lines of holes.



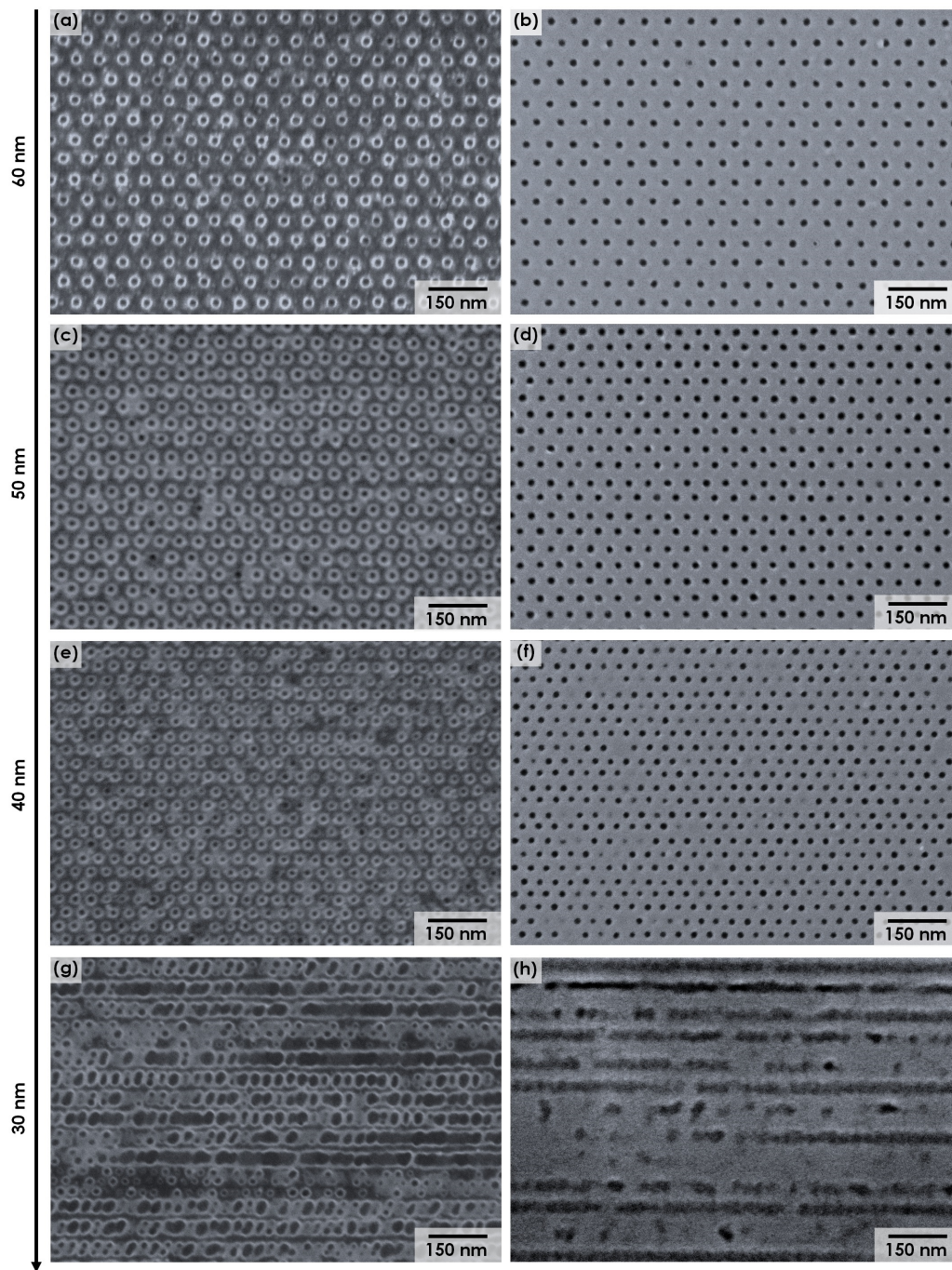


Figure 4.10 – SEM images acquired on (left) the  $\text{SiO}_2$  surface after the RIE etching and (right) the  $\text{In}_{0.53}\text{Ga}_{0.47}\text{As}$  QW surface after the HF etching of the  $\text{SiO}_2$  film. The periodicities of the triangular arrays are 60 nm (a) and (b), 50 nm (c) and (d), 40 nm (e) and (f), 30 nm (g) and (h).



### 4.2.3 The final 40 nm periodicity honeycomb lattice

Ordered honeycomb structures having a periodicity of 40 nm were nanofabricated by taking into account all the improvements obtained from the fabrication tests. We used almost the same process presented in Subsection 4.2.2. The main difference was the EBL SEQ writing method. This mode helps in getting a more homogeneous line spacing of pores. Furthermore, few seconds were added in the development time of the PMMA resist, reducing drastically the amount of missing sites. Figure 4.11 shows an example of an optimized process yielding a high quality triangular array of holes. The SEM image and the AFM topography [see Figure 4.11 (a) and (b)] reveal a really good order in the lattice. Missing sites are not present and the lines of holes are properly separated from each other. In Figure 4.11 (c) a cross-section of the sample obtained by Transmission Electron Microscopy (TEM) shows that the 10 nm of  $\text{In}_{0.53}\text{Ga}_{0.47}\text{As}$  QW were totally etched in the pores. In contrast, the measured profile along the red line on the AFM image, reveals an average hole depth of 4.5 nm meaning that the AFM tip cannot fully enter into the holes.

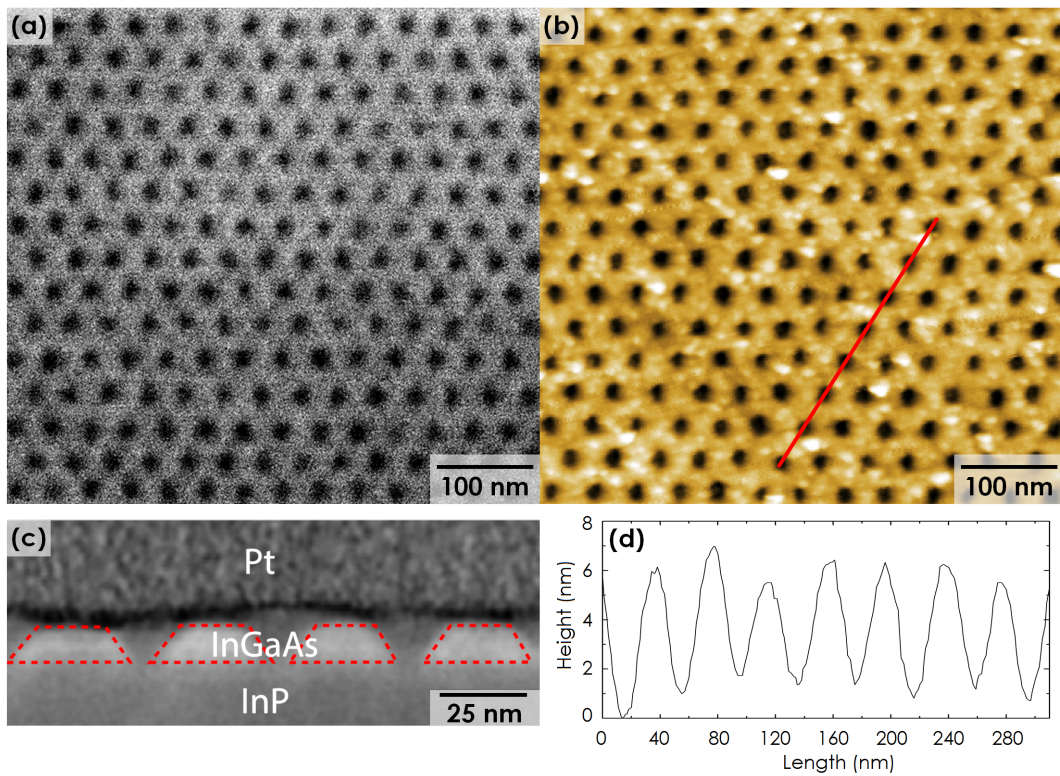


Figure 4.11 – (a) SEM image and (b) AFM topography acquired on the final optimized 40 nm periodicity honeycomb structure. (c) TEM cross-section of the heterostructure and (d) height profile acquired along the red line on the AFM image.

In addition, the etching of the holes appears conical instead of cylindrical. Theoretical calculations performed by Athmane Tadjine and Christophe Delerue using a tight-binding approach, show that this hole profile favors a broadening of the dispersion, albeit a decreasing of the confinement. The  $s$ -region of the CB structures was calculated for arrays with  $a = 40$  nm and  $r = 9$  nm, considering a 10 nm thick  $\text{In}_{0.53}\text{Ga}_{0.47}\text{As}$  layer with a triangular array of

cylindrical (red bands) or conical (blue bands) holes are reported. As one can see in Figure 4.12, the conical shape of the holes allows an increase of the linear dispersion width with respect to the cylindrical one, rising the probability to detect the Dirac cone.

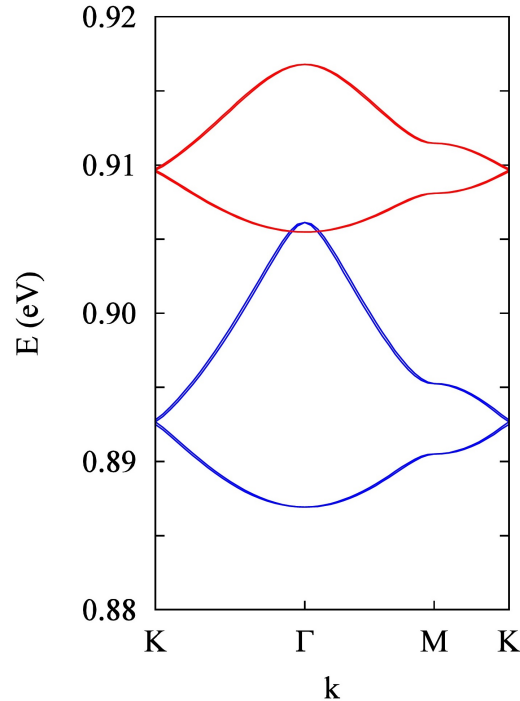


Figure 4.12 –  $s$  region of the CB structures predicted for a nanoporated  $\text{In}_{0.53}\text{Ga}_{0.47}\text{As}$  QW with a honeycomb structure of cylindrical (red bands) and conical (blue bands) holes.

### 4.3 Creating honeycomb structures on the $\text{In}_{0.53}\text{Ga}_{0.47}\text{As}$ QW using BCPL

As anticipated in the first chapter (Subsection 1.2.4), the BCPL is a powerful technique based on the self-assembly of copolymers. It allows the realization of high-resolution patterns down to 20 nm and, therefore, it is a strong alternative to the EBL. In Figure 4.6 a summary of the full process that will allow the realization of the Dirac superlattice by employing the block copolymer (BCP) self-assembly approach is illustrated. 16 nm of  $\text{SiO}_2$  are deposited by PECVD on the  $\text{In}_{0.53}\text{Ga}_{0.47}\text{As}/\text{InP}$  heterostructure after the MBE growth. Following, a honeycomb mask is created on the  $\text{SiO}_2$  layer by using the BCP self-assembly technique. A solution of PMMA and poly(styrene) (PS) is deposited on the surface and annealed to induce the self-assembly process. After that, the PMMA is removed by etching, leaving the PS honeycomb mask. Once the mask is prepared, we dry-etch the  $\text{SiO}_2$  layer and remove the PS, both by using RIE etching but with different gases. At this point, the array of holes is transferred on the  $\text{SiO}_2$  film. This  $\text{SiO}_2$  mask is used to transfer the honeycomb lattice on the 10 nm thick  $\text{In}_{0.53}\text{Ga}_{0.47}\text{As}$  QW, by employing the ICP etching technique. HF wet etching allows the removal of the 16 nm of  $\text{SiO}_2$ . The fabrication process ends with the reintroduction of the sample in the MBE chamber in order to be cleaned

by H plasma and capped with a 10 nm thick amorphous As layer. As anticipated in the previous section, this step will be discussed at the end of the chapter.

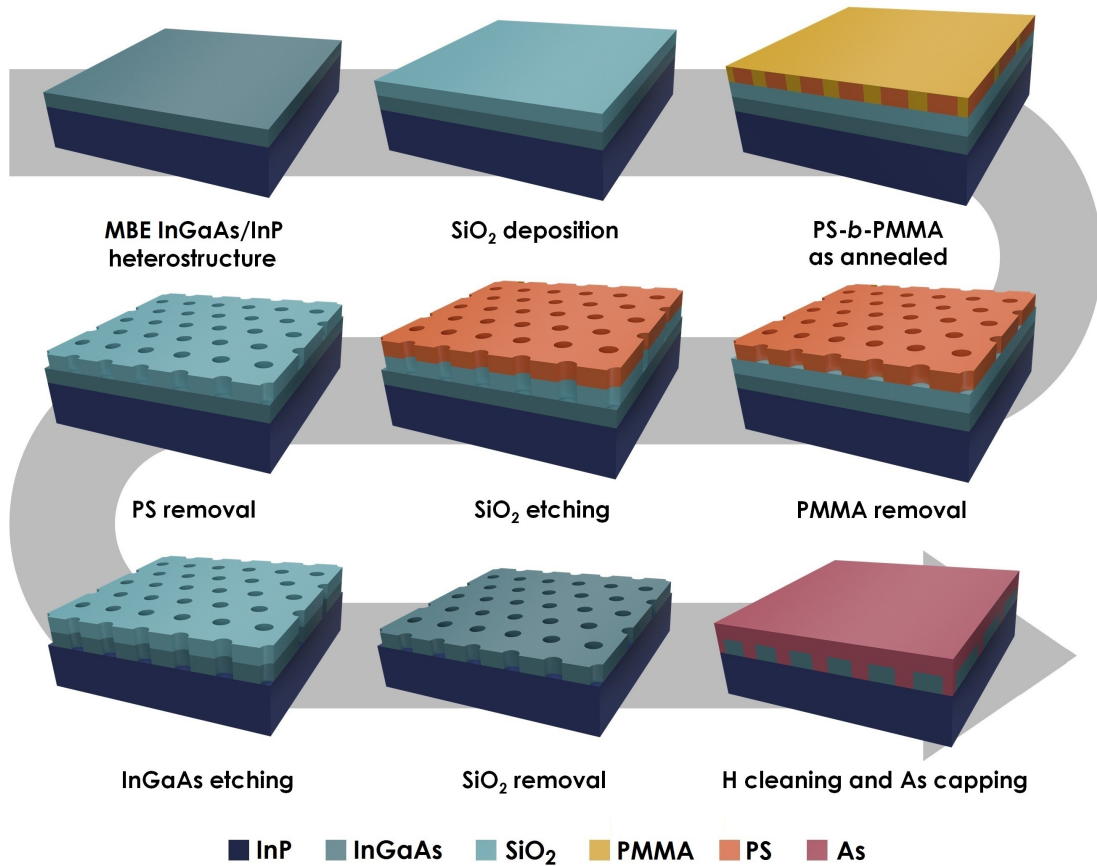


Figure 4.13 – Schematic of the technological processes used to pattern a honeycomb structure on the  $\text{In}_{0.53}\text{Ga}_{0.47}\text{As}$  by BCPL.

### 4.3.1 Honeycomb mask from BCP self-assembly

The realization of the mask was performed using the BCPL developed in the LCPO laboratory of Bordeaux. This technique is based on the self-assembly of BCP in thin films which can lead to the formation of nano-patterns of defined symmetry and periodicity. The PS-b-PMMA copolymers used in this study were synthesized using sequential anionic polymerization of styrene and methyl methacrylate leading to well-defined BCP architectures with low dispersity. The resulting BCP was dissolved in toluene (2 wt%) and spin-coated onto chemically-modified  $\text{SiO}_2$  surface. The self-assembly of the BCP layer was further promoted by thermal annealing at 220 °C leading to out-of-plane PMMA cylinders packed into an hexagonal lattice. By selectively removing the PMMA domains using plasma chemistry, this process results in the formation of a PS honeycomb mask which can be subsequently used to pattern the  $\text{In}_{0.53}\text{Ga}_{0.47}\text{As}$  QW.

Two honeycomb masks with 35 and 23 nm periodicities were fabricated for this project. The SEM images of both arrays are presented in Figure 4.14 (a) and (b), respectively. The honeycomb



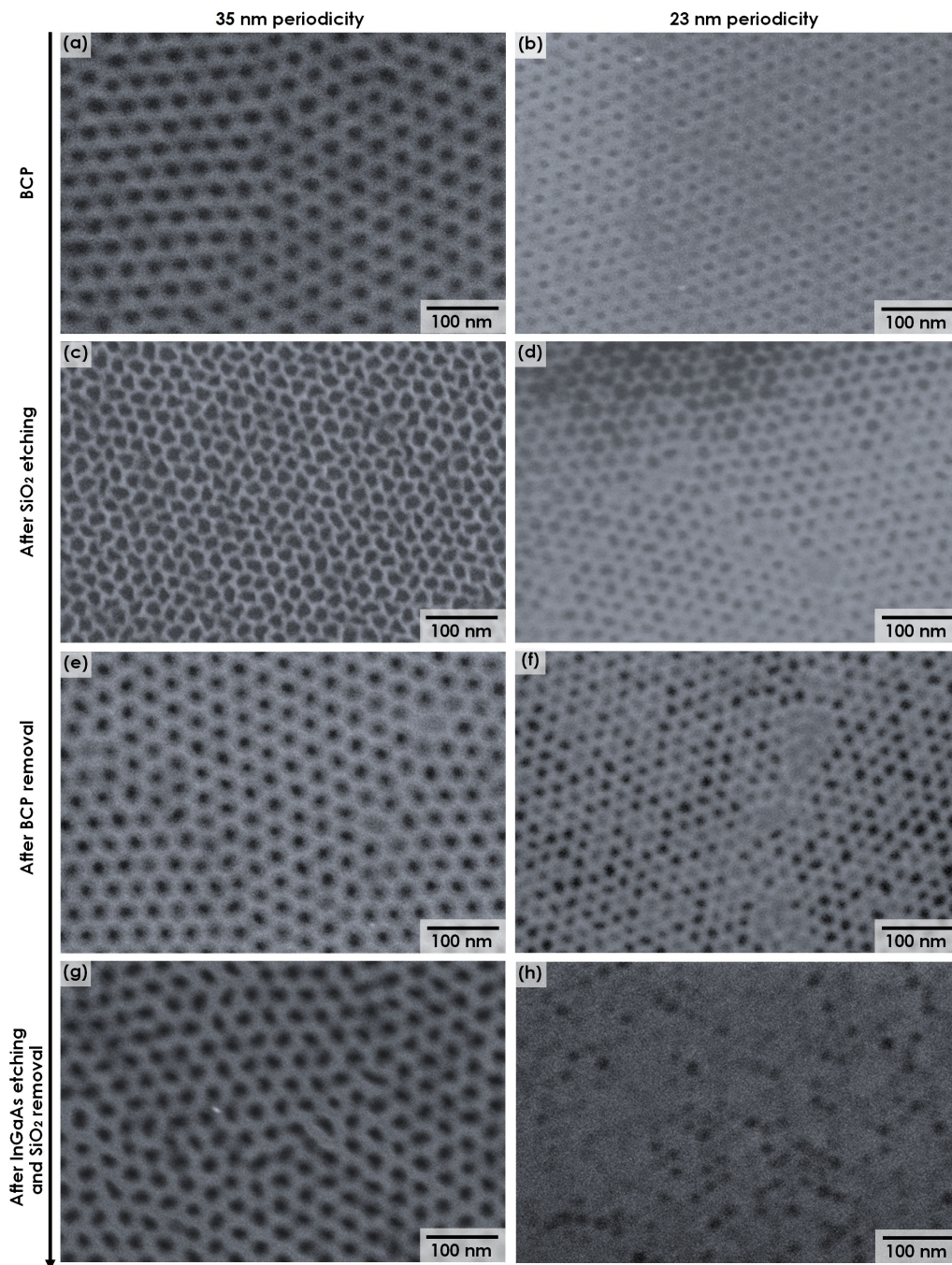


Figure 4.14 – SEM images acquired on the honeycomb arrays at different steps of the nanofabrication for periodicities of 35 (left) and 23 nm (right), respectively. (a) and (b) BCP mask, (c) and (d) BCP mask after the  $\text{SiO}_2$  etching, (e) and (f)  $\text{SiO}_2$  surface after the BCP removal, (g) and (h) nanopatterned  $\text{In}_{0.53}\text{Ga}_{0.47}\text{As}$  QW surface after the HF etching of the  $\text{SiO}_2$  layer.

lattice appears ordered on areas of about  $200 \times 200 \text{ nm}^2$ . On the other hand, at bigger scale, the presence of grain boundaries that are visible here and there in Figure 4.14 distort the order of the lattice. For our main objectives, we are first interested on the local study of the array. Furthermore,  $200 \times 200 \text{ nm}^2$  areas are a optimum maximum size to be analyzed by STM and STS at LT.

### 4.3.2 Transfer of the BCP mask on the $\text{In}_{0.53}\text{Ga}_{0.47}\text{As}$ QW

The PS mask was transferred on the 16 nm thick  $\text{SiO}_2$  layer. For this purpose, RIE etching was performed by employing the parameters previously reported in Table 4.4. After the etching of this thin film, the residual BCP was removed by using  $\text{O}_2$  plasma, employing the parameters reported in Table 4.5. Therefore, the  $\text{SiO}_2$  layer became the honeycomb mask to be transferred on the 10 nm thick  $\text{In}_{0.53}\text{Ga}_{0.47}\text{As}$  QW. At this point the honeycomb patterns were etched in the III-V material by ICP etching. The main parameters used during the process were reported in Table 4.7. The last step was the removal of the  $\text{SiO}_2$  layer by plunging the sample in HF diluted at 1% for 30 s.

SEM images were acquired on the BCP mask, the  $\text{SiO}_2$  and the  $\text{In}_{0.53}\text{Ga}_{0.47}\text{As}$  QW surfaces at different steps of the honeycomb array fabrication. The results are presented in Figure 4.14. On the left side of the picture, we report the fabrication of the 35 nm periodicity array and on the right side, the one of the 23 nm periodicity lattice. Figures 4.14 (c) and (d) display the BCP mask after the  $\text{SiO}_2$  etching. The array with a periodicity of 35 nm reveals a good uniformity in the opening of the holes, suggesting that the BCP is regularly distributed along the  $\text{SiO}_2$  surface. Contrarily, the smaller periodicity array shows that some holes are clearly not open: dark regions of holes and flat bright regions are distinguishable on the image. This effect is confirmed by looking at the  $\text{SiO}_2$  surface after the BCP removal in Figure 4.14 (f): the array is not well transferred, indicating that the BCP was thicker in the regions where there are not holes and the etching time was not enough to open the patterns. On the other hand, Figure 4.14 (e) reveals a good honeycomb structure on the  $\text{SiO}_2$  surface. Finally, as expected, the  $\text{In}_{0.53}\text{Ga}_{0.47}\text{As}$  QW surface reported in Figures 4.14 (g) and (h) show a good honeycomb transfer for the lattice with a periodicity of 35 nm and no triangular array for the 23 nm one.

### 4.3.3 The final 35 nm periodicity honeycomb lattice

Figure 4.15 shows the structural characterization of the triangular array of holes made from the 35 nm periodicity BCP mask. The AFM topography indicates a good quality of the lattice [see Figure 4.15 (a)]. The measured profile along the red line in the AFM image reveals an average hole depth of 7.1 nm. On the other hand, the cross-sectional Focused Ion Beam (FIB) of Figure 4.15 (c) shows that the 10 nm of  $\text{In}_{0.53}\text{Ga}_{0.47}\text{As}$  QW were totally etched. Furthermore, as already observed in Figure 4.11 for the sample nanofabricated per EBL, the shape of the holes appears conical instead of cylindrical, leading again to a broadening of the dispersion.

## 4.4 Hydrogen cleaning and arsenic capping

As anticipated during the description of the technological processes, the final step of the nanofabrication consists in the cleaning and As capping of the surface. For this purpose, after the wet HF etching of the  $\text{SiO}_2$  layer, the semiconductor heterostructures are reintroduced in the MBE setup. Here the samples are annealed up to  $430 \text{ }^\circ\text{C}$  and bombarded with H plasma for the deoxidization of the surface. The H plasma is performed under an As flux to compensate the As desorption caused by the high temperature. At the end of the deoxidization, the temperature is decreased

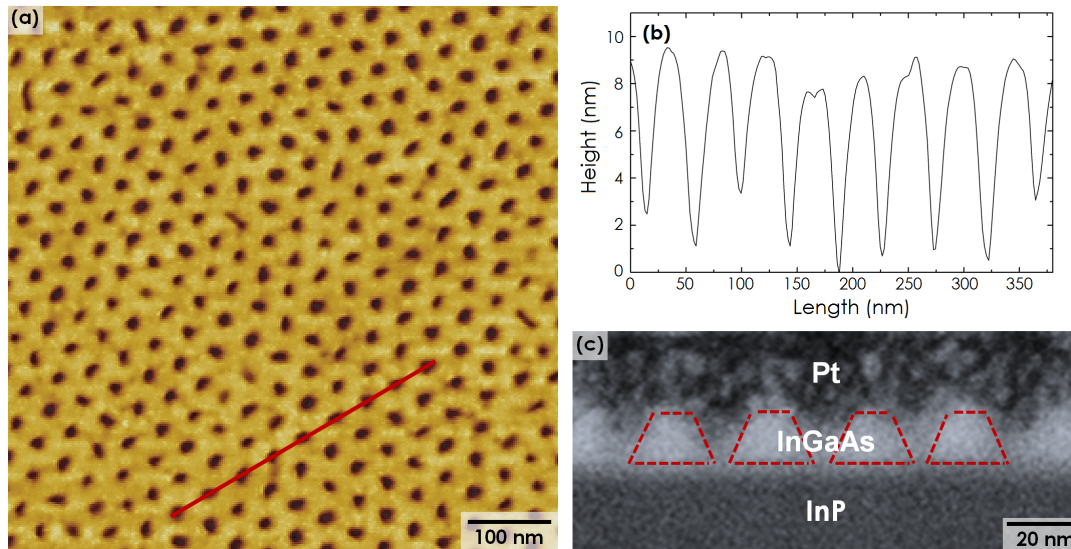


Figure 4.15 – (a) AFM topography acquired on the final optimized 35 nm periodicity honeycomb structure; (b) height profile acquired along the red line on the AFM image; (c) FIB cross-section of the heterostructure.

down to 10 °C and the surface is capped with 10 nm of amorphous As to preserve the surface from contamination during the transfer in air from the MBE to the STM system. As already discussed in Chapter 3 this thin As layer can be desorbed in the preparation chamber of the STM at 350 °C for 2 hours to recover the surface of the nanoporated  $\text{In}_{0.53}\text{Ga}_{0.47}\text{As}$  QW.

## 4.5 Conclusion

Two different routes were followed to pattern a honeycomb array of holes on the  $\text{In}_{0.53}\text{Ga}_{0.47}\text{As}$  QW/InP heterostructure. The EBL technique allowed the realization of a well ordered triangular array of pores with a periodicity of 40 nm. This lithographic process was pushed to its limit, revealing that a 30 nm periodicity array remains still a technological challenge. On the other hand, using the BCP approach, we were able to create 35 nm periodicity honeycomb arrays. The PS-*b*-PMMA copolymers self-assembly allows to realize honeycomb masks with a periodicity down to 23 nm. Nevertheless, the good transfer of the pattern on the  $\text{In}_{0.53}\text{Ga}_{0.47}\text{As}$  QW was not successful for this small periodicity, probably because of the non-homogeneity of the BCP layer.

At this point we have two  $\text{In}_{0.53}\text{Ga}_{0.47}\text{As}$  QWs nano-structured by a triangular array of holes having different periodicities. The sample fabricated using EBL revealed a well ordered 40 nm periodicity honeycomb structure, both at large and small scale. However, being limited in areas of  $60 \times 20 \mu\text{m}^2$ , its localization with the STM tip is not straightforward even in presence of the STM marks. Therefore, we decided to start the STM analysis on the sample obtained from the BCP self-assembly technique with the realization of a 35 nm periodicity honeycomb array extending over the whole  $\text{In}_{0.53}\text{Ga}_{0.47}\text{As}$  QW surface. Albeit it appears ordered in small areas of around  $200 \times 200 \text{nm}^2$ , this size should be enough to allow the formation of the expected band structure.





# Characterization of the $\text{In}_{0.53}\text{Ga}_{0.47}\text{As}/\text{InP}$ quantum well nanostructured

## Outline of the current chapter

<b>5.1 Morphology of the honeycomb array</b>	<b>96</b>
<b>5.2 Interplay between surface states and FL position</b>	<b>98</b>
<b>5.3 Electronic features in the DOS</b>	<b>101</b>
<b>5.4 Conclusion</b>	<b>105</b>

As presented in the fourth chapter, two different approaches allowed the realization of honeycomb arrays of holes in the semiconductor heterostructure. Both the EBL and BCPL led to a good quality triangular array of pores with 40 and 35 nm periodicities, respectively. As the bandwidth of the Dirac cone increases with stronger lateral confinement, we focus the last chapter on STM and STS analysis on the sample prepared by BCPL. In the first part, we will present and analyze the honeycomb array morphology. We will show that, despite all the technological steps which were used to produce the triangular array of holes, the top reconstruction of the  $\text{In}_{0.53}\text{Ga}_{0.47}\text{As}$  (001) is preserved. In the holes, the STM data are more difficult to interpret due to tip artifact, but an attempt to compare the cross-sectional SEM views with the STM height profiles will be made to get a deeper insight into the true geometry of the etched holes. After that, the STS results acquired on the artificial honeycomb structure at 77 K will be compared with those related to the QW before the nanostructuring, reported in the third chapter. We will first study the influence of the surface states on the ability to resolve features of the CB and then show the existence of additional features at the position of the characteristic steps of the 2D-DOS. In order to interpret these features, STS measurements at 4 K will also be performed. Comparison with a theoretical prediction of the DOS of the nanoporated QW will help in assigning the measured peaks. Finally, spatially resolved spectra will be discussed in light of the morphology of the nanoporated QW deduced from the first section of this chapter.

## 5.1 Morphology of the honeycomb array

STM measurements were performed on the 35 nm periodicity honeycomb array of pores at 77 K. These preliminary set of measurements were done to assess the quality of the surface after the last step of the nanofabrication (H cleaning and As capping deposition) and the evaporation of the As capping under UHV. As for the as-grown heterostructures of Chapter 3, the 10 nm thick As protective layer was desorbed at 350 °C for two hours in the preparation chamber of the STM system under UHV. Figure 5.1 shows a STM topography acquired on a  $400 \times 335 \text{ nm}^2$  area of the nanoperforated  $\text{In}_{0.53}\text{Ga}_{0.47}\text{As}$  QW surface. The quality of the surface appears very good. Albeit the number of technological steps, including the H cleaning and the As capping deposition at the end of the nanofabrication, the  $\text{In}_{0.53}\text{Ga}_{0.47}\text{As}$  QW surface seems recovered, clean and well-ordered. In addition, it is possible to distinguish the jagged terraces observed during the study of the bare QW. Although few holes are not well transferred, the quality of the honeycomb structure appears good, in particular in areas of  $150 \times 150 \text{ nm}^2$ . On the other hand, the presence of grain boundaries distort the order of the array at large scale. From the STM image we measured an array periodicity of  $35 \pm 5 \text{ nm}$  and a pore radius of  $7 \pm 1 \text{ nm}$ . The periodicity and the radius of the pores were also measured in the SEM image acquired at the end of the nanofabrication [Figure 4.14 (g), Chapter 4]. We obtained  $36.6 \pm 2.8 \text{ nm}$  and  $10.2 \pm 0.6 \text{ nm}$ , respectively. The values of the pore periodicity are in good agreement. On the contrary, the radius of the holes seems a bit smaller in the STM image.

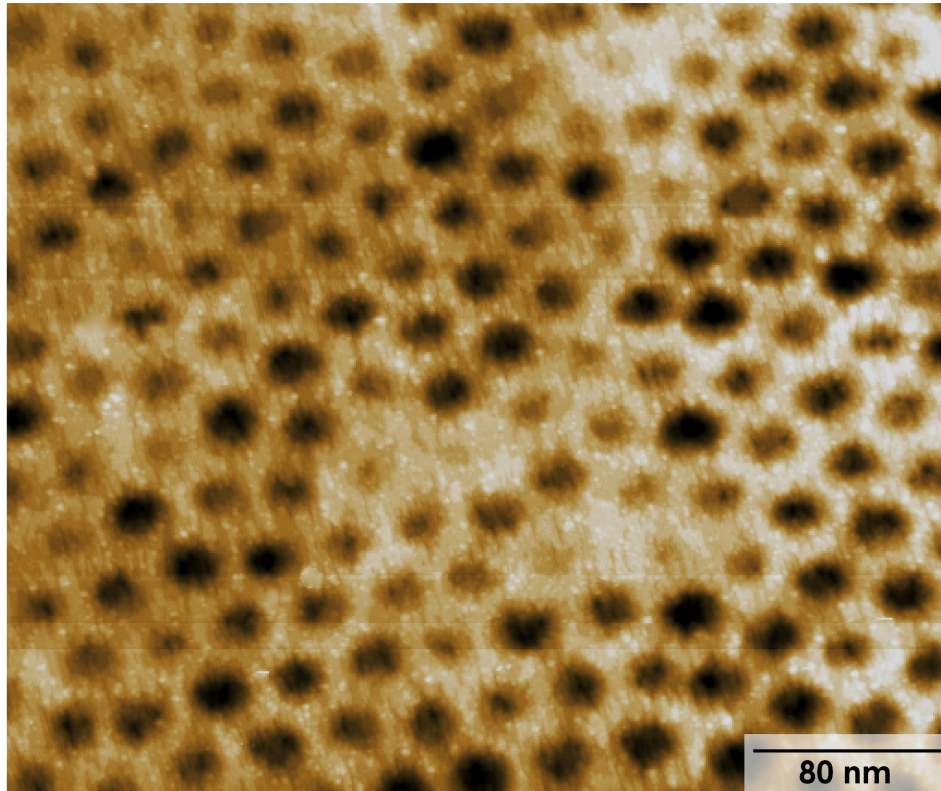


Figure 5.1 – STM image acquired on a  $400 \times 335 \text{ nm}^2$  area of the honeycomb structure at 77 K. Topography acquired using  $V_S = +2 \text{ V}$ ,  $I_{setpoint} = 20 \text{ pA}$ .

In Figure 5.2 (a), a STM image of a  $190 \times 190 \text{ nm}^2$  area of the nanoporated  $\text{In}_{0.53}\text{Ga}_{0.47}\text{As}$  QW surface is reported. Between the holes, the top surface is preserved with an average width of 10 nm. It appears flat and consists of parallel rows, which we attribute to the dimer rows, as discussed later. At the edge of the honeycomb pores, a bunch of a few (001) terraces showing the same reconstruction are visible. In the holes where the etching was not complete, for example

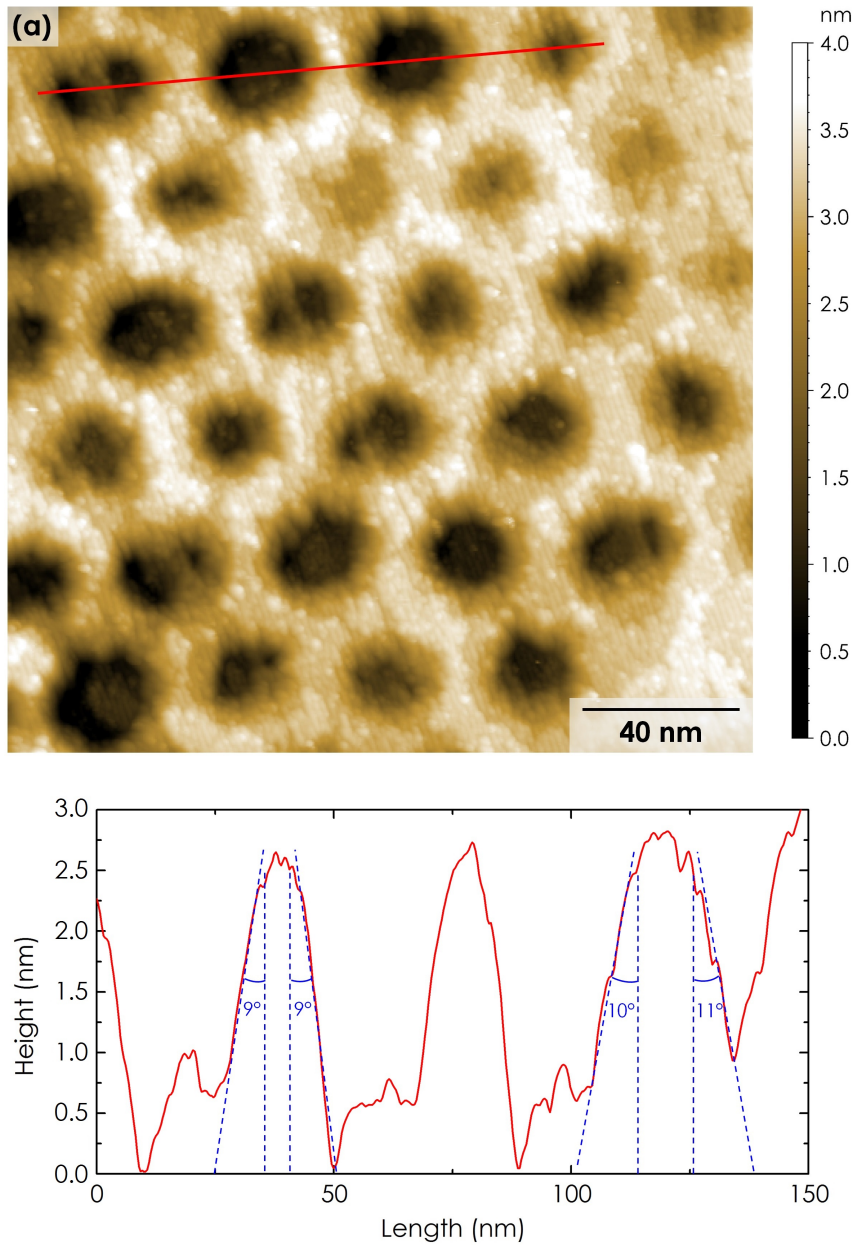


Figure 5.2 – (a) STM image acquired on a  $190 \times 190 \text{ nm}^2$  area of the honeycomb structure at 4 K. Topography acquired using  $V_S = +2 \text{ V}$ ,  $I_{\text{setpoint}} = 20 \text{ pA}$ . (b) Height profile acquired along the red line on the STM image.

to the top right part of the STM image, this effect is clearly visible. In these pores, the lowest contrast is obtained in the middle of the pore, meaning that the etching proceeds by a gradual removal of single atomic layers starting from the center of the pores. In the deeper pores, the morphology appears different. The bottom of the pores appears flat, but on the left edge, there is always a small depression. This is better seen in the height profile across three pores [Figure 5.2 (b)]. Based on this morphological difference between the partially etched pores and the fully etched pores, we attribute this effect to a tip artifact. Such an effect is supported by the measured height profile. The maximum depth of the pores is about 3 nm. This value is too small in comparison with the depth of the pores measured in cross-sectional SEM view, that was determined to be about the thickness of the  $\text{In}_{0.53}\text{Ga}_{0.47}\text{As}$  QW, e.g. 10 nm [see Chapter 4, Figure 4.15 (c)]. It is also smaller than the depth found with AFM [Figure 4.15 (b)]. Therefore, the STM tip is not sharp enough to resolve the bottom of the pores and the contrast seen in the darker pores results from multiple tips that image the top surface between the pores.

Although the tip cannot resolve the bottom of the pores, we believe that the first nanometers are correctly imaged. Therefore, we measured the slope at the edge of the pores. The value of a few angles between the vertical direction and the slopes are given in Figure 5.2 (b). We find an average value of  $10^\circ$ . Comparison with one deduced from the cross-sectional SEM analysis yields a more abrupt sidewall. The SEM technique generates images thanks to the electrons scattered from the sample. This signal is an average value that can include electrons backscattered by a volume that is wider than the pore boundaries. As a result, the edge detection could be broadened if the cross-section is not performed right across the widest part of the pores. Therefore, we believe that the shape of the pore is less conical than we thought based on the SEM analysis performed in Chapter 4.

## 5.2 Interplay between surface states and FL position

Figure 5.3 (a) shows a high resolution STM topography of a  $120 \times 120 \text{ nm}^2$  area of the nanoperforated  $\text{In}_{0.53}\text{Ga}_{0.47}\text{As}$  QW surface. In terms of nanofabrication the zone is not the best probed: the holes are not completely transferred and therefore, they appear irregular. On the contrary, the top surface is highly resolved. Jagged terraces are clearly distinguishable. The measurement of the step height between two terraces reported in Figure 5.3 (b) gives a value of about 0.30 nm. Bright rows of As dimers separated by dark trenches are clearly resolved. The distance between the rows is around 1.6 nm [see Figure 5.3 (c)]. The results are consistent with the terrace step heights and the trench widths measured in the third chapter (see Section 3.3) for a typical As-rich ( $2 \times 4$ ) surface reconstruction. That means that after the nanofabrication processes the surface of the  $\text{In}_{0.53}\text{Ga}_{0.47}\text{As}$  QW is entirely recovered. We would like to emphasize that the  $\text{In}_{0.53}\text{Ga}_{0.47}\text{As}$  QW surface has faced several technological steps, with different depositions, etching techniques and evaporations. For this reason, we underline the high quality of the surface after the nanofabrication processes.

STS was performed on the honeycomb array of holes. In Figure 5.4 (b) a typical spectrum acquired in the region between the pores is reported. For comparison, in Figure 5.4 (a) we show the  $dI/dV$  curve obtained on the bare  $\text{In}_{0.53}\text{Ga}_{0.47}\text{As}$  QW before the nanoperforation (G170401 sample), as presented in the third chapter. The top of the VB is indicated with  $E_V$ . Based on the onset of the VB, the position of the FL  $E_F$ , is found to be located  $0.27 \pm 0.03 \text{ eV}$  above the top of the VB. This value is bigger than the one measured for the bare  $\text{In}_{0.53}\text{Ga}_{0.47}\text{As}$  QW ( $0.17 \pm 0.03 \text{ eV}$ ). At positive voltages three step-like features are clearly visible, labeled  $E_1$ ,  $E_2$  and  $E_3$ , consistent with the voltage dependence observed before the fabrication. From the position of

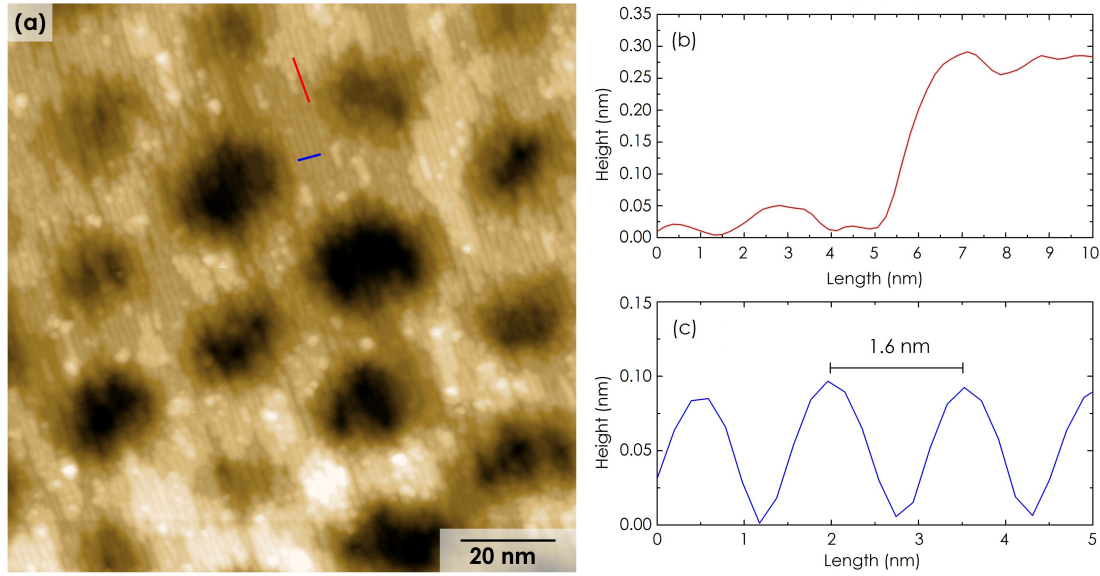


Figure 5.3 – (a) STM image acquired on a  $120 \times 120 \text{ nm}^2$  area of the honeycomb structure at 4 K. Topography acquired using  $V_S = +2 \text{ V}$ ,  $I_{setpoint} = 20 \text{ pA}$ . (b) Height profile acquired between two terraces; (c) profile acquired perpendicularly to the bright rows.

$E_1$  and the VB edge, we determine an apparent band gap of  $0.98 \pm 0.03 \text{ eV}$ , that is a bit larger than the one previously reported ( $0.90 \pm 0.03 \text{ eV}$ ). These spectroscopic results highlight the absence of surface states in the band gap region, likewise the QW. As discussed in the third chapter, the pinning of  $E_F$  in the band gap region is an indication of their presence. Furthermore, here  $E_F$  is shifted towards midgap. We suspect that two effects account for this shift. First, the nanoporation leads to a higher density of terraces. Their step edges increase the concentration of defect states that are able to pin  $E_F$  midgap more strongly. Moreover, the etching and removal of the oxide layer induce the formation of new facets in the pores. We do not know exactly the chemistry of the facets but we could expect the presence of dangling bonds that are expected to have an effect on the FL pinning also. Another important point concerning the nanofabrication are the  $\text{SiO}_2$  deposition and evaporation steps. Oxygen penetrates the  $\text{In}_{0.53}\text{Ga}_{0.47}\text{As}$  surface during the deposition of the  $\text{SiO}_2$  layer. As a result, its removal with the H cleaning process will decrease the thickness of the QW by one to two nanometers at most. However, we have seen in Chapter 3, that the Be dopants strongly segregate to the surface. Therefore the removal of the oxide layer causes the  $\delta$ -doped surface layer to become thinner. Decreasing the density of acceptors leads to an upward shift of  $E_F$  for a p-type doped (001) surface<sup>[70]</sup>, which is consistent with the measured shift. Such an effect can also explain the larger width of the apparent band gap. First, screening of the electrical field induced by the tip is less efficient and results in larger apparent band gap. Then, a thinner QW slightly increases the confinement and hence the band gap.

By reducing the voltage window to center it on the CB and increasing the resolution of the measurements, we note that the plateaux corresponding to the three energy levels of the  $\text{In}_{0.53}\text{Ga}_{0.47}\text{As}$  QW are no longer flat [see inset in Figure 5.4 (b)]. Peaks are now visible, signature of a change of the DOS. Nevertheless, as anticipated in Subsection 2.5.3, the effects of the temperature broadening are important at 77 K and they prevent the observation of fine features



requiring resolution in the ten meV range. Therefore, the STS experiments must be performed at 4 K to improve the quality of the spectroscopic measurements.

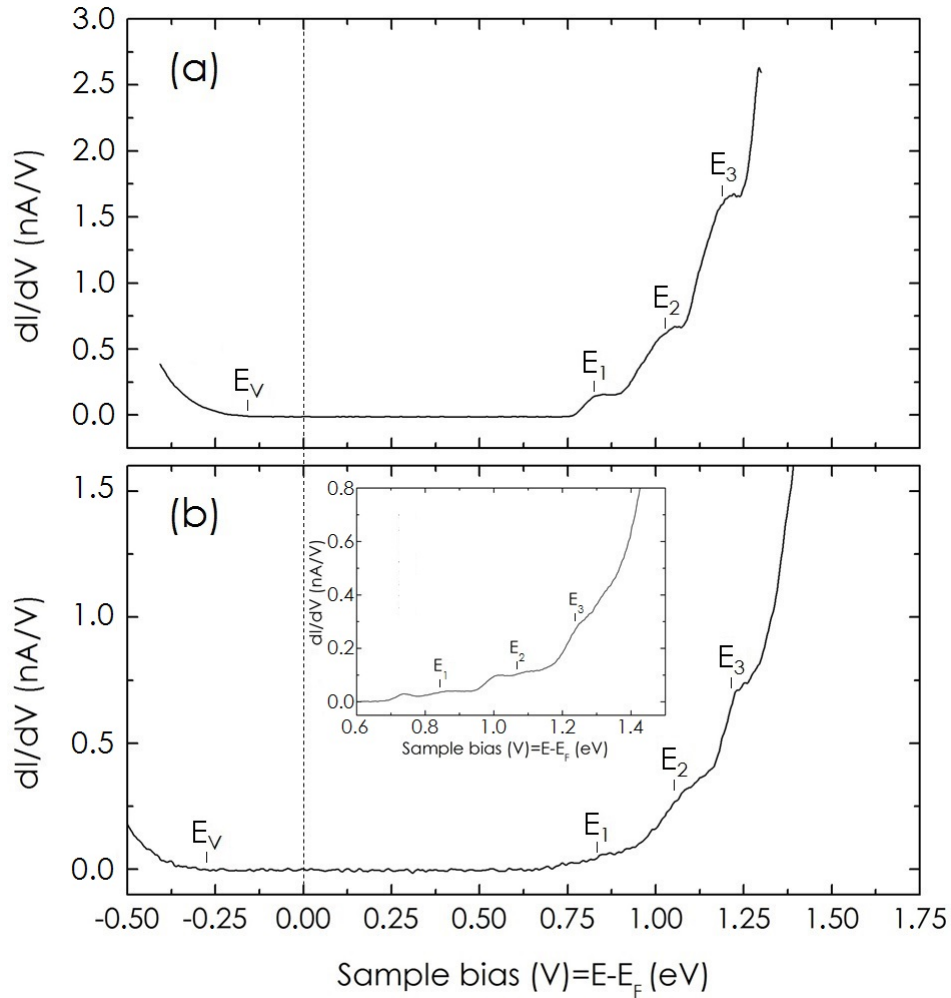


Figure 5.4 –  $dI/dV$  spectra acquired on (a) G170401 sample and (b) the related nanostructured  $\text{In}_{0.53}\text{Ga}_{0.47}\text{As}$  QW measured at 77 K. The three electron sub-bands and the top of the VB are labeled  $E_1$ ,  $E_2$  and  $E_3$  and  $E_V$ . Inset in (b):  $dI/dV$  acquired in the CB region of the  $\text{In}_{0.53}\text{Ga}_{0.47}\text{As}$  QW. Feedback parameters: (a)  $V_S = +1.30 \text{ V}/I_{\text{setpoint}} = 400 \text{ pA}$ , (b)  $V_S = +1.50 \text{ V}/I_{\text{setpoint}} = 200 \text{ pA}$  and inset  $V_S = +1.50 \text{ V}/I_{\text{setpoint}} = 200 \text{ pA}$ . The differential conductance  $dI/dV$  was acquired with a lock-in amplifier using a bias modulation of 9 mV RMS at a frequency of 490 Hz. The apparent band gap was measured by plotting the differential conductance in a log scale to precisely determine the noise level.

### 5.3 Electronic features in the DOS

We did not notice any difference in the morphology of the nanoporated surface between 4 K and 77 K. Likewise in the third chapter, we were able to image the surface with similar feedback parameters [see Figure 5.5 (a)], meaning that the decrease of the dopant concentration at the surface is limited. We maximized the resolution in the CB region by setting the feedback voltage

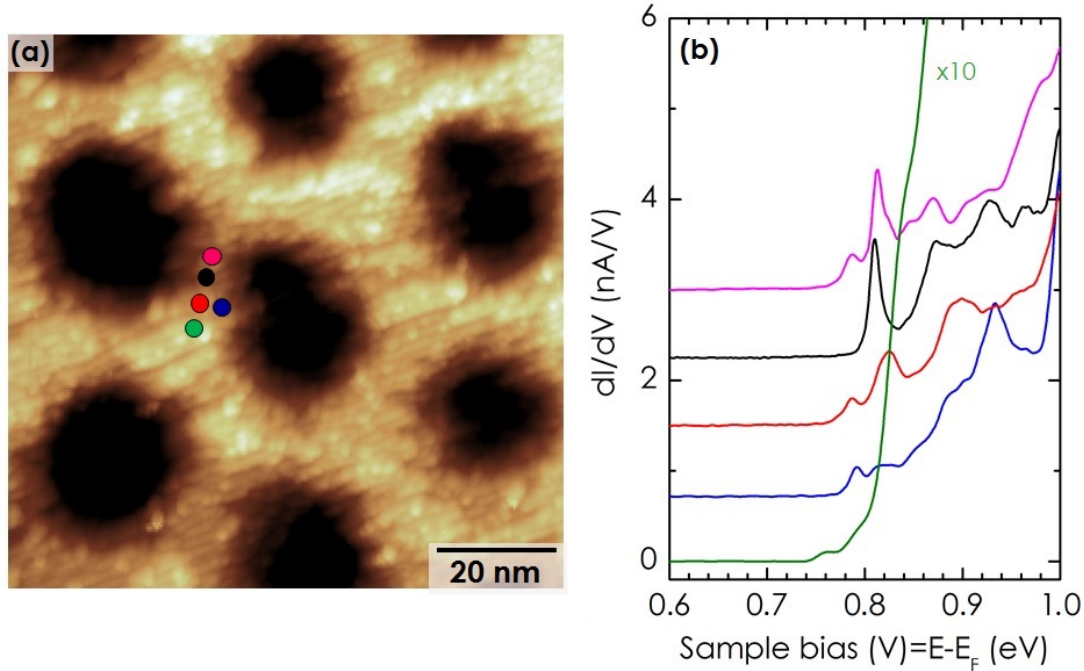


Figure 5.5 – (a) STM image acquired on a  $100 \times 100 \text{ nm}^2$  area of the  $\text{In}_{0.53}\text{Ga}_{0.47}\text{As}$  honeycomb structure. (b)  $dI/dV$  spectra acquired at the different positions highlighted in the STM topography. Feedback parameters: (a)  $V_S = +3 \text{ V}$ ,  $I_{\text{setpoint}} = 20 \text{ pA}$ , (b)  $V_S = +1 \text{ V}$ / $I_{\text{setpoint}} = 250 \text{ pA}$  except for the green curve acquired using  $V_S = +0.88 \text{ V}$ / $I_{\text{setpoint}} = 300 \text{ pA}$ . The  $dI/dV$  curves were acquired with a lock-in amplifier using a bias modulation of 1.5 mV RMS (1 mV RMS for the green curve) at a frequency of 490 Hz. Measurements performed at 4 K.

at +1.0 V in the area located between two pores, underlined in Figure 5.5 (a). For simplicity we will call this region bridge site. Figure 5.5 (b) shows five averaged  $dI/dV$  curves. A sharp peak centered at 0.810 V is observed in the middle of the bridge site (black curve). 2 nm far from this point, towards the top part of the STM image, the differential conductance reveals again the same sharp peak (pink curve). Furthermore, a small band appears lower in energy (0.780 V). The intensity of the sharp peak decreases when one looks on the other side of the bridge, 4 nm far from it (red curve). Moreover, it totally disappears in the spectra acquired close to the edge of the pore (blue curve), leaving alone the small band. Finally, a second shoulder appears at 0.760 V, when one starts to approach the center of three pores (called for simplicity atomic site). This behavior is visible in the green curve, for which intensity has been multiplied by a factor of 10 to be better resolved and compared with the other differential conductances.

Theoretical results, predicted by Christophe Delerue, were obtained using a tight-binding approach and considering a 10 nm thick  $\text{In}_{0.53}\text{Ga}_{0.47}\text{As}$  layer including a triangular array of



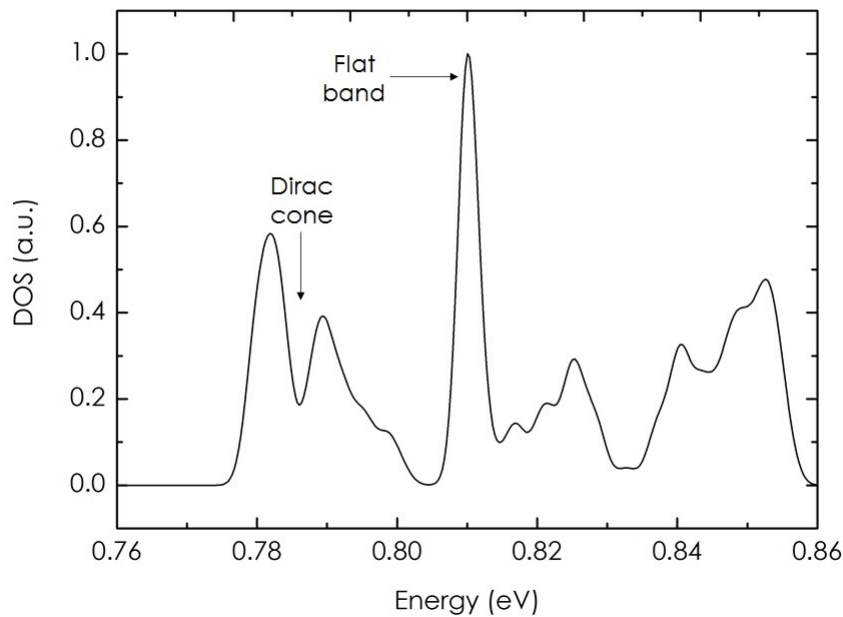


Figure 5.6 – DOS calculated using tight binding calculations.

cylindrical holes with 35.2 nm periodicity and a pore radius of 20.6 nm. As shown in Figure 5.6 the DOS reveals the formation of a Dirac cone and a flat band higher in energy. By comparing this result with the spectra of Figure 5.5 (b), we can attribute the sharp peak centered at 0.810 V to the flat band. In agreement with the experimental results, this peak has been predicted to be more or less intense depending on the location of the measurements in the unit cell (unpublished result from Utrecht university). It is maximum at the center of the unit cell, corresponding to the intersection of the diagonals of the rhombus defined by four adjacent pores. It is minimum at the cross-point between three pores. As in Figure 5.6, the theoretical DOS is spatially averaged, the energy of the peak can be compared with the experiments and not the peak intensity. Therefore we expect the sharp peak measured experimentally to be caused by the flat band. A similar situation occurs for the next peaks. Only the Dirac cone of the  $s$ -sector in the CB is fully delocalized and should be found everywhere between the pores<sup>[40]</sup>. In our case, the Dirac cone should be located in the region between the peaks at 0.750 V and the 0.770 V. Moreover, as visible from Figure 5.5 (b), it is not yet well detected.

From the analysis of Figure 5.5 (a) and other STM topographies it was observed that the surface is often characterized by a particular corrugation. As visible from Figure 5.7 (a), the atomic sites are higher in height with respect to the bridge sites. Furthermore, as summarized in Figure 5.5 (c), a weak Dirac cone was detected on the atomic site while it became more defined in between the atomic and the bridge sites. This behavior can be attributed to the corrugation of the surface. The atomic sites being higher with respect to the bridge sites, the transmission probability between the tip state and the lowest quantized states of the nanoporated QW decreases when the tip scans an atomic site. Therefore, the measurements lack of sensitivity and it might be difficult to detect the Dirac cone right at the atomic sites, unless the surface between

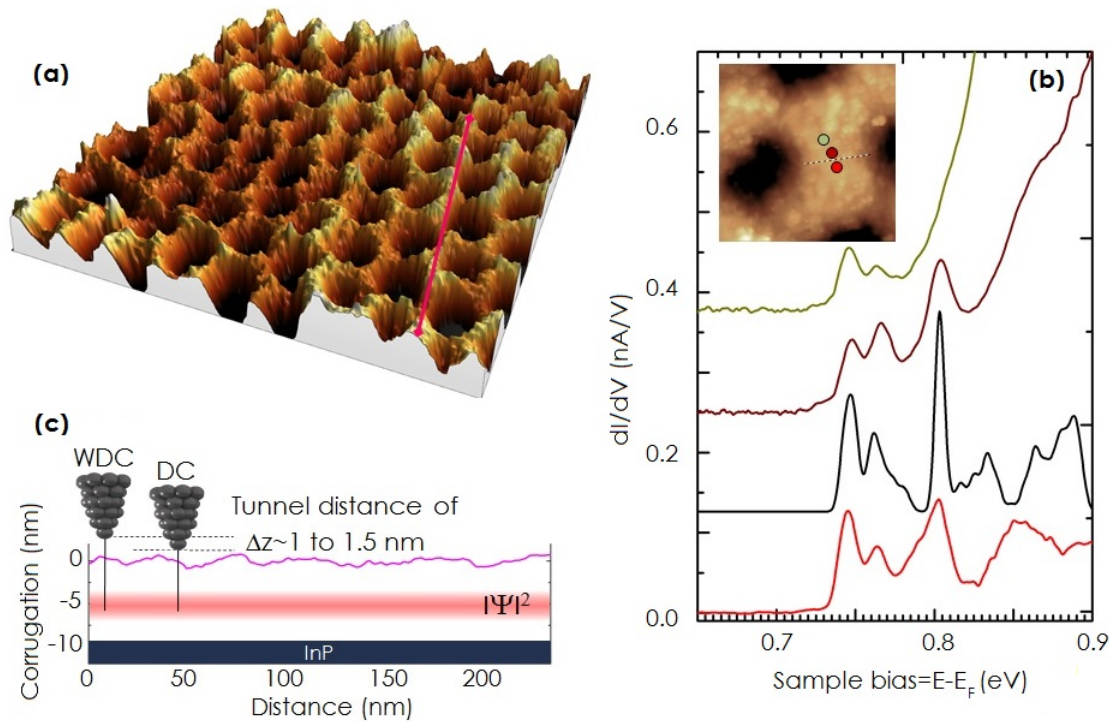


Figure 5.7 – (a) 3D STM image acquired on the nanostructured  $\text{In}_{0.53}\text{Ga}_{0.47}\text{As}$  QW. (b)  $dI/dV$  spectra acquired at the three different positions highlighted in the STM topography (inset). (black curve) DOS calculated using tight binding calculations. (c) Height profile acquired along the pink line on the 3D STM image. The atomic sites are 1-1.5 nm higher in height with respect to the bridge sites while the maximum of the electron probability distribution is located almost in the middle of the QW. Therefore, at the atomic sites the tip detects a weak Dirac cone (WDC). Close to the bridge site it probes a better defined Dirac cone (DC). Feedback parameters: (a)  $V_S = +3$  V,  $I_{\text{setpoint}} = 20$  pA, (b)  $V_S = +1$  V/ $I_{\text{setpoint}} = 100$  pA. The  $dI/dV$  curves were acquired with a lock-in amplifier using a bias modulation of 4 mV RMS at a frequency of 490 Hz. Measurements performed at 4 K.

the atomic site and the bridge site is flat. In the example of Figure 5.7 (b), we purposely chose an area which was atomically flat. Three spectra acquired on a flat region of the nanostructured  $\text{In}_{0.53}\text{Ga}_{0.47}\text{As}$  QW (inset) are reported. The  $dI/dV$  curves are compared with the theoretical DOS showed in Figure 5.6, multiplied by a factor of two in energy. A sharp peak at 0.810 V is clearly resolved at the positions close to the bridge site, in agreement with the previous results. This peak disappears when the  $dI/dV$  signal is acquired close to the atomic site (green curve). Lower in energy two small peaks are revealed at around 0.750 V and 0.760 V, respectively. We can see a good match with the theory. Based on this comparison, we can attribute the gap between the two lowest peaks to the Dirac cone. The sharp peak arises from the flat band. Preliminary calculations (not published yet) have revealed the importance of the pore size on the separation and width of the peaks. We attribute the factor of two that we considered here to the formation of a dead layer around the pore. It makes the pore electrostatically bigger than the etched one. Such an effect could be caused by a small variation of the FL pinning at the facets of the pores with respect to the (001) surface.

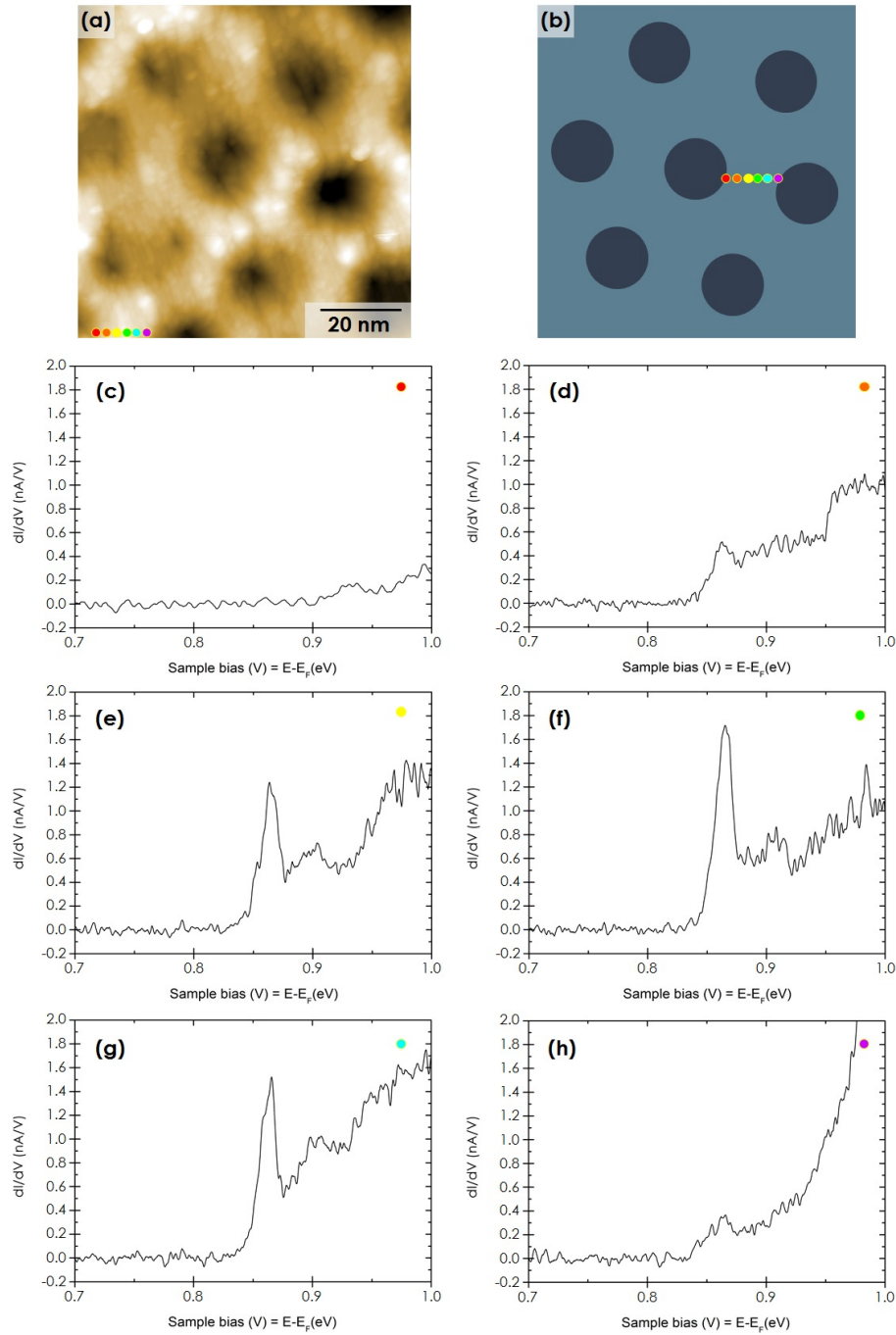


Figure 5.8 – (a) STM image acquired on a  $100 \times 100 \text{ nm}^2$  area of the nanostructured  $\text{In}_{0.53}\text{Ga}_{0.47}\text{As}/\text{InP}$  QW surface (using  $V_S = +2 \text{ V}$ ,  $I_{setpoint} = 20 \text{ pA}$ ) and [(c)-(h)] spatial variation of the  $dI/dV$  spectra along a bridge site of the honeycomb structure (highlighted in the STM topography) measured at 4 K. (b) Schematics showing a bridge site. Feedback parameters:  $V_S = +1 \text{ V}/I_{setpoint} = 50 \text{ pA}$ . The differential conductance  $dI/dV$  was acquired with a lock-in amplifier using a bias modulation of 2 mV RMS at a frequency of 490 Hz.

In order to confirm the assignment of the flat band, which should be strongly localized curves, a series of spectra was measured along the short segment highlighted in the STM image of Figure 5.8. Seven spectra were acquired every 2 nm in the bridge site (underlined in the STM image). As one can see, from the leftmost position to the right part of the bridge site, there is a gradual formation and disappearance of the sharp peak. The intensity of this peak reaches a maximum at the center of the bridge site and its FWHM is  $\sim 11$  meV. On the other hand, the peak disappears 4 nm further away, meaning that it is strongly spatially dependent. In this example, we note that the onset of the first peak is shifted to 0.85 V in comparison with Figure 5.5 (c). This shift of the potential can be caused by a slight increase of the vertical quantum confinement due to the fluctuation of the QW thickness or/and by disorder in the lateral confinement.

## 5.4 Conclusion

The artificial honeycomb structure with a periodicity of 35 nm, created from BCPL, was investigated by STM and STS. At a large scale, the topography revealed a good patterning of the  $\text{In}_{0.53}\text{Ga}_{0.47}\text{As}$  QW surface. The periodicity and the radius of the pores measured in the STM images were compared with those measured in the SEM image. A good agreement was found for the periodicities while the radius measured from the STM topography appeared smaller. The STM hole profile was compared with the FIB cross-section, revealing a shape that is less conical than initially thought. The quality of the  $\text{In}_{0.53}\text{Ga}_{0.47}\text{As}$  QW surface was high. Despite the number of technological steps, we were able to recover the As-rich ( $2\times 4$ ) surface reconstruction: bright rows of As dimers separated by dark trenches of 1.6 nm were observed.

The STS performed on the nanostructured  $\text{In}_{0.53}\text{Ga}_{0.47}\text{As}$  QW at 77 K showed the lack of detection of the surface states, the apparent band gap width and the pinning of the FL, in good agreement with the results obtained on the bare  $\text{In}_{0.53}\text{Ga}_{0.47}\text{As}$  QW before the technological processes. Small variations were nevertheless observed and may be attributed to the presence of additional surface states on the facets of the pores and to a decrease of the dopant concentration at the surface of the QW. Finally, the STS measurements performed at 4 K revealed exciting features in the differential conductance. From the comparison of a highly resolved spectrum with tight-binding calculations we suggest that the two lowest peaks and the sharp peak observed in the CB of the nanoperforated QW arise from the presence of a Dirac cone and a flat band, respectively. Their spatial dependencies are consistent with delocalized states of the Dirac cone induced by  $s$  orbitals and localized states of the flat band induced by planar  $p$  orbitals. Moreover, these features can shift in energy because of inhomogeneities in the geometry of the array.



# Conclusion

The aim of this thesis was the realization and the characterization of an artificial honeycomb structure nanofabricated on epitaxially grown III-V semiconductors to engineer a complex band structure. The idea was to use a two-dimensional electron gas hosted in an  $\text{In}_{0.53}\text{Ga}_{0.47}\text{As}/\text{InP}$  heterostructure and to confine the motion of the electron gas by creating a honeycomb array of pores directly in the active layer. For this purpose, high resolution e-beam or block copolymer lithographies, combined with dry etching techniques, were pushed to their limit in order to reach the smallest possible honeycomb lattice periodicity.

As the raw material relies on the use of a quantum well, a preliminary study was required to determine the growth and protection conditions that made the presence of the two-dimensional gas detectable with scanning tunneling spectroscopy. We have shown that by considering a clean and well-ordered  $\text{In}_{0.53}\text{Ga}_{0.47}\text{As}$  (001) surface, the small contribution of the surface states allows the observation of the conduction band quantized states in the well. However, this observation strongly depends on the hole concentration in the sample and the current that is transferred from the tip to recombine with the majority carriers in the well.

Having set the proper parameters for the structure so that tunneling spectroscopy exhibits the typical step-like function for a two-dimensional density of states, the nanostructuring of the  $\text{In}_{0.53}\text{Ga}_{0.47}\text{As}$  QW was performed following two routes, by writing the honeycomb pattern with e-beam lithography on a resist mask or by transferring the honeycomb pattern from a block copolymer mask. Minimizing geometrical disorder in the array of holes was at the forefront of the first approach and yielded a well ordered honeycomb array of pores with a periodicity of 40 nm on areas of  $60 \times 20 \mu\text{m}^2$ . On the other hand, by using the block copolymer lithography, we were able to fabricate a triangular lattice with a 35 nm periodicity extending over the whole  $\text{In}_{0.53}\text{Ga}_{0.47}\text{As}$  quantum well surface. As our main objective was to study the formation of Dirac cones, the sample with a 35 nm periodicity was selected, since it was expected to show the largest bandwidth for the Dirac cone.

The 35 nm periodicity artificial honeycomb structure was investigated by scanning tunneling microscopy and spectroscopy at low temperature. The surface analysis of the sample showed a high quality of the transferred patterns, the As-rich reconstruction of the surface being preserved despite all the technological steps involved in the nanoporation of the  $\text{In}_{0.53}\text{Ga}_{0.47}\text{As}$  quantum well. Again, the surface states did not hide the measurement of the conduction band states in tunneling spectroscopy. Tunneling spectroscopy revealed a complex characteristic that was compared with theoretical predictions. The experimental results are consistent with the existence of a Dirac cone in the  $s$ -sector and a flat band in the  $p$ -sector of the conduction band. Furthermore, spatially resolved spectra showed a strong spatial dependence of the peak intensity that reflect the degree of localization of the different states and inhomogeneities in the surface



morphology.

While our method to produce a material with an artificial graphene-like band structure is promising, the surface corrugation and the fluctuations in the pore size and pore depth have to be reduced. Without such an improvement, the resolution of features that do not exist in graphene and are inherent to the nanoperforated quantum well, such as a Dirac cone in the  $s$ -sector and a flat band in the  $p$ -sector of the conduction band, is very difficult. While we have considered two routes for the lithography, other routes, such as ion lithography or scanning probe lithography, exist and could help in reducing the pitch size and, as a result, expand the energy width of the characteristic electronic features of Dirac materials. Therefore, we believe that this work is a first step towards the controlled nanoperforation of III-V heterostructures in order to engineer exotic band structures.

# Bibliography

- [1] T. Ando, A. B. Fowler, and F. Stern. "Electronic properties of two-dimensional systems". In: *Reviews of Modern Physics* 54 (1982), p. 437.
- [2] A. Ohtomo and H. Y. Hwang. "A High-Mobility Electron Gas at the LaAlO<sub>3</sub>/SrTiO<sub>3</sub> Heterointerface". In: *Nature* 427 (2004), p. 423.
- [3] A. F. Santander-Syro et al. "Two-Dimensional Electron Gas with Universal Subbands at the Surface of SrTiO<sub>3</sub>". In: *Nature* 469 (2011), p. 189.
- [4] T. C. Rödel et al. "Universal Fabrication of 2D Electron Systems in Functional Oxides". In: *Advanced Materials* 28 (2016), p. 1976.
- [5] M. Morgenstern et al. "Coverage dependence of the Fe-induced Fermi-level shift and the two-dimensional electron gas on InAs(110)". In: *Physical Review B* 61 (2000), p. 13805.
- [6] M. J. Kelly and R. J. Nicholas. "The physics of quantum well structures". In: *Reports on Progress in Physics* 48 (1985), p. 1699.
- [7] Z. I. Alferov. "Nobel Lecture: The double heterostructure concept and its applications in physics, electronics, and technology". In: *Reviews of Modern Physics* 73 (2001), p. 767.
- [8] F. Capasso. "Band-Gap Engineering: From Physics and Materials to New Semiconductor Devices". In: *Science* 235 (1987), p. 172.
- [9] U. Banin et al. "Identification of atomic-like electronic states in indium arsenide nanocrystal quantum dots". In: *Nature* 400 (1999), p. 542.
- [10] D. D. D. Ma et al. "Small-Diameter Silicon Nanowire Surfaces". In: *Science* 299 (2003), p. 1874.
- [11] A. Urbieto et al. "Scanning tunneling spectroscopy of cleaved InAs/GaAs quantum dots at low temperatures". In: *Physical Review B* 77 (2008), p. 155313.
- [12] R. M. Feenstra et al. "Interface roughness and asymmetry in InAs/GaSb superlattices studied by scanning tunneling microscopy". In: *Physical Review Letters* 72 (1994), p. 2749.
- [13] K. Suzuki et al. "Spatial Imaging of Two-Dimensional Electronic States in Semiconductor Quantum Wells". In: *Physical Review Letters* 98 (2007), p. 136802.
- [14] Thomas Schäpers. *Superconductor/Semiconductor Junctions*. Springer, 2001.
- [15] Hans Lüth. *Solid Surfaces, Interfaces and Thin Films*. Springer, 2010.
- [16] J. Wiebe et al. "From quantized states to percolation: Scanning tunneling spectroscopy of a strongly disordered two-dimensional electron system". In: *Physical Review B* 68 (2003), p. 041402.
- [17] M. Morgenstern et al. "Co on p-InAs(110): An island-induced two-dimensional electron system consisting of electron droplets". In: *Physical Review B* 65 (2002), p. 155325.

- [18] S. Becker et al. "Scanning tunneling spectroscopy of a dilute two-dimensional electron system exhibiting Rashba spin splitting". In: *Physical Review B* 81 (2010), p. 155308.
- [19] R. M. Feenstra and Stroscio J. A. "Tunneling spectroscopy of the GaAs (110) surface". In: *Journal of Vacuum Science & Technology B: Microelectronics and Nanometer Structures* 5 (1987), p. 923.
- [20] R. M. Feenstra. "Tunneling spectroscopy of the (110) surface of direct-gap III-V semiconductors". In: *Physical Review B* 50 (1994), p. 4561.
- [21] M. Morgenstern et al. "Scanning tunneling microscopy of two-dimensional semiconductors: spin properties and disorder". In: *Physica E: Low-dimensional Systems and Nanostructures* 44 (2012), p. 1795.
- [22] M. Morgenstern et al. "Direct Comparison between Potential Landscape and Local Density of States in a Disordered Two-Dimensional Electron System". In: *Physical Review Letters* 89 (2002), p. 136806.
- [23] S. Perraud et al. "Imaging the percolation of localized states in a multisubband two-dimensional electronic system subject to a disorder potential". In: *Physical Review B* 76 (2007), p. 195333.
- [24] Simon Perraud. "Etude de puits quantiques semiconducteurs par microscopie et spectroscopie à effet tunnel". PhD thesis. Université Pierre et Marie Curie, 2007.
- [25] K. S. Novoselov et al. "Electric Field Effect in Atomically Thin Carbon Films". In: *Science* 306 (2004), p. 666.
- [26] P. R. Wallace. "The Band Theory of Graphite". In: *Physical Review* 71 (1947), p. 622.
- [27] A. H. Castro Neto et al. "The electronic properties of graphene". In: *Reviews of Modern Physics* 81 (2009), p. 109.
- [28] Y. Zhang et al. "Experimental Observation of the Quantum Hall Effect and Berry's Phase in Graphene". In: *Nature* 438 (2005), p. 201.
- [29] K. S. Novoselov et al. "Two-Dimensional Gas of Massless Dirac Fermions in Graphene". In: *Nature* 438 (2005), p. 197.
- [30] G. Li, A. Luican, and E. Y. Andrei. "Scanning Tunneling Spectroscopy of Graphene on Graphite". In: *Physical Review Letters* 102 (2009), p. 176804.
- [31] G. L. Yu et al. "Interaction Phenomena in Graphene Seen through Quantum Capacitance". In: *Proceedings of the National Academy of Sciences* 110 (2013), p. 3282.
- [32] S. Z. Butler et al. "Progress, Challenges, and Opportunities in Two-Dimensional Materials Beyond Graphene". In: *ACS Nano* 7.4 (2013), p. 2898.
- [33] C.-H. Park and S. G. Louie. "Making Massless Dirac Fermions from a Patterned Two-Dimensional Electron Gas". In: *Nano Letters* 9 (2009), p. 1793.
- [34] E. Kalesaki et al. "Dirac Cones, Topological Edge States, and Nontrivial Flat Bands in Two-Dimensional Semiconductors with a Honeycomb Nanogeometry". In: *Physical Review X* 4 (2014), p. 011010.
- [35] S. Cahangirov et al. "Two- and One-Dimensional Honeycomb Structures of Silicon and Germanium". In: *Physical Review Letters* 102 (2009), p. 236804.
- [36] P. Vogt et al. "Silicene: Compelling Experimental Evidence for Graphenelike Two-Dimensional Silicon". In: *Physical Review Letters* 108 (2012), p. 155501.

- [37] M. Derivaz et al. "Continuous Germanene Layer on Al(111)". In: *Nano Letters* 15 (2015), p. 2510.
- [38] B. Aufray et al. "Graphene-like silicon nanoribbons on Ag(110): A possible formation of silicene". In: *Applied Physics Letters* 96 (2010), p. 183102.
- [39] M. Polini et al. "Artificial honeycomb lattices for electrons, atoms and photons". In: *Nature Nanotechnology* 8 (2013), p. 625.
- [40] A. Tadjine, G. Allan, and C. Delerue. "From lattice Hamiltonians to tunable band structures by lithographic design". In: *Physical Review B* 94 (2016), p. 075441.
- [41] K. K. Gomes et al. "Designer Dirac fermions and topological phases in molecular graphene". In: *Nature* 483 (2012), p. 306.
- [42] L. Tarruell et al. "Creating, moving and merging Dirac points with a Fermi gas in a tunable honeycomb lattice". In: *Nature* 483 (2012), p. 302.
- [43] S. Bittner et al. "Observation of a Dirac point in microwave experiments with a photonic crystal modeling graphene". In: *Physical Review B* 82 (2010), p. 014301.
- [44] J. J. Geuchies et al. "In Situ Study of the Formation Mechanism of Two-Dimensional Superlattices from PbSe Nanocrystals". In: *Nature Materials* 15 (2016), p. 1248.
- [45] M. P. Boneschanscher et al. "Long-range orientation and atomic attachment of nanocrystals in 2D honeycomb superlattices". In: *Science* 344 (2014), p. 1377.
- [46] V. Apaja, M. Hyrkäs, and M. Manninen. "Flat bands, Dirac cones, and atom dynamics in an optical lattice". In: *Physical Review A* 82 (2010), p. 041402.
- [47] H.-M. Guo and M. Franz. "Topological insulator on the kagome lattice". In: *Physical Review B* 80 (2009), p. 113102.
- [48] S. Mukherjee et al. "Observation of a Localized Flat-Band State in a Photonic Lieb Lattice". In: *Physical Review Letters* 114 (2015), p. 245504.
- [49] M. R. Slot et al. "Experimental realization and characterization of an electronic Lieb lattice". In: *Nature Physics* 13.7 (2017), p. 672.
- [50] Z. Li et al. "Realization of flat band with possible nontrivial topology in electronic Kagome lattice". In: *Science Advances* 4 (2018), p. 4511.
- [51] S. Melinte et al. "Laterally Modulated 2D Electron System in the Extreme Quantum Limit". In: *Physical Review Letters* 92 (2004), p. 036802.
- [52] G. De Simoni et al. "Delocalized-localized transition in a semiconductor two-dimensional honeycomb lattice". In: *Applied Physics Letters* 97 (2010), p. 132113.
- [53] A. Singha et al. "Two-Dimensional Mott-Hubbard Electrons in an Artificial Honeycomb Lattice". In: *Science* 332 (2011), p. 1176.
- [54] S. Wang et al. "Observation of Dirac bands in artificial graphene in small-Period nanopatterned GaAs quantum wells". In: *Nature Nanotechnology* 94 (2017), p. 29.
- [55] D. Scarabelli et al. "Fabrication of artificial graphene in a GaAs quantum heterostructure". In: *Journal of Vacuum Science Technology B* 33 (2015), p. 555.
- [56] Wang. "Observation of electron states of small period artificial graphene in nanopatterned GaAs quantum wells". In: *Applied Physics Letters* 109 (2016), p. 113101.
- [57] X. Wallart, B. Pinsard, and F. Mollot. "High-mobility InGaAs/InAlAs pseudomorphic heterostructure on InP (001)". In: *Journal of Applied Physics* 97 (2005), p. 053706.

- [58] L. Mo, E. Lind, and L.-E. Wernersson. "Asymmetric InGaAs/InP MOSFETs With Source/Drain Engineering". In: *IEEE Electron Device Letters* 35 (2014), p. 515.
- [59] J. Zhang et al. "Advances in InGaAs/InP single-photon detector systems for quantum communication". In: *Light: Science & Applications* 4 (2015), e286.
- [60] M. B. Panish et al. "Optical properties of very thin GaInAs(P)/InP quantum wells grown by gas source molecular beam epitaxy". In: *Applied Physics Letters* 49 (1986), p. 164.
- [61] M. S. Skolnick et al. "Investigation of InGaAs-InP quantum wells by optical spectroscopy". In: *Semiconductor Science and Technology* 1 (1986), p. 29.
- [62] M. G. Shorthose et al. "Optical studies of excitons in GaInAs/InP quantum wells grown by low-pressure metal-organic vapour-phase epitaxy". In: *Semiconductor Science and Technology* 3 (1988), p. 616.
- [63] U. Cebulla et al. "Excitonic lifetimes in thin  $\text{In}_x\text{Ga}_{1-x}\text{As}/\text{InP}$  quantum wells". In: *Physical Review B* 39 (1989), p. 6257.
- [64] C. H. Henry et al. "Radiative and nonradiative lifetimes in n-type and p-type  $1.6 \mu\text{m}$  InGaAs". In: *Electronic Letters* 20 (1984), p. 358.
- [65] E. H. Reihlen et al. "Photoluminescence study of carrier collection and recombination in thin GaInAs/InP single quantum wells". In: *Journal of Applied Physics* 66 (1989), p. 5554.
- [66] R. Chen, H. Y. Liu, and H. D. Sun. "Electronic energy levels and carrier dynamics in InAs/InGaAs dots-in-a-well structure investigated by optical spectroscopy". In: *Journal of Applied Physics* 107 (2010), p. 013513.
- [67] V. Lacatena et al. "Phononic engineering of silicon using "dots on the fly" e-beam lithography and plasma etching". In: *Microelectronic Engineering* 121 (2014), p. 131.
- [68] F. S. Bates and G. H. Fredrickson. "Block Copolymers - Designer Soft Materials". In: *Physics Today* 32 (1999), p. 131.
- [69] S. Perraud, K. Kanisawa, and Y. Wang Z.-Z. and Hirayama. "Unpinning of the Fermi Level at (111)A clean surfaces of epitaxially grown n-type  $\text{In}_{0.53}\text{Ga}_{0.47}\text{As}$ ". In: *Applied Physics Letters* 89 (2006), p. 192110.
- [70] M. D. Pashley et al. "Different Fermi-level pinning behavior on n- and p-type GaAs(001)". In: *Physical Review B* 48 (1993), p. 4612.
- [71] M.A. Herman and H. Sitter. *Molecular Beam Epitaxy*. Springer, 1996.
- [72] W. Patrick McCray. "MBE Deserves a Place in the History Books". In: *Nature Nanotechnology* 2 (2007), p. 259.
- [73] J. A. Bittencourt. *Fundamentals of Plasma Physics*. Springer, 2004.
- [74] A. N. Broers, A. C. F. Hoole, and J. M. Ryan. "Electron beam lithography - Resolution limits". In: *Microelectronic Engineering* 32 (1996), p. 131.
- [75] A. N. Broers. "Resolution limits for electron-beam lithography". In: *IBM Journal of Research and Development* 32 (1988), p. 502.
- [76] I A Morozov et al. "Effect of temperature on dry etching of III-V structures". In: *Journal of Physics: Conference Series* 1124 (2008), p. 041031.
- [77] Nojiri Kazuo. *Dry Etching Technology for Semiconductors*. Springer, 2015.
- [78] T. Maeda et al. "Inductively coupled plasma etching of III-V semiconductors in  $\text{BCl}_3$ -based chemistries: II. InP, InGaAs, InGaAsP, InAs and AlInAs". In: *Applied Surface Science* 143 (1999), p. 183.

- [79] G. Binnig et al. "Surface Studies by Scanning Tunneling Microscopy". In: *Physical Review Letters* 49 (1987), p. 57.
- [80] G. Binnig and H. Rohrer. "Scanning tunneling microscopy-from birth to adolescence". In: *Reviews of Modern Physics* 59 (1987), p. 615.
- [81] J. Tersoff and D. R. Hamann. "Theory of the scanning tunneling microscope". In: *Physical Review B* 31 (1985), p. 805.
- [82] R. M. Feenstra, Stroscio J. A., and Fein A. P. "Tunneling spectroscopy of the Si (111) 2x1 surface". In: *Surface Science* 181 (1987), p. 295.
- [83] Maxime Berthe. "Electronic transport in quantum connected systems". PhD thesis. Université des Sciences et Technologies de Lille, 2007.
- [84] J. Klein et al. "Inelastic-Electron-Tunneling Spectroscopy of Metal-Insulator-Metal Junctions". In: *Physical Review B* 7 (1973), p. 2336.
- [85] I. Miccoli et al. "The 100th anniversary of the four-point probe technique: the role of probe geometries in isotropic and anisotropic systems". In: *Journal of Physics: Condensed Matter* 27 (2015), p. 223201.
- [86] G. Hoffmann, J. Kröger, and R. Berndt. "Color imaging with a low temperature scanning tunneling microscope". In: *Review of Scientific Instruments* 73 (2002), p. 305.
- [87] Weilie Zhou and Zhong Lin Wang. *Scanning Microscopy for Nanotechnology*. Springer, 2006.
- [88] G. Binnig, C. F. Quate, and C. Gerber. "Atomic Force Microscope". In: *Physical Review Letters* 56 (1986), p. 930.
- [89] Greg Haugstad. *Atomic Force Microscopy: Understanding Basic Modes and Advanced Applications*. Wiley, 2012.
- [90] Y. Gan. "Atomic and subnanometer resolution in ambient conditions by atomic force microscopy". In: *Surface Science Reports* 64 (2009), p. 99.
- [91] S. Kasai, N. Negoro, and H. Hasegawa. "Conductance gap anomaly in scanning tunneling spectra of MBE-Grown (001) surfaces of III-V compound semiconductors". In: *Applied Surface Science* 175-176 (2001), p. 255.
- [92] W. Melitz et al. "Scanning tunneling spectroscopy and Kelvin probe force microscopy investigation of Fermi energy level pinning mechanism on InAs and InGaAs clean surfaces". In: *Journal of Applied Physics* 108 (2010), p. 023711.
- [93] L. Ö. Olsson et al. "Charge Accumulation at InAs Surfaces". In: *Physical Review Letters* 76 (1996), p. 3626.
- [94] M. D. Pashley and K. W. Haberern. "Compensating surface defects induced by Si doping of GaAs". In: *Physical Review Letters* 67 (1991), p. 2697.
- [95] S. Perraud, Z.-Z. Kanisawa K. and Wang, and Y. Hirayama. "Dramatic dependence of the Fermi level pinning strength on crystal orientation at clean surfaces of n-type  $\text{In}_{0.53}\text{Ga}_{0.47}\text{As}$  grown by molecular beam epitaxy". In: *Journal of Crystal Growth* 301-302 (2007), p. 148.
- [96] C. D. Yerino et al. "Review Article: Molecular beam epitaxy of lattice-matched InAlAs and InGaAs layers on InP (111)A, (111)B, and (110)". In: *Journal of Vacuum Science & Technology B* 35 (2017), p. 010801.



- [97] W. Melitz et al. "InGaAs surface preparation for atomic layer deposition by hydrogen cleaning and improvement with high temperature anneal". In: *Journal of Applied Physics* 110 (2011), p. 013713.
- [98] W. Melitz et al. "Atomic imaging of atomic layer deposition oxide nucleation with trimethylaluminum on As-rich InGaAs (001) 2x4 vs Ga/In-rich InGaAs (001) 4x2". In: *The Journal of Chemical Physics* 136 (2012), p. 154706.
- [99] S. Koumetz et al. "Be diffusion mechanisms in InGaAs during post-growth annealing". In: *Applied Physics Letters* 67 (1995), p. 2161.
- [100] J. Shena et al. "Real Space Surface Reconstructions of Decapped As-rich  $\text{In}_{0.53}\text{Ga}_{0.47}\text{As}$  (001)-(2x4)". In: *Journal of solid state science and technology* 16 (1998), p. 463.
- [101] K. W. Carey et al. "Structural and photoluminescent properties of GaInAs quantum wells with InP barriers grown by organometallic vapor phase epitaxy". In: *Applied Physics Letters* 51 (1987), p. 910.
- [102] R. M. Feenstra. "Electrostatic potential for a hyperbolic probe tip near a semiconductor". In: *Journal of Vacuum Science & Technology B: Microelectronics and Nanometer Structures* 21 (2003), p. 2080.
- [103] L. C. Post et al. "Triangular nanoporation and band engineering of InGaAs quantum wells: a lithographic route toward Dirac cones in III-V semiconductors". In: *Nanotechnology* 30 (2019), p. 155301.
- [104] I. Vurgaftman, J. R. Meyer, and L. R. Ram-Mohan. "Band parameters for III-V compound semiconductors and their alloys". In: *Journal of Applied Physics* 89.11 (2001), p. 5815.
- [105] P. E. Smith et al. "Atomic diffusion and band lineups at  $\text{In}_{0.53}\text{Ga}_{0.47}\text{As}$ -on-InP heterointerfaces". In: *Journal of Vacuum Science & Technology B: Microelectronics and Nanometer Structures Processing, Measurement, and Phenomena* 23.4 (2005), p. 1832.
- [106] P. C. Zalm. "Ultra shallow doping profiling with SIMS". In: *Reports on Progress in Physics* 58 (1995), p. 1321.
- [107] E. G. Scott et al. "Beryllium diffusion in GaInAs grown by molecular beam epitaxy". In: *Journal of Applied Physics* 66 (1989), p. 5344.
- [108] M.B. Panish et al. "Redistribution of beryllium in InP and  $\text{Ga}_{0.47}\text{In}_{0.53}\text{As}$  grown by hydride source molecular beam epitaxy and metalorganic molecular beam epitaxy". In: *Surface Science* 112 (1991), p. 343.
- [109] E. Perkins et al. "Surface-sensitive conductivity measurement using a micro multi-point probe approach". In: *Review of Scientific Instruments* 84 (2013), p. 033901.
- [110] I. Shiraki et al. "Independently driven four-tip probes for conductivity measurements in ultrahigh vacuum". In: *Surface Science* 493 (2001), p. 633.
- [111] S. Godey et al. "CBr<sub>4</sub> and Be heavily doped InGaAs grown in a production MBE system". In: *Journal of Crystal Growth* 278 (2005), p. 600.
- [112] S. Just et al. "Surface conductivity of Si(100) and Ge(100) surfaces determined from four-point transport measurements using an analytical N-layer conductance model". In: *Physical Review B* 95 (2017), p. 075310.
- [113] R. Dombrowski et al. "Tip-induced band bending by scanning tunneling spectroscopy of the states of the tip-induced quantum dot on InAs(110)". In: *Physical Review B* 59 (1999), p. 8043.

- [114] V. Swaminathan, V. M. Donnelly, and J. Long. "A photoluminescence study of Cd-related centers in InP". In: *Journal of Applied Physics* 58 (1985), p. 4565.
- [115] E. W. Williams et al. "Indium Phosphide". In: *Journal of the Electrochemical Society* 120 (1973), p. 1741.
- [116] L. Biadala et al. "Trap-Free Heterostructure of PbS Nanoplatelets on InP(001) by Chemical Epitaxy". In: *ACS Nano* 13 (2019), p. 1961.
- [117] M. Youngboon et al. "Low temperature photoluminescence characteristics of Zn-doped InP grown by metalorganic chemical vapor deposition". In: *Journal of Applied Physics* 83 (1993), p. 12261.
- [118] M. Kemerink et al. "Spectrally resolved luminescence from an InGaAs quantum well induced by an ambient scanning tunneling microscope". In: *Applied Physics Letters* 75 (1999), p. 3656.
- [119] R. Driad et al. "Passivation of InGaAs surfaces and InGaAs/InP heterojunction bipolar transistors by sulfur treatment". In: *Applied Physics Letters* 73 (1998), p. 665.
- [120] M. J. Milla, J. M. Ulloa, and A. Guzmán. "High optical sensitivity to ambient conditions of uncapped InGaAs surface quantum dots". In: *Applied Physics Letters* 100 (2012), p. 131601.



# List of publications



A. Díaz Álvarez, N. Peric, **N. A. Franchina Vergel**, J.-P. Nys, M. Berthe, G. Patriarche, J.-C. Harmand, P. Caroff, S. Plissard, P. Ebert, T. Xu, B. Grandidier, *Importance of point defect reactions for the atomic-scale roughness of III-V nanowire sidewalls*, *Nanotechnology* 30, 324002 (2019).

L.C. Post, T. Xu, **N. A. Franchina Vergel**, A. Tadjine, Y. Lambert, F. Vaurette, D. Yarekha, L. Desplanque, D. Stiévenard, X. Wallart, B. Grandidier, C. Delerue, D. Vanmaekelbergh, *Triangular nanoperforation and band engineering of InGaAs quantum wells: a lithographic route toward Dirac cones in III-V semiconductors*, *Nanotechnology* 30, 155301 (2019).

**N. A. Franchina Vergel**, A. Tadjine, V. Notot, M. Mohr, A. Kouassi N'Guissan, C. Coinon, M. Berthe, L. Baidala, K. K. Sossoe, M. M. Dzagli, J.-C. Girard, G. Rodary, L. Desplanque, R. Berndt, D. Stiévenard, X. Wallart, C. Delerue, B. Grandidier, *Influence of doping level and surface states in tunneling spectroscopy of an  $In_{0.53}Ga_{0.47}As$  quantum well grown on p-type doped InP(001)*, *Physical Review Materials*, 3, 094604 (2019).



# Importance of point defect reactions for the atomic-scale roughness of III–V nanowire sidewalls

Adrian Díaz Álvarez<sup>1,5</sup>, Nemanja Peric<sup>1</sup>,  
Nathali Alexandra Franchina Vergel<sup>1</sup>, Jean-Philippe Nys<sup>1</sup>, Maxime Berthe<sup>1</sup>,  
Gilles Patriarche<sup>2</sup>, Jean-Christophe Harmand<sup>2</sup>, Philippe Caroff<sup>1,6</sup>,  
Sébastien Plissard<sup>1,7</sup> , Philipp Ebert<sup>3</sup>, Tao Xu<sup>1,4</sup> and Bruno Grandidier<sup>1</sup> 

<sup>1</sup> Univ. Lille, CNRS, Centrale Lille, ISEN, Univ. Valenciennes, UMR 8520—IEMN, F-59000 Lille, France

<sup>2</sup> Centre de Nanosciences et de Nanotechnologies (C2N), UMR 9001 CNRS, University Paris Sud, University Paris-Saclay, avenue de la Vauve, F-91120 Palaiseau, France

<sup>3</sup> Peter Grünberg Institut, Forschungszentrum Jülich GmbH, D-52425 Jülich, Germany

<sup>4</sup> Key Laboratory of Advanced Display and System Application, Shanghai University, Shanghai 200072, People's Republic of China

E-mail: [xtld@shu.edu.cn](mailto:xtld@shu.edu.cn) and [bruno.grandidier@isen.iemn.univ-lille1.fr](mailto:bruno.grandidier@isen.iemn.univ-lille1.fr)

Received 23 January 2019, revised 29 March 2019

Accepted for publication 17 April 2019

Published 13 May 2019



CrossMark

## Abstract

The surface morphology of III–V semiconductor nanowires (NWs) protected by an arsenic cap and subsequently evaporated in ultrahigh vacuum is investigated with scanning tunneling microscopy and scanning transmission electron microscopy. We show that the changes of the surface morphology as a function of the NW composition and the nature of the seed particles are intimately related to the formation and reaction of surface point defects. Langmuir evaporation close to the congruent evaporation temperature causes the formation of vacancies which nucleate and form vacancy islands on {110} sidewalls of self-catalyzed InAs NWs. However, for annealing temperatures much smaller than the congruent temperature, a new phenomenon occurs: group III vacancies form and are filled by excess As atoms, leading to surface As<sub>Ga</sub> antisites. The resulting Ga adatoms nucleate with excess As atoms at the NW edges, producing monoatomic-step islands on the {110} sidewalls of GaAs NWs. Finally, when gold atoms diffuse from the seed particle onto the {110} sidewalls during evaporation of the protective As cap, Langmuir evaporation does not take place, leaving the sidewalls of InAsSb NWs atomically flat.

Keywords: III–V semiconductor nanowires, {110} sidewall, surface morphology, roughness, point defect, scanning tunneling microscopy

(Some figures may appear in colour only in the online journal)

## 1. Introduction

Compound semiconductor nanowires (NWs) have attracted wide interest for optoelectronic and photovoltaic applications, due to their unique ability to relax strain and hence enabling the realization of a much wider range of non-lattice matched heterostructures and polytypes than in planar growth. Numerous examples of heterogeneous integrations have been demonstrated, either axially with III–V NWs directly grown

<sup>5</sup> Present address: International Center for Materials Nanoarchitectonics, National Institute for Materials Science, Tsukuba, Ibaraki 305-0044, Japan.

<sup>6</sup> Present address: Microsoft Quantum Lab Delft, Delft University of Technology, 2600 GA Delft, The Netherlands.

<sup>7</sup> Present address: CNRS-Laboratoire d'Analyse et d'Architecture des Systèmes (LAAS), Univ. de Toulouse, 7 Avenue du Colonel Roche, F-31400 Toulouse, France.



on Si substrates [1, 2] or radially with semiconductor–semiconductor, semiconductor–ferroelectric and semiconductor metal core–shell NWs [3–6]. However, the quality of the interface, in particular in the radial configuration, where the surface to volume ratio is high, critically affects the NW properties. Hence, controlling the surface morphology and chemistry of NWs is becoming of utmost importance for tuning manifold NW properties, not only for the growth of core–shell structures, but also to prepare NWs with strong confinement effects [7] or enhanced luminescence [8].

Indeed, apparently small surface effects can have a strong impact on the physical properties of semiconductor heterostructures. For example, a pronounced roughness of the sidewall facets will reduce the sharpness of radial interfaces and increase the scattering of electrons and phonons, influencing their propagation. Also, surface steps induce a Fermi-level pinning at the NW sidewall facets, which modifies the band offsets between different axially arranged polytypes or heteromaterials [9, 10], hence influencing greatly the axial electrical conductivity and optical emission of NWs. Moreover, this pinning governs the incorporation of defects and isoelectronic impurities during lateral overgrowth, affecting the electronic properties of core–shell heterostructures.

These effects are likely to occur when the growth processes require the evaporation of chemical elements that take place in separate growth systems, implying stringent conditions to preserve the interfacial layer from contamination accumulated during the sample transfer [11]. For III–V semiconductor NWs, a smart protection scheme relies on the use of a thin arsenic amorphous layer to cap the NW sidewalls [12, 13], that can then be easily sublimated once the sample has been transferred in a different growth system. However, it is still not clear how the protective cap affects the morphology of the NW sidewalls. This is even more important in the light of very different surface morphologies observed by scanning tunneling microscopy, ranging from very rough to atomically smooth facets [14], but without good understanding thus far.

In this work, we examine clean and well-ordered (110) sidewalls of III–V semiconductor NWs with scanning tunneling microscopy (STM) and spectroscopy (STS) after the sublimation of an As protective cap. We find pronounced differences in the morphology and roughness of NW sidewalls of different III–V compounds. The morphologies are shown to correlate with point defect formation and reaction processes during the sublimation of the As protective cap. These point defect-based processes lead to sidewall morphologies characterized by nucleated islands, vacancy clusters, atomically smooth sidewalls, as well as to highly off-stoichiometric or perfectly stoichiometric surfaces depending on annealing and Fermi-level position at the NW surface.

## 2. Methods

For the experiments, InAs, GaAs and InAs<sub>1-x</sub>Sb<sub>x</sub> NWs were synthesized by molecular beam epitaxy with seed particles to drive the NW growth in the vapor–liquid–solid regime. In and

Ga droplets were used for the growth of self-catalyzed InAs and GaAs NWs on [111]-oriented Si substrates covered with a native oxide layer at the surface. As described in [15], optimized conditions with oxide thickness of 0.9 nm were chosen to obtain the highest yield of vertical growth. The growth of InAs NWs was done at 0.02 monolayer per second, given as equivalent to the growth rate on planar GaAs, with an As<sub>4</sub> partial pressure of  $3.6 \times 10^{-7}$  mbar, an In partial pressure of  $4.1 \times 10^{-8}$  mbar and a temperature of 420 °C. The growth of GaAs NWs was carried out at a nominal growth rate of  $0.3 \text{ \AA s}^{-1}$ , with an As<sub>4</sub> partial pressure of  $2.5 \times 10^{-6}$  mbar, a Ga partial pressure of  $1.4 \times 10^{-7}$  mbar and a temperature of 620 °C. At the end of the growth, the In and Ga droplets were consumed by closing the In or Ga shutter for 30 min under As<sub>4</sub> flux. Then, the As<sub>4</sub> flux was stopped, what reduced the As-related pressure substantially, and the temperature was lowered to room temperature. At room temperature, the As<sub>4</sub> flux was opened again and the NWs were capped with a 10–20 nm thick amorphous As layer for protection against air exposure (oxidation). A high yield of vertical NWs grown along the  $\langle 111 \rangle$  direction was obtained, with a diameter distribution between 60 and 90 nm [16]. InAs<sub>1-x</sub>Sb<sub>x</sub> NWs and GaAs NWs were also grown with gold seed particles, as thoroughly described in [12] and [17]. The capping procedure was similar except that the gold seed particle was left at the end of the growth and embedded in the As capping layer.

After the growth, the NWs were investigated with a Jeol 2200 FS scanning transmission electron microscope (STEM) operating at 200 keV and with a low-temperature scanning tunneling microscope working at 77 K in ultrahigh vacuum (UHV). The STEM analysis required to work with cleaved and dispersed NWs in toluene that were dropcasted onto E-chip supports (Protochips). The annealing of the NWs to sublimate the As-capping layer was performed *in situ* and the temperature of the E-chip in the STEM was measured with a thermocouple. For the STM characterization, the sublimation process was performed in the preparation chamber connected to a low-temperature scanning tunneling microscope with a base pressure lower than  $10^{-10}$  mbar. The substrate that was used to grow the NWs was annealed by direct current heating. The As desorption was monitored by mass spectrometry and the temperature of the sample was probed with a pyrometer, yielding an uncertainty of  $\pm 10$  °C on the substrate temperature. While the pressure increased around  $2\text{--}5 \times 10^{-10}$  mbar for a few tens of seconds and then decreased, we usually kept the sample heating for 30 min. At the end of this process, the NWs were transferred to a *n*-type Si(111) substrate coated with a thin layer of Ag. The transfer was performed by mechanical cleavage of the NWs without interruption of UHV [18], to have one of the sidewalls parallel to the host substrate and accessible to the tungsten STM tip. For the STM study, we did not consider the base or the top region of the NWs, since the morphology of these regions can be different from the rest of the NWs. Tunneling spectroscopic curves were acquired with an open feedback loop at constant tip-sample separation.

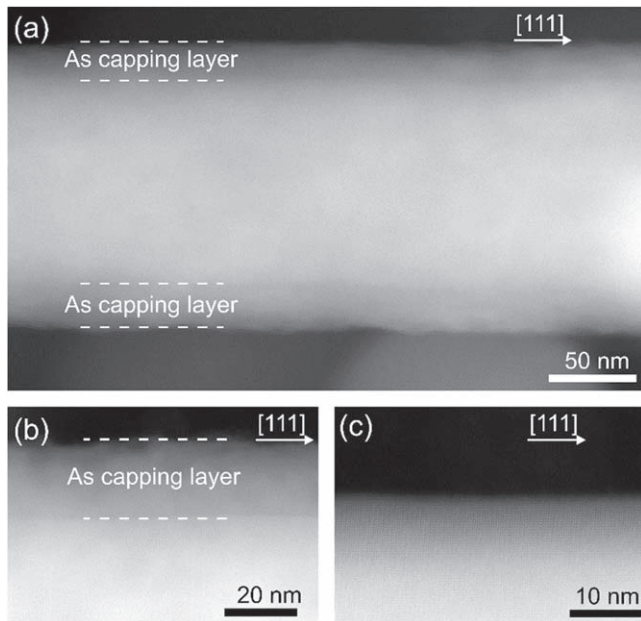


**Figure 1.** (a) STEM image of a self-catalyzed GaAs NW capped with a thin protective layer of amorphous As. (b) and (c) TEM images of the same GaAs NW after the annealing of the sample at 250 °C for 10 min and then 270 °C for 10 min. At 250 °C, the amorphous As cap is still present and blurs the NW's atomic structure (b). In contrast, at 270 °C the As cap evaporated fully (c), revealing the underlying atomic structure of the NW.

### 3. Results

In order to determine the range of temperatures that enable the complete sublimation of the As protective cap, temperature-dependent STEM experiments were first performed with self-catalyzed GaAs NWs. Figure 1(a) shows a typical STEM image of such a GaAs NW capped by an amorphous As capping layer. The capping layer is identified from its slightly darker contrast in the upper and lower parts of the NW in comparison with the GaAs core. The thickness of the capping layer is 20 nm. Heating the NW at 250 °C for 10 min does not produce any significant modification of the protective cap (figure 1(b)). Further annealing at 270 °C for 10 min leads to the disappearance of the dark As shell and the appearance of the NW atomic lattice in the STEM image, as shown in figure 1(c). Both observations indicate the sublimation of the protecting As cap. However, annealing at this temperature was found to leave a lot of defective areas in the STM images of the NWs sidewalls. Therefore, for the subsequent STM analyses, the As capping layer was always sublimated above 310 °C–320 °C and below 370 °C–380 °C. The upper limit corresponds to the congruent evaporation temperature of InAs [19].

Figure 2 shows an overview of STM images for three different III–V NWs after the sublimation of the As-capping layer at the maximum temperature of 370 °C–380 °C allowed for this study. The morphologies of the sidewalls for the NWs appear different, despite the same  $\langle 110 \rangle$  orientation of the sidewalls and similar conditions to sublimate the capping layer. First, the InAs and GaAs NWs have straight sidewalls

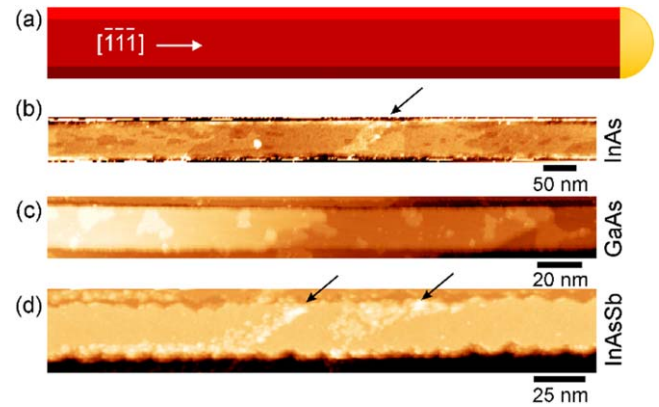


**Figure 2.** STM images of the  $\{110\}$  sidewall of (a) an In-catalyzed InAs NW, (b) a Ga-catalyzed GaAs NW and (c) a Au-catalyzed InAs<sub>0.9</sub>Sb<sub>0.1</sub> NW obtained after the sublimation of the As capping layer at 370 °C–380 °C, tunneling conditions: (a)  $V_{\text{sample}} = +3.0 \text{ V} / I_{\text{tunneling}} = 10 \text{ pA}$ , (b)  $V_{\text{sample}} = -4.0 \text{ V} / I_{\text{tunneling}} = 20 \text{ pA}$ , (c)  $V_{\text{sample}} = -3.0 \text{ V} / I_{\text{tunneling}} = 10 \text{ pA}$ . The arrows point to defective areas.

while the InAs<sub>1-x</sub>Sb<sub>x</sub> NW appear with sawtooth-like sidewalls. This difference has been explained by the epitaxial overgrowth of the sidewalls [20].  $\langle 111 \rangle$ -oriented NWs have initially twelve alternating  $\{110\}$  and  $\{112\}$  sidewalls. However, if overgrowth takes place, the grooves induced by the  $\{111\}$ -A and B-type facets in the  $\{112\}$  planes, which give rise to the sawtooth-like shape, are filled in and the  $\{112\}$  planes becomes narrower. As a result, the  $\{110\}$  sidewalls almost connect with each other giving rise to straight edges along the growth axis.

More importantly for this study, we compare the roughness of the  $\{110\}$  sidewalls. The InAs NW sidewall consists of propagating terraces along the growth direction, with pits sparsely distributed into the terraces (figure 2(b)). We note the presence of a small defective area, which is presumably a damaged region that might affect the complete removal of the As capping layer in its vicinity. The GaAs NW sidewalls exhibit terraces also. But opposite to the pits observed on the InAs NW sidewalls, islands appear on top of these terraces (figure 2(c)). Interestingly, the majority of the islands are connected to the sidewall and terrace edges, whereas the pits seem to be randomly distributed on a terrace. In contrast to the InAs and GaAs NWs, the InAs<sub>1-x</sub>Sb<sub>x</sub> NW sidewall is atomically flat, except in two small defective areas (figure 2(d)). While the absence of terraces might be related to the limited duration of the lateral overgrowth process as compared with the InAs and GaAs NWs, this third example shows that the  $\{110\}$  sidewalls can also exist without any pits or islands.

In order to get further insight into the origin of the formation of these clusters and islands, figure 3 highlights the height profiles measured on the sidewalls of the self-catalyzed InAs and GaAs NWs. At the surface of the InAs NW, the pits have a depth of about 2 Å, whereas the islands that are found on the GaAs NWs show a height of 2 Å. These heights correspond to the separation of single atomic (110) planes in

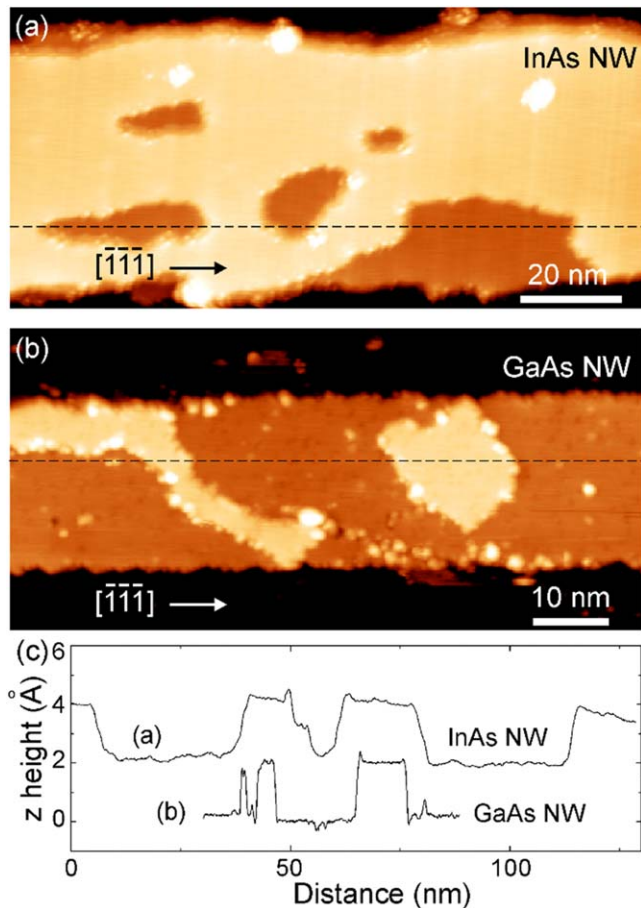


**Figure 3.** STM images of the {110} sidewall of self-catalyzed (a) InAs and (b) GaAs NWs after the removal of the As capping layer at 370 °C–380 °C. (c) Height profiles measured along the horizontal lines in (a) and (b). Tunneling conditions:  $V_{\text{sample}} = +2.0$  V (a)/ $-3.5$  V (b),  $I_{\text{tunneling}} = 20$  pA. Vacancy islands are found to form on InAs NW sidewalls, whereas islands nucleate on GaAs NW sidewall at edges.

InAs and GaAs crystals, meaning that single-layer vacancy clusters or islands with monoatomic step height were formed.

In order to get further insight into the origin of the formation of these clusters and islands, we examined surfaces of III–V semiconductor bulk crystals. Figures 4(a)–(c) shows atomically flat (110) surfaces of a cleaved *p*-type InP crystal, a cleaved *p*-type GaAs crystal and a cleaved *n*-type GaAs crystal respectively. All three crystals show single vacancies, but depending on the doping of the crystals, the nature of the vacancies is different. Group V vacancies are observed in the filled state images of figures 4(a) and (b), while Ga (group III) vacancies are visible in the unoccupied state image of figure 4(c), consistent with previous studies [21–23]. We note that the STM image of the *p*-type InP surface was acquired after sample annealing at 205 °C for 42 h in UHV. Upon further annealing at 300 °C for 6 h, the *p*-type InP surface shows the formation of pits (figure 4(d)), similar to those produced upon exposure to electrons, photons or ions [24–26].

For surfaces initially covered with a thin As capping layer and then annealed to desorb the capping layer, such as

the InAs (001) surface in figure 4(e) and the GaAs (110) surface in figure 4(f), the same pits are also found. Once the amorphous capping layer has been desorbed, desorption of atoms from the crystal occurs and gives rise to the holey surface seen on the InAs NW sidewalls. The surface morphology is fully consistent with the formation of vacancy clusters resulting from stoichiometric Langmuir evaporation of group III and group V elements. Both elements leave the surface at equal fluxes because the annealing temperature is lower than the congruent temperature [27].

In contrast, the GaAs NW sidewalls do not show a pit-dominated morphology, but rather an island morphology. Understanding this requires a deeper examination of the possible presence of defects on the GaAs NW sidewalls. The atomically resolved STM image of figure 5(a) corresponds to a filled state image and shows rows of As atoms on the {110} sidewall of the NW. Interestingly, atomically confined protrusions at Ga lattice sites are seen between the As rows. Counting their number yields a surface density of protrusions of  $4 \times 10^{13} \text{ cm}^{-2}$ . These defects do not cause a change of contrast in their surroundings and can be found next to each other in the same row, suggesting that they are uncharged. We anticipate that the protrusions correspond to As atoms substituted to Ga atoms. This is supported by their comparison with the STM image of an  $\text{As}_{\text{Ga}}$  antisite defect in the surface layer simulated with density functional calculations of the integrated filled local density of states [28]. As we do not observe any contrast associated with subsurface  $\text{As}_{\text{Ga}}$  antisite defects as found previously in low-temperature grown GaAs planar layers as well as GaAs NWs [29–31], our result suggests that the antisites are exclusively formed at the GaAs surface during the post-growth decapping process.

An additional insight into the post-growth mechanism is provided by the statistical analysis of the one-monolayer-height islands. The Abbott curve calculated with the STM image shown in the inset of figure 5(c) reveals that 18% of the sidewall is covered with islands. As the cation concentration at the GaAs (110) surface is  $2.2 \times 10^{14} \text{ cm}^{-2}$ , it means that  $4 \times 10^{13} \text{ cm}^{-2}$  Ga atoms are necessary to form these islands. This quantity corresponds exactly to the Ga atoms substituted by the  $\text{As}_{\text{Ga}}$  antisites.

#### 4. Discussion

In order to explain the different morphologies obtained for the InAs NWs and the GaAs NWs despite identical post-growth treatments, we recall that the morphology is governed by the atomic processes occurring during the annealing procedure used to desorb the As cap from the NWs. These atomic processes are intimately related to point defects at the sidewall surfaces. It is well known that the types of point defects formed on III–V (110) surfaces are highly sensitive to the position of the Fermi level [32–34]. Since the formation process of point defects during desorption is a kinetically limited process, we cannot base the discussion on equilibrium energies of point defects, but rather need to consider the formation barriers. Experimentally it has been shown that



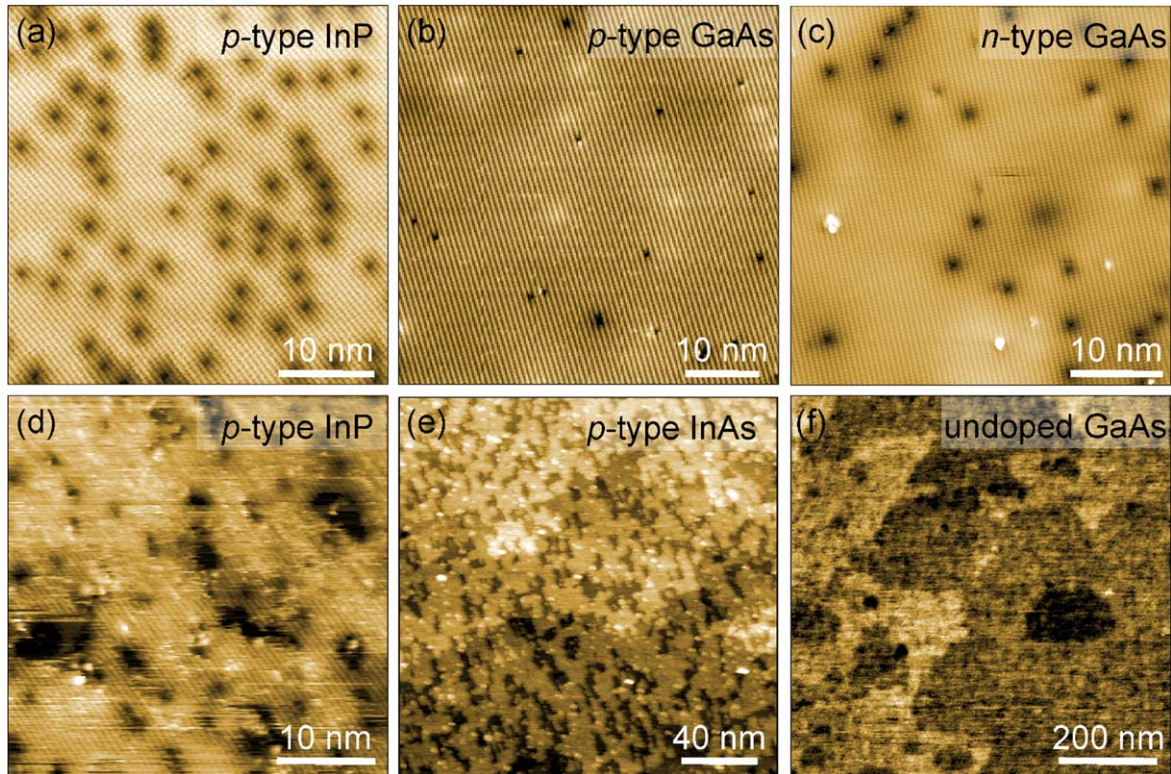


**Figure 4.** STM images of (a) a *p*-type InP(110) crystal annealed at 200 °C for 42 h in UHV, (b) a *p*-type GaAs (110) crystal, (c) a *n*-type GaAs (110) surface, (d) a *p*-type InP (110) surface annealed at 300 °C for 6 h in UHV, (e) a *p*-type InAs(001) crystal, initially capped with As and annealed at 400 °C for 2 h, (f) an undoped GaAs (110) crystal initially capped with As and annealed at 450 °C for 4 h in UHV. Tunneling conditions:  $V_{\text{sample}} = -2.7$  V (a),  $-2.6$  V (b),  $+1.2$  V (c),  $-2.8$  V (d),  $+1.5$  V (e),  $+2.0$  V (b);  $I_{\text{tunneling}} = 800$  pA (a), 600 pA (b), 300 pA (c), 600 pA (d), 10 pA (e), 10 pA.

negatively charged group III (positively charged group V) vacancies form kinetically on *n*-type (*p*-type) surfaces even at room temperature [21–23]. No other point defect, such as antisite or adatom, is experimentally found to form thermally in significant concentrations on (110) surfaces. This is confirmed by the defects visible in figures 4(a) and (c).

Therefore, we performed tunneling spectroscopy measurements on sidewalls of the self-catalyzed InAs and GaAs NWs in order to determine the electrical nature of the sidewalls. For the GaAs NWs, the band edges are clearly resolved in figure 6: at negative (positive) sample voltages, the branches of the current correspond to a tunneling out of (into) the valence (conduction) band states. The Fermi level position, measured at 0 V, is found midgap, 0.75 eV above the valence band edge, in agreement with a previous study which attributed this position to a pinning induced by the surface steps [9]. For the InAs NWs, three regions of tunneling current are also observed. In this case, the central component turning on at 0 V and extending to negative voltages is not equal to zero. This component arises from electrons tunneling out of the partially occupied conduction band, due to a pinning slightly above the conduction band minimum. This Fermi level position within the conduction band is in agreement with measurements performed on the planar InAs(110) surface [35] and InAs NW sidewall [36]. It is caused by the formation of an electron accumulation layer near the NW sidewalls, giving a *n*-type character to the sidewall.

On this basis, one can explain the atomic processes on the (110) InAs sidewall facet: during the post-growth annealing, the amorphous As cap is progressively removed. Once crystalline (110) facets become uncovered, In vacancies form. Since the annealing temperature of 380 °C is close enough to the InAs congruent sublimation temperature of 387 °C [19], the In adatoms desorb and leave behind negatively charged In vacancies [32], with weakly bonded neighboring As atoms. These neighboring As atoms can detach and form As adatoms, which desorb by forming  $\text{As}_2$  molecules [21]. As a result, uncharged divacancies form, which, due to the lack of repulsive Coulomb interactions, migrate and agglomerate to form pits of one monolayer depth on the whole sidewall of the InAs NW. The fact that the majority of the pits do not touch the sidewall edges indicates that their nucleation occurs randomly on the sidewall facets. Note that during these processes no charging of the surface by point defects occur. Similar effects can be expected to occur when the oxidized sidewalls of InAs NWs are cleaned with atomic hydrogen at 370 °C. Indeed the morphology observed on such prepared InAs NW sidewall facets is also dominated by holes of one monolayer depth elongated along the [111] direction [37]. It should be noted that the fraction of holes on the sidewall facet is essentially determined by the annealing time, the longer the more holes.

For the GaAs NWs an analogous effect may occur: as soon as the stoichiometric GaAs surface becomes uncovered

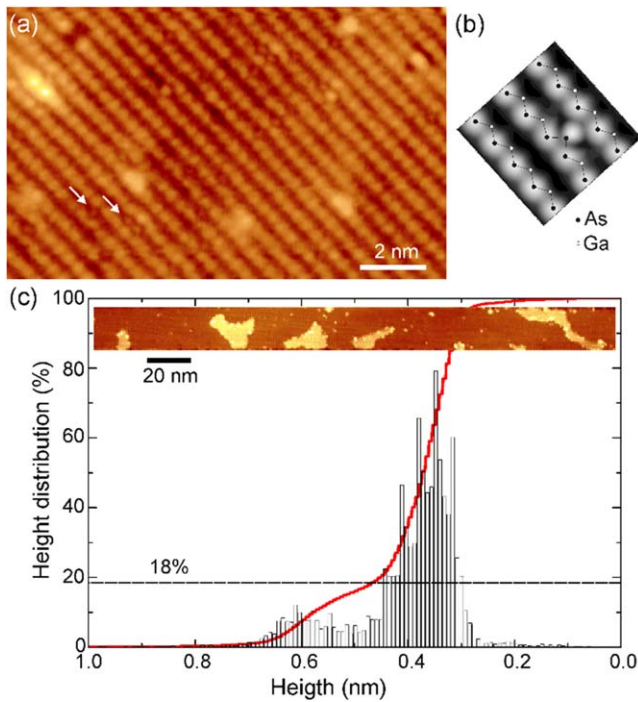


**Figure 5.** (a) Atomic scale STM image of the {110} sidewall of a Ga-catalyzed GaAs NW. Tunneling conditions:  $V_{\text{sample}} = -3.5$  V,  $I_{\text{tunneling}} = 20$  pA. The arrows point to protrusions at Ga lattice sites that correspond to a single surface  $\text{As}_{\text{Ga}}$  antisite and a pair of surface  $\text{As}_{\text{Ga}}$  antisites. (b) Calculated filled state STM image of the GaAs {110} surface including states over an energy range of 0.7 eV below the top of the valence band reproduced from [28] (c) height distribution and Abbott curve obtained for the {110} sidewall of the GaAs NW shown in the inset (tunneling conditions:  $V_{\text{sample}} = -4.0$  V,  $I_{\text{tunneling}} = 20$  pA). The horizontal dashed line indicates the fraction of the total area that corresponds to the bright islands seen in the STM image of the inset.

during As decapping, negatively charged Ga vacancies form for undoped and  $n$ -type materials [22, 38]. However, in contrast to InAs, the annealing temperature used to desorb the As capping layer is much lower than the congruent sublimation temperature of GaAs [7, 27, 39], preventing the Ga adatoms to desorb. As a result, for the following discussion, we need to take into account the presence of negatively charged Ga vacancies and Ga adatoms combined with high concentrations of As adatoms originating from the amorphous As cap. Their joint presence inevitably leads to point defect reactions: a simple formation of negatively charged Ga vacancies would lead to a negative charging of the NW sidewall facets, which would quickly undermine further vacancy formation, due to repulsive Coulomb interactions. The observation of surface antisite defects in the STM image of figure 5(a) indicates that the negative charge of a Ga vacancy can be removed by inserting an As adatom on a Ga lattice site to form an uncharged  $\text{As}_{\text{Ga}}$  antisite defect in the surface layer. This point defect reaction is very likely to happen, due to the As rich conditions created by the As cap and also energetic reasons. For midgap Fermi energies in our case, the formation energy of a  $V_{\text{Ga}}$ , a negatively charged As adatom, and an uncharged  $\text{As}_{\text{Ga}}$  antisite are 1.2, 1, 0, and  $-0.25$  eV, respectively [38], hence freeing about 2.5 eV per

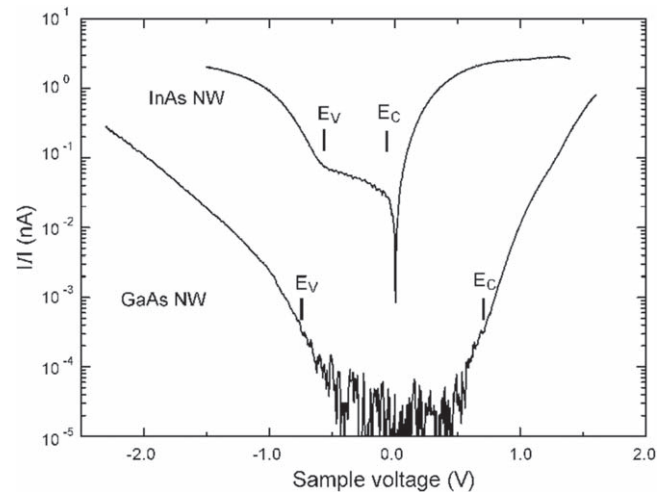


**Figure 6.** Tunneling spectra acquired on the {110} sidewall of self-catalyzed InAs and GaAs NWs.  $E_V$  and  $E_C$  indicate the position of the valence and conduction band edges respectively. The spectrum of the InAs NW has been shifted vertically for clarity.

formed surface antisite defect. In addition, this reaction results in charge neutrality. These antisite defects remain in the surface layer, as the barrier for inward diffusion is too high [38]. The lack of subsurface antisite defects corroborates this formation mechanism.

At this stage, we consider the Ga adatoms created during vacancy formation. Once the vacancy is filled by an As adatom, the Ga adatoms cannot jump back into the Ga vacancy nor desorb, since the temperature is too low. Hence they remain diffusing over the sidewall surface until they nucleate with As adatoms, preferentially at the NW edges, forming GaAs islands on the sidewalls. This effect is responsible for the distribution of one-monolayer-height islands observed on the sidewalls of the self-catalyzed GaAs NWs.

An intriguing aspect of this result is the degree of non-stoichiometry achievable at NW sidewall facets without formation of precipitates. In bulk GaAs, the equilibrium phase diagram only permits very small deviations from stoichiometry in the range of  $\sim 10^{-3}\%$  at 700 °C, before precipitation occurs. The single phase area narrows even further at lower temperatures [40, 41]. Under non-equilibrium conditions in low-temperature GaAs growth, As antisite concentrations of up to 1% are reachable, but annealing leads to As precipitation [30, 42]. Here on the NW sidewall, a deviation from stoichiometry of 18% is observed at 370 °C–380 °C and no precipitate forms during annealing.

We also note that the formation of the surface antisites occurs at relatively low temperature in comparison with the congruent temperature of GaAs. This effect is not observed on the planar GaAs {110} surface which was annealed at 450 °C. Similarly, under realistic annealing temperatures, holes cannot be avoided for InAs NWs. For example, at temperatures as low as 315 °C–325 °C, As-capped self-catalyzed InAs NWs exhibit a holey surface, as shown in figure 7, meaning that the In surface atoms already desorb rather than diffuse on the sidewalls at this temperature.



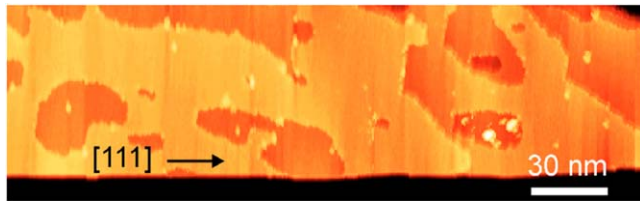


**Figure 7.** STM image of the {110} sidewall of a In-catalyzed InAs NWs after the removal of the As capping layer at 315 °C–325 °C. Tunneling conditions:  $V$  sample = +2.5 V,  $I$  tunneling = 10 pA.

Finally, due to the lower congruent temperature of InSb with respect to InAs [43], similar post-growth treatments should have produced a holey surface at the sidewall of the InAsSb NWs. Instead, the sidewalls are atomically flat. Although Sb behaves as a surfactant in the growth of III–V semiconductor alloys [44], we do not believe that it plays a role during the sublimation of the As layer, since it has been shown to preferentially incorporate into the surface lattice and substitute to As than diffusing at the NW surface [45]. Instead, our previous study of InAs<sub>1-x</sub>Sb<sub>x</sub> NWs with STM and x-ray energy-dispersive spectroscopy analysis operated in the high-angle annular dark field STEM mode have revealed the presence of gold clusters on the NW sidewalls [12]. This result is confirmed by *in situ* temperature-dependent STEM experiments of GaAs NWs grown with Au seed particles that were protected by an As cap. Figure 8 shows a STEM image of a GaAs NW with the Au particle on top. At first, the NW and the seed particle are surrounded by the amorphous capping layer. By increasing the temperature at 250 °C, the capping layer roughens and the interface between the Au droplet and the top of the NW widens drastically, indicating the interdiffusion of As and Au atoms. In fact, the droplet becomes gradually an AsAu alloy. In concomitance, as the annealing time increases, dark features appear on the sidewall, diffusing from the Au seed particle towards the bottom of the NW. Therefore, the desorption of the As capping layer from Au-catalyzed NWs inevitably leads to the presence of gold atoms and clusters on the sidewalls. We suspect these impurities to modify the Fermi level position and to prevent the formation of vacancies, keeping the {110} sidewalls atomically flat.

## 5. Conclusion

We have investigated the sidewall morphology of III–V semiconductor NWs after the desorption of a protective As cap. The desorption of the As cap for self-catalyzed NWs produces two types of morphology arising from Fermi-level-dependent point defect formation and reaction. For annealing temperatures close to the congruent evaporation temperature, the formation of vacancies from the evaporation of group III and group IV elements leads to sidewalls with pits nucleating within the sidewalls. However, when the annealing temperature is much smaller than the congruent evaporation temperature, group III vacancies are formed and substituted by the excess of As atoms on the surface of the NW. The resulting

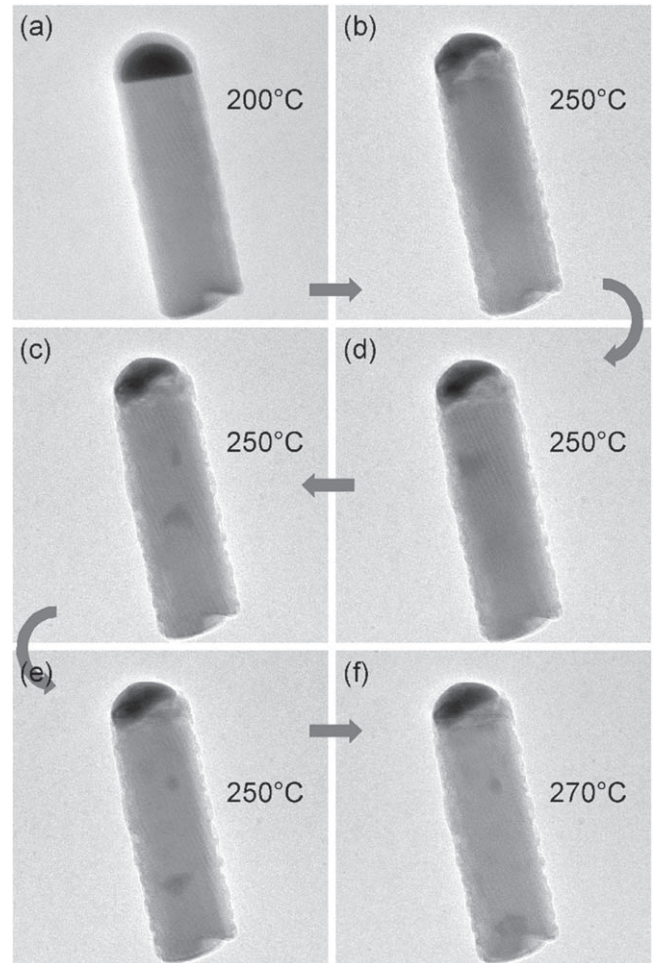


**Figure 8.** Sequence of temperature-dependent STEM images of an Au-catalyzed GaAs NW capped with a thin As cap. The annealing temperature is indicated in the images.

group III adatoms nucleate with excess As adatoms in islands, preferentially at the sidewall edges. We have furthermore found that a strongly enhanced solubility of excess As is achieved through these surface point defect reactions. Hence, besides the ability to relax strain much more efficiently than in planar growth, NW can also accommodate much larger deviations from stoichiometry at least at their surfaces. Finally, for gold-catalyzed NWs, Au from the seed is redistributed on the sidewalls upon desorption of the protective As cap. The Au induces a midgap pinning of the sidewalls which is anticipated to suppress vacancy formation, and thereby blocks the formation of islands or vacancy pits. The results highlight the critical impact, which point defect formation and reactions have on the sidewall morphology of NWs.

## Acknowledgments

This work was financially supported by the European Community's Seventh Framework Program (Grant No. PITN-GA-2012-316751, Nanoembrace project), the H2020 program (Grant No. PITN-GA-2016-722176, Indeed Project), the French state funds managed by the ANR within the

Investissements d'Avenir programme (Grant No. ANR-11-EQPX-0015, EQUIPEX Excelsior; Grant No. ANR-10-EQPX-0050), EQUIPEX Tempos), the French National Research Agency (ANR-16-CE24-0007-01, Dirac III-V project) and the RENATECH network and the Deutsche Forschungsgemeinschaft (Grant No. 390247238). T Xu acknowledges the supports of the National Natural Science Foundation of China (Grant No. 61775130). The authors thank C Coinon and X Wallart for the growth of the As capped bulk samples and C Domke, M Heinrich, M Simon, and C Dzeja for participating in some of the measurements leading to figure 4.

## ORCID iDs

Sébastien Plissard  <https://orcid.org/0000-0002-0769-5429>

Bruno Grandidier  <https://orcid.org/0000-0001-6131-7309>

## References

- [1] Svensson C P T, Mårtensson T, Trägårdh J, Larsson C, Rask M, Hessman D, Samuelson L and Ohlsson J 2008 *Nanotechnology* **19** 305201
- [2] Tomioka K, Yoshimura M and Fukui T 2012 *Nature* **488** 189
- [3] Dayeh S A et al 2012 *Nano. Lett.* **13** 1869–76
- [4] Royo M, De Luca M, Rurali R and Zardo I 2017 *J. Phys. D: Appl. Phys.* **50** 143001
- [5] Guan X et al 2016 *Nano. Lett.* **16** 2393–9
- [6] Yang M, Dvorak D, Leistner K, Damm C, Watkins S P and Kavanagh K L 2019 *Nanotechnology* **30** 025701
- [7] Loisch B et al 2015 *Adv. Mater.* **27** 2195–202
- [8] Cirlin G E, Thernycheva M, Patriarche G and Harmand J C 2012 *Semiconductor* **46** 175–8
- [9] Capiod P et al 2013 *Appl. Phys. Lett.* **103** 122104
- [10] Xu T et al 2015 *Appl. Phys. Lett.* **107** 112102
- [11] Guan X et al 2016 *Nanoscale* **8** 15637
- [12] Xu T, Dick K A, Plissard S, Nguyen T H, Makoudi Y, Berthe M, Nys J P, Wallart X, Grandidier B and Caroff P 2012 *Nanotechnology* **23** 095702
- [13] Fanetti M, Ambrosini S, Amati M, Gregoratti L, Abyaneh M K, Franciosi A, Chia A C E, LaPierre R R and Rubini S 2013 *J. Appl. Phys.* **114** 154308
- [14] Arbiol J and Xiong Q (ed) 2015 *Semiconductor Nanowires: Materials, Synthesis, Characterization and Applications* (New York: Elsevier)
- [15] Matteini F, Tütüncüoğlu G, Potts H, Jabeen F, Fontcuberta I and Morral A 2015 *Crys. Growth Des.* **15** 3105–9
- [16] Dubrovskii V G, Xu T, Díaz Álvarez A, Plissard S R, Caroff P, Glas F and Grandidier B 2015 *Nano Lett.* **15** 5580–4
- [17] Harmand J C, Patriarche G, Péré-Laperne N, Merat-Combes M N, Travers L and Glas F 2005 *Appl. Phys. Lett.* **87** 203101
- [18] Xu T, Nys J P, Addad A, Lebedev O I, Urbietta A, Salhi B, Berthe M, Grandidier B and Stiévenard D 2010 *Phys. Rev. B* **81** 115403
- [19] Lenrick F, Ek M, Deppert K, Samuelson L and Wallenberg L R 2014 *Nano Res.* **7** 1188–94
- [20] Knutsson J V, Lehmann S, Hjort M, Reinke P, Lundgren E, Dick K A, Timm R and Mikkelsen A 2015 *ACS Appl. Mater. Interfaces* **7** 5748–55
- [21] Ebert P, Heinrich M, Simon M, Urban K and Lagally M G 1995 *Phys. Rev. B* **51** 9696–701
- [22] Domke C, Ebert P, Heinrich M and Urban K 1996 *Phys. Rev. B* **54** 10288–91
- [23] Semmler U, Simon M, Ebert P and Urban K 2001 *J. Chem. Phys.* **114** 445–51
- [24] Han B Y, Nakayama K and Weaver J H 1999 *Phys. Rev. B* **60** 13846–53
- [25] Tanimura K and Kanasaki J I 2008 *Surf. Sci.* **602** 3162–71
- [26] Pechman R J, Wang X S and Weaver J H 1995 *Phys. Rev. B* **51** 10929–36
- [27] Heyn Ch and Jesson D E 2015 *Appl. Phys. Lett.* **107** 161601
- [28] Ebert P, Quadbeck P, Urban K, Henninger B, Horn K, Schwarz G, Neugebauer J and Scheffler M 2001 *Appl. Phys. Lett.* **79** 2877–9
- [29] Feenstra R M, Woodall J M and Pettit G D 1993 *Phys. Rev. Lett.* **71** 1176–9
- [30] Demonchaux T et al 2018 *Phys. Rev. Mater.* **2** 104601
- [31] Diaz A et al 2015 *Nano Lett.* **15** 6440–5
- [32] Ebert P 1999 *Surf. Sci. Rep.* **33** 121–303
- [33] Speckbacher M et al 2016 *Nano Lett.* **16** 5135–42
- [34] Alekseev P A, Dunaevskiy M S, Cirlin G E, Reznik R R, Smirnov A N, Kirilenko D A, Davydov V Y and Berkovits V L 2018 *Nanotechnology* **29** 314003
- [35] Morgenstern M, Haude D, Gudmundsson V, Wittneven C, Dombrowski R, Steinebach C and Wiesendanger R 2000 *J. Electron Spectrosc. Relat. Phenom.* **109** 127–45
- [36] Hjort M et al 2014 *ACS Nano* **8** 12346–55
- [37] Hjort M, Knutsson J V, Mandl B, Deppert K, Lundgren E, Timm R and Mikkelsen A 2015 *Nanoscale* **7** 9998–10004
- [38] Schwarz G 2002 Untersuchungen zu Defekten auf und nahe der (110) Oberfläche von GaAs und weiteren III–V–Halbleitern *PhD Thesis* Technischen Universität Berlin
- [39] Chatillon C and Chatain D 1995 *J. Cryst. Growth* **151** 91–101
- [40] Wenzl H, Dahlen A, Fattah A, Petersen S, Mika K and Henkel D 1991 *J. Cryst. Growth* **109** 191–204
- [41] Morozov A N, Bublik V T and Morozova O Y 1986 *Cryst. Res. Technol.* **21** 749–54
- [42] Melloch M R, Woodall J M, Harmon E S, Otsuka N, Pollak F H, Nolte D D, Feenstra R M and Lutz M A 1995 *Annu. Rev. Mater. Sci.* **25** 547–600
- [43] Haworth L, Lu J, Westwood D I and Macdonald J E 2000 *Appl. Surf. Sci.* **166** 253–8
- [44] Borg B M and Wernersson L-E 2013 *Nanotechnology* **24** 202001
- [45] Hjort M, Kratzer P, Lehmann S, Patel S J, Dick K A, Palmstrøm C J, Timm R and Mikkelsen A 2017 *Nano Lett.* **17** 3634–40



# Triangular nanoporation and band engineering of InGaAs quantum wells: a lithographic route toward Dirac cones in III–V semiconductors

L C Post<sup>1</sup> , T Xu<sup>2,3,4</sup> , N A Franchina Vergel<sup>2</sup>, A Tadjine<sup>2</sup>, Y Lambert<sup>2</sup>, F Vaurette<sup>2</sup>, D Yarekha<sup>2</sup>, L Desplanque<sup>2</sup> , D Stiévenard<sup>2</sup>, X Wallart<sup>2</sup>, B Grandidier<sup>2</sup> , C Delerue<sup>2</sup> and D Vanmaekelbergh<sup>1,4</sup>

<sup>1</sup> Condensed Matter and Interfaces, Debye Institute for Nanomaterials Science, Utrecht University, 3584 CC Utrecht, The Netherlands

<sup>2</sup> IEMN, UMR8520, Université de Lille1, F-59652 Villeneuve d'Ascq Cédex, France

<sup>3</sup> Key Laboratory of Advanced Display and System Applications, Shanghai University, 200072 Shanghai, People's Republic of China

E-mail: [xtld@shu.edu.cn](mailto:xtld@shu.edu.cn) and [d.vanmaekelbergh@uu.nl](mailto:d.vanmaekelbergh@uu.nl)

Received 27 September 2018, revised 6 December 2018

Accepted for publication 10 January 2019

Published 8 February 2019



CrossMark

## Abstract

The design of two-dimensional periodic structures at the nanoscale has renewed attention for band structure engineering. Here, we investigate the nanoporation of InGaAs quantum wells epitaxially grown on InP substrates using high-resolution e-beam lithography and highly plasma based dry etching. We report on the fabrication of a honeycomb structure with an effective lattice constant down to 23 nm by realising triangular antidot lattice with an ultimate periodicity of 40 nm in a 10 nm thick InGaAs quantum well on a p-type InP. The quality of the honeycomb structures is discussed in detail, and calculations show the possibility to measure Dirac physics in these type of samples. Based on the statistical analysis of the fluctuations in pore size and periodicity, calculations of the band structure are performed to assess the robustness of the Dirac cones with respect to distortions of the honeycomb lattice.

Supplementary material for this article is available [online](#)

Keywords: InGaAs quantum well, honeycomb semiconductor, dirac cone, electron beam lithography, band structure engineering, lattice disorder

(Some figures may appear in colour only in the online journal)

## 1. Introduction

III–V semiconductor quantum wells have obtained a central place in opto-electronics and advanced logics. In more recent quests for semiconductors with entirely new functions, the effects of a periodic potential at the nanometre scale on the electronic band structure have been theoretically anticipated [1, 2]. In the case where the charge carriers are confined in a

honeycomb geometry, the quantum well semiconductor bandgap remained, but the highest hole valence and lowest electron conduction bands become Dirac cones with a linear energy-momentum relationship around the K-points in the Brillouin zone. This means that the beneficial properties of a semiconductor, such as a bandgap and a controllable density of carriers, can be combined with valence and conduction bands with a K-region similar as for graphene. Moreover, the combination of Dirac (mini) bands and spin-orbit coupling may result in topological phases, such as non-trivial flat bands

<sup>4</sup> Authors to whom any correspondence should be addressed.

and the quantum spin Hall effect [3–6]. Hence, honeycomb semiconductors (HC-SC) form a new material class with unseen electronic functions.

With respect to the question of how to fabricate such HC-SC, two possibilities have been put forward, recently. The first route is based on the two-dimensional (2D) assembly and attachment of semiconductor nanocrystals providing HC-SC of Pb- and Cd-chalcogenides [7, 8] with a periodicity in the 5–10 nm range, supported by calculations [3, 9]. The second route is based on nanopatterning of 2D semiconductors by means of lithography. Importantly, a hexagonal array of pores in a semiconductor quantum well would result in a remaining crystal with a honeycomb geometry.

Such a lithographic nanoporation to form HC-SC has several advantages: (i) it can be applied to families of well-established semiconductor materials with low effective carrier mass and very high electron mobilities, such as several III–V semiconductors; (ii) nanoporation would enable to change the size of the honeycomb unit cell and the size of the pores in an independent way. This allows for a precise tuning of the electronic band structure. (iii) The lithographic procedures can be directly applied to semiconductor quantum wells incorporated in classic transistor devices, allowing for direct investigation of the band structure and transport properties of the HC-SC with a controllable position of the Fermi-level.

Previous works used a modulation-doped GaAs heterostructure subjected to a lateral attractive potential with honeycomb geometry [10–13]. Experiments revealed interesting many-body effects but direct evidence for massless Dirac fermions (MDFs) remains elusive because the width of the Dirac band was too small ( $\ll 0.1$  meV) due to the relatively large lattice constant ( $> 100$  nm) [14]. Recently, Wang *et al* realised a HC-SC in a nanopatterned GaAs quantum well with a very small lattice constant of 50 nm. Resonant inelastic light-scattering spectra revealed some features of Dirac type bands [15]. However, it was reported that the lattice parameter of HC-SC based on GaAs heterostructures should be as low as 20 nm to directly observe MDFs in standard cryogenic conditions [2]. As a result, nanofabrication techniques should be pushed to their ultimate limit in terms of resolution. We note that it is more effective to etch a triangular antidot lattice with a repulsive potential, than using an attractive potential. With this approach, the lattice constant of the honeycomb unit cell can be decreased by a factor  $\sqrt{3}$  compared with previous results, which will significantly increase the width of the Dirac band [16].

Devices with remote metallic gates have been commonly used in the previous works. Nevertheless, the potential modulation induced by the top and back gates is necessarily slowly varying in space due to the long-range decay of the Coulomb potentials. In addition, these nanostructures are not suitable for local-probe spectroscopy experiments due to the presence of the top gate. In this work, we have considered another approach allowing to create potential barriers directly in an InGaAs quantum well with steepest variations and thus better definition of the honeycomb lattice.

The width of the Dirac cone is not only dependent on the lattice constant of the honeycomb lattice, but also on the effective mass of the charge carriers in the employed semiconductor material [12]. When lowering the effective mass of the semiconductor material, the effects of the lateral confinement are enhanced, resulting in a broader Dirac cone. Calculations from Tadjine *et al* show that the energy range of the Dirac cone can extend over tens of meV in HC-SC with a reasonable size of lattice parameters in InAs heterostructures [1]. In-based semiconductor materials are therefore promising candidates as 2DEG channel materials for realising Dirac semiconductors. For instance, InGaAs with a relatively low electron effective mass ( $0.041 m_0$  for  $\text{In}_{0.53}\text{Ga}_{0.47}\text{As}$  lattice-matched to InP), can be grown by molecular beam epitaxy (MBE) on InP substrates using well-established routes, leading to 2DEG with high carrier mobility ( $> 1.3 \times 10^5 \text{ cm}^2 \text{ V}^{-1} \text{ s}^{-1}$  at 77 K) [17–20]. Finally, another important factor which is usually not considered is the quality of the build-in honeycomb symmetry etched in the QW. Positional disorder in the antidot lattice can greatly affect the symmetry in the lattice, perturbing the Dirac cone and providing mass to the carriers [21]. The fabrication of high quality antidot triangular lattices is essential for the observation of Dirac physics in these samples.

In the present work, we describe a lithographic nanoporation route towards honeycomb InGaAs on an InP substrate. We describe how a hexagonal array of pores (antidot lattice) is perforated to force the electrons in a honeycomb geometry. The 2D InGaAs layer has a thickness of 10 nm, and is grown on an InP substrate by MBE. Using high-resolution electron beam lithography (EBL) and plasma based dry etching, a triangular antidot lattice is obtained in the InGaAs quantum well with a periodicity of 40 nm which gives an effective honeycomb lattice constant down to 23 nm. We show that the radius of the pores can be tuned in an independent way. Our band structure calculations anticipate that Dirac cones can be obtained with a width of 5.0 meV, allowing for electrical spectroscopy and transport measurements at liquid helium temperature. The morphology of the samples was studied with atomic force microscopy (AFM), energy dispersive electron spectroscopy (EDS) and cross-section transmission electron microscopy (TEM). The disorder in the lattices is quantified on the basis of scanning electron microscopy (SEM) images. We estimate the electronic effects of structural disorder on the density of states (DOS) in the fabricated honeycomb InGaAs structures using a muffin-tin calculation.

## 2. Experimental

### 2.1. Sample fabrication

Figure 1 illustrates the fabrication process of the InGaAs antidot lattices. An  $\text{In}_{0.53}\text{Ga}_{0.47}\text{As}$  layer (10 nm) was grown onto the InP substrate using MBE. To protect the surface of the QW layer from carbon contaminations, 16 nm of  $\text{SiO}_2$  was grown on top of the QW using plasma-enhanced chemical vapour deposition, presented in figure 1(a). The sample

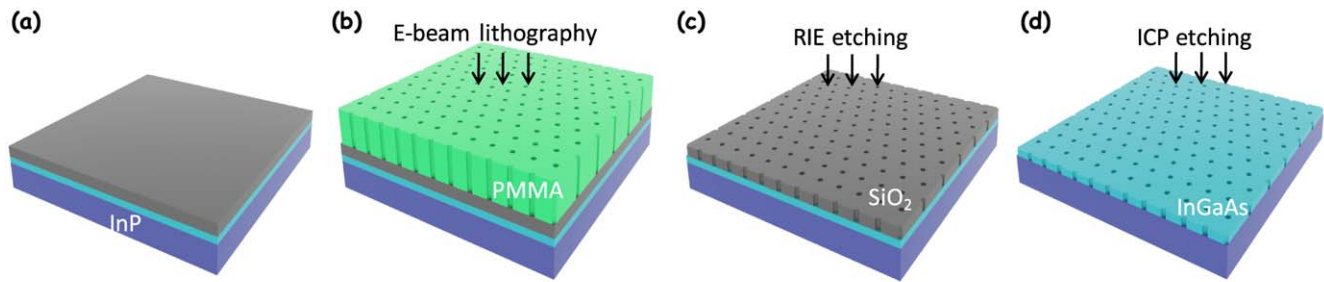


**Figure 1.** Overview of the fabrication process required to obtain a nanoperforated InGaAs/InP heterostructure with a honeycomb lattice. (a) The starting point is a 10 nm InGaAs quantum well grown with MBE on an InP substrate, on which a SiO<sub>2</sub> layer (16 nm in thickness) and a PMMA layer are deposited. (b) A triangular pattern of pores is created in the PMMA by electron beam lithography, (c) the triangular pattern is transferred into the SiO<sub>2</sub> layer by reactive ion etching. (d) The triangular pore pattern is transferred into the InGaAs quantum well by BCl<sub>3</sub> based inductive coupled plasma etching.

was dehydrated by heating the surface to 180 °C for 10 mins and a diluted polymethylmethacrylate (PMMA) 950 K 4% resist with a thickness of 50 nm was spin-coated on top of the sample, followed by an annealing step at 80 °C for 1 min on a hot plate and a bake out at 180 °C for 10 min.

E-beam exposure was performed using Raith EBPG 5000Plus equipment, taking advantage of the improved recipes of our previous work [22]. Triangular nanopatterns with different periodicities of 60, 50 and 40 nm were exposed in  $20 \times 5 \mu\text{m}^2$  areas with an accelerating voltage of 100 kV, a beam current of 200 pA and an e-beam dose of  $10\,000 \mu\text{C cm}^{-2}$ . By slowly modulating the electron beam dose and the aperture in the lithography process, triangular lattices with nanoscale dimensions can be obtained. Since the array fabrication is near the lithography resolution, an additional degree of freedom consists in varying the electron beam dose to slightly change the radius of the pores. The position of the patterns on the sample can be located by printing large markers around the patterns. The resist was developed in a 1:2 methyl-isobutyl ketone:isopropanol (MIBK:IPA) solution for 60 s, removing the exposed resist. The sample was further rinsed in IPA for at least 30 s to stop the development and dried under low N<sub>2</sub> flow (figure 1(b)).

The triangular pattern was first etched inside the SiO<sub>2</sub> layer using reactive ion etching (RIE) in a Plasmalab 80+ (Oxford) system with a mixture of CHF<sub>3</sub> and CF<sub>4</sub> (figure 1(c)). The chamber pressure was set to 10 mTorr, while the power was 300 W. The sample was etched for 40 s, removing all the SiO<sub>2</sub> inside the pores. The remaining PMMA resist on top of the SiO<sub>2</sub> was removed by placing the sample in a SVC bath at 70 °C (2 mins), followed by an acetone bath (2 mins) and finally a IPA bath (2 mins). The sample was further rinsed with IPA and low N<sub>2</sub> flow.

In the final step, the triangular pattern was etched inside the InGaAs QW using BCl<sub>3</sub> based inductively coupled plasma (ICP) etching with a ICP power of 200 W and a RIE power of 50 W. The pressure inside the chamber is set to 2 mTorr and the sample is etched for 40 s, removing the InGaAs inside the pores. The advantage of using ICP etching over conventional RIE is the separate control over the generated plasma density and the accelerating ion energy,

allowing for a better selectivity on the etched sample [23]. The remainder of SiO<sub>2</sub> mask on the sample was removed by wet etching (1% HF for 1 min). The final result of the whole fabrication process is presented in figure 1(d).

## 2.2. Characterisation

SEM images of the etched SiO<sub>2</sub> and InGaAs layers are shown in figure 2. The left three images (a1, a2, a3) show the triangular antidot array of the 16 nm SiO<sub>2</sub> layer after the first etching step in the patterning process. The triangular pore arrays have a lattice constant of 60, 50 and 40 nm, respectively. The triangular arrays in the InGaAs QW with the same lattice parameters are presented in the right three SEM images (b1, b2, b3) after the ICP etching. Differences in intensity at the edges of the pores can be explained by an accumulation of electrons around the pores.

Over large areas of  $20 \times 5 \mu\text{m}^2$ , a uniform pore radius and periodicity can be achieved after optimising the EBL and etching process, with very few pore defects such as missing or misplaced sites. The ability to fabricate the high quality triangular pores with periodicity of 40 nm which gives an effective honeycomb lattice constant of 23 nm ( $40/\sqrt{3}$ ), is essential for optimal tuning of the triangular potential that generates the honeycomb geometry inside the QW with a periodicity of 23 nm.

AFM measurements were performed on the etched samples to check the height profile of the pores and alignment markers (figure 3). Figure 3(a) shows that 18 nm of the substrate sample has been etched in the marker, indicating that the InGaAs QW with initial thickness of 10 nm is completely removed. These results are supported by EDS measurements: on the non-etched area (square 1 of figure 3(a)), Ga and As are found, consistent with the top InGaAs layer, while on the etched area (square 2 of figure 3(a)), these peaks are absent, demonstrating the complete etching of the InGaAs QW. The spectrum acquired on the QW also shows that the remaining SiO<sub>2</sub> on the QW is removed using the wet etching, since no Si peaks are visible and the amplitude of the O peak is similar to the one observed on the InP substrate.



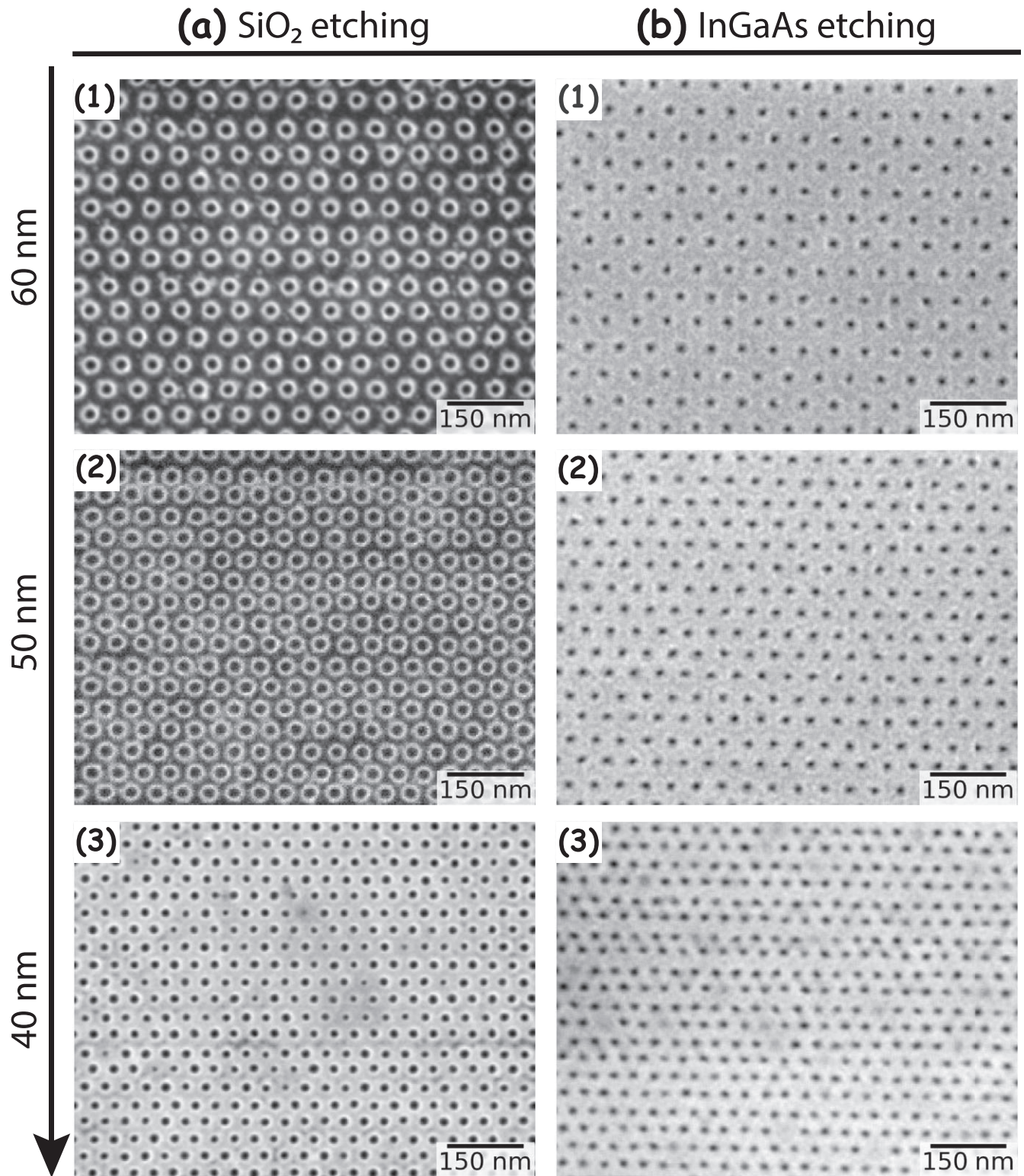


**Figure 2.** Results of the lithographic patterning in every intermediate stage of the process. (a) SEM images of the triangular pore pattern in the SiO<sub>2</sub> layer after RIE etching. The periodicities of the lattices are 60 (1), 50 (2) and 40 nm (3) in the top, middle, and bottom image, respectively. Differences in intensity at the edges of the pores can be explained by an accumulation of electrons around the pores. (b) SEM images of the pore pattern in the InGaAs quantum well layer after the ICP etching step for 60 (1), 50 (2) and 40 nm (3) periodicity in the top, middle and bottom images, respectively.

When performing AFM measurements directly onto the antidot lattice, a similar uniformity of the lattice parameters is observed, consistent with the SEM results. However, the full depth of the QW cannot be measured, due to the broadness of

the AFM tip, making it impossible to enter the tip inside the pores as presented in figure 3(b). The shape of the pores was therefore characterised with cross-section TEM carried out in a Fei Strata DB 235 Dual-Beam focus ion beam (FIB) system

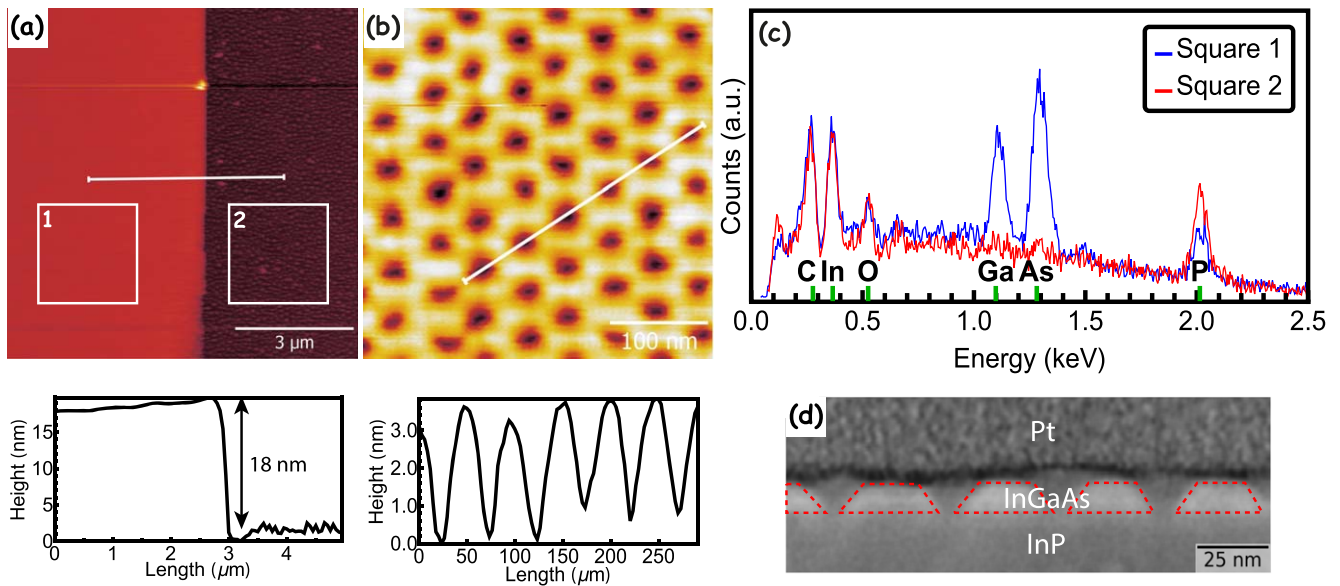


**Figure 3.** Structural and chemical characterisation of the nanoporated InGaAs/InP heterostructure. (a) AFM image and height profile acquired along the horizontal direction. (b) AFM image of the nanoporated InGaAs QW and height profile acquired along a tilted direction. (c) Chemical EDS analysis of the sample after ICP etching. The spectra were acquired in areas 1 and 2 defined in (a). (d) Cross-section scanning TEM image of the nanoporated InGaAs/InP heterostructure, revealing the formation of conical pores instead of cylindrical pores.

operated at 30 kV equipped with a field emission gun. The spatial resolution was about 2 nm. The TEM foils were prepared by a FIB setup with Ga ions with a resolution of about 7 nm. The sample was protected by growing a layer of Pt on the top of the surface and a thin slice of the sample with a thickness of 200 nm is cut out.

The scanning TEM image of figure 3(d) shows the shape of the pores from the inner side. The pores have a conical shape instead of a cylindrical shape due to the non-perfect anisotropic etching process. However, the pores are fully etched down to the InP substrate.

### 2.3. Band structure calculations

In order to determine the band structure of the nanoporated heterostructure, calculations were performed based on the geometry of the HC-SC material schematized in figures 4(a), (b). Muffin-tin (black) and tight binding (red) calculations of the band structure of a 10 nm thick InGaAs with a pore periodicity of 40 nm and pore radius  $r$  of 9.6 nm show a clear Dirac cone at the K point with an energy width of about 5.0 meV (figure 4(c)), due to coupling of the s-type on site envelope functions. The width is much larger with respect to the thermal energy of liquid helium (4.4 K, 0.38 meV), opening up the possibility to measure Dirac physics in lithography patterned heterostructures. At higher energies, we find a quasi flat band and a second Dirac cone due to coupling of the p-envelope functions. More details about the tight binding and the muffin-tin calculations can be found in the supplementary information (SI), available online at [stacks.iop.org/NANO/30/155301/mmedia](https://stacks.iop.org/NANO/30/155301/mmedia).

When decreasing the periodicity  $a$  of the antidot lattice, muffin-tin calculations show that the energy width of the

Dirac cone increases according to  $1/a^2$  (figure 4(d)), which is consistent with previous reports [10]. Since the pores are empty, they can be treated as hard repelling cylinders where the potential barrier of the pores is infinitely high. The relative size of the pore, defined by radius/periodicity, is kept constant in the calculation. When fixing the periodicity to 40 nm and varying the radius of the pores between very small (4 nm) to very large (16 nm), a maximal value of the energy width of the Dirac cone can be determined for an optimal pore radius (figure 4(e)). This maximum energy width can be found at a hole radius of approximately 8.5 nm, which gives an energy width of 5.3 meV.

The conical shape was taken into account in the tight-binding calculations for a periodicity of 40 nm and a pore radius of 14.2 nm (figure 4(f)). The radius of the pores was reduced from 100% on the top surface of the QW down to 20% at the bottom. The calculated band structure of such a type of sample is illustrated in figure 4(f). The band structure shows almost no change in the shape and energy width of the Dirac cone between the conical and cylindrical pores. Although the confinement effect will decrease when lowering the size of the pores further down, the coupling strength will increase. This interplay between the confinement effect and the coupling strength explains why the Dirac cone is only weakly affected by the conical shape of the pores. As a result, we can conclude that there is almost no negative effect to have conical pores over cylindrical pores on the Dirac band.

### 3. Effects of disorder in the DOS

The previous sections described the fabrication route of a 2D InGaAs semiconductor with a honeycomb geometry, and the



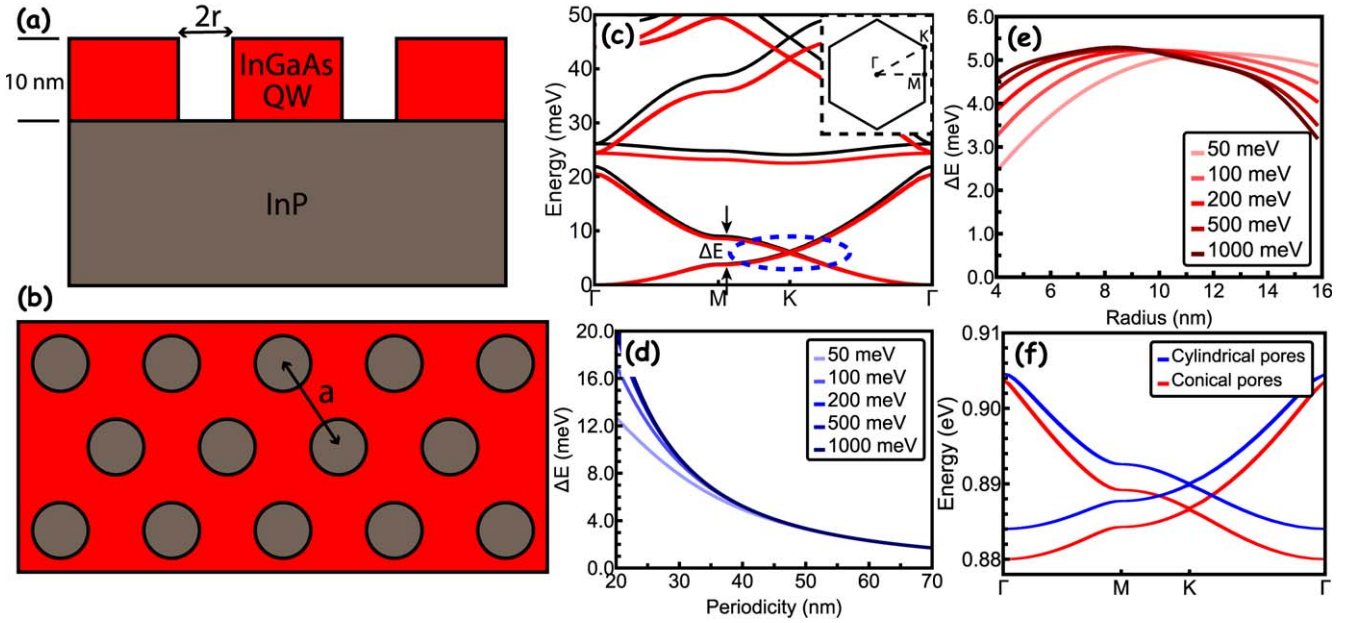


**Figure 4.** Schematic of the structure used to perform the muffin-tin and tight-binding calculations. (a), (b) Side and top view of a 10 nm InGaAs single crystal, 10 nm in thickness (red) with a triangular array of etched pores, thus forming a lattice inside the InGaAs/InP heterostructure. Critical structural parameters for the electronic band structure are the thickness of the InGaAs, here 10 nm, the radius  $r$  of the pores, and the periodicity, i.e. the distance between the centre of two adjacent pores corresponding to the unit cell constant  $a$ . (c) Conduction band structure for an InGaAs honeycomb lattice, with a periodicity  $a$  of 40 nm, a pore radius  $r$  of 9.6 nm and an electron repulsive potential of the pores of 1000 meV. The results of the muffin-tin calculations and tight-binding calculations are presented in black and red respectively. The bandwidth where the energy dispersion for the lowest Dirac cone is located is highlighted by a dotted ellipse. The width of the Dirac cone  $\Delta E$  is defined as the energy difference of the first two bands at the M point. (d) Dirac cone width (taken at M) as a function of the honeycomb periodicity  $a$ . The size of the pores defined by the ratio  $r/a$  is kept constant. The calculations were performed for several repulsive potential values in the pores. (e) Dirac cone width (taken at M) as a function of the radius  $r$  of the pores for a fixed periodicity  $a$  of 40 nm. The calculations were performed for several values of the repulsive potential in the pores. (f) Tight binding calculations on conical pores (red) and cylindrical pores (blue) show that the Dirac cones in the band structures are almost unaltered with respect to each other.

resulting band structure. However, the robustness of the linear dispersion in the nanostructured InGaAs quantum well is questionable. First, point defects and surface states exist and fluctuations of their charge states might disrupt the periodicity of the potential or cause a scattering of the charge carriers, reducing the carrier mobility and preventing the detection of Dirac cones in electrical measurements. High surface state densities could also make the direct observation of the local DOS in tunnelling spectroscopic measurements difficult. But previous experiments have shown that the step-like function of a quantum well DOS states can be probed for an InGaAs quantum well [24]. Moreover, treatments exist to efficiently passivate the surfaces of III–V semiconductors [25–27] and in particular the InGaAs(001) surface [28], so that the surface states become transparent to the tunnelling electrons in the energy range corresponding to energy levels of the quantum wells. However, even with a good passivation of the nano-perforated surfaces, other effects can significantly alter the band structure: a variation in the lattice constant (i.e. distance between pores), a variation in the radius of the pores and a variation in the shape of the pores. Among these three types of geometric variations, disorder in the periodicity should affect negatively the band structure, while variation in the 3D shape of the pore is expected to have a minor effect on the band structure (see e.g. the effect of the conical shape).

### 3.1. Particle detection script

We developed a particle detection protocol to quantify the disorder in the triangular antidot lattice, imaged by SEM. First, the quality of the image is improved by removing excessive number of pixels using Gaussian blurring. A black–white image of the SEM is obtained with an adaptive Gaussian threshold, making the pores detectable. All the pores are labelled, and small grains and hollows which are overlapping with the edge of the image are removed. The total number of pixels in the contour and area of each pore is detected, which is used to find the centre coordinates of each pore. The radius of each pore is calculated by fitting a perfect circle to every pore, and the circularity of each pore is determined using

$$C = \frac{4\pi A}{P^2}, \quad (1)$$

where  $A$  is the surface of the pore and  $P$  the perimeter of the pore. For a perfect round circle, this equation will yield one. The value  $C$  will go down when the pores are less round. Using the centre coordinates, all the nearest neighbour distances between the pores are computed. With the obtained data, we obtain three distributions that are plotted in histograms and fitted with a standard Gaussian distribution in order to determine their mean and the standard deviation. Using this particle detection script on the obtained SEM images, short



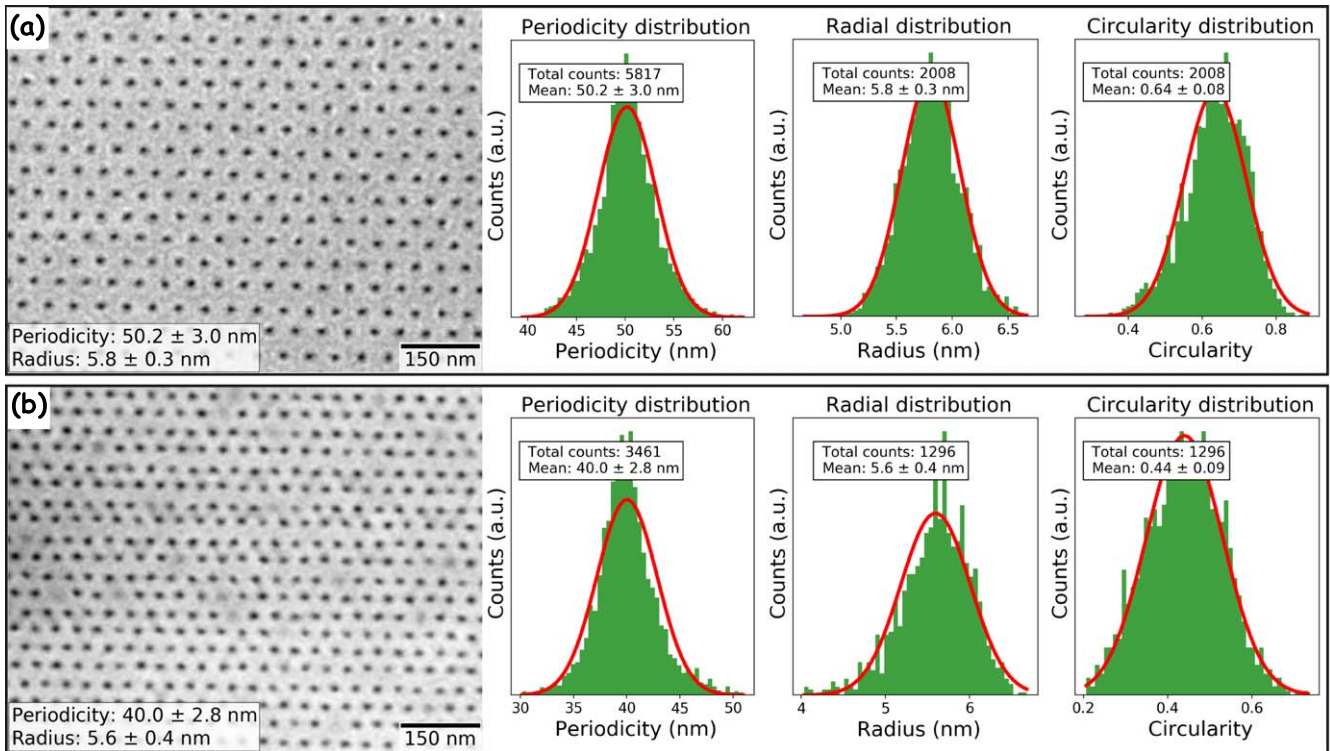


**Figure 5.** Analysis of the structural disorder parameters in a 2D honeycomb InGaAs sample with 50 nm (a) and 40 nm (b) periodicity. Distributions of the periodicity, pore radius and circularity are plotted next to the SEM images. The distributions are fitted with a standard Gaussian distribution. The total number of counts, the mean value and the standard deviation are indicated for each histogram.

range positional disorder and disorder in the shape of the pores can be immediately characterised.

The results of the particle detection script are presented in figure 5. For the 50 nm lattice (a), the calculated periodicity is  $50.2 \pm 3.0$  nm with a pore radius of  $5.8 \pm 0.3$  nm and a circularity of  $0.64 \pm 0.08$ . For the 40 nm lattice (b), the calculated periodicity yields  $40.0 \pm 2.8$  nm with a pore radius of  $5.6 \pm 0.4$  nm and a circularity of  $0.44 \pm 0.09$ , showing that the lattice constant in the 40 nm lattice is relatively more distorted than the 50 nm lattice, and the pores are less round than the pores in the 50 nm lattice.

### 3.2. Radial distribution function

For an accurate characterisation of long-range positional disorder inside the triangular antidot lattice, a 2D radial distribution function of the lattice is calculated to check if the disorder is completely random and independent of the disorder on other positions, or if any structural disorder is present in the lattice. A uniform disorder is obtained when the pore positions of a perfect lattice are displaced by a random displacement which is sampled from a Gaussian distribution. Conversely, a structural disorder is present when the disorder is not uniform. In order to discriminate whether the disorder is structural or random, the radial distribution function of the lattice can be fitted using two types of models: an ideal and a real paracrystal model [29, 30].

In an ideal paracrystal model, the spacing between two neighbouring lattice sites is generated by a variable  $D_i^{\text{ideal}}$  drawn from a Gaussian distribution with mean  $a$  and variance

$\sigma_{\text{ideal}}$  which does not depend on the positions of the other lattice sites. In this model, the variance of the distribution of the  $n$ th lattice site will be  $n$  times larger compared with the reference site, describing propagating disorder only.

The other model used for the analysis is the real paracrystal lattice. This model is generated by first creating an ideal paracrystalline lattice, and then shifting the lattice positions with an extra displacement  $D_i^{\text{real}}$  drawn from a Gaussian distribution with variance  $\sigma_{\text{real}}$ . When looking at the  $n$ th lattice site away from a reference point, the total variance of the distribution is a summation of  $\sigma_{\text{ideal}}$  which scales linearly with  $n$ , and  $\sigma_{\text{real}}$  which does not scale with  $n$ . Therefore,  $\sigma_{\text{real}}$  can describe the non-propagating disorder in the lattice. More information about the mathematical background of the two different models can be found in the SI.

The calculated radial distribution functions of the 50 and 40 nm antidot triangular lattices are fitted with both models, which are presented in figure 6. For both the 50 and 40 nm antidot lattices, the real paracrystalline model is a better fit than the ideal model, showing that random disorder dominates over structural disorder in both antidot lattices. For the 50 nm antidot lattice, the structural disorder term  $\sigma_{\text{ideal}}$  is 0.83 nm and the random disorder term  $\sigma_{\text{real}}$  is 2.15 nm. For the 40 nm antidot lattice, the structural disorder term is 1.02 nm and the random disorder term is 1.79 nm, showing that there is more random disorder in the 50 nm antidot lattice compared with the 40 nm one, and that there is more structural disorder in the 40 nm antidot lattice compared with the 50 nm one. This effect is highlighted in figures 6(c) and (f):

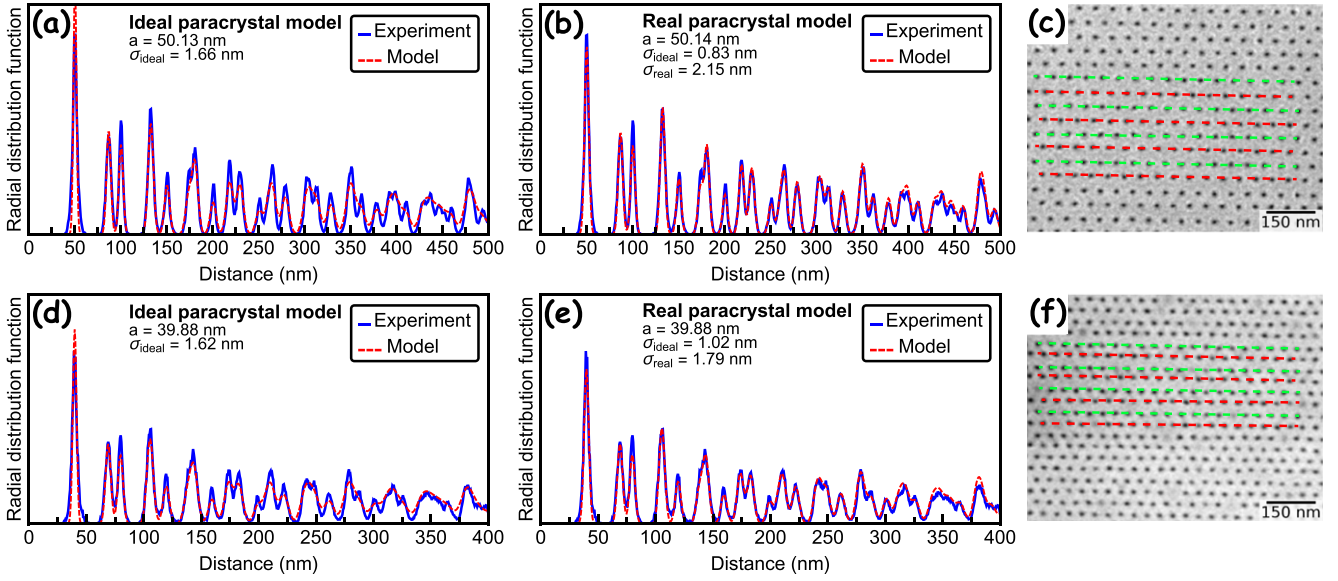


**Figure 6.** Order–disorder characterisation in two InGaAs triangular antidot lattices with periodicity of 50 and 40 nm. (a), (b), (d), (e) Radial distribution function for the InGaAs experimental lattice of 50 nm (a), (b) and 40 nm (d), (e) in blue fitted with a ideal paracrystalline model (a), (d) and a realistic paracrystalline model (b), (e) in red. (c), (f) SEM image of the InGaAs triangular antidot lattice with a periodicity of 50 nm (c) and 40 nm (f), including green and red dashed lines along the  $x$ -direction of the lattice. (c) The 50 nm lattice shows no visible propagating disorder in the  $y$ -direction, while (f) the 40 nm lattice show a clear structural disorder in the  $y$ -direction.

for the 50 nm antidot lattice, the distances between the pores stay visibly the same in the  $y$ -direction, while for the 40 nm antidot array the distances change alternately, indicating that a structural disorder is present inside the lattice. The origin of the structural disorder is still unknown, but different writing techniques [31] and different types or resist [32] for the EBL can be investigated to lower the structural disorder in the antidot lattice.

### 3.3. DOS calculations

The effect of the disorder inside the antidot lattices on the DOS can be calculated by distorting the on-site energy terms of the Hamiltonian, obtained from the muffin-tin calculations. First, a large super cell with  $M \times M$  lattice sites is defined. The Hamiltonian of every  $k$ -mesh point inside the Brillouin zone framed by the high-symmetry lines  $\Gamma \rightarrow K \rightarrow M \rightarrow \Gamma$  is calculated, and all the on-site energy terms  $\mathcal{H}_{i,i}$  of the lattice sites of the unit cell are distorted with an energy term  $E^{\text{dis}}$ :

$$\mathcal{H}_{i,i}^{\text{dis}} = \mathcal{H}_{i,i} + E^{\text{dis}}. \quad (2)$$

Every separate energy term  $E^{\text{dis}}$  is determined by drawing a random value from a Gaussian distribution with mean 0 and a standard deviation  $\sigma_{\text{dis}}$ .

The energy disorder  $\sigma_{\text{dis}}$  calculated in the antidot lattice can be directly linked to the disorder obtained from the analysis on the antidot lattices by calculating several band structures with different periodicities while keeping the ratio  $r/a$  and potential constant. By varying the periodicity of the lattice, the height of the Dirac cone will change and the difference in energy height of the Dirac cone with respect to the 40 nm lattice can be calculated (figure 7(a)). For a disorder of 2.8 nm, an energy disorder between  $-1.5$  and  $2.0$  meV is found, indicated by the dotted line. We note that this result is

obtained for a pore radius of 5.6 nm. If the pore radius increases to 14 nm, a disorder of 2.8 nm implies an energy disorder of about 6 meV due to stronger particle confinement, which can possibly destroy the Dirac cone in the DOS (see supporting SI). Therefore, small pore sizes should be preferred as they cause less change in the DOS when the lattice is distorted. More information on the distorted DOS calculation can be found in the SI.

Results for a disordered lattice are presented in figure 7(b). This calculation is performed on a  $24 \times 24$  lattice. For a perfect lattice, a straight V-like shape centred around 7 meV, signature of a perfect Dirac cone can be observed. The asymmetry of the DOS is caused by the interaction with the  $p$  states that are close to the  $s$  states due to the small radius of the pores. When adding disorder  $E^{\text{dis}}$  up to 2.5 meV to the on-site lattice site  $\mathcal{H}_{i,i}$  consistent with the values deduced above, the presence of a Dirac cone in the DOS is still recognisable, although the magnitude of the V-shape is reduced and the apex of the V-shape less resolved.

## 4. Summary and conclusions

To summarise, a route has been described to create HC-SC samples in InGaAs/InP QW heterostructures which are perforated with a 2D triangular antidot lattice using EBL. Triangular antidot lattice with periodicities of the pores down to 40 nm have been demonstrated, giving an effective honeycomb lattice constant of 23 nm. The morphology of the samples is thoroughly studied by using various tools, revealing a good degree of control on the lattice parameters. At the smallest periodicity, muffin-tin and tight binding calculations show a clear Dirac cone at the K point with an

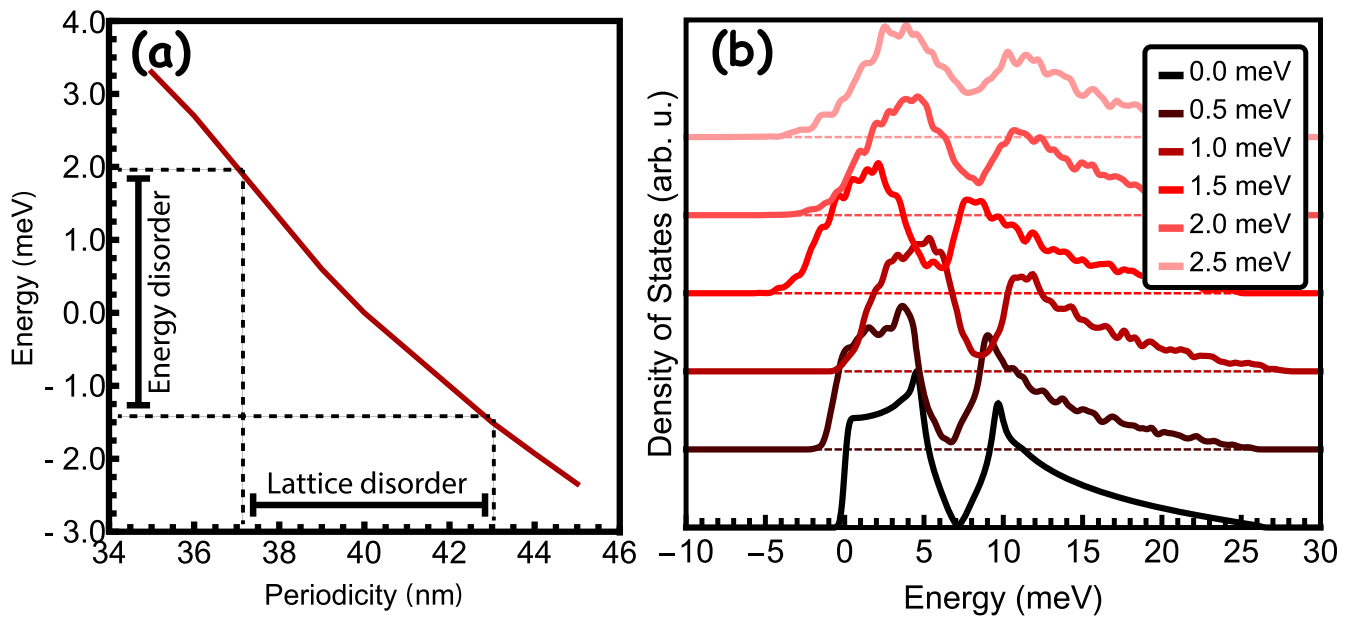


**Figure 7.** Density of states calculations for a perfect and a distorted 40 nm triangular antidot lattice inside an InGaAs QW with a potential height of 1000 meV and 2500 k-mesh points inside the Brillouin zone. (a) To determine the disorder energy term, the change in the energy height at the K point is calculated from the band structure for several periodicities around 40 nm. For a disorder of 2.8 nm, an energy disorder up to 2.0 meV is found. (b) Distorted DOS of the InGaAs triangular antidot lattice with random distorted energy terms with a variance of 0, 0.5, 1.0, 1.5, 2.0 and 2.5 meV. A clear Dirac cone can be observed for a perfect lattice, and it broadens but remains visible when adding more disorder to the calculation.

energy width of several meV. The disorder of the antidot lattices has been thoroughly studied using an effective particle detection protocol and by calculating the radial distribution function of the antidot lattices. Two different models have been considered to discriminate between random and structural disorder in the antidot lattice. Although both types of disorder exist in the antidot lattice with a periodicity of 40 nm, theoretical calculations of the DOS have revealed that the signature of the Dirac cone survives to the fluctuations of the pore periodicity and sizes that were measured. Because lattice disorder is inherent in structures prepared with EBL at the ultimate resolution, our results provide general guidelines to be able to probe Dirac cones in HC-SC consisting of III–V heterostructures. The next step is to passivate the surface of the nanostructured QW by using wet chemical passivation methods to suppress surface states and surface defects. Other methods, such as regrowth processes used in selective area epitaxy [33–35] could also be applied to improve the electronic quality of the HC-SC.

### Acknowledgments

This work was financially supported by the Netherlands Organisation for Scientific Research (Grant No. BC.000672.1, TOP Punt), the National Natural Scientific Foundation of China (Grant No. 61775130), the French National Research Agency (Dirac III-V project ANR-16-CE24-0007-01), the French state funds managed by the ANR within the Investissements d’Avenir programme EQUIPEX

Excelsior (ANR-11-EQPX-0015) and the RENATECH network.

### ORCID iDs

L C Post <https://orcid.org/0000-0001-9271-7225>

T Xu <https://orcid.org/0000-0003-1410-9261>

L Desplanque <https://orcid.org/0000-0002-2197-4408>

B Granddier <https://orcid.org/0000-0001-6131-7309>

### References

- [1] Tadjine A, Allan G and Delerue C 2016 *Phys. Rev. B* **94** 075441
- [2] Polini M, Guinea F, Lewenstein M, Manoharan H C and Pellegrini V 2013 *Nat. Nanotechnol.* **8** 625–33
- [3] Kalesaki E, Delerue C, Morais Smith C, Beugeling W, Allan G and Vanmaekelbergh D 2014 *Phys. Rev. X* **4** 011010
- [4] Du X, Skachko I, Duerr F, Luican A and Andrei E Y 2009 *Nature* **462** 192–5
- [5] Bolotin K I, Ghahari F, Shulman M D, Stormer H L and Kim P 2009 *Nature* **462** 196–9
- [6] Novoselov K S, Geim A K, Morozov S V, Jiang D, Katsnelson M I, Grigorieva I V, Dubonos S V and Firsov A A 2005 *Nature* **438** 197–200
- [7] Boneschanscher M P *et al* 2014 *Science* **344** 1377–80
- [8] Geuchies J J *et al* 2016 *Nat. Mater.* **15** 1248–54
- [9] Delerue C and Vanmaekelbergh D 2015 *2D Mater.* **2** 034008
- [10] Gibertini M, Singha A, Pellegrini V, Polini M, Vignale G, Pinczuk A, Pfeiffer L N and West K W 2009 *Phys. Rev. B* **79** 241406

- [11] Park C H and Louie S G 2009 *Nano Lett.* **9** 1793–7
- [12] Nádvořník L *et al* 2012 *New J. Phys.* **14** 053002
- [13] De Simoni G, Singha A, Gibertini M, Karmakar B, Polini M, Piazza V, Pfeiffer L N, West K W, Beltram F and Pellegrini V 2010 *Appl. Phys. Lett.* **97** 132113
- [14] Singha A *et al* 2011 *Science* **332** 1176–9
- [15] Wang S *et al* 2018 *Nat. Nanotechnol.* **13** 29–33
- [16] Du L *et al* 2018 *Nat. Commun.* **9** 3299
- [17] Yuzeeva N A, Sorokoumova A V, Lunin R A, Oveshnikov L N, Galiev G B, Klimov E A, Lavruchin D V and Kulbachinskii V A 2016 *J. Low Temp. Phys.* **185** 701–6
- [18] Wallart X, Pinsard B and Mollot F 2005 *J. Appl. Phys.* **97** 053706
- [19] Millunchick J, Riposan A, Dall B, Pearson C and Orr B 2003 Surface reconstructions of InGaAs layers 2003 *Int. Symp. on Compound Semiconductors* (IEEE: Piscataway, NJ) pp 43–4
- [20] Li H, Wu J, Wang Z, Liang J, Xu B, Jiang C, Gong Q, Liu F and Zhou W 1998 *J. Cryst. Growth* **186** 309–14
- [21] Flindt C, Mortensen N A and Jauho A P 2005 *Nano Lett.* **5** 2515–8
- [22] Xu T *et al* 2018 *Nanoscale* **10** 7519–25
- [23] Maeda T, Cho H, Hong J and Pearton S J 1999 *J. Electron. Mater.* **28** 118–23
- [24] Perraud S, Kanisawa K, Wang Z Z and Hirayama Y 2006 *Appl. Phys. Lett.* **89** 192110
- [25] van Vugt L K, Veen S J, Bakkers E P A M, Roest A L and Vanmaekelbergh D 2005 *J. Am. Chem. Soc.* **127** 12357–62
- [26] Durand C, Berthe M, Makoudi Y, Nys J P, Leturcq R, Caroff P and Grandidier B 2013 *Nanotechnology* **24** 275706
- [27] Nadar S, Rolland C, Lampin J F, Wallart X, Caroff P and Leturcq R 2015 *Nano Res.* **8** 980–9
- [28] Melitz W, Kent T, Kummel A C, Droopad R, Holland M and Thayne I 2012 *J. Chem. Phys.* **136** 154706
- [29] Savitzky B H, Hovden R, Whitham K, Yang J, Wise F, Hanrath T and Kourkoutis L F 2016 *Nano Lett.* **16** 5714–8
- [30] Whitham K, Yang J, Savitzky B H, Kourkoutis L F, Wise F and Hanrath T 2016 *Nat. Mater.* **15** 557–63
- [31] Trasobares J, Vaurette F, François M, Romijn H, Codron J L, Vuillaume D, Théron D and Clément N 2014 *Beilstein J. Nanotechnol.* **5** 1918–25
- [32] Okazaki S 2015 *Microelectron. Eng.* **133** 23–35
- [33] Fahed M, Desplanque L, Troadec D, Patriarache G and Wallart X 2016 *Nanotechnology* **27** 505301
- [34] Desplanque L, Bucamp A, Troadec D, Patriarache G and Wallart X 2018 *Nanotechnology* **29** 305705
- [35] Pastorek M *et al* 2019 *Nanotechnology* **30** 035301



## Influence of doping level and surface states in tunneling spectroscopy of an $\text{In}_{0.53}\text{Ga}_{0.47}\text{As}$ quantum well grown on $p$ -type doped $\text{InP}(001)$

N. A. Franchina Vergel,<sup>1</sup> A. Tadjine,<sup>1</sup> V. Notot,<sup>1</sup> M. Mohr,<sup>2</sup> A. Kouassi N'Guissan,<sup>3</sup> C. Coinon,<sup>1</sup> M. Berthe,<sup>1</sup> L. Biadala,<sup>1</sup> K. K. Sossoe,<sup>3</sup> M. M. Dzagli,<sup>3</sup> J.-C. Girard,<sup>4</sup> G. Rodary,<sup>4</sup> L. Desplanque,<sup>1</sup> R. Berndt,<sup>2</sup> D. Stiévenard,<sup>1</sup> X. Wallart,<sup>1</sup> C. Delerue,<sup>1</sup> and B. Grandidier<sup>1,\*</sup>

<sup>1</sup>Université Lille, CNRS, Centrale Lille, ISEN, Université Valenciennes, UMR 8520 - IEMN, F-59000 Lille, France

<sup>2</sup>Institut für Experimentelle und Angewandte Physik, Christian-Albrechts-Universität zu Kiel, D-24098 Kiel, Germany

<sup>3</sup>Laboratoire de Physique des Matériaux et Composants à Semi-Conducteurs (LPMCS), Département de Physique, FDS, Université de Lomé, 01 BP 1515 Lomé 1, Togo

<sup>4</sup>Centre de Nanosciences et de Nanotechnologies (C2N), UMR 9001 CNRS, University Paris Sud, University Paris-Saclay, 10 bd Thomas Gobert, 91120 Palaiseau, France



(Received 10 May 2019; revised manuscript received 25 August 2019; published 20 September 2019)

A steplike density of states is the hallmark of a two-dimensional electron gas. Here, scanning tunneling spectroscopy is used to investigate this property in the differential conductance of an  $\text{In}_{0.53}\text{Ga}_{0.47}\text{As}$  quantum well grown on  $p$ -type doped  $\text{InP}(001)$ . We show that the appearance of a steplike function in the conduction band strongly depends on both the hole concentration in the quantum well and the current injected into the quantized states. Based on four-point probe transport measurements and tunneling-induced light-emission spectroscopy, we discuss the physical mechanisms at the origin of the current and unveil the significant contribution of midgap surface states in the relaxation of the tunneling electrons. These surface states, via pinning of the Fermi level, also affect the potential landscape across the quantum well, as demonstrated by tight-binding calculations of the quantum well electronic structure.

DOI: [10.1103/PhysRevMaterials.3.094604](https://doi.org/10.1103/PhysRevMaterials.3.094604)

### I. INTRODUCTION

Scanning tunneling spectroscopy (STS) can provide a direct measurement of the electronic local density of states (LDOS) in quantum semiconductor structures [1–3]. In particular, when the electrons are confined in a quantum well, the density of states exhibits a sequence of steps that was directly observed in the conductance spectra of cleaved III-V semiconductor quantum wells, each step corresponding to an electron subband in the conduction band [4–6]. Crucial to the successful observation of a two-dimensional electron gas is the absence of surface states in the energy range corresponding to the electron subbands, a phenomenon which occurs when III-V zinc-blende semiconductors are cleaved to expose a (110) surface. This natural passivation repels the surface states far away from the band edges, allowing a direct tunneling into bulk states such as those corresponding to the low-lying states of the electron gas.

Even in the absence of surface states, the observation of the two-dimensional density of states (2D-DOS) may not be straightforward. First, the probability amplitude distribution varies from one subband to the other one. If the maximum of the distribution of a subband is too deep below the passivated surface, the contribution of this subband to the tunneling current becomes negligible due to the exponential decay of the current with the distance between the scanning tunneling microscopy (STM) tip and the surface of the sample [7].

Fluctuations in the distribution of subsurface dopants or point defects also affect the surface potential and may prevent the observation of the 2D-DOS. Next, the electric field induced by the STM tip can penetrate into the semiconductor and locally modify the band. Depending on the tip work function and shape, this effect may lead to the formation of a tip-induced quantum dot with additional peaks superimposed to the 2D-DOS, which differs from the expected steplike function [8]. Finally, the observation of a 2D-DOS not only depends on the injection of the current into the related states of the electron gas but also on how the electrons escape. Confining the electrons in a quantum well implies the existence of potential barriers. When the transmission probability through the potential barriers is high enough, a 2D-DOS is probed [9]. But when the transfer rate of the electron out of the quantum wells is similar to or smaller than the tunneling rate from the tip, the characteristic steplike LDOS may be lost due to charging.

In this work, we study the LDOS of an  $\text{InGaAs}$  quantum well grown on top of a  $p$ -type  $\text{InP}(001)$  substrate with STM. The  $\text{In}_{0.53}\text{Ga}_{0.47}\text{As}$  ternary compound semiconductor lattice matched to  $\text{InP}$  is widely used as a channel for high-frequency III-V metal oxide semiconductor field effect transistors (MOSFETs) due to its high electron mobility [10]. Moreover, it is a type-I heterostructure, where both the electrons and the holes are confined in the quantum well, producing light emission in the wavelength range from 1.3 to 1.6  $\mu\text{m}$ . As these wavelengths are close to the minimum attenuation and dispersion in optical fibers, it is also a key material for fiber-optic communication systems [11,12]. We

\*Corresponding author: [bruno.grandidier@isen.iemn.univ-lille1.fr](mailto:bruno.grandidier@isen.iemn.univ-lille1.fr)

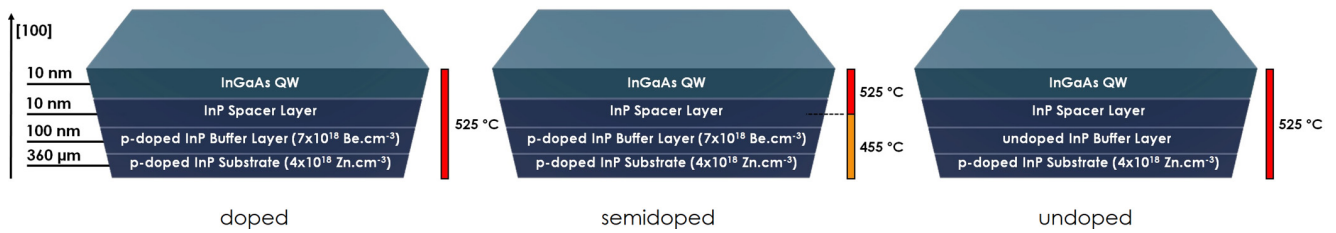


FIG. 1. Layer structure of the  $\text{In}_{0.53}\text{Ga}_{0.47}\text{As}$  quantum wells grown on InP (001) by molecular beam epitaxy. The doping of the InP buffer layer and the occurrence of an interruption step during the growth of the heterostructure to change the sample temperature allows growth of quantum wells with different hole doping levels. Depending on the degree of Be diffusion during the growth, the samples are labeled *doped*, *semidoped*, and *undoped*.

show that scanning tunneling spectroscopy performed on the InGaAs (001) surface can reveal the 2D-DOS of the quantum well. However, the spectral shape is found to strongly depend on the doping level and the tunneling current. At high doping level and low tunneling setpoint currents, three steps in the DOS are observed in the conduction band of the quantum well, consistent with tight-binding calculations, in which the potential confinement is modified from a square to a triangular well due to a pinning of the Fermi level by midgap surface states. For decreasing doping levels, the observation of the steplike function becomes erratic and even disappears. At the lowest doping level, a new peak occurs close to the Fermi level. Based on STM-induced luminescence experiments and four-point probe STM transport measurements, we are able to rationalize this behavior and explain the charge-transport mechanisms that account for the presence of a 2D-DOS in the tunneling spectra. These experiments highlight the importance of surface states in the relaxation of tunneling electrons.

## II. EXPERIMENTAL AND THEORETICAL DETAILS

$\text{In}_{0.53}\text{Ga}_{0.47}\text{As}/\text{InP}$  quantum well (QW) heterostructures were grown by molecular beam epitaxy on a Zn *p*-type doped InP (001) substrate with a concentration of  $4 \times 10^{18} \text{cm}^{-3}$ . The samples (Fig. 1) consist of a top 10-nm-thick  $\text{In}_{0.53}\text{Ga}_{0.47}\text{As}$  quantum well, a 10-nm-thick InP spacer layer, and a 100-nm-thick undoped/*p*-doped InP buffer layer. Three samples with different Be dopant concentrations were prepared. For the sample denoted “doped,” the whole structure was grown at 525 °C. This high temperature favors the diffusion of beryllium in the quantum well [13]. In order to reduce the amount of dopants in the quantum well, a second structure, the “semidoped” structure, was prepared at a lower temperature of 455 °C up to the half part of the InP spacer layer. The growth was then interrupted and the temperature was raised to 525 °C before growing the  $\text{In}_{0.53}\text{Ga}_{0.47}\text{As}/\text{InP}$  heterointerface. As to the third sample, labeled the “undoped” sample, the growth temperature was set at 525 °C and no dopant was intentionally incorporated during the growth. At the end of the growth, a 10-nm-thick amorphous As layer was deposited on top of the samples to protect their surface from air exposure. In order to measure the dopant concentrations in these samples with secondary ion mass spectrometry (SIMS), similar samples were grown. But instead of capping the heterostructure with a thin As layer, a 10-nm-thick undoped InP layer was grown on top of the  $\text{In}_{0.53}\text{Ga}_{0.47}\text{As}$  quantum well in

order to minimize SIMS artefacts during the initial stage of the sputtering process [14].

As the temperature used to desorb the As capping layer of an InGaAs (001) surface is known to affect the surface reconstruction [15], arsenic decapping tests were directly done after the deposition of the protective layer and monitored using reflection high-energy electron diffraction (RHEED). In this way, we were able to follow the temperature dependence of the surface reconstruction. At 340 °C, the surface exhibited a  $(2 \times 4)$  As reconstruction. This As-rich surface reconstruction survived up to 445 °C before being replaced by the group-III rich  $(4 \times 2)$  reconstruction. In order to limit the diffusion of impurities, the As protective layer was decapped at a low temperature of 350 °C for 2 h, thus yielding a  $(2 \times 4)$  As reconstruction. Any modification of the surface properties due to this annealing step was further analyzed with ultraviolet photoelectron spectroscopy (UPS). This study was performed with a discharge lamp operating at 21.2 eV (He-I) in the same ultrahigh vacuum (UHV) system as the growth chamber. As shown in Fig. 2, both UPS spectra measured on the *semidoped* sample prior to the As capping or after the sublimation of the As capping layer exhibit a Fermi-level pinning  $0.50 \pm 0.05$  eV above the top of the valence band

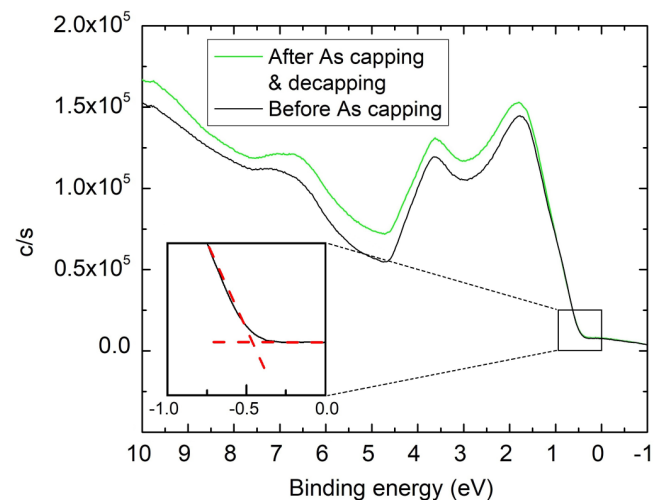


FIG. 2. UPS spectra acquired before the As capping (black line) and after the As decapping (green line). Inset: High magnification of the valence band edge. The top of the valence band is given by the intersection of the dashed straight lines.



edge. A stable position of the Fermi level is consistent with the preservation of the  $(2 \times 4)$  As reconstruction. It also indicates that the dopant concentration in the quantum well is certainly not affected by the annealing, since a significant diffusion of  $p$ -type dopants close to the surface is known to shift the Fermi level towards the valence band edge, despite a high concentration of surface states in the bulk band gap [16].

STM experiments were performed in four different UHV systems. Low-temperature (LT) STM measurements were done at 77 or 5 K with an Omicron LT-STM and an Unisoku USM 1300 LT-STM. In these systems, the differential conductance was acquired with a lock-in amplifier using a bias modulation of 10 mV rms at a frequency of 490 Hz. The apparent band gap was measured by plotting the differential conductance in a log scale to precisely determine the noise level. Light-emission spectroscopy with STM (STM-LE) was done at 5 K combining a home-built LT-STM with a system of lenses mounted inside the vacuum chamber [17]. The collected tip-sample junction emission was then guided via an optical fiber to a spectrometer (Horiba iHR 320) and a liquid-nitrogen-cooled CCD detector (Horiba Symphony II CCD). A four-probe STM (Nanoprobe, Omicron) that was operated at room temperature with a control system able to run four STM tips independently was used to measure the DC conductivity of the InGaAs QW. For these measurements, the tips were positioned in a linear configuration, either with equidistant tip spacing or with a linear nonequidistant probe arrangement, in order to minimize the number of tips to be repositioned at the surface of the  $\text{In}_{0.53}\text{Ga}_{0.47}\text{As}$  quantum well [18]. Prior to all the characterizations performed with the different STM setups, the As capping layer was sublimated in a connected preparation chamber using the temperature and time given above.

The calculations of the electronic structure of the  $\text{In}_{0.53}\text{Ga}_{0.47}\text{As}/\text{InP}$  heterostructure were performed using a tight-binding approach. The  $\text{In}_{0.53}\text{Ga}_{0.47}\text{As}$  alloy was considered as a virtual crystal in which a virtual atom (Va) replaces each In or Ga atom. Each atom in the heterostructure (Va, As, In, P) was described by 20 atomic orbitals,  $sp^3d^5s^*$  for each spin orientation. We used the tight-binding parameters of Ref. [19] which give an energy gap of 816 meV for the  $\text{In}_{0.53}\text{Ga}_{0.47}\text{As}$  bulk, consistent with Ref. [20]. Based on the literature [21], we assumed a conduction-band offset between  $\text{In}_{0.53}\text{Ga}_{0.47}\text{As}$  and InP of 204 meV and an infinite potential barrier at the vacuum/ $\text{In}_{0.53}\text{Ga}_{0.47}\text{As}$  interface. Free surfaces were saturated by pseudohydrogen atoms described by a single  $s$  orbital.

### III. RESULTS AND DISCUSSION

#### A. Spectral shape of the $I(V)$ characteristics

Figure 3(a) shows a typical STM topograph of the  $\text{In}_{0.53}\text{Ga}_{0.47}\text{As}$  (001) surface. The large-scale image reveals jagged terraces with an average width of 40 nm. The measured step height is around 2.9 Å, corresponding to an atomic bilayer thickness. At higher resolution [Fig. 3(b)], rows of bright protrusions are clearly resolved. As depicted in the structural model of Fig 3(c), the largest protrusions correspond to two adjacent As dimers. The trenches between the rows are caused

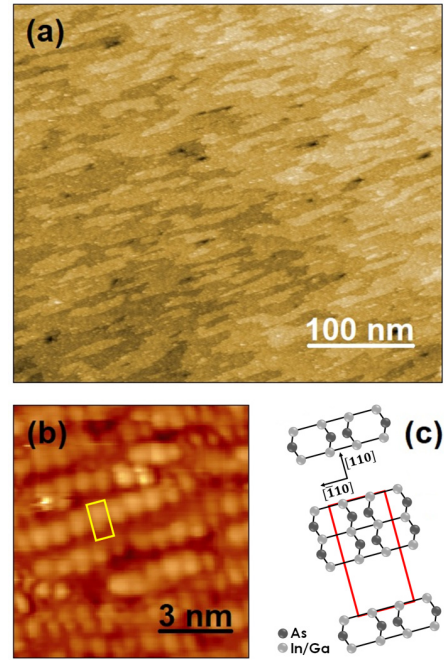


FIG. 3. (a) Large-scale STM image of the (001) surface of the  $\text{In}_{0.53}\text{Ga}_{0.47}\text{As}/\text{InP}$  heterostructure. (b) High-resolution STM image. Feedback parameters:  $V_s = +1.8$  V and  $I_t = 10$  pA,  $T = 77$  K. (c) Structural model of the  $\text{In}_{0.53}\text{Ga}_{0.47}\text{As}(001)-(2 \times 4)$  surface reconstruction with the rectangular unit cell.

by missing dimers. The zigzag structure indicates that the smallest protrusions are single As dimers, located either on the left or the right of a row. This reconstruction is typical of the As-rich  $(2 \times 4)$  structure observed for the  $\text{In}_{0.53}\text{Ga}_{0.47}\text{As}$  (001) surface [15].

Tunneling spectroscopy was first performed on the *doped* sample [Fig. 4(a)]. In the spectra, the valence band states are probed at negative bias. The Fermi-level  $E_F$  is determined at 0 V, and based on the onset of the valence band (labeled  $E_V$ ), it is found to be positioned  $0.17 \pm 0.03$  eV above the top of the valence band. A sequence of three steps is visible at positive voltages. Based on the position of the first step edge and the onset of the valence band, we measure an apparent band gap of  $0.90 \pm 0.03$  eV, which is consistent with the energy of the photoluminescence peak obtained for a 10-nm-thick  $\text{In}_{0.53}\text{Ga}_{0.47}\text{As}$  QW inserted between two InP potential barriers [22,23]. In a previous report on tunneling experiments [9], the three steps were attributed to the electron subbands of the QW. Although the thickness of the  $\text{In}_{0.53}\text{Ga}_{0.47}\text{As}$  QW grown on InP (111)A was identical, the potential barrier consisted of an  $\text{In}_{0.58}\text{Al}_{0.42}\text{As}$  layer, resulting in a stronger confinement in the conduction band. Moreover, the doping of the InP buffer was  $n$  type instead of  $p$  type in the present work. Therefore, to understand the origin of the three steps, we assessed the confinement potential profile in the heterostructure that is likely to change with the type of doping. For that purpose, we estimated the band bending at the surface of the quantum well, taking into account the proximity of the STM tip. To simplify the problem, we considered a bulk  $\text{In}_{0.53}\text{Ga}_{0.47}\text{As}$  sample and solved the Poisson equation, taking into account the

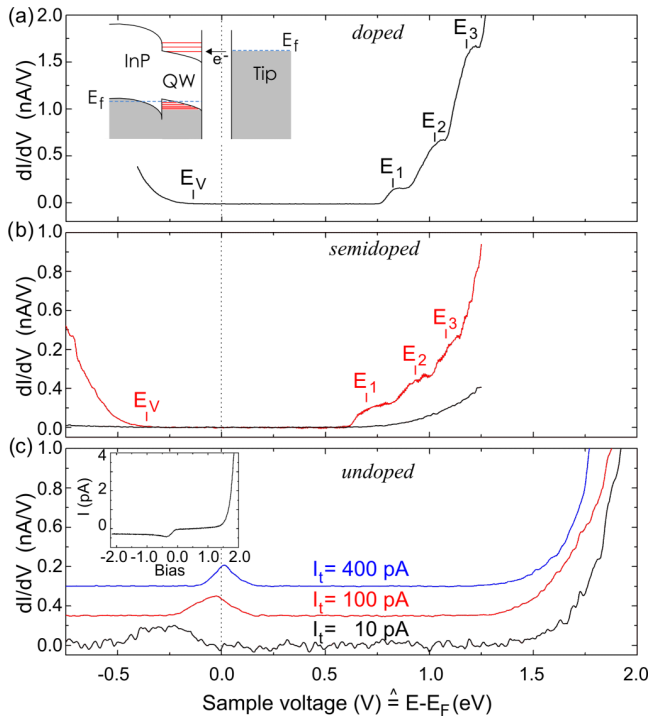


FIG. 4.  $dI/dV$  spectra acquired on the (a) *doped*, (b) *semidoped*, and (c) *undoped*  $\text{In}_{0.53}\text{Ga}_{0.47}\text{As}/\text{InP}$  heterostructures measured at 77 K. For the *semidoped* sample, two different types of spectra were measured as a function of the area probed by the STM tip. For the *undoped* sample, the same area was probed with different setpoint currents indicated in the graph. The three electron subbands and the top of the valence band are labeled  $E_1$ ,  $E_2$  and  $E_3$  and  $E_V$  in (a) and (b). Insets: (a) Band diagram of the tunneling junction with the first electron subband aligned with the tip Fermi level  $E_f$ . (c)  $I(V)$  characteristic measured at a setpoint current of 10 pA. Feedback parameters: (a)  $V_s = +1.30 \text{ V}/I_{\text{setpoint}} = 400 \text{ pA}$ , (b)  $V_s = +1.25 \text{ V}/I_{\text{setpoint}} = 400 \text{ pA}$ , and (c)  $V_s = +2.0 \text{ V}$ .

boundary condition at the vacuum/semiconductor interface [24]. We assumed a Gaussian band of surface states centered 0.4 eV above the top of the valence band with a density of  $3 \times 10^{12} \text{ cm}^{-2}$  that was found for a *p*-type GaAs (001) surface having the same reconstruction [16]. This density pins the Fermi level close to midgap for small doping levels, consistent with the UPS measurements of the *semidoped* sample. It is, however, insufficient to keep the Fermi-level midgap at higher doping levels, so that it complies with a shift of the Fermi level closer to the valence band, as the doping level in the quantum well increases. As seen in the inset of Fig. 5, taking a *p*-type doping concentration of  $1 \times 10^{18} \text{ cm}^{-3}$  results in a downward band bending extending over 10 nm in the semiconductor material, even at a positive bias of 0.8 V. This bias corresponds to the alignment of the tip Fermi level with the first electron subband of the quantum well. A similar band profile is also found at a bias of +1.0 V, although the band bending is reduced by 50 meV. These results indicate that the potential distribution in the well can be considered as triangular over the whole range of positive bias used to probe the LDOS of the QW.

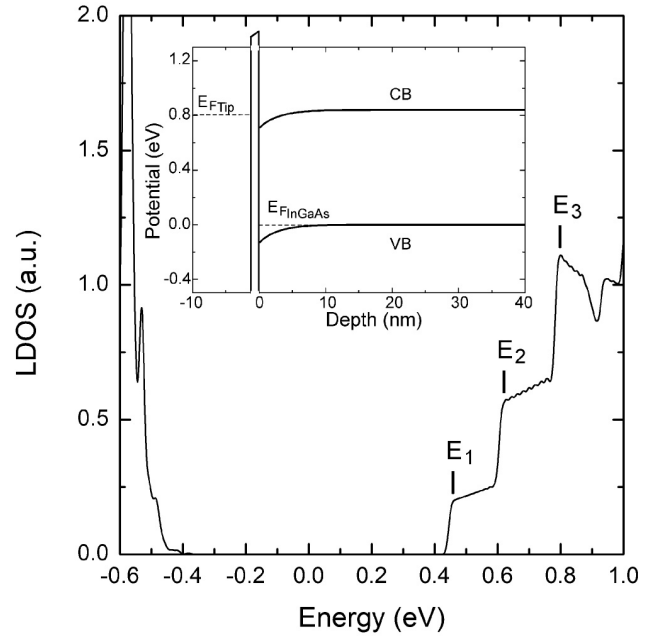


FIG. 5. Theoretical LDOS obtained from tight-binding calculations. The three electron subbands are labeled  $E_1$ ,  $E_2$ , and  $E_3$ . Inset: Band diagram of the metal-vacuum- $\text{In}_{0.53}\text{Ga}_{0.47}\text{As}$  at 77 K for a sample bias of 0.8 V. The tip-induced band bending was calculated with the SEMITIP code [24], assuming a doping level of  $1 \times 10^{18} \text{ cm}^{-3}$ , a tip radius of 5 nm, a tip-sample distance of 5 Å, and a band of surface states positioned at an energy of 0.4 eV above the top of the valence band with a density of  $3 \times 10^{12} \text{ cm}^{-2}$ . The conduction and valence bands are labeled CB and VB, respectively. The dashed lines indicate the positions of the Fermi level in the tip (left) and in  $\text{In}_{0.53}\text{Ga}_{0.47}\text{As}$  (right).

Therefore, the LDOS calculated within the tight-binding approximation was not only obtained for a flat potential distribution across the heterostructure but also for a triangular well. This potential shape results from the pinning of the Fermi level by the surface states existing at the vacuum/ $\text{In}_{0.53}\text{Ga}_{0.47}\text{As}$  interface. While a flat potential distribution leads to two quantized states in the conduction band, the calculations for the triangular well reveals three steps at positive energies (Fig. 5), consistent with the STS measurements of the *doped* sample. We note that small oscillations in the LDOS are induced by the finite  $k$  sampling in the Brillouin zone. The theoretical separation between the quantized states  $E_2-E_1$  of 0.16 eV and  $E_3-E_2$  of 0.18 eV fits well with the experimental values of 0.17 and 0.19 eV, indicating that the potential in the tip/vacuum/sample junction almost fully drops in the vacuum due to a high concentration of holes in the quantum well.

In contrast to the *doped* sample, where the three steps are observed on the whole surface, the *semidoped* sample shows two types of spectra [Fig. 4(b)]. The first one is similar to the *doped* sample: the differential conductance yields three steps at positive bias. We note that the step width and the apparent band gap ( $1.00 \pm 0.03 \text{ eV}$ ) are slightly larger. Moreover, the Fermi-level position is shifted to a higher energy at the surface of the  $\text{In}_{0.53}\text{Ga}_{0.47}\text{As}$  quantum well. It is now  $0.38 \pm 0.03 \text{ eV}$

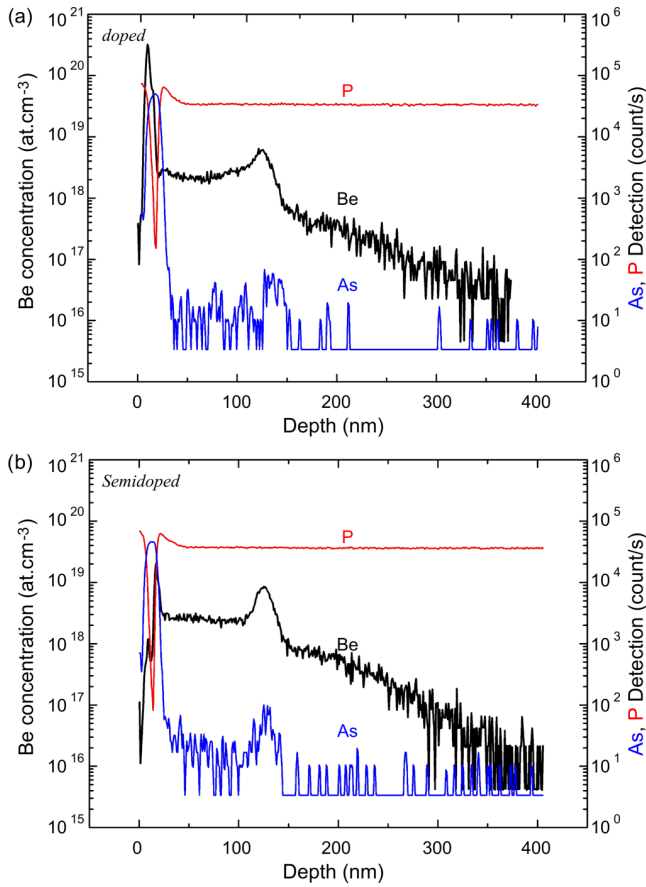


FIG. 6. Depth profiles of the Be, P, and As atomic elements in the (a) *doped* and (b) *semidoped* samples capped with a 10-nm-thick InP layer instead of the As amorphous layer.

above the onset of the valence band, closer to the energy measured with UPS in Fig. 2. As to the second type of spectra, the differential conductance does not show the steplike function expected for a quantum well at positive bias. The weaker signal measured at both positive and negative biases corresponds to an exponential increase of the current with the bias, yielding an apparent band gap of  $1.20 \pm 0.03$  eV.

Finally, for the *undoped* sample, spatially resolved tunneling spectra do not show any features in the energy range of the three steps [Fig. 4(c)]. The onset at positive bias is shifted to 1.25 V at a setpoint current of 400 pA. This value corresponds to the transition between the third step and the exponential increase obtained for the *semidoped* sample. At negative bias, no signal is measured and a peak is clearly seen in the vicinity of the Fermi level. This peak is found to shift towards the Fermi level with increasing setpoint currents and its origin will be discussed later. Based on the different spectra observed between the three samples, it is straightforward that the doping level of the structure has a direct impact on the occurrence of the 2D-DOS.

### B. Importance of the hole concentration in the quantum well

Despite the similarity of the doping level incorporated during the growth of the *doped* and *semidoped* samples, the different spectra of Fig. 4 indicate a significant modification

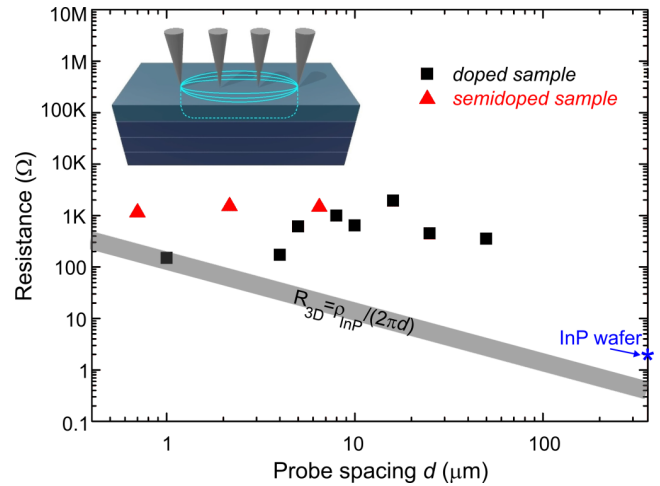


FIG. 7. Room-temperature four-point probe resistance of the  $\text{In}_{0.53}\text{Ga}_{0.47}\text{As}/\text{InP}$  heterostructure for the *doped* and *semidoped* samples as a function of the probe spacing  $d$ . The probes are arranged in a collinear array with equidistant contact spacing, as shown by the inset. The penetration depth of the current distribution is limited to the quantum well. The light-gray band highlights the variation of the resistance for three-dimensional semi-infinite bulk InP, which is inversely proportional to the probe spacing with a bulk resistivity of  $0.08 \Omega \text{ cm}$ . The blue star shows the measured four-point probe resistance of the InP substrate only.

of the doping profile in the heterostructure. As a result, the Be concentration was analyzed by SIMS. Figure 6 reveals a strong Be dopant redistribution with respect to the intended dopant profile, since the incorporation of Be dopants during the growth occurred in the 100-nm-thick InP buffer located 30 nm below the surface only. In both profiles, a smaller Be concentration than  $7 \times 10^{18} \text{ cm}^{-3}$  was measured in this region, whereas several peaks are visible at the interfaces and surface of the sample. This redistribution agrees with previous analyses of InGaAs and InGaAs/InP heterostructures upon annealing [13,25,26]. It increases with higher growth temperatures and results in a much higher doping level of the QW for the *doped* sample in comparison with the *semidoped* sample, consistent with the STS findings. To ascertain the electrical activation of the Be dopants in the quantum well region, four-point probe measurements of the resistivity were performed. For the *undoped* sample, the absence of doping in the whole structure led to poor electrical contact between the tips and the surface, preventing the measurement of the four-probe resistance  $R_{4p}$ . As to the *doped* and *semidoped* samples, we were able to measure  $R_{4p}$  as a function of the tip separation, as shown in Fig. 7. Although the data scatter more for the *doped* sample due to a repositioning of the tips in different areas of the sample and along different crystallographic orientations, the resistance can be considered independent of the distance between the probes [27]. This behavior is in contrast to the typical increase of the resistance for a homogeneous and isotropic thick-enough three-dimensional resistive doped InP semiconductor indicated by the tilted band in Fig. 7 [28]. It is the signature of a two-dimensional transport [29].



While the band offset is large enough to prevent the penetration of the current into the InP layers, transport involves two current paths that we consider to be spatially separated: one in the quantum well and one at its surface through the band of surface states. Thus we assume a parallel-circuit model, where the four-probe resistance  $R_{4p}$  is given by

$$\frac{1}{R_{4p}} = \frac{1}{R_{QW}} + \frac{1}{R_{SS}}, \quad (1)$$

with  $R_{QW}$  the resistances of the QW and  $R_{SS}$  the resistance related to the transport through the surface states. The conductivity of the quantum well varies with the hole concentration, which itself imposes the position of the Fermi level at the surface of the quantum well. Due to the pinning of the Fermi-level midgap at the surface of the *semidoped* sample and a hole concentration that is smaller than  $1 \times 10^{19} \text{ cm}^{-3}$  over a large fraction of the QW thickness, the QW of the *semidoped* sample is largely depleted in holes. Taking a conductance channel with a width  $t$  smaller than the full width of the QW, the resistance of the QW is

$$R_{QW} = \frac{\ln 2}{\pi t e \mu_p p}, \quad (2)$$

where  $\mu_p$  and  $p$  are the hole mobility and the hole concentration, respectively. A hole concentration of  $1 \times 10^{19} \text{ cm}^{-3}$  results in a mobility of about  $70 \text{ cm}^2 \text{ V}^{-1} \text{ s}^{-1}$  [30]. Assuming a QW width of 5 nm at most yields a four-probe resistance higher than  $4 k\Omega$ , which cannot explain the measured resistance of  $1373 \Omega$ . Therefore, the second channel through the band of surface states is less resistive. Neglecting the transport through the QW gives a sheet resistance  $R_{\text{sheet}} = \pi R_{4p} / \ln 2$ , which corresponds to a surface conductivity of  $1.6 \times 10^{-4} \text{ S}/\square$ . This value is in the range of the typical surface conductivities measured for the Ge(001) and Si(001) surfaces consisting of rows of dimers [31] and accounts for the transport properties at the surface of the *semidoped* sample.

For the *doped* sample, the resistance  $R_{4p}$  is smaller. Due to the high doping level of the QW, as found by SIMS, the contribution of the QW cannot be neglected anymore. Also, the surface-state density should not be affected by the change of the  $p$ -type doping level [16]. Therefore, assuming a similar surface conductivity as the one found for the *semidoped* sample, a mean resistance  $R_{4p}$  of  $661 \Omega$  yields a conductivity in the quantum well of  $173 \text{ S cm}^{-1}$ . This high conductivity matches an average hole concentration of a few  $10^{19} \text{ cm}^{-3}$ , for which the mobility is about  $50 \text{ cm}^2 \text{ V}^{-1} \text{ s}^{-1}$  [30]. Such a concentration, which is smaller than the measured concentration of Be atoms in the QW, suggests that the Be atoms that have segregated to the surface of the sample might not be electrically active.

### C. Origin of transport through the quantum states

At this point, while a high concentration of holes in the quantum well is required to detect the 2D-DOS, its impact for the formation of a steady-state current measured through the quantum well states is not yet clear. At low temperature, a conduction-band offset around 200 meV prevents the emission of electrons from  $E_1$  into the InP conduction band. Hence, the electrons must recombine with holes from the valence

band. This effect is clearly demonstrated by the tunneling spectra of the “undoped” sample in Fig. 4(c), where the steplike function is not visible. When holes are absent, the tunneling electrons that are transferred from the tip to the first electron subband cannot recombine with holes in the quantum well, causing the charging of the quantum well. A higher voltage is thus required to transfer electrons from the tip states to the InP conduction band via the delocalized states of the quantum well. The onset of the exponential increase of the current occurs at a bias of +1.25 V instead of +0.50 V, which corresponds to the resonance of the tip Fermi level with the bottom of the InP conduction band via the delocalized states of an uncharged quantum well.

In the *doped* and *semidoped* samples, the presence of holes in the quantum well allows a current to run through the electron subbands. With increasing setpoint currents, we expect the tip-induced band bending to be stronger, causing a local modification of the potential that is known to extend over tens of nanometers laterally [32]. This effect induces a weak confinement of  $E_1$ . Assuming a small degree of localization for  $E_1$  allows the current injected from the STM tip via  $E_1$  to be written as

$$I = -e(1 - f)W_t, \quad (3)$$

with  $e$  the electron charge,  $W_t$  the transmission probability per unit of time across the tunneling barrier, and  $f$  the occupation probability of the quantum level. In the steady-state regime, this current is equal to the current emitted from  $E_1$  to the valence band of the quantum well:

$$I = -efW_r, \quad (4)$$

where  $W_r$  is the recombination rate of the electron on  $E_1$ .

Eliminating  $f$  from both equations results in the following expression for the current:

$$I = -e \frac{1}{\left(\frac{1}{W_t} + \frac{1}{W_r}\right)}. \quad (5)$$

Therefore, the current should be limited by the slowest process. As shown in Fig. 8, the differential conductance was acquired at different setpoint currents on the *doped* sample. The three electron subbands are visible up to 600 pA without any energy shift in their position. Focusing on the variation of the current measured at the plateau corresponding to the ground states  $E_1$  (inset of Fig. 8), the current increases smoothly below 300 pA, more abruptly between 300 and 400 pA, and then saturates at around 10 pA, consistent with transport through a single quantum level involving two processes. As long as the probability  $W_t$ , which increases exponentially with setpoint current, is smaller than  $W_r$ , the current increases. Once it exceeds  $W_r$ , the current transferred through  $E_1$  saturates, yielding a recombination rate  $W_r$  of one electron every 16 ns. We note that a further increase of the setpoint current to 700 pA causes a change of the differential conductance characteristic. At positive bias, the onset is shifted to a smaller bias, whereas at negative bias, a strong peak appears, indicating a change of the potential distribution across the heterostructure that could be caused by the proximity of the STM tip. From these observations, we infer a stronger downward band bending, which causes

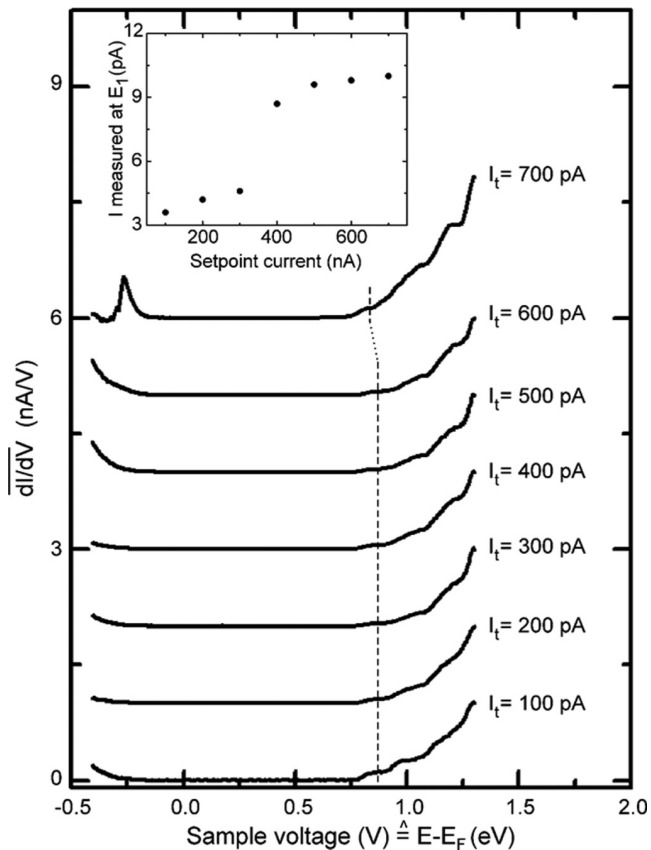


FIG. 8. Normalized  $dI/dV$  spectra acquired on the *doped*  $\text{In}_{0.53}\text{Ga}_{0.47}\text{As}/\text{InP}$  heterostructure with different setpoint currents at 77 K. Feedback parameters:  $V_s = +1.30$  V, the setpoint currents are indicated in the graph. Inset: Current measured at a bias of  $+0.86$  V between 100 and 600 pA and  $+0.83$  V for 700 pA. These biases, highlighted by the dashed line in the main figure, correspond to the plateau of the first electron subband  $E_1$  in the  $dI/dV$  characteristics.

the depletion of the wells with holes. As a result, once the tunneling electrons have left the highest occupied valence quantized states, the states become charged, which accounts for the asymmetric peak measured at negative bias.

In order to determine the nature of the recombination processes, the *doped* sample was analyzed with STM-LE. High currents had to be used to detect the emission of photons with energies smaller than the InP bulk band gap. The data of Fig. 9 were recorded at a sample voltage of  $+3.0$  V, i.e., for electron injection, and a current of  $20 \mu\text{A}$ . The spectrum exhibits several emission bands with photon energies smaller than the bulk band gap of InP (1.42 eV at 5 K). The most intense band at high energy (HEB), with a maximum centered at 1.37 eV, is similar to the peak found in typical photoluminescence spectra of *p*-type InP substrates [33]. Its shape is known to change with the acceptor chemical nature, the acceptor concentration, and the excitation power [34,35]. The origin of the photoluminescence has been attributed to the free-to-bound exciton transition at higher energy and transitions between donor and acceptor bands at lower energy, accounting for two contributions in this band.

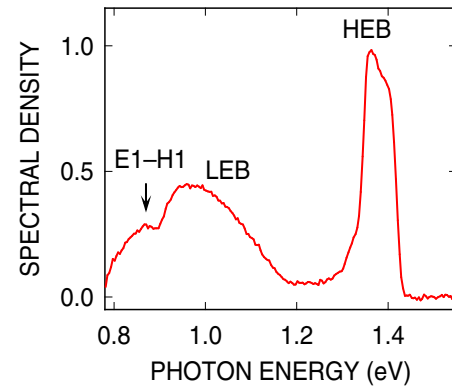


FIG. 9. Normalized tunneling-induced luminescence spectrum recorded at a sample voltage  $V_s = +3.0$  V and tunneling current  $I = 20 \mu\text{A}$  over an integration time of 400 s. The spectrum is corrected for detector response. The direct transition in the  $\text{In}_{0.53}\text{Ga}_{0.47}\text{As}$  quantum well is labeled  $E_1\text{-H}_1$ , while the low and high energy bands arising from the InP layers and substrates are labeled LEB (low-energy band) and HEB (high energy band), respectively.

At lower energies, the spectrum exhibits a broad band extending from 0.9 to 1.2 eV. Comparison with photoluminescence experiments of InP substrates with a high concentration of Zn acceptor impurities suggests that this band is the so-called low-energy band (LEB) [36]. It was found to be stable over a wide range of excitation powers in photoluminescence [36] and has been attributed to deep levels of the *p*-type InP substrate. Conversely, the band below 0.9 eV has never been reported from *p*-type InP. It is centered at an energy of 0.85 eV, which matches the energy of the exciton measured in an  $\text{In}_{0.53}\text{Ga}_{0.47}\text{As}/\text{InP}$  heterostructure with the same quantum well thickness [22,23]. As a result, we assign it to the radiative emission of the  $\text{In}_{0.53}\text{Ga}_{0.47}\text{As}$  quantum well.

Comparison of the recombination rate  $W_r$  with the exciton lifetime of similar heterostructures reveals a slightly longer lifetime with respect to a few to tens of nanoseconds range usually measured [37,38]. This difference could be caused by a reduced overlap between the electron and hole wave functions in the triangular well of the STM junction, with the electron localized at the surface and the hole at the  $\text{In}_{0.53}\text{Ga}_{0.47}\text{As}/\text{InP}$  interface. However, the proximity of the STM tip in the light-emission experiments may modify the potential across the well. Moreover, the high current used is likely to saturate all nonradiative recombination centers at the surface, allowing a large fraction of the tunneling electrons to recombine radiatively [39]. We therefore believe that the relaxation of the tunneling electrons transferred to the conduction quantum levels also involves a nonradiative recombination process through the surface states [40,41].

While it is not clear why the surface states are not detected in the tunneling spectra measured on the *doped* and *semi-doped* samples, consistent with previous studies [9,16,42], the existence of surface states clearly appears when tunneling spectroscopy is performed on the “*undoped*” sample. A peak is observed in the differential conductance at small negative bias in Fig. 4(c). This peak shifts towards higher energies as the tip gets closer to the surface, to become finally centered at the Fermi level. Also, the current converges towards zero

as the sample voltage becomes more negative, as seen in the inset of Fig. 4(c). We attribute this effect to the charging of the surface states near the Fermi level. Due to the lack of enough free charge carriers in the quantum well, the electrons transferred at negative bias from the surface states to the unoccupied tip states cannot be replaced at a rate high enough, leading to positively charged surface states. Hence, the downward band bending increases, preventing the unoccupied tip states from becoming resonant with the valence band states of the quantum well for voltages higher than  $-2.0$  V. In this voltage range, the number of states contributing to the current does not significantly increase, but the transmission across the tunneling barrier gets smaller as the bias decreases. This effect accounts for the  $I(V)$  characteristic obtained at negative bias and demonstrates the key role of the surface states in the tunneling spectra of the “undoped” sample. We note that the significant surface conductivity of the  $\text{In}_{0.53}\text{Ga}_{0.47}\text{As}$  (001) surface could help in discharging the surface states. However, similar to the localization of the electron subbands induced by the proximity of the polarized STM tip, we expect a localization of the surface states under the STM tip that strongly decouples the states from the band of surface states.

#### IV. CONCLUSION

In summary, we have investigated the density of states of an  $\text{In}_{0.53}\text{Ga}_{0.47}\text{As}$  QW grown on a  $p$ -type doped InP barrier. We show that the appearance of a steplike function in the tunneling spectra, the signature of a 2D-DOS, depends on the

hole concentration in the QW. As the conduction-band offset between the  $\text{In}_{0.53}\text{Ga}_{0.47}\text{As}$  quantum well and the InP barrier does not allow the escape of electrons from the quantized states into the InP conduction band at low temperature, the tunneling electrons recombine with the holes provided by the diffusion of Be dopant atoms during the growth. We show that two mechanisms are at work in this recombination: a radiative transition that gives rise to luminescence and a nonradiative recombination through the surface states of the quantum well. For the As-rich surface reconstruction of the  $\text{In}_{0.53}\text{Ga}_{0.47}\text{As}$  quantum well, these surface states are located in the lowest part of the quantum well band gap, away from the conduction quantized levels, leaving the electron subbands accessible to tunneling electrons. While their presence greatly benefits the electron relaxation, they also account for the observation of three electron subbands in the conduction band of the QW. However, their density is insufficient to screen the electrical field induced by the proximity of the tip. As a result, fluctuation in the hole density at smaller Be concentrations results in stronger tip-induced band potential fluctuations at the surface of the QW, which alters the 2D-DOS and prevents the observation of the steplike function.

#### ACKNOWLEDGMENTS

This study was financially supported by the French National Research Agency (Dirac III-V Project No. ANR-16-CE24-0007-01, Mechaspin Project No. ANR-17-CE24-0024-02), the EQUIPEX program Excelsior (Grant No. ANR-11-EQPX-0015), and the RENATECH network.

- 
- [1] U. Banin, Y. Cao, D. Katz, and O. Millo, *Nature (London)* **400**, 542 (1999).
  - [2] D. D. D. Ma, C. S. Lee, F. C. K. Au, S. Y. Tong, and S. T. Lee, *Science* **299**, 1874 (2003).
  - [3] A. Urbietta, B. Grandidier, J. P. Nys, D. Deresmes, D. Stiévenard, A. Lemaître, G. Patriarche, and Y. M. Niquet, *Phys. Rev. B* **77**, 155313 (2008).
  - [4] R. M. Feenstra, D. A. Collins, D. Z.-Y. Ting, M. W. Wang, and T. C. McGill, *Phys. Rev. Lett.* **72**, 2749 (1994).
  - [5] K. Suzuki, K. Kanisawa, C. Janer, S. Perraud, K. Takashina, T. Fujisawa, and Y. Hirayama, *Phys. Rev. Lett.* **98**, 136802 (2007).
  - [6] S. Becker, M. Liebmann, T. Mashoff, M. Pratzner, and M. Morgenstern, *Phys. Rev. B* **81**, 155308 (2010).
  - [7] M. Morgenstern, A. Georgi, C. Straßer, C. R. Ast, S. Becker, and M. Liebmann, *Phys. E (Amsterdam, Neth.)* **44**, 1795 (2012).
  - [8] M. Morgenstern, J. Klijn, Chr. Meyer, M. Getzlaff, R. Adelung, R. A. Römer, K. Rosnagel, L. Kipp, M. Skibowski, and R. Wiesendanger, *Phys. Rev. Lett.* **89**, 136806 (2002).
  - [9] S. Perraud, K. Kanisawa, Z. Z. Wang, and T. Fujisawa, *Phys. Rev. B* **76**, 195333 (2007).
  - [10] J. A. Del Alamo, *Nature (London)* **479**, 317 (2011).
  - [11] G. Ribordy, N. Gisin, O. Guinnard, D. Stuck, M. Wegmüller, and H. Zbinden, *J. Mod. Opt.* **51**, 1381 (2004).
  - [12] N. Namekata, S. Sasamori, and S. Inoue, *Opt. Express* **14**, 10043 (2006).
  - [13] S. Koumetz, J. Marcon, K. Ketata, M. Ketata, C. Dubon-Chevallier, P. Launay, and J. L. Benchimol, *Appl. Phys. Lett.* **67**, 2161 (1995).
  - [14] P. C. Zalm, *Rep. Prog. Phys.* **58**, 1321 (1995).
  - [15] J. Shen, D. L. Winn, W. Melitz, J. B. Clemens, and A. C. Kummel, *ECS Trans.* **16**, 463 (2008).
  - [16] M. D. Pashley, K. W. Haberern, R. M. Feenstra, and P. D. Kirchner, *Phys. Rev. B* **48**, 4612 (1993).
  - [17] G. Hoffmann, J. Kröger, and R. Berndt, *Rev. Sci. Instrum.* **73**, 305 (2002).
  - [18] S. Just, M. Blab, S. Korte, V. Cherepanov, H. Soltner, and B. Voigtländer, *Phys. Rev. Lett.* **115**, 066801 (2015).
  - [19] L. C. Post, T. Xu, N. A. Franchina Vergel, A. Tadjine, Y. Lambert, F. Vaurette, D. Yarekha, L. Desplanque, D. Stiévenard, X. Wallart, B. Grandidier, C. Delerue, and D. Vanmaekelbergh, *Nanotechnology* **30**, 155301 (2019).
  - [20] I. Vurgaftman, J. R. Meyer, and L. R. Ram-Mohan, *J. Appl. Phys.* **89**, 5815 (2001).
  - [21] P. E. Smith, S. H. Goss, M. Gao, M. K. Hudait, Y. Lin, S. A. Ringel, and L. J. Brillson, *J. Vac. Sci. Technol. B* **23**, 1832 (2005).



- [22] K. W. Carey, R. Hull, J. E. Fouquet, F. G. Kellert, and G. R. Trott, *Appl. Phys. Lett.* **51**, 910 (1987).
- [23] E. H. Reihlen, A. Persson, T. Y. Wang, K. L. Fry, and G. B. Stringfellow, *J. Appl. Phys.* **66**, 5554 (1989).
- [24] R. M. Feenstra, *J. Vac. Sci. Technol. B* **21**, 2080 (2003).
- [25] E. G. Scott, D. Wake, G. D. T. Spiller, and G. J. Davies, *J. Appl. Phys.* **66**, 5344 (1989).
- [26] M. B. Panish, R. A. Hamm, D. Ritter, and H. S. Luftman, *J. Cryst. Growth* **112**, 343 (1991).
- [27] E. Perkins, L. Barreto, J. Wells, and P. Hofmann, *Rev. Sci. Instrum.* **84**, 033901 (2013).
- [28] I. Shiraki, F. Tanabe, R. Hobarra, T. Nagao, and S. Hasegawa, *Surf. Sci.* **493**, 633 (2001).
- [29] I. Miccoli, F. Edler, H. Pfnür, and C. Tegenkamp, *J. Phys.: Condens. Matter* **27**, 223201 (2015).
- [30] S. Godey, S. Dhellemmes, A. Wilk, M. Zaknoute, and F. Mollot, *J. Cryst. Growth* **278**, 600 (2005).
- [31] S. Just, H. Soltner, S. Korte, V. Cherepanov, and B. Voigtländer, *Phys. Rev. B* **95**, 075310 (2017).
- [32] R. Dombrowski, Chr. Steinebach, Chr. Wittneven, M. Morgenstern, and R. Wiesendanger, *Phys. Rev. B* **59**, 8043 (1999).
- [33] V. Swaminathan, V. M. Donnelly, and J. Long, *J. Appl. Phys.* **58**, 4565 (1985).
- [34] E. W. Williams, W. Elder, M. G. Astles, M. Webb, J. B. Mullin, B. Straughan, and P. J. Tufton, *J. Electrochem. Soc.* **120**, 1741 (1973).
- [35] L. Biadala, W. Peng, Y. Lambert, J. H. Kim, D. Canneson, A. Houppé, M. Berthe, D. Troadec, D. Deresmes, G. Patriarche, T. Xu, X. Pi, X. Wallart, C. Delerue, M. Bayer, J. Xu, and B. Grandidier, *ACS Nano* **13**, 1961 (2019).
- [36] Y. Moon, S. Si, E. Yoon, and S. J. Kim, *J. Appl. Phys.* **83**, 2261 (1998).
- [37] C. H. Henry, R. A. Logan, F. R. Merritt, and C. G. Bethea, *Electron. Lett.* **20**, 358 (1984).
- [38] U. Cebulla, G. Bacher, A. Forchel, G. Mayer, and W. T. Tsang, *Phys. Rev. B* **39**, 6257, (1989).
- [39] M. Kemerink, J. W. Gerritsen, P. M. Koenraad, H. van Kempen, and J. H. Wolter, *Appl. Phys. Lett.* **75**, 3656 (1999).
- [40] R. Driad, Z. H. Lu, S. Charbonneau, W. R. McKinnon, S. Laframboise, P. J. Poole, and S. P. McAlister, *Appl. Phys. Lett.* **73**, 665 (1998).
- [41] M. J. Milla, J. M. Ulloa, and A. Guzmán, *Appl. Phys. Lett.* **100**, 131601 (2012).
- [42] S. Kasai, N. Negoro, and H. Hasegawa, *Appl. Surf. Sci.* **175**, 255 (2001).





## DIRAC ANTIDOT SUPERLATTICES FOR ELECTRONS IN III-V SEMICONDUCTORS

### Abstract

Graphene is one of the most fascinating materials ever discovered. The achievement of this single-layer carbon atoms in 2004, generated a lot of enthusiasm in the physics community. It represents the first realization of a naturally occurring two-dimensional material. In addition, the unique organization of the carbon atoms confers graphene exotic electronic properties, that are difficult to observe in any other conventional systems. Nevertheless, being a natural material, the carbon sheet comes in only one atomic arrangement: the atoms are organized in a hexagonal lattice and their positions are fixed. Nowadays, the electronic properties of graphene can be obtained by creating artificial materials having a triangular symmetry. These materials, known as "Dirac materials", represent a perfect platform for testing new quantum mechanical phenomena that cannot be observed in graphene.

Based on previous works and predictive atomistic tight-binding calculations, this thesis aims at creating a periodic potential with a honeycomb geometry in a two-dimensional electron gas. The electron gas will be hosted by an InGaAs quantum well grown on an InP layer by molecular beam epitaxy. Low temperature scanning tunneling microscopy and spectroscopy will be employed to characterize the InGaAs quantum well and evaluate the robustness of its two-dimensional nature as a function of the growth parameters. By pushing to their limit high resolution electron-beam or block copolymer lithographies, potential barriers with a honeycomb geometry will be nanopatterned in the InGaAs layer to directly confine the motion of the electrons. Thus, the realization of such hexagonal arrays of pores having between 45 and 20 nm periodicity will allow the formation of Dirac cones and non-trivial flat bands covering energy ranges up to tens of meV. The final Dirac material and its exciting physics will be investigated using low temperature scanning tunneling microscopy and spectroscopy. Based on the versatility of the nanopatterning process, the demonstration of the existence of Dirac cones and flat bands in the InGaAs/InP heterostructure could open new avenues in the engineering of more complex band structures in condensed matter physics.

**Keywords:** Antidot superlattices, III-V heterostructures, band structure engineering, Dirac cones, scanning tunneling microscopy, nano-fabrication

---

### Résumé

Le graphène est l'un des matériaux les plus fascinants jamais découverts. L'observation de cette monocouche d'atomes de carbone en 2004, a suscité beaucoup d'enthousiasme dans la communauté de la physique. Il représente en fait la première réalisation d'un matériau bidimensionnel naturel. De plus, l'organisation unique des atomes de carbone en réseau hexagonal lui confère des propriétés électroniques exotiques qui n'existent pas dans d'autres systèmes conventionnels. Néanmoins, étant un matériau naturel, les positions des atomes dans un feuillet de graphène sont figées et l'application d'une contrainte pour modifier le réseau ne permet pas d'altérer significativement la structure de bande du graphène. Ces dernières années, les propriétés électroniques du graphène ont été obtenues dans d'autres systèmes artificiels qui possédaient la particularité d'avoir une symétrie triangulaire. Ces matériaux, connus sous le nom de « matériaux de Dirac », représentent une plate-forme parfaite pour tester de nouveaux phénomènes quantiques non observables dans le graphène.

A partir des travaux antérieurs et de prédictions théoriques basées sur la méthode des liaisons fortes, ce travail de thèse vise à appliquer un potentiel périodique avec une géométrie en nid d'abeille à un gaz d'électrons bidimensionnel. Le gaz d'électrons sera créé dans un puit quantique d'InGaAs épitaxié par jet moléculaire sur une couche d'InP. Le puit d'InGaAs et en particulier, sa nature bidimensionnelle, seront d'abord caractérisées par microscopie et spectroscopie à effet tunnel à basse température pour déterminer les paramètres de croissance qui donnent la densité d'états électroniques la plus homogène possible. En poussant à leur limite les lithographies de faisceau d'électrons à haute résolution ou de copolymères à blocs, des barrières de potentiel en nid d'abeilles seront ensuite nanostructurées dans la couche d'InGaAs pour confiner directement le mouvement des électrons. Ainsi, la réalisation de réseaux hexagonaux ayant une périodicité comprise entre 45 et 20 nm permettra la formation de cônes de Dirac et de bandes plates non triviales couvrant des gammes d'énergie allant de quelques meV jusqu'à des dizaines de meV. Le matériau de Dirac obtenu et notamment sa densité d'états seront étudiés en utilisant la microscopie et la spectroscopie à effet tunnel à basse température. En raison de la souplesse des procédés de nanofabrication utilisés, la démonstration de l'existence de cônes de Dirac et de bandes plates dans la bande de conduction de l'hétérostructure InGaAs/InP donne des perspectives intéressantes pour élargir le champ des matériaux artificiels possédant des structures de bandes toujours plus complexes.

**Mots clés :** Super-réseau d'antipoints, hétérostructures à base III-V, ingénierie de structure de bande, cônes de Dirac, microscopie à effet tunnel, nano-fabrication

---

**Institut d'électronique de microélectronique et de nanotechnologie**

Avenue Henry Poincaré – CS60069 – 59652 – Villeneuve d'Ascq – FRANCE